Title

A study of time-dependent responses of a mechanical displacement ventilation (DV) system and an underfloor air distribution (UFAD) system : building energy performance of the UFAD system

Author

Yu, Jong Keun

Publication Date

2010

Peer reviewed|Thesis/dissertation

UNIVERSITY OF CALIFORNIA, SAN DIEGO

A study of time-dependent responses of a mechanical Displacement Ventilation (DV) system and an Underfloor Air Distribution (UFAD) system; Building energy performance of the UFAD system

A dissertation submitted in partial satisfaction of the
requirements for the degree
Doctor of Philosophy

in

Engineering Sciences (Mechanical Engineering)

by

Jong Keun Yu

Committee in charge:

Professor Paul F. Linden, Chair
Professor Sutanu Sarkar
Professor Stefan Llewellyn Smith
Professor Robert Pinkel
Professor Kraig B. Winters

2010

The dissertation of Jong Keun Yu is approved, and it is acceptable in quality and form for publication on microfilm and electronically:

_____

_____

_____

_____

Chair

University of California, San Diego

2010

DEDICATION

To my two lovely daughters, Ashley and Chloe, my wife, and my parents who gave me endless loves.

TABLE OF CONTENTS

LIST OF FIGURES

LIST OF TABLES

ACKNOWLEDGEMENTS

I am deeply thankful to my academic advisor, Prof. Paul F. Linden. I cannot imagine any moment of my graduate study without his supports and encouragements. I also thank his support in writing and proof-reading this thesis. I am especially grateful to my parents and my family, my wife and my lovely daughters, Ashley and Chloe for their endless supports and loves. It is an honor for me to thank all thesis committees, Prof. Sutanu Sarkar, Prof. Stefan Llewellyn Smith, Prof. Robert Pinkel and Prof. Kraig B. Winters for their helpful comments. I would like to thank the financial supports of UCEI (University of California Energy Institute) and BERG (Building Energy Research Grant) programs for completing this thesis. It is also an honor for me to work with all BERG project members, Tom Webster, Fred Bauman, Stefano Schiavon, Kwang Ho Lee and Allan Daly. They inspired me what a real teamwork is and broadened my understanding of building energy simulation. I cordially thanks to Nick Daish for proof-reading and revising Chapter 4 & 5. I also thanks to all of emotional supports and advices from my friends.

Chapter 4 & 5, in part, includes reprints of the material as it appears in "Final report: Simulation of energy performance of Underfloor Air Distribution (UFAD) system", *Building energy research grant (BERG) program.*, (Grant number: 54917A/06-05B), Linden, P., Webster, T., Bauman, F., Yu, J.K., Lee, K.H., Schiavon S., and Daly, A. 2009. The dissertation author was the primary investigator and author of the paper.

VITA

2002	B. S. Mechanical Engineering, Chung Ang University, Seoul, Rep. of Korea
2005	M. S. Mechanical Engineering, University of San Diego
2005-2010	Graduate Research Assistant, University of California, San Diego
2010	Ph. D. Mechanical Engineering, University of San Diego

PUBLICATIONS

Linden, P F, & Yu, J. K. 2007. "Modeling the Flow in an Underflow Plenum.", *UC Berkeley: University of California Energy Institute., UC Berkeley* **Development and Technology, UER-381-FR**

Linden, P., Webster, T., Bauman, F., Yu, J.K., Lee, K.H., Schiavon S., and Daly, A. 2009, "Final report: Simulation of energy performance of Underfloor Air Distribution (UFAD) system", *Building energy research grant (BERG) program.*, **Grant number: 54917A/06-05B**

ABSTRACT OF THE DISSERTATION

A study of time-dependent responses of a mechanical Displacement Ventilation (DV) system and an Underfloor Air Distribution (UFAD) system; Building energy performance of the UFAD system

by

Jong Keun Yu

Doctor of Philosophy in Engineering Sciences (Mechanical Engineering)

University of California, San Diego, 2010

Professor Paul F. Linden, Chair

As alternative systems for saving cooling energy compared to conventional overhead (OH) air-conditioning systems, mechanical displacement ventilation (DV) systems and underfloor air distribution (UFAD) systems have been widely adopted for commercial buildings. In these alternative systems, supply air is discharged from low momentum diffusers located at lower positions close to the floor in the DV system, and the supply air of the UFAD system is distributed by an underfloor plenum and discharged from floor diffusers. To predict transient vertical temperature responses when the heat source or the ventilation flow rate vary in time, we introduce transient two-layer stratification models of the DV and UFAD systems, non-dimensionalize them by competing

the filling box time (Baines & Turner 1969) and the replenishment time in which all the air in the enclosure is replaced by supply air and validate them by laboratory experiments using a salt-water analogy. In various scenarios of the heat source and the ventilation flow rate, the models show a good agreement with the laboratory experiments.

Building energy simulation, which predicts cooling and heating demands of a building, has been used for building design, environment, economics, and occupant comfort. EnergyPlus, which is a building energy simulation tools developed by the U.S. Department of Energy, has integrated capability to predict cooling and heating demands as well as the HVAC (heating, ventilation and air conditioning) energy consumption. To evaluate performance of energy savings of UFAD, we developed prototype office buildings adopting OH and UFAD, and the UCSD-UFAD model was used to estimate realistic cooling and heating demands by simulating the stratified temperature profile in a room. In Californian climates, annual electricity consumption of UFAD is always lower than that of OH by up to 20 %, since UFAD has more opportunities to utilize the economizer "free cooling" compared to OH. For electricity demand reduction of various Demand Response (DR) activities, increasing room set point temperature is the most effective DR activity and UFAD has higher peak demand reduction compared to OH by approximately 6-10 % when the room set point temperature is higher than 26 ^{o}C.

Chapter 1

Introduction

1.1 Motivation

The indoor environment in a building, or within a built environment, provides occupants a space with desirable thermal comfort and indoor air quality (IAQ) in various climates. For example, in climates which have hot and humid summers, which typically occur in eastern and mid Asia, southern American or European countries, a building is required to keep occupants cool and dry. However, in northern countries of each continent (in the northern hemisphere), a building should provide occupants sufficient heating to keep them warm during survive from the cold weather. Characteristics of various climates strongly influenced ways of cooling or heating before modern cooling or heating systems were widely adopted.

For example, in locations with very hot and dry weather, a typical residential building has thick exterior walls to reduce heat transfer through the walls. However, such a building may have poor ventilation for removing interior heat loads such as metabolism of occupants, heat transfer through walls etc. without proper ways of ventilating indoor air. To enhance the ventilation, a windcatcher, a chimney specially designed for supplying outdoor air into the room from wind and extracting the interior heat, was used to keep the indoor environment fresh and cool by delivering outdoor fresh air to occupants and extracting indoor heated and polluted air from the room (Figure 1.1). Additionally, the system is only operated by wind, which means that a building can be ventilated without using energy. There are the examples of modern natural ventilation

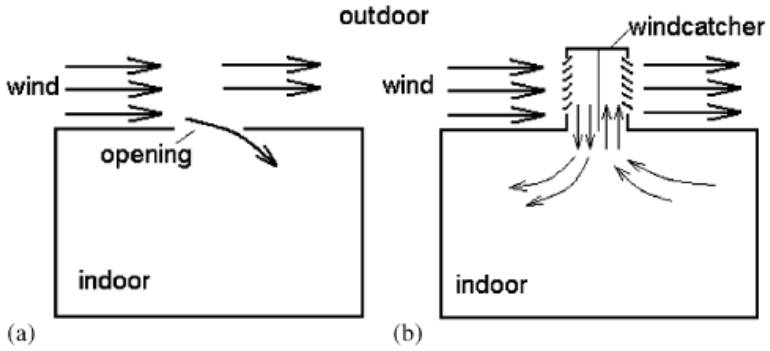

Figure 1.1: Comparison of different ventilated rooms. (a) Rooms without windcatcher; (b) Rooms with windcatcher: Figures obtained from [36]

system applied to commercial buildings, such as the Queens Building at Demonfort University and the BRE office of the future in the U.K [36].

In Eastern Asia, where there are a hot and humid summers and a cold winter, a building needs to provide occupants sufficient cooling as well as heating. A traditional building in Eastern Asia had relatively large openings such as windows or doors for promoting interior ventilation efficiency. However, to overcome the cold winter, heating was also critical for residential buildings. For example, Korean traditional residences adopted underfloor heating system, which is called an “Ondol”. Smoke from a fireplace is delivered to a space (which is an open plenum to allow the smoke to travel freely) below the floor slab which heats the slab through convective heat transfer as seen in Figure 1.2. The heated floor slab warms the room through convective heat transfer as well as radiative heat transfer. Additionally, the floor slab was also used as thermal storage to keep the slab warm for a long time [48]. Enhanced occupant thermal comfort was also achieved by even temperature distribution over whole floor slab. The thermal comfort of the system inspired Frank Lloyd Wright, the famous American architect, to adopt the system in the Imperial Hotel, built in Tokyo, Japan in the 1920s. As a modernized underfloor heating system, the heated air plenum is replaced by electrical system with electrical heating coil or hot water system with hot water coil. According to [48], in Korea, approximately 90 % of residential buildings use the underfloor systems and recently, 30 $\sim$ 50 % of new residential buildings in Germany, Austria and Denmark

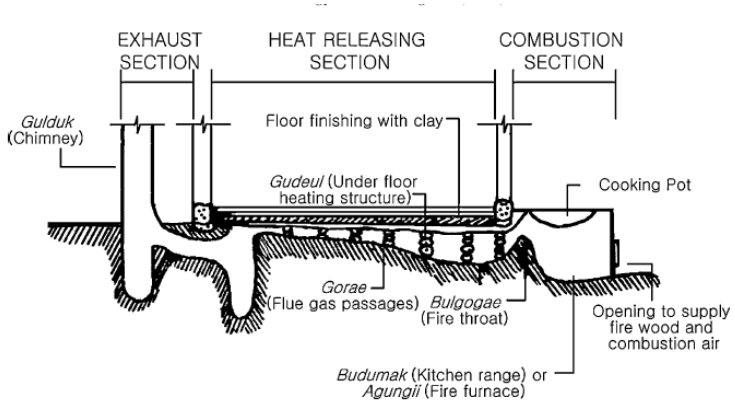

Figure 1.2: Schematic of traditional underfloor heating system, “Ondol” in Korea [63]

also adopted the system in 2002.

Even though the traditional ways of cooling or heating in various climate had provided successfully desirable indoor environments, rapid growth of urban areas after the industrial revolution in the 18th century increased strong demands for alternative cooling and heating systems to substitute for tradition cooling or heating systems which had limited capability to provide sufficient cooling or heating in a building which has relatively high occupancy or large indoor spaces such as theaters, libraries and atria, etc..

After the revolutionary Frank Lloyd Wright’s Larkin Building, which is the first atrium office building to use a form of air conditioning (main pillars cooled by water mist circulated and cooled air) in 1905 [59], various concepts for replacing the traditional systems had been proposed. As a pioneering leap to the modern cooling system, in 1950, Carrier in the U.S, developed an air conditioning system with a chiller, or heat exchanger, operated by an evaporator and compressor to cool down interior air. During heat exchange within an evaporator, humidity can be also removed by condensation, so the system reduces room humidity as well as temperature. After the great success of this air conditioning system, it became a standard for cooling in most indoor environments

worldwide.

As a consequence, electricity usage for cooling in urban area has increased because most air conditioning system uses electricity to operate a chiller or a fan. In 2008, UN claimed “half the world’s population will live in urban areas by end of 2008” (International Herald Tribune (February 26, 2008)), so the cooling electricity consumption has become important issue for energy sustainability or national energy policy. Electricity consumption for air conditioning system (cooling) for residential buildings was 8 % of entire residential electricity usage in the U.S in 2005 (RECS) and the percentage for commercial buildings was 16 % for cooling and 12 % for ventilation of the entire commercial building energy usage (CBECS). In the southern U.S. which has relatively hot summers, the electricity consumption for air conditioning was 17 % for residential buildings and 19 % for commercial buildings based on RECS and CBECS. Even in California which has relatively mild summers, commercial buildings used 13 % for cooling and 12 % for ventilation. Furthermore, recently, the average retail price of electricity to commercial customers in 2009 has increased by about 28 % compared to 2000 according to the U.S. Department of Energy [47].

As a solution to energy saving for cooling, improving ventilation efficiency is one of the most important engineering issues, but it is not easily achieved without a knowledge of the internal flow dynamics in a room. Conventional cooling systems, or over head (OH) systems, introduce cool air from the ceiling which effectively stirs the cool air into the interior hot air by mixing (Figure 1.3(a)). To enhance the ventilation efficiency, a higher temperature difference between supply air temperature and return temperature is necessary. However, in an OH, mixing makes the room temperature the same as the return temperature. In a system which induces stable stratification (warmest air near ceiling) in a space, the temperature difference increases and the ventilation efficiency also increases. Alternative ventilation systems such as displacement ventilation or underfloor air distribution (UFAD) systems can keep a room stably stratified, so these ventilation efficiencies of the systems are expected to be higher than OH. Descriptions of the alternative systems are given below.

1.1.1 Displacement Ventilation system

As a successful alternative cooling system to an OH system, displacement ventilation (DV) system has been used in Scandinavia countries ([55]) which have relatively mild summers. Supply air is discharged from low momentum diffusers located at lower positions close to the floor. This configuration avoids direct mixing between heat plumes and the supply air due to low momentum of the supply air. Consequently, a stable thermal stratification (high temperature near ceiling and low temperature close to floor) forms, which increases the return air temperature at the ceiling. The increased return temperature in DV improves its ventilation efficiency compared to OH. However, due to the thermal stratification, occupants may experience "cold feet". As a remedy for "cold feet", the supply air temperature of DV is suggested to be at least $4 \sim 8$ ^{o}C higher than that of OH.

There is another issue of thermal discomfort of DV system caused by the thermal stratification. The vertical temperature profile is not uniform in a room conditioned by DV, which may cause occupants to have discomfort due to temperature difference between head and feet. According to ASHRAE standard 55-2004, the vertical temperature difference between 0.1 and 1.7 m above the floor should be no more than 3 ^{o}C. In practice, a thermal interface which separates the lower cool air zone, or occupied zone, to upper mixed hot air zone near the ceiling is observed [19], which causes discomfort when the interface is within the occupied zone and the temperature difference is higher than 3 ^{o}C. To avoid this thermal discomfort, DV should maintain desirable veritcal temperature profile under various interior heat loads, which is not easily achieved without knowing the physical relation between the temperature profile, the strength of heat plumes and supply air quantity. Various models considering the physical relations were proposed from the end of 1980s ([53], [51], [46]). Those models were developed to predict vertical temperature profile and were validated by experimental measurements. However the models were restricted to steady states and did not predict the time dependence of the temperature profile. Because, in practice, the interior heat loads vary dynamically in time, the steady-state models cannot provide us with accurate temperature prediction in transient cases. Therefore, in our study, we propose to develop a transient model to predict temporal response of the temperature profile based on the

strength of heat plumes and the supply air quantity in Chapter 2.

Despite the superior ventilation efficiency of the DV system, there are several disadvantages of the DV system for residential or commercial buildings. First, the DV system has trouble maintaining desirable thermal stratification. To improve ventilation efficiency of the DV system, the supply air diffuser with lower momentum is required to be installed in the lower part of a room, which makes it hard to distribute the conditioned air in a room compared to OH. If the lower momentum diffusers are sparsely positioned, an occupant could experience thermal discomfort, i.e. “cold feet” caused by horizontally and vertically unevenly distributed conditioned air. For that reason, maintaining an even temperature distribution in a DV system is regarded as an important problem to improve occupant’s thermal comfort. Additionally, DV has a lower cooling capacity compared to OH due to the difficulty of distributing the low momentum supply air diffuser in practice. These are the reasons why the DV system had not been popular in a residential or commercial buildings.

1.1.2 Underfloor Air Distribution system

The UFAD system was introduced as an alternative cooling system for a data center or lab facility which had high cooling demands in 1960 because of higher ventilation efficiency compared to OH. UFAD overcomes a disadvantage of DV’s low cooling capacity by distributing the conditioned air through an underfloor plenum, which is an open space to allow the air to travel freely. Consequently, UFAD can increase cooling capacity compared to DV while UFAD also has same advantage of higher ventilation efficiency of DV system. Additionally, UFAD also can avoid ventilation inefficiency caused by the closeness between the inlet and the outlet. While inlets and outlets in UFAD are separately positioned at floor and the ceiling, respectively, those in OH are positioned only at the ceiling as seen in Figure 1.3.

From 1970, UFAD was installed in residential and commercial buildings as an alternative cooling system. In west Germany, UFAD was applied in an office building as it also provided advantages of easiness of electrical cable installation in addition to ventilation efficiency [54]. In the past 10 years, the popularity of UFAD has been growing in the U.S. [7]. There are several potential benefits of improved thermal comfort,

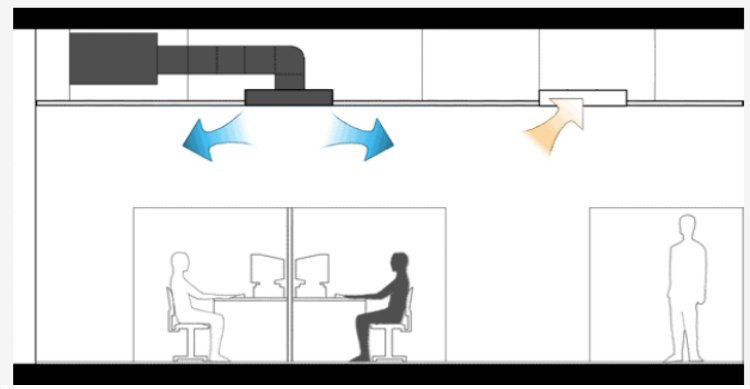

(a)

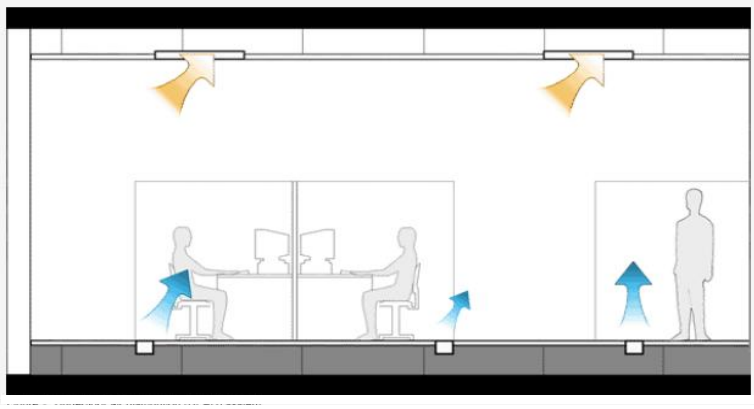

(b)

Figure 1.3: Schematics of OH and UFAD. (a) OH (b) UFAD; figures obtained from [7]

improved indoor air quality and reduced cooling energy. For example, various recent projects of commercial buildings have been successfully implemented; Two Market-Pointe, St. Paul, MN, U.S. and Richard J. Klarchek Information Commons in Chicago, IL ([41]).

In UFAD, supply air is distributed by an underfloor plenum and discharged from floor diffusers. Similar to DV, the vertical temperature profile in UFAD is dominated by two physical quantities, the strength of heat plumes and the supply air quantity. The temperature is stably stratified, so the same concerns about the stratification on comfort occur with both UFAD and DV. Steady-state models of the stratification determined by the strength of heat plumes and the supply air quantity were proposed for a single plume and diffuser flow in [29] and multi plumes and diffusers in [37]. The UFAD models had physical concepts of the formation of the thermal stratification and conservation of volume and buoyancy fluxes across the thermal interface similar to the DV models. Additionally, the UFAD models also considered a process to warm the occupied zone when the diffuser jet perturbs or penetrates the interface. The diffuser jet takes the form of a negatively buoyant jet because the cold supply air is heavier than its surrounding environment. Penetrative entrainment across the thermal interface is the main cause of the warm-up process. Detailed reviews of a heat or buoyant plume, a negatively buoyant jet and the penetrative entrainment will be provided in § 1.2.

However, in practical UFAD operation, interior heat loads and the supply air quantity cannot be assumed to be constant in time, and the current steady-state models can not capture the temporal response of the temperature profile in the practical operation. For this reason, a transient UFAD model is proposed to predict the temporal responses of vertical temperature profile when the strength of heat plumes and supply air quantity vary in time. The transient model is also validated by salt-water analogy experiments to simulate various UFAD operating condition. Details of the model and experimental validation are given in Chapter 3.

1.2 Theoretical concepts

1.2.1 Buoyant plume

The entrainment hypothesis, which was introduced by [44], proposed that inflow mean velocity across edge of buoyant plume or jet is proportional to the averaged vertical maximum velocity over the cross section at a certain height when the plume or jet is surrounded by homogeneous environment. Even though velocity and density profiles over the cross section of the plume have been observed and described as Gaussian profiles, a top-hat distribution of velocity and density of the plume or jet proposed in [44] should simplify the Gaussian profiles to two constant values, $\bar{w}$ and $\bar{g'}$, respectively, given as

$$\bar{w} = \frac{1}{\pi b^2(z)} \int_0^{b(z)} 2\pi r w_g(r,z) dr, \tag{1.1}$$

$$\bar{g'} = \frac{1}{\pi b^2(z)} \int_0^{b(z)} 2\pi r g'_g(r,z) dr, \tag{1.2}$$

where the Gaussian profile of velocity and reduced gravity are defined as

$$w_g(r,z) = w_m(z) exp\{-r^2/(2b_m^2(z))\}, \tag{1.3}$$

$$g'_g(r,z) = g'_m(z) exp\{-r^2/(2b_m^2(z))\} \tag{1.4}$$

($w_m(z)$, $b_m(z)$ and $g'_m(z)$ are cross-sectional mean values of velocity, radius, and reduced gravity at z). A schematic of the top-hat profile of buoyant plume is given in Figure 1.4.

From dimensional analysis of a plume using buoyancy flux B and height z, the top-hat velocity $\bar{w}$ and reduced gravity $\bar{g'}$ scale as

$$\bar{w} \sim B^{1/3} z^{-1/3}, \quad \bar{g'} \sim B^{2/3} z^{-5/3}, \quad \text{and} \quad b \sim z. \tag{1.5}$$

Based on the entrainment hypothesis, conservation of volume flux, momentum

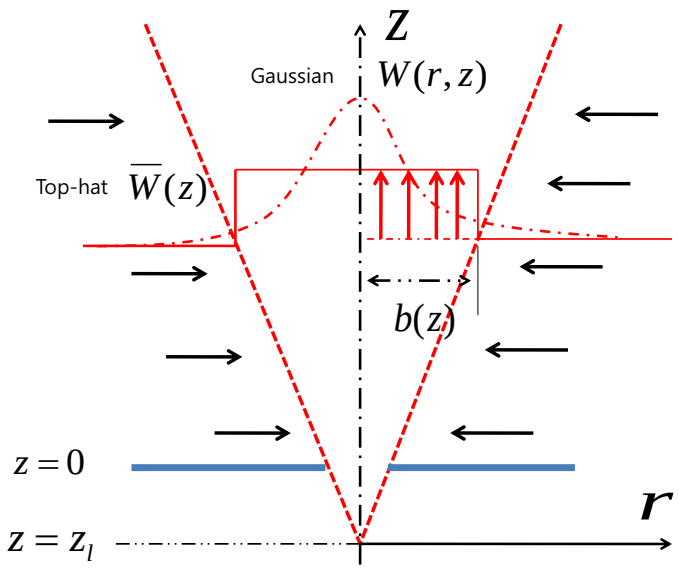

Figure 1.4: Schematic of a turbulent plume with a top-hat vertical velocity and a linearly increasing radius with height. Ambient fluid is entrained into the plume; solid line (red) is top-hat profile : $w(z)$ and dot dash is gaussian profile : $w(r,z)$, the half width $b = b(z)$

flux and buoyancy flux became

$$\frac{d\ b^2\bar{w}}{dz} = 2b\alpha\bar{w} \tag{1.6}$$

$$\frac{d\ b^2\bar{w}^2}{dz} = b^2(g'_o - \bar{g'}), \tag{1.7}$$

$$\frac{d\ b^2\bar{w}(g'_o - \bar{g'})}{dz} = b^2\bar{w}\frac{dg'_o}{dz}, \tag{1.8}$$

where α is the entrainment coefficient and g'_o is reduced gravity of ambient fluid surrounding the plume or jet. In a homogeneous ambient ($\frac{dg'_o}{dz} = 0$), (1.6) and (1.8) can be solved analytically to give

$$b = \frac{6}{5}\alpha z \tag{1.9}$$

$$\bar{w} = \frac{1}{C\pi^2\alpha^2}B_o{}^{1/3}z^{-1/3} \tag{1.10}$$

$$\bar{g'} = \frac{1}{C}B_o{}^{2/3}z^{-5/3} \tag{1.11}$$

where B_o is buoyancy flux at the plume source and $C = (\frac{5}{6})(\frac{9}{10}\pi^2)^{-1/3}\alpha^{-4/3}$ is a constant value related to the entrainment coefficient α. From the solutions, we obtain the volume flux $Q = \pi b^2 \bar{w}$,

$$Q = CB_o^{1/3} z^{5/3}. \tag{1.12}$$

The analytic solutions of b, $\bar{w}$ and $\bar{g'}$ in homogeneous ambient fluid agree with the proportional relations of the dimensionless analysis in (1.5).

With volume flux $Q = \pi b^2 \bar{w}$, momentum flux $M = \pi b^2 \bar{w}^2$ and buoyancy flux $B = Q\bar{g'}$, (1.6)-(1.8) can be rewritten as

$$\frac{dQ}{dz} = 2\pi^{1/2}\alpha M^{1/2}, \tag{1.13}$$

$$\frac{dM}{dz} = \frac{BQ}{M}, \tag{1.14}$$

$$\frac{dB}{dz} = -N^2 Q, \tag{1.15}$$

where $N^2 = -\frac{dg'_o}{dz}$ is the buoyancy frequency of the ambient fluid. In homogeneous ambient ($N^2 = 0$), the buoyancy flux B is conserved ($\frac{dB}{dz} = 0$), so $B(z) = B_o$ at all heights. For inhomogeneous ambient ($N^2 \neq 0$), the buoyancy flux is not conserved and it is not guaranteed to have analytic solution for all circumstances ([44]).

The ideal plume itself has no volume flux ($Q_o = 0$) at the origin. The given analysis are provided for the ideal situation, (1.6)-(1.8) need to be reformulated to consider any situation in which Q_o is non zero. To make the reformulation as simple as possible, virtual origin corrections ([44], [43], [4], [45]) were proposed. The virtual origin correction sets the origin of the actual plume as a virtual point $z = z_v$, at which it has zero volume flux (See Figure 1.4).

Among various approaches to estimate the virtual origin, we choose a method of source correction based on the plume properties, such as initial buoyancy flux F_o, momentum flux M_o and volume flux Q_o. Morton [43] showed that a plume flow of (F_o, M_o, Q_o) at $z = 0$ can be equivalent to a modified plume flow of $(F_o, \gamma M_o, 0)$ at $z = z_v$. A equation to estimate z_v was given as

$$\frac{z_v}{L_m} = -10^{1/2}|\gamma|^{3/2} sgn(F_o) \int_{sgn(\gamma)}^{1/|\gamma|} |T^5 - sgn(\gamma)|^{-1/2} T^3 dT, \tag{1.16}$$

where $\gamma^5 = 1 - \Gamma$ (Γ is defined as a source parameter $\Gamma = \frac{5Q_o^2 F_o}{4\alpha M_o^{5/2}}$)and momentum jet length scale $L_m = 2^{-3/2}\alpha^{-1/2}\frac{M_o^{3/4}}{F_o^{1/2}}$, $sgn(F_o) = \pm 1$ and $sgn(\Gamma) = \pm 1$. Physical interpretations of Γ are i) a pure plume when $\Gamma = 0$, ii) forced buoyant plume when $0 < \Gamma < 1$ and iii) a lazy plume in which momentum flux by buoyancy force is traded off against the initial momentum flux by forcing the buoyant fluid downward to produce positively buoyant plume with low ascending velocity at $z = 0$ when $\Gamma > 1$. However, it is physically unrealistic to have $\gamma < 0$ when $\Gamma > 1$ for a lazy plume, so a two-step correction was required.

To provide a physically realistic solution of a laze plume, Kaye and Hunt [21] proposed an equation to estimate z_v:

$$\frac{z_v}{\frac{5}{6\alpha_g\sqrt{2\pi}}\frac{Q_o}{M_o^{1/2}}} = \Theta^{-1/5}(1-\delta) \quad \text{for} \quad \Theta > \frac{1}{2}, \tag{1.17}$$

where α_g is the entrainment coefficient for a Gaussian profile and a source parameter Θ is defined as

$$\Theta = \frac{5}{2^{7/2}\alpha_g\sqrt{\pi}}\left(\frac{Q_o^2 B_o}{M_o^{5/2}}\right). \tag{1.18}$$

δ denotes the summation

$$\delta = \frac{3}{5}\sum_{n=1}^{\infty}\left(\frac{\phi^n}{5^{n-1}n!(10n-3)}\prod_{j=1}^{n}(1+5(j-1))\right) \tag{1.19}$$

where $\phi = \frac{\Theta - 1}{\Theta}$.

Because the plume flow in our experiment was assumed to be a lazy plume, (1.17) is used for estimating z_v which ranged from 1.0 to 2.0 cm. The range of z_v is relatively small compared total height of experimental tank (25 cm or 39 cm). With z_v, the equation for the plume flow rate (1.12) should be reformulated as

$$Q = CB_o^{1/3}(z + z_v)^{5/3}. \tag{1.20}$$

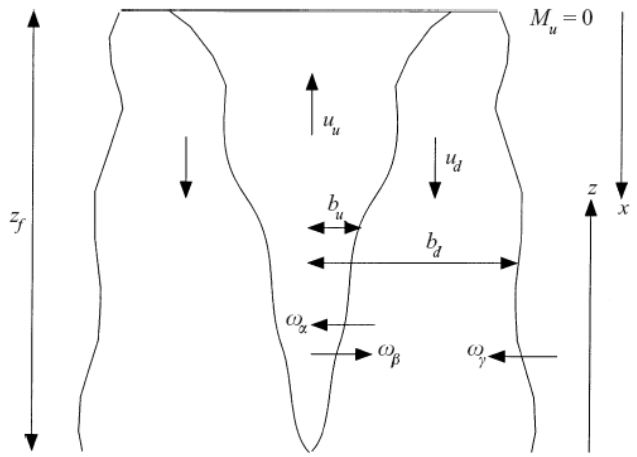

Figure 1.5: Model of a turbulent fountain, indicating the various quantities and properties that are included in the equations. [11]

1.2.2 Negatively buoyant jet

A denser jet surrounded by lighter ambient is called a negatively buoyant jet. To overcome the negative buoyancy, sufficient initial momentum at the origin of the denser jet is required. The jet rises to reach a maximum height and falls back to the bottom. When the jet shoots upwards (against gravity), the falling flow wraps around the original upward jet flow and increases the chance to have additional shear between the upflow an the downflow. Numerous studies ([10], [1], [20]) have been performed to propose corrections of the entrainment coefficient of the upflow ($0.076 \pm 0.004 \leq \alpha \leq 1.117 \pm 0.004$).

The jet properties of volume flux, momentum flux and buoyancy flux of upflow (subscript 'u') and downflow (subscript 'd') at certain height are given as

$$Q_u = \pi b_u^2 u_u, \quad Q_d = \pi (b_d^2 - b_u^2) u_d, \tag{1.21}$$

$$M_u = \pi b_u^2 u_u^2, \quad M_d = \pi (b_d^2 - b_u^2) u_d^2, \tag{1.22}$$

$$F_u = \pi b_u^2 u_u \Delta_u, \quad F_d = \pi (b_d^2 - b_u^2) u_d^2 \Delta_d, \tag{1.23}$$

where $\Delta_u = g/\rho_o(\rho_o - \rho_u)$ ($\Delta_u > 0$) and $\Delta_d = g/\rho_o(\rho_d - \rho_o)$ ($\Delta_d < 0$). Bloomfield &

Kerr [11] suggested that the entrainment velocities is relevant to the total shear, so the entrainment velocities were defined as

$$w_\alpha = \alpha u_u, \quad w_\beta = \beta u_d, \quad w_\gamma = \gamma u_d \tag{1.24}$$

with entrainment coefficients, α, β and γ. In homogeneous fluid, by satisfying the conservation of volume flux, the equations of the upflow and the downflow are given as

$$\frac{d}{dz}(b_u^2 u_u) = 2b_u w_\alpha - 2b_u w_\beta, \tag{1.25}$$

$$\frac{d}{dx}([b_d^2 - b_u^2]u_d) = 2b_d w_\gamma - 2b_u w_\alpha + 2b_u w_\beta, \tag{1.26}$$

respectively, and the equations for conserving buoyancy flux for the upflow and the downflow are given as

$$\frac{d}{dz}(b_u^2 u_u \Delta_u) = -2b_u w_\alpha \Delta_d - 2b_u w_\beta \Delta_u, \tag{1.27}$$

$$\frac{d}{dx}([b_d^2 - b_u^2]u_d \Delta_d) = -2b_d w_\gamma \Delta_d - 2b_u w_\beta \Delta_u, \tag{1.28}$$

respectively. By solving the equations (1.25) - (1.28) numerically, the jet properties were obtained. The models for stratified fluids were also derived in [11]. The final shooting height z_f was estimated by solving the equations to find the height where $M_u = 0$

In UFAD, the numerical solutions of the negatively buoyant jet of [11] are only useful when the density interface reaches the ceiling at which point the density interface is assumed to disappear and two layer stratification is no longer valid. The surrounding fluid then becomes homogeneous. However, when a two-layer stratification forms, the solutions are no longer valid to predict the jet properties because the downflow of the jet does not wrap the upflow below the upper zone. According to [3], in a two-layer fluid, the downflow can become trapped at density interface, then go on to spread radially outward, so a straightforward application of the diagnostic in [11] is inappropriate for two-layer fluids.

In our study, the diffuser jets are assumed to be strong enough to penetrate the upper zone and in every experiment penetration occurred, so we do not consider the

numerical solutions of [11]. Instead, we used an alternative approach, which is called the Lagrangian method described in [27], to estimate the jet properties, especially volume flux of the diffuser jet where the penetration across the interface occurs, similar to [3] which derived the solutions of the final shooting height and volume flux at a height for a point source flow ($Q_o = 0$ at $z = 0$). In practice, because the diffuser jet cannot be assumed to be a point source, we derived an alternative solution when the source has a radius $Q_o > 0$. The detailed description will be given in § 3.2.2.3.

1.2.3 Penetrative entrainment across the density interface

Penetrative entrainment across a density interface is a mechanism of entraining fluid at the interface between buoyancy layers caused by externally driven turbulence. To generate the external turbulence, mechanical stirring, such as an oscillating grid ([56]) and penetrative plume or jet ([4]), or shear-flow turbulence produced by a surface stress ([23]) were used.

In Turner's experiment [56], to parameterize the entrainment at the interface, local variables, such as the buoyancy step $\Delta\rho$, the velocity scale w and integral length scale l at the interface were chosen and local Richardson number Ri was defined as

$$Ri = \frac{\Delta\rho\ l}{w^2}. \tag{1.29}$$

The entrainment velocity u_e was indirectly measured by the rate of the density interface height change

$$u_e = \frac{dh}{dt} \tag{1.30}$$

where h is the the interface height. Defining the dimensionless entrainment rate $E = u_e/w$, the experimental results showed a good agreement with

$$E \sim Ri^n \tag{1.31}$$

where $n = -1$ for thermal step or $n = -3/2$ for salinity step across the interface.

Baines [4] conducted a set of experiments in which the plume or jet is strong enough to penetrate the density interface and showed that entrainment across the density

interface depends only on the buoyancy step across the interface and plume properties when the plume impinges the interface, such as the width of plume and the centerline velocity, which are combined into a dimensionless parameter Ri (Baines [4] suggested using Fr which is $Fr = Ri^{-1/2}$, but we use Ri instead of Fr for simplicity):

$$Ri = \frac{\Delta\rho b}{w^2}, \tag{1.32}$$

where w is the centerline velocity of the plume at the interface, b is the impinging radius at the interface, and $\Delta\rho$ is the reduced gravity step across the interface. An empirical relation was found in his experiment between Ri and entrainment rate E ($E = Q_e/Q_i$ where Q_e is measured entrainment volume flux and Q_i is volume flux of impinging plume flow) of the form

$$E \sim 0.1Ri^{-3/2} \tag{1.33}$$

when $Ri > 0.83$.

According to [32], a proportional the relation $E \sim Ri^{-3/2}$ agrees with experimental measurements of grid-generated turbulence ([56]) and a plume incident on the interface ([5]). A similar proportional relation between Ri and E, $E \sim Ri^{-3/2}$ was also suggested when a vortex ring interacted with a sharp density interface by Linden [32].

Kumagai [26] examined a broader range of the Richardson numbers, $0.1 < Ri < 70$ for the plume incident on the interface than that in [5] and suggested an empirical relation:

$$E = \frac{Ri^{-3/2}}{1 + 3.1Ri^{-1} + 1.8Ri^{-3/2}}. \tag{1.34}$$

He also suggested a mixing law of $E =$ constant when $Ri \to 0$ ($Ri < 0.25$) based on his experimental results. According to [12], Kumagai's results in an intermediate range of Ri, $1.2 < Ri < 30$ can also be modeled as $E \propto Ri^{-1}$.

The penetrative entrainment can also explain how much heat exchange between the upper hot air zone and the lower occupied zone occurs when the diffuser jet penetrate into the upper zone in UFAD. The entrainment caused by the penetration of the diffuser jet brings the upper hot air into the lower zone to warm the lower zone. Lin and Linden [31] suggested a constant entrainment rate E in a range between 0.55 and 0.65 when $0.2 < Ri < 1$, which is the range of Ri when the diffuser jet has relatively

high momentum flux M_o compared to buoyancy flux F_o. Liu [37] examined broader Ri, $1 < Ri < 40$, which suggested a model which $E \sim 0.6$ if $Ri < 8$ and $E \propto Ri^{-1}$ if $Ri > 8$.

1.3 EnergyPlus : a building energy simulation

Building energy simulation has been developed to predict cooling or heating energy consumption for various building configurations or climates since 1960. For the past 40 years, building simulation has been used for building design, environment, economics, occupant comfort and safety. For example, the simulation was extended to investigate various applications for predicting the impact of climate change on building thermal performance ([58]), optimizing building energy consumption of HVAC operation ([18]), or validating energy saving of renewable energy resources such as geothermal energy ([28]) or solar energy produced by photovoltaics ([42]). In 1995, the U.S. Department of Energy (DOE) planned a new generation of building simulation tools for integrating the DOE pre-sponsored programs, DOE-2 developed by LBNL, and BLAST developed by U.S. Army Construction Engineering Research Laboratories and University of Illinois, to create a well-organized and modular structured program which facilitates newly developed features or simulation models ([15]). The first working version EnergyPlus 1.0 was released to the public in 2001.

Input data of EnergyPlus contains building geometry, material properties, HVAC configuration and operating schedule. EnergyPlus supports a simple input format to accept any input data produced by preprocessors for BLAST and DOE-2. Third party developers, such as Designbuilder (DesignBuilder Software Ltd, UK), are also capable of generating EnergyPlus input format of building geometry.

For weather information, the DOE also provides text-based format EnergyPlus weather data derived from the typical meteorological year 2 (TMY2) weather format for more than 2100 locations; 1042 locations in the USA, 71 locations in Canada, and more than 1000 locations in 100 other countries throughout the world. As outputs, EnergyPlus can save results for each time step in a simple variable-based format to provide easy linkage to a post-processing program.

Among various improvements from the DOE pre-sponsored programs, BLAST

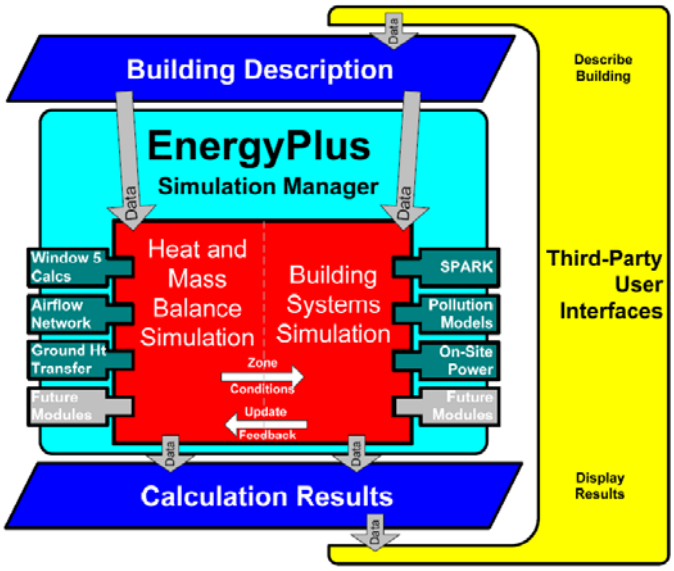

Figure 1.6: Overall Energyplus structure: [15]

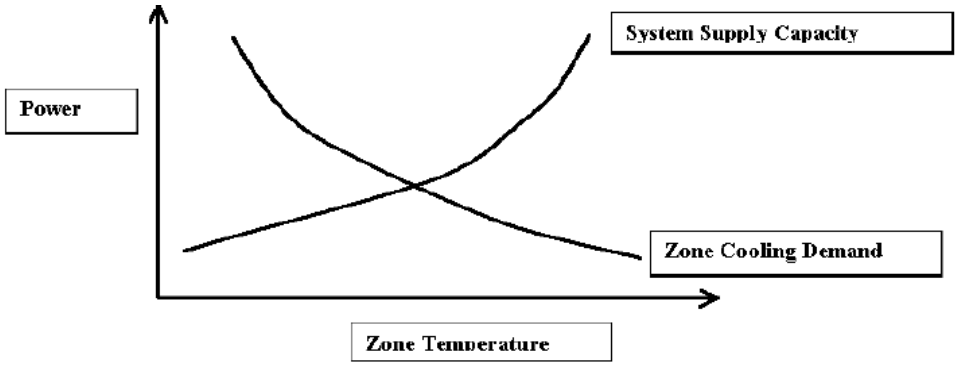

Figure 1.7: Sequential simulation supply/demand relationship: [16]

and DOE-2, EnergyPlus features a simulation manager for combining a heat and mass balance simulation with a building HVAC systems simulation for enhancing space temperature prediction (See in Figure 1.6). The pre-sponsored programs sequentially simulated building zones, air handling systems and central plants to predict cooling and heating demands but there was no feedbacks from one to the other, which causes the unrealistic zone temperature predictions. To obtain physically realistic solutions, in EnergyPlus, initial zone temperature prediction by performing a heat and mass balance simulation is corrected by the HVAC simulation because a zonal cooling or heating demand should be equivalent to the supply demand of a HVAC system at zone temperature as seen in Figure 1.7 [16].

In the heat and mass balance simulation, a zone temperature T_z, which corresponds to the zone cooling demand, is calculated by a equation given below,

$$C_z\frac{dT_z}{dt} = \sum_{i=1}^{N_{sl}} \dot{Q}_i + \sum_{i=1}^{N_{surfaces}} h_i A_i (T_{si} - T_z) + \sum_{i=1}^{N_{zones}} \dot{m}_i C_p (T_{zi} - T_z) + \dot{m}_\infty C_p (T_\infty - T_z) + \dot{Q}_{sys} \tag{1.35}$$

where

$$\sum_{i=1}^{N_{sl}} \dot{Q}_i = \text{sum of the convective internal loads,} \tag{1.36}$$

$$\sum_{i=1}^{N_{surfaces}} h_i A_i (T_{si} - T_z) = \text{convective heat transfer from the zone surfaces,} \tag{1.37}$$

$$\sum_{i=1}^{N_{zones}} \dot{m}_i C_p (T_{zi} - T_z) = \text{heat transfer due to infiltration of outside air,} \tag{1.38}$$

$$\dot{m}_\infty C_p (T_\infty - T_z) = \text{heat transfer due to interzone air mixing,} \tag{1.39}$$

$$\dot{Q}_{sys} = \text{system output,} \tag{1.40}$$

$$C_z\frac{dT_z}{dt} = \text{energy stored in zone air} \tag{1.41}$$

(h_i is convective heat transfer coefficient on each interior surface, and $\dot{m}_\infty$ and $\dot{m}_i$ are mass flow rate of the infiltration and interior air, respectively. T_{si}, T_{infty}, and T_{zi} are temperature of interior surface, outdoor air and a zone associated with the interzone

mixing.) The cooling or heating energy $\dot{Q}_{sys}$ is calculated by

$$\dot{Q}_{sys} = \dot{m}_{sys} C_p (T_{SA} - T_z) \tag{1.42}$$

where T_{SA} is the supply air temperature and $\dot{m}_{sys}$ is the mass flow rate of the supply air. A third order finite difference approximation is used to solve (1.35) in EnergyPlus. Once a desirable zone temperature $T_{desired}$ is determined, initial cooling or heating demands are calculated by T_z and $T_{desired}$. The initial demand becomes a good starting point to predict realistic cooling or heating demand of the given HVAC system. After the HVAC simulation predicts the actual supply capability to provide the realistic cooling or heating demand, T_z is adjusted when the initial demands mismatch the actual supply capability. The process in EnergyPlus is called a "Predictor/Corrector" process which is an enhanced feature of EnergyPlus compared to the pre-sponsored programs.

In the heat balance model (1.35), a room is assumed to have the uniform air temperature and the surface of the room is assumed to be uniform temperature. Any room air models which have non-uniform temperature violate the assumption in the heat model. However, the modular capability of EnergyPlus allows the use of a room air model which has non uniform temperature. The version (EnergyPlus v2.1.1) included several room air models with non uniform temperature, such as Mundt model and UCSD displacement model for simulating DV or UCSD UFAD interior model and UCSD UFAD exterior model. (The details of the UCSD UFAD models will be given in the next section). The UFAD models are chosen to simulate non uniform temperatures and predict the system cooling or heating demands in our study. Then we performed comparison studies of energy performance of UFAD in Chapter 4 and demand response of UFAD in Chapter 5.

1.3.1 UCSD-UFAD model

A zone operated by UFAD has non-uniform vertical temperature which is dominated by internal loads (i.e. occupants and workstation) which generate heat plumes. The non-uniform temperature is regarded as a stable stratification which primarily depends on the strengths of the loads, supply air quantity and the type and number of

diffusers. After Lin & Linden [31] proposed a single plume and single diffuser model and validated by small scale salt-water analogy experiments, the model was extended to predict non-uniform temperature with multi plumes and multi jets and validated by small scale and full scale experiments ([38]). In Energyplus, there are two UFAD models, the UCSD UFAD interior zone model and the UCSD UFAD exterior zone model, which are suitable to simulate the interior zone in which the plume arises from the internal loads and the exterior zone in which the plume arises from the window as well as the internal loads, respectively. For simplicity, we only introduce the concept of the interior zone model in this section. The detail of exterior zone model is described in [16].

To simplify the non-uniform temperature, the model defines a vertical temperature profile as a combination of lower occupied zone temperature T_{OZ} and upper hot air mixed zone temperature T_{RA} and the interface height h (further details of two layer temperature profile in UFAD will be given in Chapter 3). To find a relation between the temperature profile and the external parameters, such as buoyancy flux of heat source B, total air flow rate on diffuser Q and effective area of diffuser A_d, two non-dimensional parameters, ϕ and Γ are defined by

$$\phi = \frac{T_{RA} - T_{OC}}{T_{RA} - T_{SA}}, \tag{1.43}$$

$$\Gamma = \frac{Q^{3/2}}{m(n/mA_d)^{5/4}B^{1/2}}, \tag{1.44}$$

where T_{SA} is the supply air temperature, n is the number of diffusers, and m is the number of plumes. Physically, Γ represents competition between stratification and mixing. With fixed A_d, for large Γ, the mixing dominates and a room is weakly stratified, which corresponds to $\phi \to 0$. However, for small Γ, the buoyancy dominates to form stronger stratification in a room, which corresponds to $\phi \to 1$. The Γ and ϕ relation is validated by small scale and fulls scale experiments as seen in Figure 1.8 [37]. The interface height h is also related to Γ. Physically, large Γ lifts the density interface h while small Γ lowers h. Using a non dimensional parameter $\hat{h} = h/\sqrt{n/m \cdot A_d}$, in the experimental data given in Figure 1.9, the relation between $\ln(\Gamma)$ and $\hat{h}$ followed the physical interpretation.

Based on the Γ vs. ϕ relation and the Γ vs.$\hat{h}$ relation, three simple formulas to predict T_{RA}, T_{OC} and h corresponding to the heat load W (kW), A_d and Q were proposed

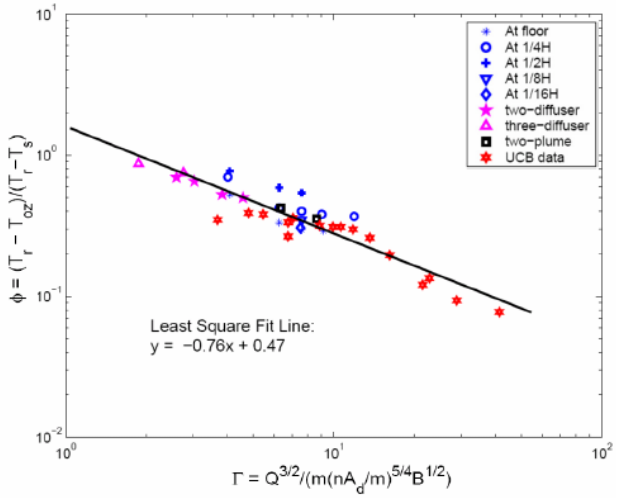

Figure 1.8: Log-Log Γ-ϕ plot: UCB data obtained from full scale experiments and other data are obtained from the small scale experiments [37]

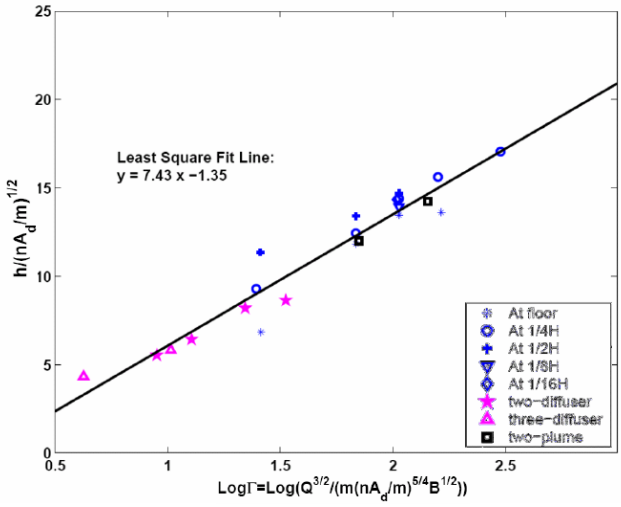

Figure 1.9: Log Γ - $\hat{h}$ plot: UCB data obtained from full scale experiments and other data are obtained from the small scale experiments [37]

as

$$T_{RA} = \frac{0.1281W}{Qg} T_{SA} + T_{SA}, \tag{1.45}$$

$$T_{OZ} = T_{RA} - 1.6\Gamma^{-0.76}(T_{RA} - T_{SA}), \tag{1.46}$$

$$h = \sqrt{A_d \frac{n}{m}}(7.43ln(\Gamma) - 1.35) + \frac{1}{2}h_s, \tag{1.47}$$

where h_s is the vertical height of the elevated heat source in [37]. The detailed implementation for the Energyplus module of the model is given in [16]. Daly [17] showed good agreement between the UCSD UFAD interior model prediction by a Energyplus simulation and full scale experimental measurement, which suggests that Energyplus simulation data using the UFAD models can provide realistic building energy consumption. EnergyPlus were used to simulate a UFAD system as well as OH in a prototype office building model in three different Californian climate zones. Annual energy consumptions of both systems were examined and we performed comparison studies between both systems in Chapter 4. To examine the effectiveness of demand response (DR), we will define a parameter to measure the effectiveness of demand response from EnergyPlus simulation data and compare the performance of the DR effectiveness between OH and UFAD in the different climates in Chapter 5.

Chapter 2

Transient responses of mechanical Displacement Ventilation system

2.1 Introduction

Highly variable energy world wide energy markets attract concerns about how we save and use limited energy resources without sacrificing our needs and the environment. In the building industry, these growing concerns of sustainability have caused reconsideration of the definition of high performance building. Energy savings for HVAC (heating, ventilating, and air conditioning) equipment is crucial for achieving a high performance buildings. Even though there are energy savings associated with individual HVAC equipment, major savings can also be obtained by the air flow regime of the ventilation system.

The conventional over head (OH) ventilation system is a popular choice because of the ease of temperature control: it provides, in "theory", a homogeneous temperature distribution over the space. Based on an OH system, ventilation efficiency depends on the air tightness of the space and mixing between the whole volume of air and conditioned air. Improving air tightness is expensive and difficult in a practical installation and mixing enhancement is difficult to achieve due to the complexity of the air flow. Additionally, an OH system cools the whole volume of the space even though occupants mostly stay below a certain height, typically around $1.8 \sim 2$ m. The zone below this

height is called the “ Occupied Zone” (OZ).

The mechanical displacement ventilation (DV) system is one of the ways of ventilating a room by introducing conditioned air (or supply air) near the lower part of the room and letting the OZ be filled with the conditioned air directly. Because the conditioned air discharges with lower momentum (compared to that of OH system), any heat sources in the OZ ideally do not mix with the surroundings, and the DV system typically has a thermal or density interface between a upper hot air zone and lower cold air zone. These characteristics of a DV system produce vertical thermal stratification over the space and the system maintains a higher return air temperature compared to OH system, leading to better cooling efficiency.

Additionally, in a moderate climate, the higher return air temperature allow the uses of an economizer which mixes the return air with outside air to reduce the air temperature without any energy consumption. Energy savings due to this “free cooling” by using the economizer are increased when the return air is warmer than the outside air, so the higher return air temperature in a DV system allow us to get more energy savings compared to OH system.

Since the occupied zone is, in theory, at the supply temperature, it is possible to use a higher supply temperature in DV compared to an OH system. This relatively higher supply air temperature of a DV system can achieve energy savings using a heat exchanger. The energy required to cool the return air by the heat exchanger or Air Handling Unit (AHU) is reduced at the higher supply air temperature, since the energy consumption is governed by the temperature difference between supply air and return air.

However, there is an issue of thermal discomfort of a DV system caused by vertical temperature gradients within the OZ ([60]). ASHRAE standard 55-1981 requires that the difference between 0.1 and 1.7 m above the floor should be no more that 3K. Wyon & Sandberg ([60]) showed that for cooling cases, the differences can go over the limit of 3K, with differences during summer measured to be around 4.5K. This undesirable temperature difference may result from the thermal interface being located within the OZ. The strength of the thermal stratification of OZ is determined by the interfacial height and the temperature of the upper hot air zone (that of the lower zone is expected

to be the same as the supply air temperature). Thus, these two variables are important for achieving occupant thermal comfort.

Time dependence of the strength of heat sources such as electric equipment or the number of occupants and external heat sources such as a radiation from the sun, makes the system dynamic rather than steady. Consequently, transient responses of a DV system need to be investigated to maintain desirable occupied zone temperatures and ensure occupant thermal comfort during changes in heat load.

In this chapter, transient responses of a DV system are studied by theory and experiments. We consider that a room heats up due to a heat source represented by a buoyant plume and cools down through cooling displacement diffusers. The models characterize the transient response of the temperature in each layer and the height of the interface by conserving mass fluxes and buoyancy fluxes. The transient behaviors of DV systems are derived by considering two competing time scales. The filling box time ([4]) provides a measure for the establishment of the stratification, and the replenishment time is the time in which all the air in the enclosure is replaced by supply air.

The models are examined by laboratory experiments using a salt-water system. The experiments are compared with theoretical predictions of the temperature of each layer and the interfacial height. The cases of the initial transient, in which the heat source and diffusers start simultaneously, time-varying heat or cooling loads, simulating dynamic thermal responses are examined.

In § 2.2, the two-layer model is developed while in § 2.3, the theoretical predictions are described. § 2.4 describes experimental set up and categorizes experimental parameters. § 2.5 shows comparisons of experiments and theory.

2.2 Transient two layer model

2.2.1 Mass balance and buoyancy flux balance

The displacement ventilation (DV) system considered in this chapter supplies conditioned air to an enclosure through low momentum diffusers that inhibit mixing into the occupied zone from the warm upper zone. Due to this prevention of mixing into the occupied zone, the temperature of the lower occupied zone is at the supply air tem-

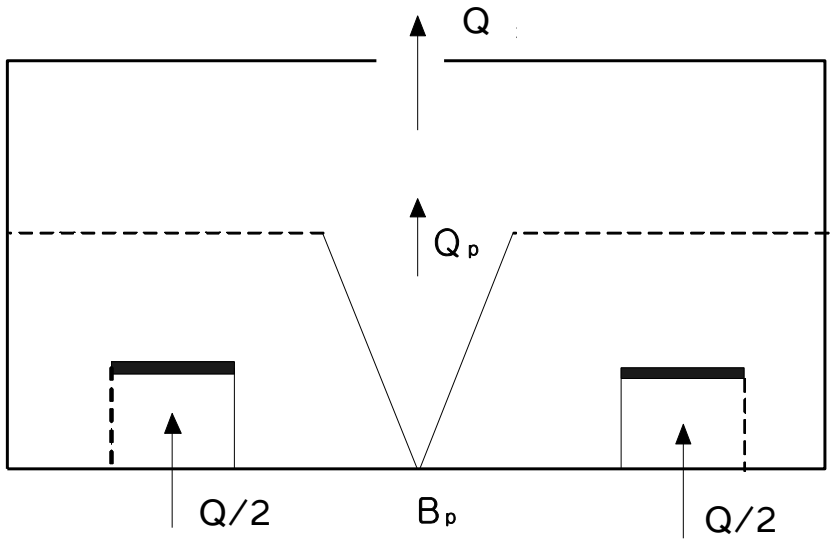

Figure 2.1: The schematic of the two-layer Displacement Ventilation (DV) model

perature and enhances ventilation efficiency by increasing the upper layer temperature.

In this transient analysis of the DV system we consider a single axisymmetric turbulent plume and pressurized supply air flows (Figure 2.1). The turbulent plume entrains ambient air in the occupied zone, rises and spreads out to form the upper warm layer. The supply air flow is split equally between the two diffusers. A density interface is formed between this upper layer and the lower occupied zone. We consider a two-layer model with lower layer volume, V_1 and buoyancy, g'_1 and upper layer volume, V_2 and buoyancy, g'_2. We assume that the walls are adiabatic so that there is no buoyancy flux through walls.

The buoyancy of the supply air, g'_f, is set to zero for simplicity. No mixing between thermal plume and ambient occurs in the lower occupied zone so $g'_1 = g'_f$ and

$\acute{g}_1 = 0$ since $\acute{g}_f = 0$, by definition. Volume and mass balances of each layer are

$$\frac{\partial V_1}{\partial t} = Q - Q_p, \tag{2.1}$$

$$\frac{\partial \acute{g}_1 V_1}{\partial t} = -\acute{g}_1 Q_p, \tag{2.2}$$

$$\frac{\partial V_2}{\partial t} = Q_p - Q, \tag{2.3}$$

$$\frac{\partial \acute{g}_2 V_2}{\partial t} = \acute{g}_1 Q_p - \acute{g}_2 Q + B, \tag{2.4}$$

where Q is total ventilation flow rate, Q_P is the flow rate generated by propagation of the plume, and B is the buoyancy flux of the plume. There is no rate of change of the occupied zone buoyancy in time because the buoyancy of occupied zone is always equal to the constant buoyancy of the supply air. Consequently, further analysis of the occupied zone in time is not necessary.

Substitute (2.3) into (2.4) and rearrange the equations to get

$$V_2 \frac{\partial \acute{g}_2}{\partial t} = \acute{g}_2 Q_p + B. \tag{2.5}$$

The equations for volume balance can be written in terms of the interface height, h, and the constant floor area, S,

$$\frac{dV_2}{dt} = S\frac{dh}{dt} = Q_p - Q. \tag{2.6}$$

The equations (2.5) and (2.6) describe the time evolution of the system. To make the equations non-dimensional, the non-dimensional interface height, ζ and the non-dimensional reduced gravity, δ_i are defined by

$$h = \zeta H, \quad \acute{g}_i = \delta_i C^{-1} B^{2/3} H^{-5/3} \tag{2.7}$$

where C is the plume constant and defined as $C = \pi(\frac{5}{2\pi\alpha_o})^{1/3}(\frac{6\alpha_o}{5})^{5/3}$ and the entrainment coefficient $\alpha_o = 0.09$ ([4],[44]) and H is total height of the enclosure.

In order to investigate unsteadiness, we define two competing time scales, the

filling box time scale T_f and 'replenishment' time scale T_n, respectively, as

$$T_f = \frac{S}{CB^{1/3}H^{2/3}}, \tag{2.8}$$

$$T_n = \frac{V}{Q} = \frac{SH}{Q}. \tag{2.9}$$

The 'filling box' time ([4]) is the time taken for all the fluid in the enclosure to pass through the plume, and it provides a measure for the establishment of the stratification. The 'replenishment' time is the time taken for all the air in the enclosure to the replaced by supply air.

Before beginning the non-dimensional rearrangement, we also need to define the plume volume flux, Q_p

$$Q_p = CB^{1/3}h^{5/3} = CB^{1/3}H^{5/3}\zeta^{5/3}. \tag{2.10}$$

The expression for Q_p in (2.10) assumes that the plume source is on the floor and no virtual origin adjustment is required for a ideal thermal plume. For comparing experiments in which the salinity plume has virtual origin, ζ_{vt}, with the given prediction of the plume, a corrected equation of plume volume flux is given below

$$Q_p = CB^{1/3}H^{5/3}(\zeta + \zeta_{vt})^{5/3}. \tag{2.11}$$

Substituting ζ and δ_2 and the time scales, T_f and T_n, we can rewrite (2.6) and rearrange the equation above to obtain

$$\frac{d(\zeta H)}{dt} = -\frac{1}{S}(CB^{1/3}\zeta^{5/3}H^{5/3} - \frac{SH}{T_n}). \tag{2.12}$$

Hence,

$$\frac{d\zeta}{dt} = -\frac{1}{T_f}\zeta^{5/3} + \frac{1}{T_n}. \tag{2.13}$$

Similarly, using $V_2 = SH(1-\zeta)$, (2.5) becomes

$$\frac{d}{dt}(\delta_2 B^{2/3}H^{-5/3}) = (-\delta_2 B^{2/3}H^{-5/3})\frac{Q_p}{SH(1-\zeta)} + \frac{BC}{SH(1-\zeta)}, \tag{2.14}$$

which on simplification becomes

$$\frac{d\delta_2}{dt} = \frac{1}{T_f(1-\zeta)}(-\zeta^{5/3}\delta_2 + 1). \tag{2.15}$$

It is convenient to introduce two new non-dimensional parameters

$$\tau = \frac{t}{\sqrt{T_n T_f}} \quad \text{and} \quad \mu = \mathrm{T_n}/\mathrm{T_f}. \tag{2.16}$$

By defining τ and μ, the two separate time scales are combined to make (2.13) and (2.15) nondimensional. The parameter μ represents a balance between 'filling box' and 'replenishment' time scales and also can describe an operating condition of DV system.

Then (2.13) and (2.15) become

$$\frac{d\zeta}{d\tau} = -\sqrt{\mu}\zeta^{5/3} + \frac{1}{\sqrt{\mu}} \tag{2.17}$$

$$\frac{d\delta_2}{d\tau} = -\frac{\sqrt{\mu}}{(1-\zeta)}\{\zeta^{5/3}\delta_2 - 1\}. \tag{2.18}$$

From (2.17) and (2.18), μ is the one parameter that determines the transient responses of ζ and δ_2.

With a virtual origin, ζ_{vt} of the salinity plume in experiment, (2.17) and (2.18) became,

$$\frac{d\zeta}{d\tau} = -\sqrt{\mu}(\zeta + \zeta_{vt})^{5/3} + \frac{1}{\sqrt{\mu}}, \tag{2.19}$$

$$\frac{d\delta_2}{d\tau} = -\frac{\sqrt{\mu}}{(1-(\zeta+\zeta_{vt}))}\{(\zeta+\zeta_{vt})^{5/3})\delta_2 - 1\}.. \tag{2.20}$$

A physical representation of μ helps us to understand the validity of two-layer model. μ can be written as

$$\mu = \frac{Q_p \text{ at H}}{Q}. \tag{2.21}$$

If $\mu > 1$, Q_p at H is larger than Q and the interface satisfying mass flux balance sits below H, so the two layer model is valid. However, if $\mu < 1$, the interface sits above H and the system is no longer assumed to be two-layered. [14] showed that when Q_p at H is smaller than Q (in this article, $\mu < 1$), the system behaves as well-mixed system.

Once the system is well-mixed over the enclosure, supply air temperature on diffusers is always less than the room set temperature because the supply air is only used for diluting heated room air and the system also requires additional flow rate of conditioned air for cooling the whole space, rather than just the occupied zone.

2.3 Theoretical prediction

The system of equations (2.17) and (2.18) is nonlinear, so in general, it is not possible to obtain analytic solutions. Therefore, the solutions of the system were obtained by numerical calculation using a 4th order Runge-Kutta method. To validate the numerical results, we can use the steady-state of the system obtained by setting the time derivative of the system to zero, in which case (2.17) and (2.18) imply

$$\mu = \zeta^{ss-5/3}, \tag{2.22}$$

$$\delta_2^{ss} = \mu, \tag{2.23}$$

where ζ^{ss} and δ_2^{ss} are steady-state values of ζ and δ_2. From Figures 3.8(a) & 3.8(b), computational results and the predictions of (2.22) and (2.23) show good agreement. However, the convergence of the system needs to be discussed because the system theoretically takes infinite time to reach steady state. To get steady-state solutions starting from the initial conditions of $\zeta^o = 0.99$ and $\delta_2^o = 0$ (hereinafter superscript o means initial conditions), times up to $\tau \sim 20$ are needed. ζ^o is chosen to avoid the singularity of (2.18) and δ_2^o is chosen because the initial interface forms when the plume reaches the ceiling. [24] also indicate the convergence criteria for steady-state values of ζ and δ_2. Therefore, we define convergence criteria as

$$|\zeta - \zeta^{ss}| < \varepsilon, \tag{2.24}$$

$$|\delta_2 - \delta_2^{ss}| < \varepsilon, \tag{2.25}$$

where $\varepsilon \sim 10^{-4}$ in which the system is assumed to be steady-state in our study.

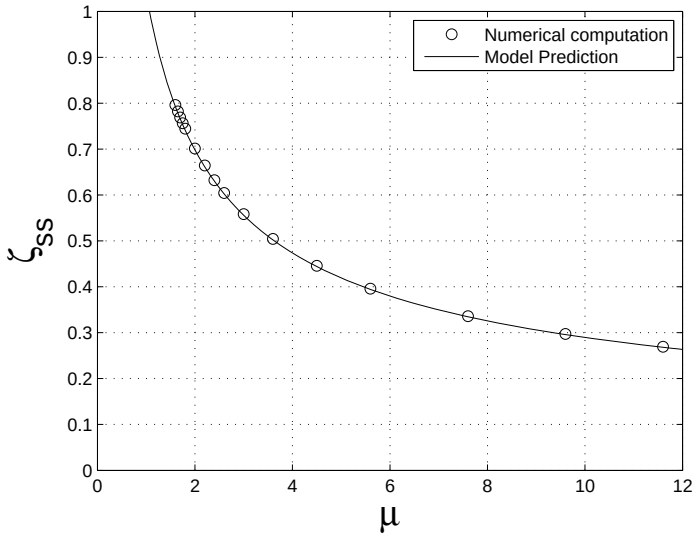

(a)

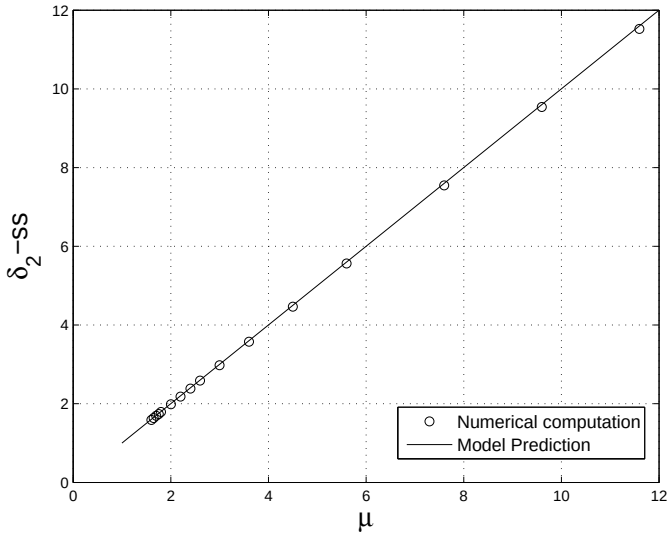

(b)

Figure 2.2: Comparison between steady state solutions of (2.22) and (2.23) and numerical results to get the steady state solutions by solving the transient two layer DV model, (2.17) and (2.18) with initial conditions, $\zeta = 0.99$ and $\delta_2 = 1$: (a) ζ^{ss} .vs. μ and (b) δ_2^{ss} .vs. μ

2.3.1 Ascending interface

2.3.1.1 Numerical solutions

The various transient responses of ζ and δ_2 for different initial conditions vary and the responses are not easily explained by transient temperature models shown in conventional well-mixed ventilation systems. In the cases of 'ascending interface', ζ starts from the bottom and reaches ζ_{ss}, which represents the situation in which the room is preheated and the ventilation system starts introducing cold air at the bottom of the room. The initial conditions of "Ascending ζ" vary depending on how much the room is preheated. In Figures 2.3(a) & 2.3(b), the initial conditions of ζ and δ_2 are $\zeta^o = 0$ and $\delta_2^o = 10$ which is arbitrarily chosen and represents a strongly preheated room.

The transient responses of ζ show no overshoot and converge in relatively short time compared to time scales for δ_2. Interestingly, the transient responses of δ_2 overshoot initially when $\tau < 3$. Physically, the overshoot can be explained by the difference of the time scales ($\mu > 1$) between ζ and δ_2, because fast movement of the interface ζ reduces the volume of upper layer in a relatively short time but the buoyancy flux balance of the upper layer tends to change slowly. The height of overshoot increases as the difference of the time scales μ is larger.

The temporal development of ζ is faster than that of δ_2 for all cases and the difference between their adjustment time scales increases when μ is larger. In order to measure the difference in time scales, the time taken for convergence of ζ and δ_2 to their respective steady states are used. The ratio of $\tau_{\zeta^{ss}}$ and $\tau_{\delta_2^{ss}}$ is defined as

$$\kappa = \frac{\tau_{\zeta^{ss}}}{\tau_{\delta_2^{ss}}}. \tag{2.26}$$

We estimate κ for ascending interface and we get

$$\kappa_{asc} \approx \mu^{-0.7} \tag{2.27}$$

as seen in Figure 2.4(b).

When $\mu \sim 1$, which is the theoretical limitation of the system (if $\mu > 1$, no upper layer can be formed and a two-layer model is invalid), ζ and δ_2 change together

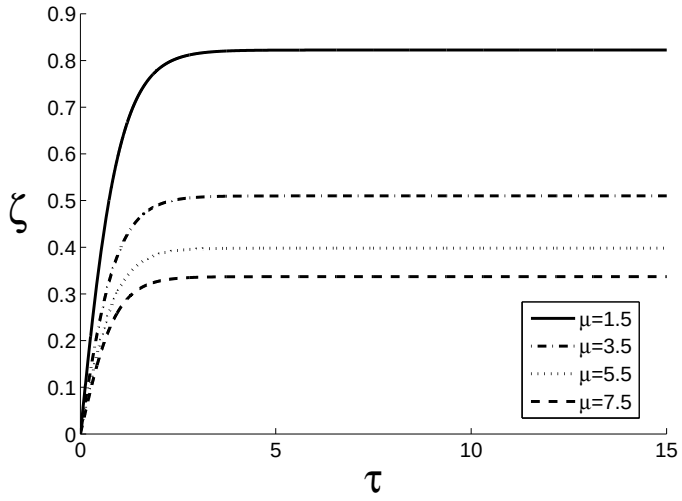

(a)

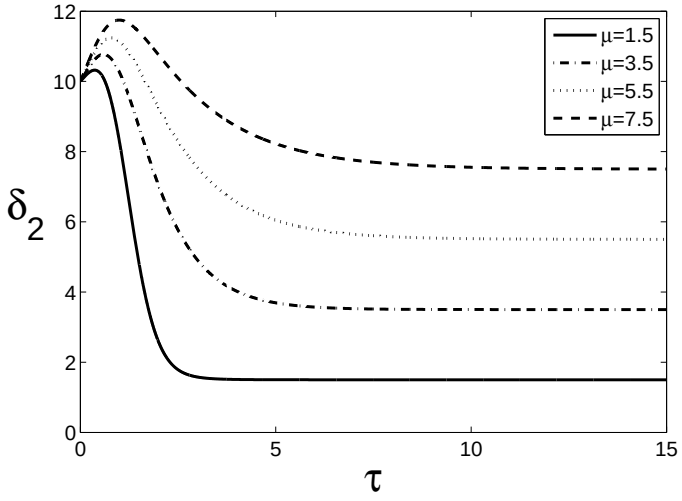

(b)

Figure 2.3: Transient responses of ascending interface against various μ (the initial conditions are $\zeta^o = 0$ and $\delta_2^o = 10$): (a) ζ .vs. τ and (b) δ_2 .vs. τ

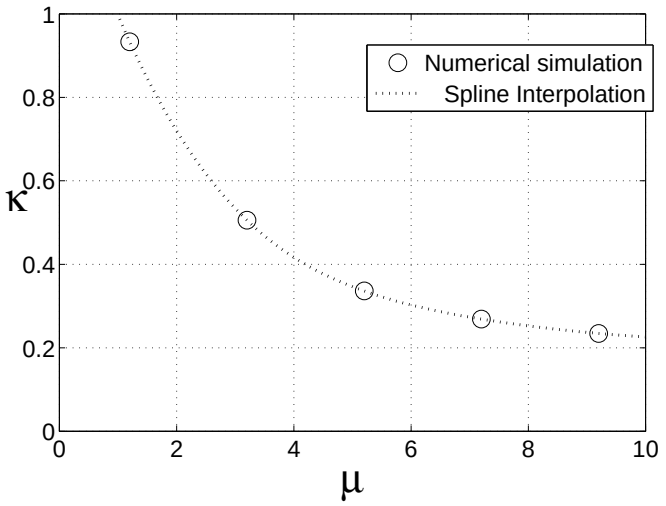

(a)

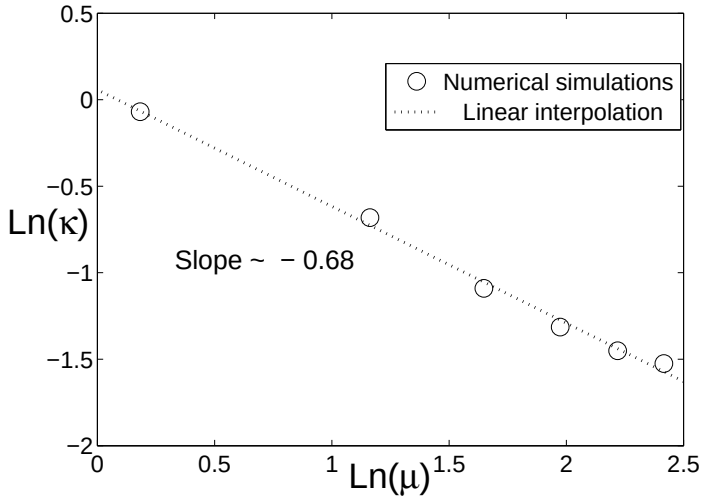

(b)

Figure 2.4: Graph of κ among various μ for ascending interface, the initial conditions of numerical solution is the same as figs. 2.3(a) and 2.3(b)

and the difference in timescale is small. When μ is large, the difference between the temporal responses between ζ and δ_2 becomes important. In (2.16), larger μ represents the buoyancy-dominant situation. The existence of a strong heat source can amplify the difference of time responses of ζ and δ_2. Physically, the difference of convergence time scales for ζ and δ_2 at large μ shows that transient response of the mass flux balance (2.17) is faster than that of the buoyancy flux balance (2.18).

2.3.2 Descending interface

2.3.2.1 Numerical solutions

A descending interface can be described as the situation where the room is pre-cooled so that its temperature is the same as the temperature of the supply air. The situation can happens at the beginning of operation hours after a non-operating period such as night time or a holiday in an office building. The initial condition of $\zeta = 0.99$ is chosen to avoid singularity of (2.18) and that of $\delta_2 = 1$ is arbitrarily chosen for the initial density of the upper layer. Unlike the ascending interface, no overshoot of δ_2 exists because the initial density δ_2^o of the upper layer is relatively smaller than that of the case of ascending interface. In most operating situations, the cases of descending interface have relatively smaller δ_2^o than those of ascending interface. From the phase diagrams, Figure 2.7(a), 2.7(b) and 2.7(c), we find that overshoot or undershoot behaviors of δ_2 depends on δ_2^o and further discussions of the behaviors are given in §3.3.1.

The difference of convergence timescales of ζ and δ_2 still occurs for the descending interface, so κ is also used for measuring the difference. The relation between κ and μ is shown in Figure 2.6(a) and 2.6(b) and with the similar relation as ascending interface, the relation between them suggests a power law relation of the form

$$\kappa_{dsc} \approx \mu^{-0.7}. \tag{2.28}$$

κ_{dsc} of descending interface also decreases when μ increases and follows the similar power law as the descending interface and for similar reasons.

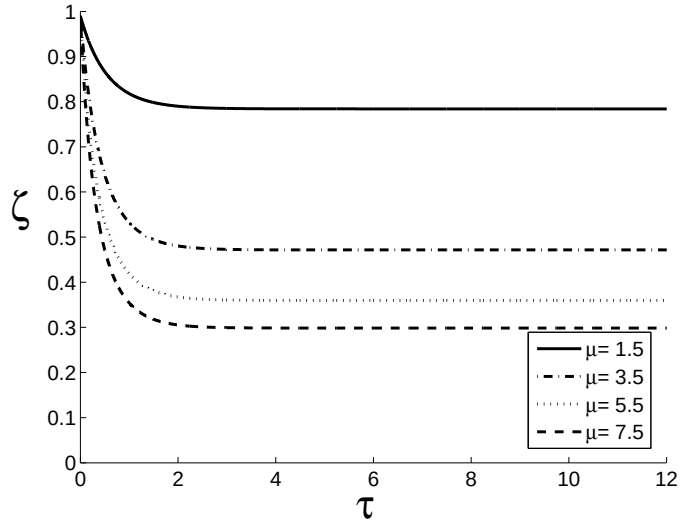

(a)

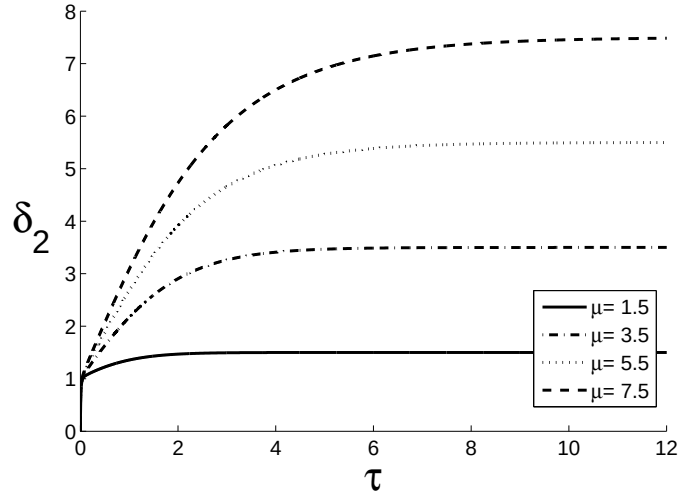

(b)

Figure 2.5: Transient responses of Descending ζ against various μ (the initial conditions are $\zeta^o = 0.99$ and $\delta_2^o = 1$): (a) ζ .vs. τ and (b) δ_2 .vs. τ

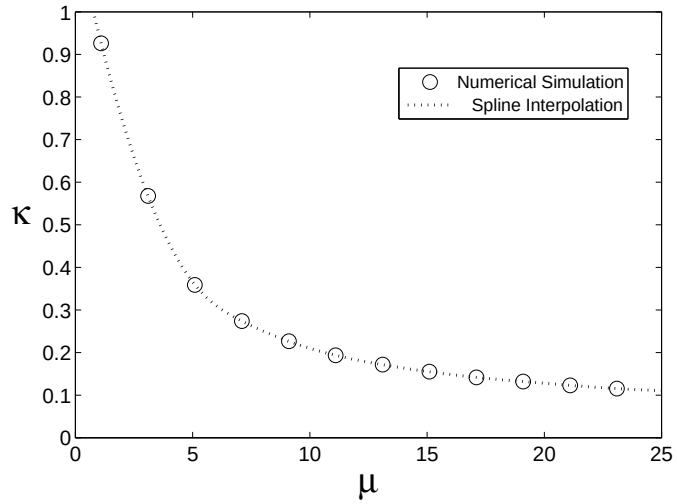

(a)

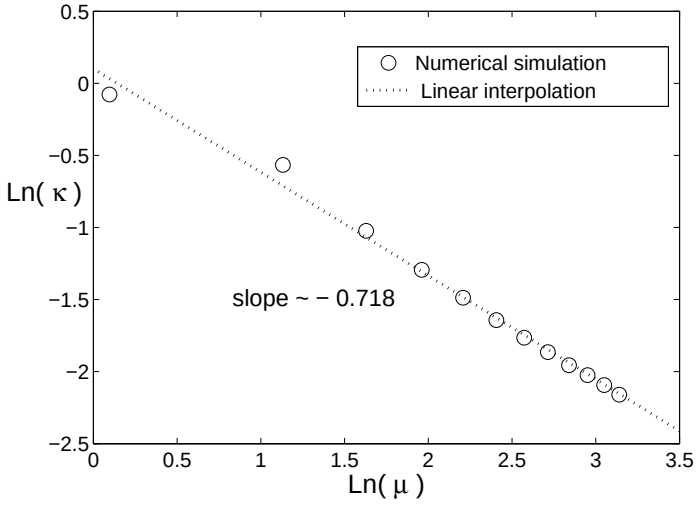

(b)

Figure 2.6: Graph of κ_{dsc} among various μ for descending interface, the initial conditions of numerical solution is the same as figs. 2.5(a) and 2.5(b)

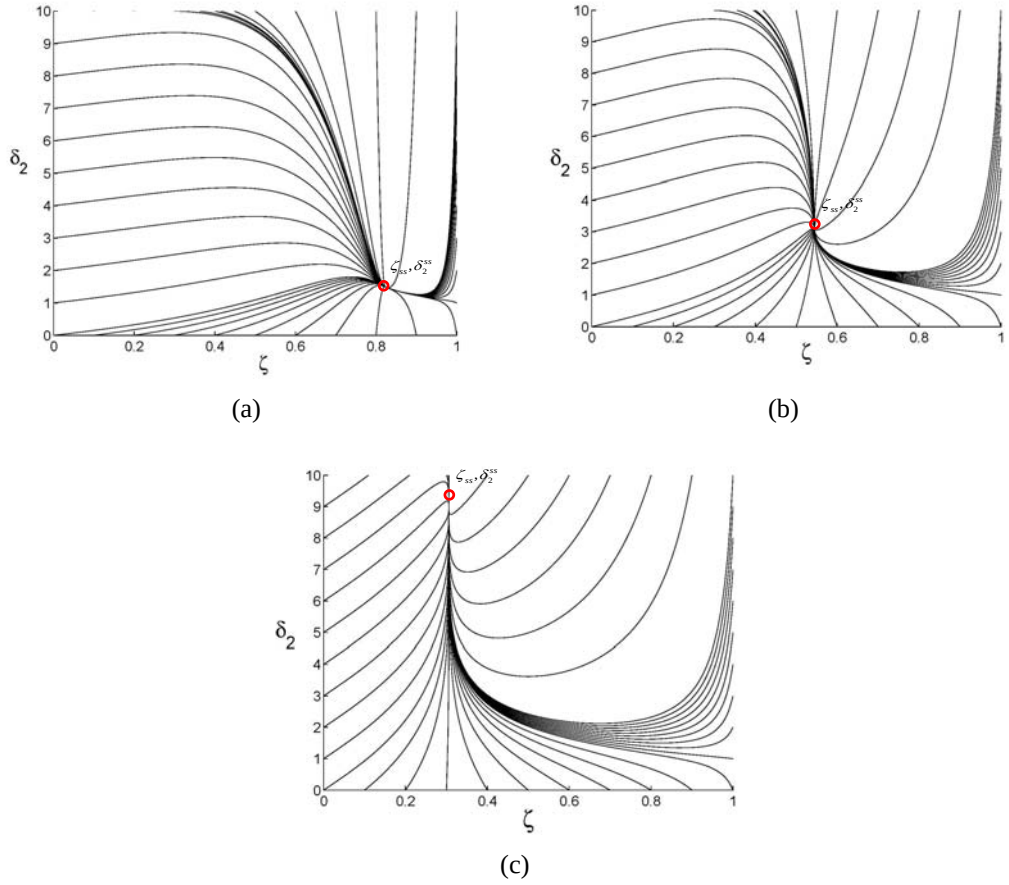

Figure 2.7: Phase diagrams of ζ and δ_2 when initial conditions, ζ^o and δ_2^o are placed on outer edges on graphs : (a) $\mu = 1.5$, (b) $\mu = 3$ and (c) $\mu = 9$

2.3.3 Phase diagram of interface height and upper layer buoyancy

2.3.3.1 Ascending and Descending interface

From the phase diagram of ζ and δ_2, we can determine the responses to be expected for various initial conditions. Because the system of equations, (2.17) and (2.18) is a nonlinear ODE, numerical simulations of (2.17) and (2.18) are used to plot the diagram. Figure 2.7(a), 2.7(b) and 2.7(c) show that the phases diagrams for $\mu = 1.5$, 3 and 9, respectively. Provided $\zeta < 1$, the system always converges to the steady state solutions of (2.22) and (2.23) for all initial conditions of ζ and δ_2. The diagrams for different μ are topologically similar to each other.

We observe that the interface height ζ has no overshoot (for 'ascending inter-

face') or undershoot (for 'descending interface') behavior which means that $\zeta > \zeta^{ss}$ or $\zeta < \zeta_{ss}$ on trajectories to the steady state, respectively, in contrast to the natural ventilated system ([24]). Any trajectories starting from $\zeta^o < \zeta_{ss}$ represents the cases of the ascending interface and trajectories staring from $\zeta^o > \zeta_{ss}$ of the descending interface.

However, δ_2 exhibits overshoot or undershoot behavior which means $\delta_2 > \delta_2^o$ and $\delta_2 > \delta_2^{ss}$ (for 'ascending interface') or $\delta_2 < \delta_2^o$ and $\delta_2 < \delta_2^{ss}$ (for 'descending interface'), respectively, on trajectories to the steady state. There are two scenarios to explain this behavior. :

- 1. The gradient of (2.18) is steep enough to make the system over or undershoot along the trajectory,
- 2. Initial conditions, ζ^o and δ_2^o, make initial gradient of (2.18) opposed to the direction of convergence. For example, right hand side of (2.18) with ζ^o and δ_2^o, the initial gradient of (2.18), becomes positive ($1 - \delta_2^o {\zeta^o}^{5/3} > 0$) during initial transition when the direction of convergence is negative ($\delta_2^o > \delta_2^{ss}$) and vice versa.

Following both scenarios, the system experiences a reversal of δ_2 due to the transition of gradient direction of (2.18). A maximum or a minimum of δ_2 occurs when $\delta_2 \zeta^{5/3} = 1$ during the transition and after the overturn of δ_2, δ_2 follows inequalities given as

$$\delta_2 \geq \frac{1}{\zeta^{5/3}} \quad \text{for} \quad \delta_2^o < \delta_2^{ss}, \tag{2.29}$$

$$\delta_2 \leq \frac{1}{\zeta^{5/3}} \quad \text{for} \quad \delta_2^o > \delta_2^{ss}. \tag{2.30}$$

The instantaneous gradient of δ_2 is also determined by μ and ζ and a proportional relation can be obtained as

$$\left|\frac{\partial \delta_2}{\partial \tau}\right| \propto \frac{\sqrt{\mu}}{1-\zeta}. \tag{2.31}$$

The case of Figure 2.3(b) has initial conditions, ζ^o and δ_2^o which make the gradient positive when $\delta_2^o > \delta_2^{ss}$ (the second scenario of the overshoot), so overshoot behavior of δ_2 occurs. Larger μ representing operating condition increases the overshoot during

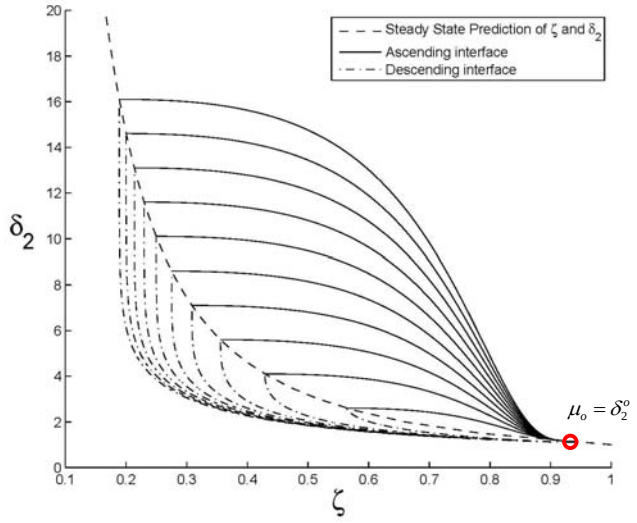

Figure 2.8: Phase diagrams of ζ and δ_2 for various μ_2 with $\mu_o = 1.1$ ($\mu_o = \delta_2^o$)

initial transition and the proportion relation (2.31) suggest that a steep gradient of (2.18) causes higher overshoot of δ_2. The overshoot behavior of δ_2 was also observed for transient model of natural ventilation system ([24]) only for one of the cases of 'descending interface'. The phase diagrams of DV system suggests that the overshoot or undershoot may exist on 'ascending interfaces' and 'descending interfaces' depending on the initial conditions, ζ^o and δ_2^o and the operating condition μ.

2.3.3.2 Demand Response

A demand response (DR) strategy is the electricity demand limit strategy which forces the system to reduce the usage of energy during a peak load period. In order to satisfy the demand limiting by the DR strategies, the system increases the room set point temperature by limiting the volume flow rate of supply air or increasing the temperature of supply air through the diffusers. At the start and the end of the DR events, the system changes rapidly to reach a second equilibrium state.

While the phase diagrams discussed above only consider initial conditions that are placed outside of the steady state or the equilibrium state, we now examine the cases of initial conditions which satisfy the steady-state solutions, (2.22) and (2.23) (the initial

conditions can be represented as μ_o and the operating conditions to reach second steady state is expressed as μ_2).

One example of an operating condition of a DR events is shown in Figure 2.8 with the initial operating condition, $\mu^0 = 1.1$. The phase diagrams show the processes of $\mu_o \rightarrow \mu_2$ and $\mu_2 \rightarrow \mu_o$ which are similar situations of the transitions at the start (initial transition) and the end (restoration) of the DR events, respectively. Independent trajectories of ζ andδ_2 during the processes of $\mu_o \rightarrow \mu_2$ and $\mu_2 \rightarrow \mu_o$ are shown. If ζ is below the occupied zone (OZ) during the DR events, trajectories of initial transition and restoration represent temporal variations of occupant thermal comfort because intensity of thermal stratification and temperature within OZ are determined by ζ and δ_2. Further discussions of thermal comfort during DR events are given in § 2.5.2.

2.3.4 Initial Transient

The initial transient (IT) represents one of the situations of a descending interface when initial environment is homogeneous. Once the heat source is turned on, the initial density layer is formed after the plume reaches the ceiling of the enclosure and spreads out horizontally. Before the layer forms, there is a mismatch between the transient model and experiment. [24] indicated the initial depth of the layer is about $0.2 \times H$ for the case of a naturally ventilated enclosure. The depth of the layer in our experiments is also observed to be close to $0.2 \times H$, from which we conclude that the formation of the layer does not depend on the ventilation but is a characteristic of the plume. A density or temperature front similar to a gravity current propagating along the ceiling, can be observed which takes a finite time to form the layer. Therefore, we assume that the initial conditions for IT is $\zeta^o = 0.8$, the height of the initial density layer and $\delta_2^o = 0.5$, the density of the layer which are obtained at our experimental results at $\tau = 0$ (Figures 2.14(a) & 2.14(b)). During the transitional movement of IT, ζ only descends from the height of the initially formed layer to ζ^{ss}.

The times to reach to steady-state of IT, $\tau_{\zeta^{ss}}$ and $\tau_{\delta_2^{ss}}$ are estimated by calculating the minimum time to satisfy the inequalities in (2.24) and (2.25). The graphs on Figures 2.9(a) & 2.9(b) show $\tau_{\zeta^{ss}}$ and $\tau_{\delta_2^{ss}}$ plotted against various μ. We observe that ζ decreases and δ_2 increases and there was no overshoot nor undershoot response on the approaches

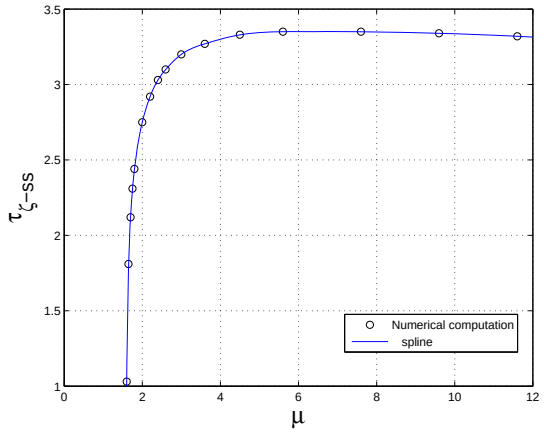

(a)

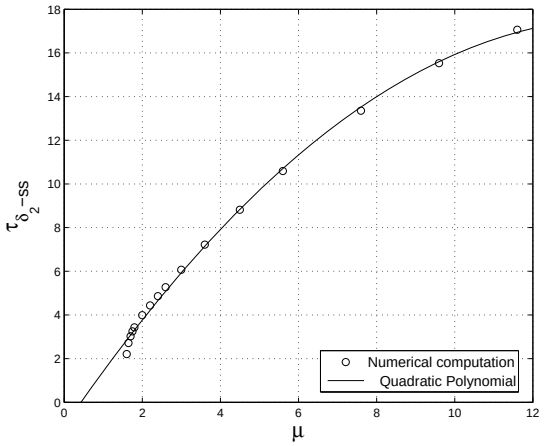

(b)

Figure 2.9: Numerical results of Initial Transient using transient two layer DV model with $\zeta^o = 0.8$ and $\delta_2 = 1 : \mu$ vs. $\tau_{\zeta ss}$ (a) and μ vs. $\tau_{\delta_2^{ss}}$ (b)

to steady states. In Figure 2.9(a), $\tau_{\zeta^{ss}}$ steeply increases then slowly decreases and a maximum of $\tau_{\zeta^{ss}}$ exists around $\mu \sim 6$.

These transitional responses can be explained by the balance of competing time scales, T_f and T_n. If T_n is much smaller than T_f ($\mu \ll 1$), the system response is governed by T_n, which is determined by the total ventilation flow rate Q. Smaller Q corresponding to larger μ (see (2.9) and (2.16)) implies that the time to reach steady state increases. If T_f is larger than T_n ($\mu \gg 1$), the system is dominated by the strength of the buoyancy source, which means that the stronger buoyancy source causes the system adjust more quickly, so that when μ increases, $\tau_{\zeta^{ss}}$ decreases. We observe that $\tau_{\delta_2^{ss}}$ increases when μ increases and a quadratic polynomial curve is a good match to the results except when $\mu < 2$. The monotonic behavior of $\tau_{\delta_2^{ss}}$ with μ results from the fact that the stratification is established by the plume.

2.4 Experimental set up

The experiments are based on the analogy between buoyancy-driven thermal convection at full scale and salt-water experiments in small-scale enclosures. A similar configuration to former experiments ([29] and [37]) were employed for this study. The Plexiglass tank with dimensions of 58cm (width) $\times$ 27cm (depth) $\times$ 58cm (height) was used for the enclosure. The flow was driven by a salinity plume source analogous to a single heat source and had diffusers supplying fresh water to ventilate the enclosure (Figure 2.10). The enclosure has sufficient space to avoid unwanted interaction between the plume and the diffuser flows.

The plume and the diffusers were placed on the top of the enclosure and the experimental set up is inverted from a real room for ease of experimental operation. The sink located near the bottom of the tank maintains a mass balance in the enclosure, which can be checked from the level of the water surface during the experiments. The flow rate of the sink is controlled by siphoning (Figure 2.10). The specially-designed chamber of the plume gives a virtual origin of approximately 1 cm, which is small compared to the tank height. The virtual origin of the plume chamber is an adjustment to the height of the plume propagation because an ideal plume has no volume flux at its origin, unlike

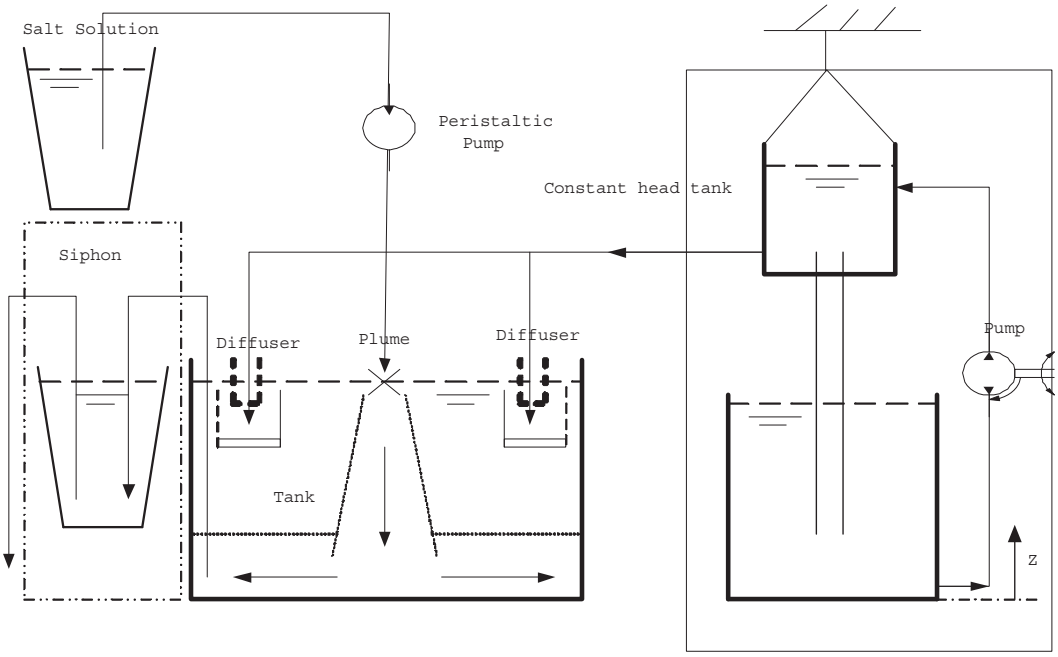

Figure 2.10: The schematic of the experimental set up

the salinity plume in our experiment, and the analytic expressions to obtain the location of the virtual origin was proposed in [21].

The diffusers had solid plates placed in front of them designed to block vertical momentum of the flow from the diffuser (Figure 2.11). In order to minimize the perturbation caused by the impinging diffuser flow against the walls, partitions between the plume and grid meshes were installed (Figure 2.11). The partitions intentionally inhibited the interaction between the plume and the diffuser. The grid meshes around the diffusers spread the flow horizontally and reduced the strength of the horizontal momentum of the flow, thereby reducing additional perturbations at the density interface. Because turbulence at the interface can cause entrainment, which transfers the salinity from the lower denser layer to the upper layer, these experimental modifications were necessary to eliminate mixing between the layers.

In order to provide a sufficient flow rate from the diffusers and to have a steady flow, a constant head system was used (Figure 2.10). The flow rate of the salt water for the plume was supplied by a peristaltic pump which produces flow pulsation by squeezing the supply tube between rollers. These pulsations make the plume more turbulent,

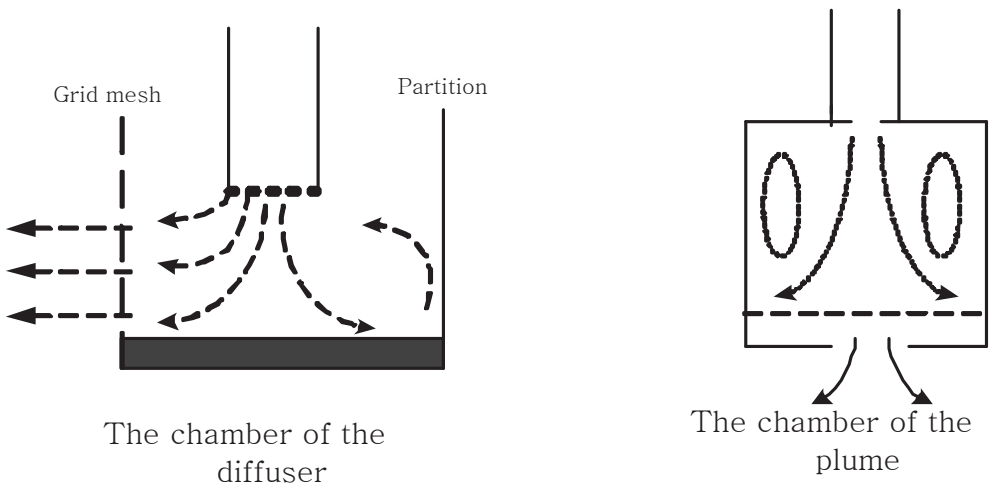

Figure 2.11: The schematic of the chambers of the plume and diffusers

providing a better simulation of a turbulent thermal plume at full scale.

Experiments were set up to simulate two realistic situations. One situation is IT (Initial Transient) which starts the heat source and diffusers simultaneously when the enclosure is initially at the same temperature of the supply air. In the experiment, the tank was filled with fresh water with the same density as the diffuser flow, and the salt plume source and diffuser start simultaneously. The transient models and experiments to simulate IT provide predictions of rapid transitions of vertical temperature profiles, represented by the interfacial height ζ and upper layer reduced gravity δ_2, not available from the current steady-state models of a DV system.

The other situations are DR, introduced in § 2.5.2. We consider the limit of buoyancy flux B and the limit of the ventilation flow rate Q for satisfying DR. Experiments only observe the start and the end of DR and investigate transitional response of ζ and δ_2 because dynamical responses can be seen during the periods.

2.4.1 Dye attenuation technique

A dye attenuation technique was used for measuring the density field by processing the image data from the experiment with a light intensity index calibration (Figure 2.12(a)). Unlike a conductivity probe measurement, which only can measure the density at one location, the technique captures the two-dimensional field of density in time,

so it is suitable for determining a vertical density field and analyzing spatial distributions of density. In our experiment, the salt solution in the plume is colored by red food coloring. One reason to choose the food coloring is that there is no chemical reaction between salt water and the dye because the reaction can cause a mismatch between the light intensity index and experimental data. Maintaining the same concentration of salt ($\rho = 1.0778\text{g}/\text{cm}^3$) and dye ($1.121\text{ml}/\text{liter}$), the accuracy of measurements has been confirmed from experimental results to $\pm 10^{-4}$ g/cm^3.

Because measurements of the dye attenuation rely on light intensity through the salt solution and the tank, any defects on the default background image need to be corrected. To measure the density by the light intensity index, the corrected light intensity, C is introduced by

$$C = 255 \times \frac{O}{B}, \tag{2.32}$$

where "255" is the scale of light intensity of black & white color space, O is an original captured image and B is a background image. The density corresponding to C is obtained by Anton Paar DMA 5000 density meter accurate to $\pm 10^{-6}$ g/cm^3 and the calibration curve between C and the corresponding density is shown in Figure 2.12(a). The curve is obtained by measuring fixed concentrations of salinity and dye solutions. The nonlinearity of the curve limits the range of accurate density measurement less than $1.002\ \text{g}/\text{cm}^3$. Care was taken to ensure the density values did not exceed this limit.

The accuracy of the density measurements by this technique is limited by the quality of the image captured in the experiments. Therefore, there are two major enhancements to improve the quality in our experiment.

First, digital technology for capturing the image provides one of the enhancements. Unlike analog recording device such as video tape, the digital recording devices guarantees no loss of quality of the captured images during repeated post-processing of the recorded images. The original images and the corrected images calculated by (2.32) are obtained by DIGIFLOW 3.0, the flow visualizing software developed by Dalziel Research Partners.

Second, the former experiments performed by [29] and [37] had a VGA resolution (640×480 pixels) of the image while the digital camera (JAI CM4+ digital monochrome progressive scan camera) in our experiment has semi-HD quality of the

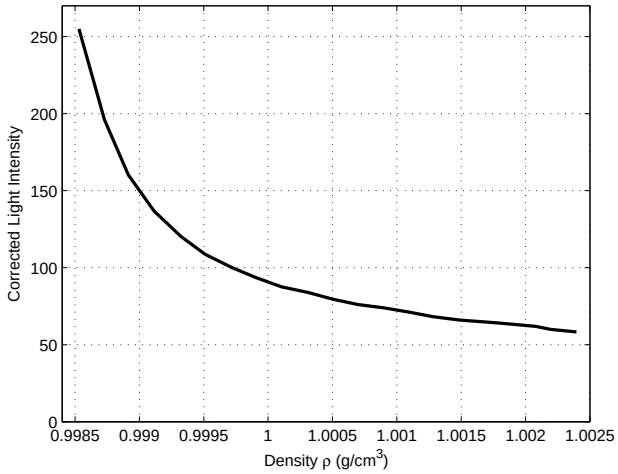

(a)

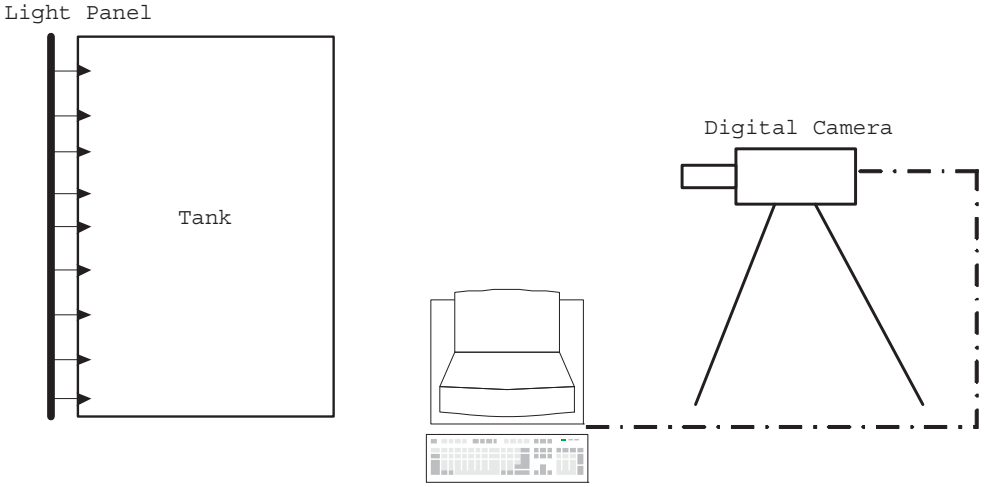

(b)

Figure 2.12: The calibration curve between density and the corrected light intensity (a) and the schematic of dye attenuation experimental set up (b)

Table 2.1: Experimental parameters for IT : the tank is filled with fresh water at the beginning of each experiment and μ is operating condition

μ	1.72	2.20	3.21
Buoyancy flux(cm^4s^{-3})	14.13	28.25	28.25
Total ventilation flow rate(cm^3/s)	50.89	50.89	35.84

image (1350 $\times$ 1080 pixels). The enhanced resolution from the camera allows us a more detailed analysis as the pixel density of current digital images is larger than the earlier experiments by a factor of 5.

Another significant improvement was the use of an Electric Vinyl Panel manufactured by Electric Vinyl Inc. This provides a time-consistent and spatial uniformly light intensity over the background (Figure 2.12(b)). The panel has superior qualities of spatial distribution of light intensity compared to the previously used light box which had a series of fluorescent lamps, providing a significant improvement of the quality. This time-consistency of the light intensity from the panel is also important for our transient analysis.

2.4.2 Experimental parameters

Operating condition, μ is controlled by two independent parameters, B, buoyancy flux and Q, total ventilation flow rate. The density of plume source $\acute{g}_s$ is obtained based on the calibration curve (Figure 2.12(a)) and remains same for all experimental cases. To get a given buoyancy flux for the plume, the flow rate for the source Q_s is calculated by

$$Q_s = \frac{B}{\acute{g}_s} \tag{2.33}$$

and obtained by adjusting rotation rates of the peristaltic pump for generating B. By using flow meters, GF-1460 manufactured by Gilmont instrument company, actual flow rate corresponding the readings of the flow meters are obtained by measuring the volume of the flow in given time.

To simulate IT, the tank is filled with fresh water and turn on the plume and the diffusers are turned on simultaneously at the start of experiments. All experiments are

Table 2.2: Experimental parameters for DR : δ_2^o is initial density of upper layer and μ is operating condition for each case of DR responses

DR cases	Operating Parameters	Buoyancy flux(cm^4s^{-3})	Total ventilation flow rate(cm^3/s)
B step up	$\delta_2^o = 1.6$	14.13	50.89
B step up	$\mu = 2.5$	56.27	50.89
B step down	$\delta_2^o = 6.0$	56.27	50.89
B step down	$\mu = 1.6$	14.13	50.89
Q step up	$\delta_2^o = 1.6$	14.13	20.80
Q step up	$\mu = 4.0$	14.13	50.89
Q step down	$\delta_2^o = 4.0$	14.13	50.89
Q step down	$\mu = 1.6$	14.13	20.80

recorded for at least 5000 sec to get steady state. The experimental parameters of IT are given in Table 2.1 and each case was performed at least three times to get error analysis.

To get initial conditions for the interfacial height ζ^o and the density of upper layer δ_2^o, experiments are delayed until the system reaches steady state with given initial buoyancy flux and total ventilation flow rate given in Table 2.2. At the beginning of DR experiments, B or Q corresponding to the operating condition μ are applied simultaneously. The cases for DR simulations are mainly categorized buoyancy flux change and total ventilation flow rate change. Each category shows 'step up' and 'step down' of the buoyancy flux or the ventilation rate at the beginning of measurements.

2.5 Comparison of experiments and theory

2.5.1 Initial transient

After filling the tank with fresh water with the same density as the flow from diffusers, the plume and diffuser started simultaneously and the initial density layer was formed within 2 minutes (Figure 2.13(a)). The initial height of the density layer ζ^o was close to 0.8 and the initial non-dimensional density of the layer δ_2^o was near 0.5 in most cases. ζ^o and δ_2^o are assumed to be initial conditions for the model prediction because the model is only valid when the upper layer exists, so we start measurements after the

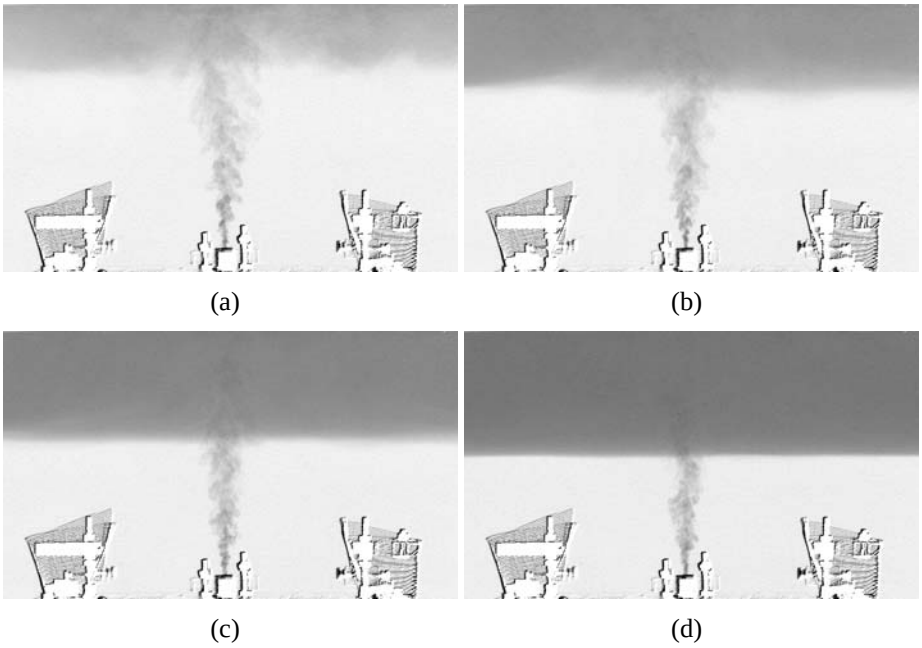

Figure 2.13: Grey-Scaled background-removal images at $\mu = 3.21$ in time : (a) 100 s, (b) 250s, (c) 500s and (d) 1000s

layer formed (the layer formed within 120 s). By using specially designed diffusers and a sufficiently large horizontal space for reducing the horizontal momentum of the diffuser flow, no mixing between upper and lower layer can be seen (Figures 2.13(a) - 2.13(d)). This characteristic of our experiments is important when the experimental results are compared to the theoretical prediction because there is no mixing between the layers in the two-layer model.

Transient responses of ζ and δ_2 are shown in Figures 2.14(a) & 2.14(b). The error bars of experimental results were obtained by three repeat experiments for each value of μ. Comparisons between experiments and the modeling on each μ show good agreement and the faster convergence of ζ compared with δ_2 given at §3.4 can be observed in the experiments. The good agreement of ζ and δ_2 during the initial transitional period also supports the notion that the well-mixed assumption for the upper layer is always valid for the prediction of ζ and δ_2 even when the layer moves dynamically in time.

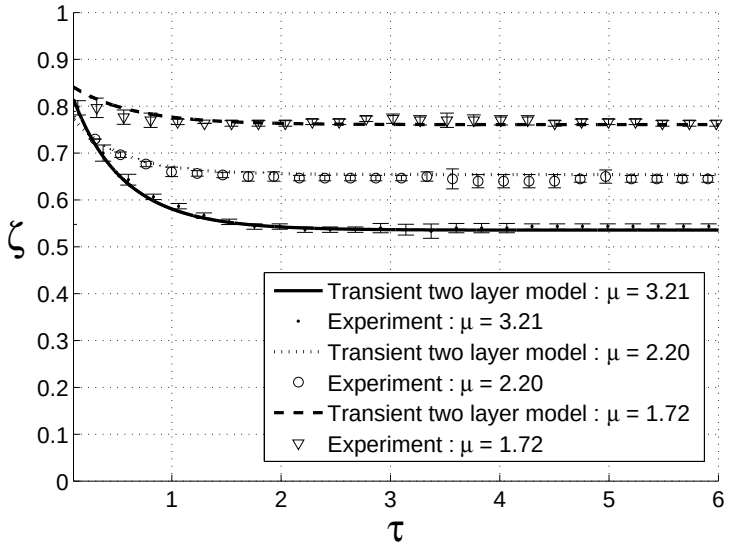

(a)

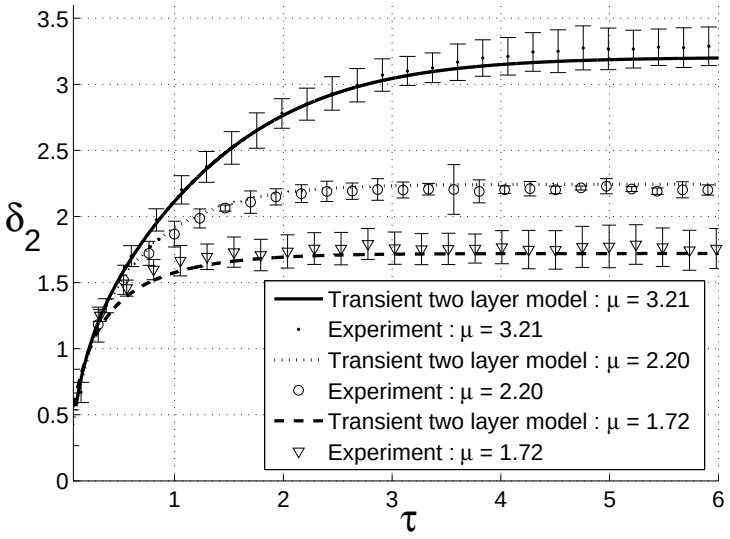

(b)

Figure 2.14: Comparison of experiments and two-layer DV model on initial transient: time response of ζ (a) and that of δ_2 (b) for various μ

2.5.2 Demand Response

Typical operating scenarios of operating a DV system involve step changes of the operating parameters μ (§ 2.3.3.2). Current demand response (DR) strategies for reducing electricity demands of HVAC components choose to reduce heat generation rate in a space by shutting off equipment, lowering blinds on windows or decreasing the ventilation flow rate Q to increase T_{rm}. Before and after DR strategies, changes of the response of DV system need to be modeled. These responses can be categorized by heat generation rate change and total ventilation rate change.

2.5.2.1 Buoyancy flux change

The heat generation rate is analogous to the buoyancy flux B. Here, we define two categories of the transitional period of DR events concerning heat generation rate change : an initial transition of DR is called as 'B : Step Down' and a restoration period of DR is called as 'B : Step Up'.

Vertical profiles during transitions of 'B : Step Up' (Figure 2.16(b)) and 'B : Step Down' (Figure 2.16(a)) show thermal stratification on the upper layer of both cases. 'B : Step Up' has a 'ceiling-to-interface' mixing process in which the initial stratification happened at the ceiling and is propagated down to the interface because additional buoyancy flux via the plume is delivered to the upper layer and the buoyancy flux is strong enough to shoot up and spreads out along the ceiling (Figure 2.17(a)).

'B : Step Down' also have vertical stratification on the upper layer during transition. The transitional profiles in Figure 2.16(a) show that relatively lower buoyancy spreads along the interface at initial stage and the lower buoyancy propagate to the ceiling later (Figure 2.17(b)). There is a scenario to explain 'interface-to-ceiling' mixing process on the upper layer; At initial transition, the buoyancy of a plume passing through the density interface is lower than that of the upper layer, so the plume stop rising and start spreading out its buoyancy from the interface.

Even though the upper layer is thermally stratified, not well-mixed during the transition, experiments and theoretical predictions agree well since the total integrated buoyancy is the driving force (Figures 2.15(a) & 2.15(b)).

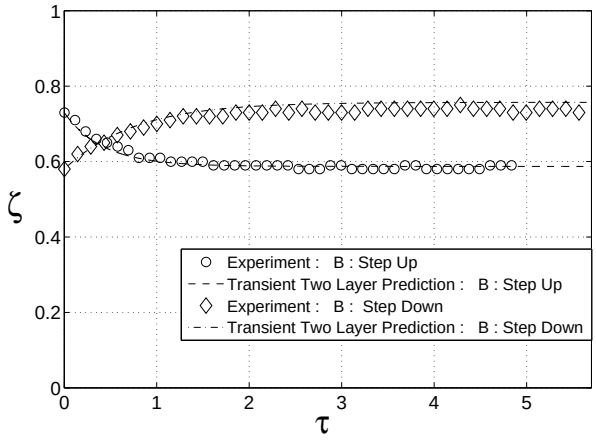

(a)

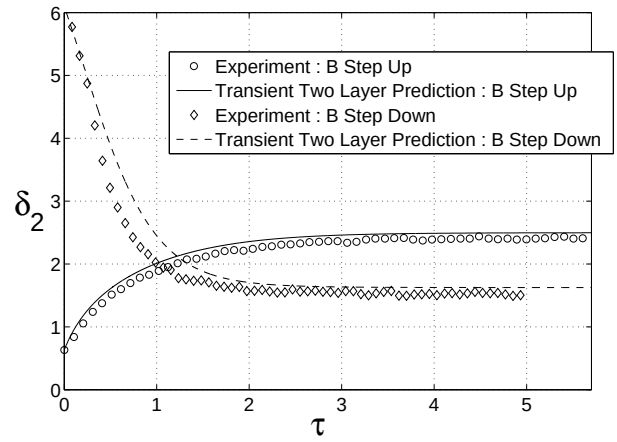

(b)

Figure 2.15: Experimental results and transient two layer model prediction of heat generation rate change (Step up (initial transition): $\delta_2^o = 1.6$ and $\mu = 2.5$, Step down (restoration): $\delta_2^o = 2.5$ and $\mu = 1.6$) : (a) Transient responses of ζ and (b) those of δ_2

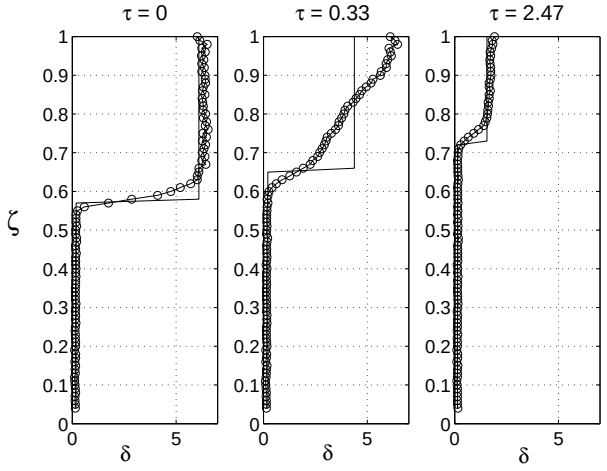

(a)

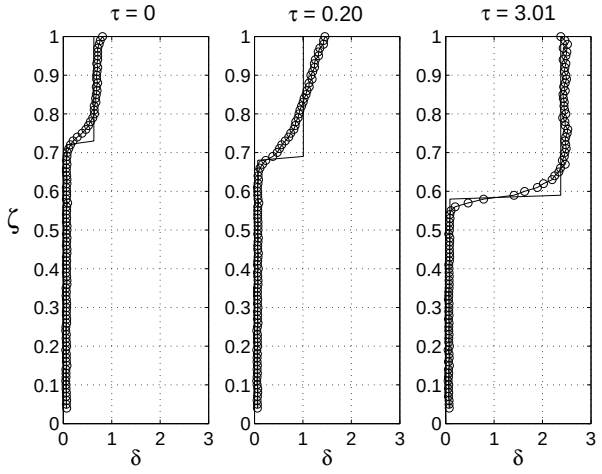

(b)

Figure 2.16: Transient responses of vertical δ of (a) 'B : Step down' (initial transition) and (b) 'B : Step Up' (restoration)

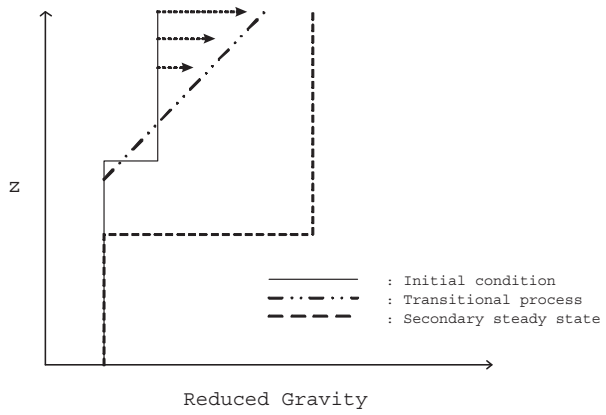

(a)

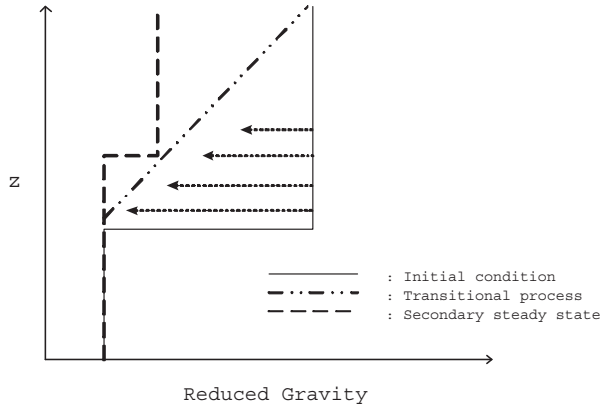

(b)

Figure 2.17: Schematics of transitional vertical profile of reduced gravity : (a) 'B : Step Up' and (b) 'B : Step Down'

2.5.2.2 Total ventilation rate change

Another DR strategy is to reduce the total ventilation rate Q. To validate the transient modeling in this situation, two experiments were performed : 'Q : Step Down' and 'Q : Step Up' which represent an initial transition and an restoration during a DR event.

Seeing Figures 2.18(a) & 2.18(b), experimental results and model predictions for both cases show good agreement. Temporal responses of ζ and δ_2 on the initial transition ('Q : Step Down') is slower than that of the restoration ('Q : Step Up'), so these results suggest that a DV system has slow initial transition and quick restoration of occupied zone (OZ) temperature, vertically averaged temperature within OZ, when the interface sits below OZ during DR period. The responses of OZ temperature minimize thermal discomfort for occupants and are advantages of DV systems over DR.

Initial stratification in the upper layer is less stronger that that of 'Buoyancy flux change' because buoyancy flux penetrating the density interface via a plume gradually increases or decreases in time unlike the stepped buoyancy flux changes of 'Buoyancy flux change' (Figures 2.19(a) and 2.19(b)). 'Q : Step Down' has no the initial stratification, which means that mixing on the upper layer is strong enough to keep the layer well-mixed during the transition period. However, 'Q : Step Up' shows initial stratification explained by the 'interface-to-ceiling' mixing process similar to 'B : Step Down'. The weaker stratification in the upper layer of 'Total ventilation rate change' supports the idea of well-mixed regimes of the layer during initial transition and explains the good agreements between experiments and model prediction.

2.6 Conclusion

A transient two-layer model of a mechanical DV system is derived to predict the time response to changes in heat fluxes and ventilation rates. Two competing time scales T_n and T_f are used for normalizing time scales between the model predictions and the experimental results. By using a dye attenuation technique to measure the density in time, the transitional responses of experiments were obtained.

Specifying practical criteria of convergence for ζ and δ_2, time scales for the

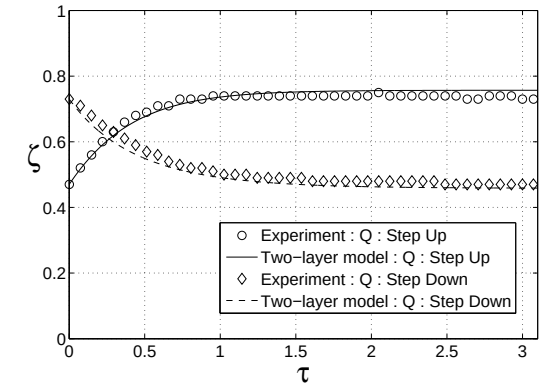

(a)

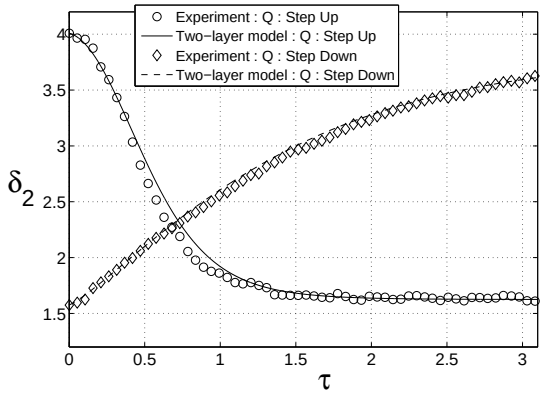

(b)

Figure 2.18: Experimental results and transient two layer model prediction of total ventilation rate change (Step up (initial transition): $\delta_2^o = 1.6$ and $\mu = 4.0$, Step down (restoration): $\delta_2^o = 4.0$ and $\mu = 1.6$) : (a) Transient responses of ζ and (b) those of δ_2

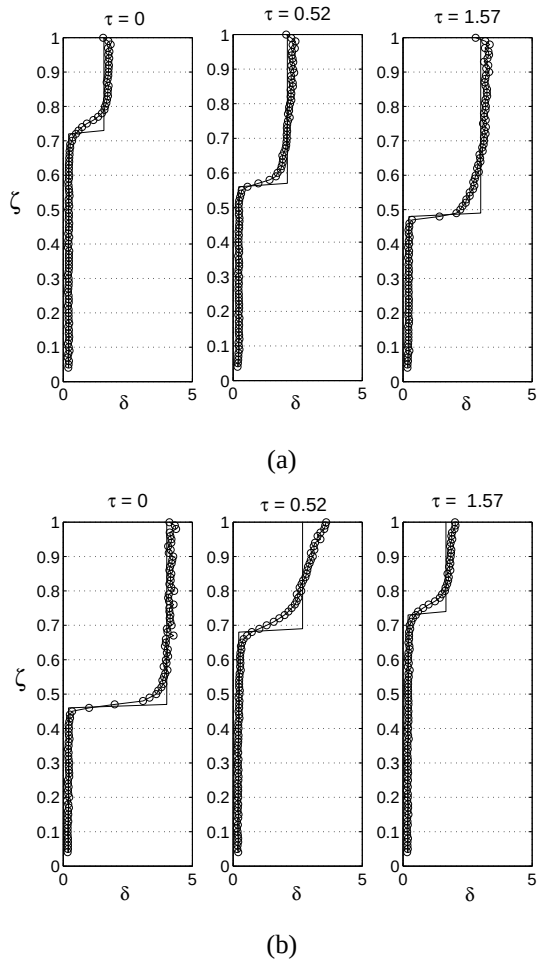

Figure 2.19: Transient responses of vertical δ of (a) 'Q : step down' and (b) 'Q : step up'

convergence were estimated by numerical simulation of the model and an approximate solution of Laurent series expansion. The difference of convergence time scales between ζ and δ_2 increases when μ increases for ascending and descending ζ cases. The phase diagrams of ζ and δ_2 show that there are no overshoot or undershoot responses of ζ but δ_2 has such responses.

Experiments for simulating IT and DR shows good agreements with the model prediction in time and support the well-mixed assumptions for the lower and upper layers. The strategies of DR responses are categorized as 'Buoyancy flux change' and 'Total ventilation rate change' which represent practical applications of DR strategies. Transitional responses of ζ and δ_2 in DV system during DR, with slow initial transition and quick restoration, minimize occupants thermal discomfort.

Chapter 3

Transient responses of Underfloor Air Distribution (UFAD) system

3.1 Introduction

A UFAD system is an energy efficient ventilation systems which has low cooling energy consumption. Unlike a conventional OH ventilation system which ideally has an uniform room temperature, the existence of a hot air zone near the ceiling of a UFAD system increases extraction temperature at vents, which allows a UFAD system to maintain a higher cooling rate compared to the OH system when the same cooling energy is provided.

However, the internal flow dynamics of a UFAD system is not as simple as the OH system due to thermal stratification. In the UFAD system, any heat source propagates upward to form the upper hot air zone and conditioned air is discharged from floor diffusers directly to cool the lower occupied zone, which establishes vertical thermal stratification in a room. The thermal stratification is ideally understood by two-layer stratification when all interior walls are insulated. A theoretical model was proposed by Lin & Linden [30] including two important physical components, the thermal plume and the negatively buoyant jet, for satisfying mass and heat balance over a space. Furthermore, the negatively buoyant jet, which is generated when the conditioned air discharges from floor diffuser, makes the UFAD modeling complicated. If the momentum of the

buoyant jet is strong enough for the jet to penetrate the density interface, turbulent entrainment across the density interface due to the penetration brings upper hot air down to lower occupied zone raising the temperature of the lower zone. The local Richardson number *Ri* characterizes the entrainment process.

Even though the thermal stratification of the UFAD system is an important advantage for improving the ventilation efficiency, the thermal stratification could cause occupant discomfort when the interface is below occupant's height, typically 1.7 2.0 m, in which the occupant experiences high temperature difference on lower and upper body. Previous studies in [31] and [37] suggested steady state models to predict the height of the interface and the temperature difference between the lower and upper zones with a single plume and single diffuser or with multiple plumes and multi diffusers. However, the thermal environment varies in time, and the models can not provide temporal responses of the vertical temperature distribution.

To investigate the temporal vertical temperature distribution corresponding to various operating conditions, in this Chapter, we describe a transient UFAD model based on two-layer stratification driven by a combination of the plume and the buoyant jet. In § 3.2, we derive three equations which represent the temporal responses of the height of density interface, the lower-layer temperature, and the upper-layer temperature when a single plume and a single diffuser exist in a room. We nondimensionalized the equations with the two time scales T_f and T_n in Chapter 2. An analytical solution of the negatively buoyant jet is derived to analyze how much the diffuser jet entrains surrounding fluid and to estimate the *Ri* which parameterized the penetrative entrainment across the density interface. The transient model is also extended to handle multiple plumes and jets in a room. In § 3.3, experimental set-ups for simulating transient responses of vertical temperature or density distribution are described. Two quantitative methods, based on numerical optimization and linear-fit techniques, are developed to estimate the height of the density interface and the densities of the lower and upper layers in terms of the instantaneous density distribution in time. Comparison studies between experimental results and theoretical predictions for various operating conditions are provided in § 3.4. The detailed discussion of the penetrative entrainment process and engineering perspectives are given in § 3.5.

3.2 Modeling

3.2.1 Penetrative entrainment induced by turbulent fountain

The flow from a floor diffuser in UFAD system can be described as a turbulent fountain [30]. By entraining surrounding fluid, the volume flux increases and the density of the fountain decreases with height. After the fountain reaches its maximum height at which the momentum of the fountain is zero, the flow reverses and the cool air falls down, causing the turbulent interaction between upflow and downflow. This interaction reduces the maximum height of the fountain, as observed in experimental studies, i.e. [44] in a homogeneous surrounding fluid and [10] in a linearly stratified fluid.

If the maximum height of flow from a diffuser is below the height H of the room, thereby avoiding impingement of the fountain on the ceiling, the volume or flowrate of the downflow of the fountain should be estimated by the entrainment of upper zone air and the interaction between the upflow and the downflow of the fountain. Several studies analyzed the downflow ([11], [35] and [39]). However, these studies consider only the cases when the fountain is surrounded by homogeneous or linearly stratified fluid. Vertical temperature profiles in UFAD systems show that there is a sharp density transition at the top of the lower (occupied) zone.

Due to the density interface, traditional turbulent fountain theory for the diffusers is not applicable to the flow in a UFAD system, because the upflow and downflow of the fountain disturb the interface and cause penetrative entrainment across the interface. The penetrative entrainment due to the downflow of a turbulent fountain across a density interface in a UFAD was studied by [30] and [37]. In their studies, the volume flux of the downflow Q_e due to penetrative entrainment across the density is assumed to be proportional to the volume flux, Q_i of the fountain at the density interface. In [5], the penetrative entrainment is assumed to be be a function of local Richardson number at the interface.

$$Ri = \frac{\triangle g' b_i}{{w_i}^2}, \tag{3.1}$$

where $\triangle g'$ is the buoyancy difference across the interface and b_i and w_i are the local width and the vertical velocity of the fountain, respectively. Lin [30] related the penetrative entrainment rate, $E \equiv Q_e/Q_i$, across the density interface to the local Richardson

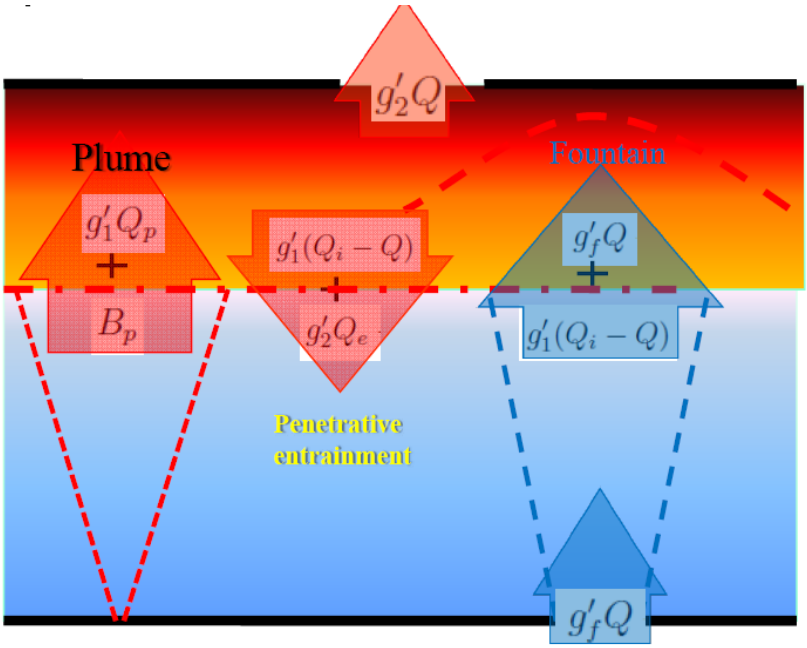

Figure 3.1: Schematic of two layer model of UFAD with single plume and single diffuser

number so that $E = E(Ri)$. Liu [37] extended Lin's study of the penetrative entrainment of a single plume and single diffuser to multiple plumes and multi diffusers. The study suggests that increasing the number of diffusers with constant total ventilation flow rate decreases E because large number of the diffusers corresponds to large Ri. Lin and Liu's studies suggested a relation between E and Ri at steady state and in our study, the relation of E and Ri for penetrative entrainment will be validated not only for the steady state but also for the transient situation.

3.2.2 Mathematical description

3.2.2.1 Mass and buoyancy balance

We develop a two-layer model of a time-dependent UFAD system from volume and buoyancy balance over the room. The room is assumed to be insulated by adiabatic walls, and cool air enters through a diffuser and leaves through a vent in the ceiling. The temperature (or density) of the room is partitioned by a horizontal interface. Lower

and upper layers are assumed to be well-mixed. We consider a single plume and single fountain, as seen in Figure 3.1, to be the only available channels for transporting heat or density between the layers.

From conservation of volume flux, the time dependent equations for the lower and upper layers are, respectively,

$$\frac{dV_1}{dt} = -Q_p + Q_e + Q, \tag{3.2}$$

$$\frac{dV_2}{dt} = Q_p - Q_e - Q, \tag{3.3}$$

where Q is the total ventilation rate and V_1 and V_2 are the volumes of lower and upper layers, respectively, and Q_p and Q_e are the volume fluxes of the plume and the penetrative entrainment, respectively.

The buoyancy flux balances for the two layers can be expressed as

$$\frac{\partial g_1' V_1}{\partial t} = g_f' Q + g_1'(Q_i - Q) + g_2' Q_e - g_1'(Q_i - Q) - g_1' Q_p - g_f' Q, \tag{3.4}$$

$$\frac{\partial g_2' V_2}{\partial t} = g_f' Q + g_1'(Q_i - Q) + g_1' Q_p + B_p - g_1'(Q_i - Q) - g_2' Q_e - g_2' Q, \tag{3.5}$$

where B_p is the buoyancy flux of the heat or density source, g_f' is reduced gravity of the fountain and g_1' and g_2' represent the temperature or density of the lower and upper layers, respectively. For simplicity, the reduced gravity of fountain, g_f' is set to zero ($g_f' = 0$). Rearranging (3.4) and (3.5), we get

$$\frac{\partial g_1' V_1}{\partial t} = -g_1' Q_p + g_2' Q_e, \tag{3.6}$$

$$\frac{\partial g_2' V_2}{\partial t} = g_1' Q_p - g_2'(Q + Q_e) + B_p. \tag{3.7}$$

Expanding the partial derivatives on the left hand side of (3.6) and (3.7), we get

$$V_1 \frac{\partial g_1'}{\partial t} = -g_1'(Q_e + Q) + g_2' Q_e, \tag{3.8}$$

$$V_2 \frac{\partial g_2'}{\partial t} = g_1' Q_p - g_2' Q_p + B_p. \tag{3.9}$$

From (3.2) and (3.3), the equation for the movement of density interface $z = h$ is

$$S\frac{dh}{dt} = -Q_p + Q_e + Q, \tag{3.10}$$

where S is the floor area. It is assumed the room has vertical walls. Equations (3.8),(3.9) and (3.10) describe the time dependent behavior of the system.

We introduce the non-dimensional interface height ζ and non-dimensional reduced gravity δ_i as defined in chapter 2 by

$$h = \zeta H, \quad g_i' = \delta_i C^{-1} B^{2/3} H^{-5/3}, \tag{3.11}$$

where the subscript $i = 1, 2$ refers to the lower and upper layers, respectively. In addition, two competing time scales, the filling box time scale T_f and the replenishment time scale T_n as defined in Chapter 2 are reintroduced for estimating the time scales as below,

$$T_f = \frac{S}{CB^{1/3}H^{2/3}}, \tag{3.12}$$

$$T_n = \frac{V}{Q} = \frac{SH}{Q}. \tag{3.13}$$

Before beginning the non-dimensional rearrangement, we also need to determine the volume flux Q_p of the plume.

$$Q_p = CB^{1/3}z^{5/3} = CB^{1/3}H^{5/3}\zeta^{5/3}, \tag{3.14}$$

where α_o is the entrainment constant taken to be 0.09 and the plume constant is $C = \pi(\frac{5}{2\pi\alpha_o})^{1/3}(\frac{6\alpha_o}{5})^{5/3}$.

All variables except Q_e, are set by the external conditions of the system. Because Q_e is not independent of the other variables, we need to define Q_e as a function of them. In chapter 2, Q_e is expressed as

$$Q_e = E\ Q_i = E\Gamma Q_d \tag{3.15}$$

where $\Gamma = Q_i/Q_d$ and Q_d is the volume flux from a single diffuser. As discussed above, E is the entrainment rate coefficient is a function of local Richardson number Ri at the

density interface. Lin [30] and Liu [37] estimated Γ via numerical simulations, but in our study analytic solutions for a negatively buoyant jet are suggested for simplifying to get Γ. The further discussion of the analytic solution is provided at next section.

If the system is cooled by a single diffuser ($Q_d = Q$), the non-dimensional forms of time dependent equations for the interface height and the buoyancy of the upper and lower layers are

$$\frac{d\zeta}{dt} = -\frac{1}{T_f}\zeta^{5/3} + (1+E\Gamma)\frac{1}{T_n}, \tag{3.16}$$

$$\frac{d\delta_1}{dt} = -\frac{(1+E\Gamma)}{\zeta T_n}\delta_1 + \frac{E\Gamma}{\zeta T_n}\delta_2, \tag{3.17}$$

$$\frac{d\delta_2}{dt} = \frac{1}{T_f(1-\zeta)}\{\zeta^{5/3}(\delta_1-\delta_2)+1\}. \tag{3.18}$$

By employing Γ, (3.16) - (3.18) can simply be non-dimensional excerpt the time, t. The two time scales, T_f and T_n are used to normalize the buoyancy B_p and the ventilation rate Q. Seeing (3.16) and (3.17), T_f and T_n are regarded as two important parameters to determine transient responses of the density interface height ζ and the lower layer density δ_1. However, T_f is only one time scale for predicting the upper layer density δ_2. By introducing μ and τ in chapter 2 given as

$$\mu = T_n/T_f, \quad t = \tau\sqrt{T_n T_f}, \tag{3.19}$$

and substituting (3.19) into (3.16)-(3.18), the system of equations for the transient UFAD model is

$$\frac{d\zeta}{d\tau} = -\sqrt{\mu}\zeta^{5/3} + (1+E\Gamma)\frac{1}{\sqrt{\mu}}, \tag{3.20}$$

$$\frac{d\delta_1}{d\tau} = -\frac{(1+E\Gamma)}{\sqrt{\mu}\zeta}\delta_1 + \frac{E\Gamma}{\sqrt{\mu}\zeta}\delta_2, \tag{3.21}$$

$$\frac{d\delta_2}{d\tau} = -\frac{\sqrt{\mu}}{(1-\zeta)}\{\zeta^{5/3}(\delta_2-\delta_1)-1\}. \tag{3.22}$$

In (3.20) - (3.22), μ represents the operating condition relating the balance of the strength of buoyancy and ventilation rate T_f and T_n and is only one parameter to dominate transient responses of ζ, δ_1 and δ_2 when Γ is independent to μ and E is constant in time.

To validate the equations (3.20) - (3.22), we consider the case of $E = 0$. The given equations becomes the same as the transient equations of a mechanical DV system. Because $E = 0$ is physically interpreted as no penetrative entrainment along the density interface which is the same situation of the DV system, the coincident of the transient equations of UFAD and mechanical DV systems with $E = 0$ guarantee the validity of (3.20) - (3.22) in this situation.

3.2.2.2 Steady state solutions

At steady state, equating the left hand sides of (3.20) - (3.22) to zero, we obtain

$$\mu = \frac{1+E\Gamma}{\zeta_{ss}^{5/3}}, \tag{3.23}$$

$$\frac{\delta_1^{ss}}{\delta_2^{ss}} = \frac{E\Gamma}{1+E\Gamma}, \tag{3.24}$$

$$\delta_2^{ss} - \delta_1^{ss} = \frac{1}{\zeta_{ss}^{5/3}}, \tag{3.25}$$

where ζ_{ss}, δ_i^{ss} and Γ^{ss} are steady-state values of ζ and δ_i and Γ, respectively. Substituting (3.25) and (3.24) into (3.23), we get

$$\delta_2^{ss} = \mu. \tag{3.26}$$

Then (3.23) and (3.24) give

$$\zeta_{ss} = (\frac{1+E\Gamma}{\mu})^{3/5} \tag{3.27}$$

$$\delta_1^{ss} = \frac{E\Gamma}{1+E\Gamma}\mu. \tag{3.28}$$

Hence, μ, which corresponds to the balance between the strength of heat source and the cooling load from the diffuser, is the most important independent parameter controlling the low layer temperature δ_1 and the interface height ζ, from which the desirable temperature δ_{oz} in the occupied zone is determined.

The steady state solutions of (3.26) - (3.28) can be estimated when Γ is determined. An analytic approach to get Γ is described in the following section.

3.2.2.3 Analytic solutions of negatively buoyant jet

In a homogeneous fluid, the momentum M and the buoyancy flux F_o of a negatively buoyant jet (NBJ) are related by the equation ([27])

$$\frac{dM}{dt} = -F_o. \tag{3.29}$$

Since the buoyancy flux is conserved, we have $M(t) = M_o - F_o t$ from the equation, where M_o is initial momentum of the jet. In contrast to a point source jet which has no volume flux and width at its source, a UFAD diffuser in the model has both an initial volume flux and width. Assuming a self similar profile, the jet width is,

$$\bar{b}(z) = \beta z + \bar{b}_o, \tag{3.30}$$

where $\bar{b}_o$ is the radius of the diffuser. We represent the velocity and density distribution using top-hat profile. Combining the spreading hypothesis $d\bar{b}/dt = \beta\bar{w}$ with $M(t) = M_o - F_o t$, where $\bar{b}$ is the width of the jet, $\bar{w}$ is the vertical top-hat velocity and β is the coefficient of jet propagation ($\beta = 6/5\alpha_f$: α_f is entrainment rate coefficient), we get

$$M = \pi\bar{w}^2\bar{b}^2 \tag{3.31}$$

$$\bar{b}\frac{d\bar{b}}{dt} = \beta\bar{w}\bar{b}. \tag{3.32}$$

By solving the partial differential equation (3.32) and substituting (3.31) into the solution of (3.32), we can get an equation for the width as a function of time as

$$\bar{b}(t) = \{\frac{4}{3}\frac{\beta}{\sqrt{\pi}}\frac{M_o^{3/2}}{F_o}(1-(1-\frac{F_o}{M_o}t)^{3/2}) + \bar{b}_o^2\}^{1/2}. \tag{3.33}$$

The height of the jet in time is easily obtained by combining (3.30) and (3.33) as

$$z(t) = \frac{\bar{b}(t) - \bar{b}_o}{\beta} \tag{3.34}$$

$$= \{\frac{4}{3\beta\sqrt{\pi}}\frac{M_o^{3/2}}{F_o}(1-(1-\frac{F_o}{M_o}t)^{3/2}) + (\frac{\bar{b}_o}{\beta})^2\}^{1/2} - \frac{\bar{b}_o}{\beta}. \tag{3.35}$$

Rearranging (3.35), we get

$$(z+\bar{b}_o/\beta)^2) = \frac{4}{3\beta\sqrt{\pi}}\frac{M_o^{3/2}}{F_o}(1-(1-\frac{F_o}{M_o}t)^{3/2}) + (\frac{\bar{b}_o}{\beta})^2 \tag{3.36}$$

$$(M_o - F_o t)^{1/2} = \{M_o^{3/2} - \frac{3\sqrt{\pi}F_o}{4\beta}((\beta z+\bar{b}_o)^2 - \bar{b}_o^2)\}^{1/3}. \tag{3.37}$$

Consequently, with (3.37), the flow rate of the NBJ, Q_i is given by

$$Q_i(t) = \sqrt{\pi}(M_o - F_o t)^{1/2}\cdot\bar{b}(t). \tag{3.38}$$

Substituting (3.36), (3.37) into (3.38), we get the flow rate of the NBJ as a function of z as

$$Q_i(z) = \sqrt{\pi}(M_o - F_o t)^{1/2}\cdot(\beta z+\bar{b}_o) \tag{3.39}$$

$$= \sqrt{\pi}[(\beta z+\bar{b}_o)^3\{M_o^{3/2} - \frac{3\sqrt{\pi}F_o}{4}(\beta z^2+2\bar{b}_o z)\}]^{1/3}. \tag{3.40}$$

$Q_i(t=0)$ from (3.38) is expected to be the same of $Q_i(z=0)$ from (3.40) and both Q_i from the two equations show the same answer as $Q_i(t=0,z=0) = \sqrt{\pi M_o}\bar{b}_o$.

Here, for normalizing $\bar{b}_o$, we define

$$\eta = \frac{H}{\sqrt{A_d}} \tag{3.41}$$

where $A_d = \pi\bar{b}_o^2$ for circular diffuser nozzle. The variable η also represents the degree of momentum flux of the diffuser compared to the ceiling height, H. Additionally, η is determined by H and A_d which are two important parameters of physical geometry of a UFAD system.

By dividing Q_o, initial flow rate of the diffuser, on both hand sides of (3.40) and plugging in $z=\zeta H$, $\bar{b}_o = \sqrt{\frac{\pi\eta}{H}}$, $M_o = C^2B_p^{2/3}H^{4/3}(\frac{\eta}{\mu})^2$ and $F_o = CB_p(\frac{\delta_1}{\mu})$ into (3.40), we get

$$\frac{Q_i}{Q_o} = \sqrt{\pi}[\eta^3(\beta\zeta+\frac{1}{\sqrt{\pi}\eta})^3 - \frac{3\sqrt{\pi}}{4C^2}\delta_1\mu^2(\beta\zeta+\frac{1}{\sqrt{\pi}\eta})^3(\beta\zeta^2+2\frac{1}{\sqrt{\pi}\eta}\zeta)]^{1/3} \tag{3.42}$$

$$= \sqrt{\pi}[J(\zeta,\eta,\beta) - P(\zeta,\eta,\beta,\delta_1,\mu)]^{1/3}. \tag{3.43}$$

where $J = \eta^3(\beta\zeta + \frac{1}{\sqrt{\pi}\eta})^3$ and $P = \frac{3\sqrt{\pi}}{4C^2}\delta_1\mu^2(\beta\zeta + \frac{1}{\sqrt{\pi}\eta})^3(\beta\zeta^2 + 2\frac{1}{\sqrt{\pi}\eta}\zeta)$. (3.72) provide us two limits: one is $J \gg P$ which is the case in which strong momentum of diffuser overcomes buoyancy and the other is $J \cong P$ which can have possible assumption that strong negative buoyancy dominates momentum flux from the diffuser so the flow from the diffuser spreads out at the bottom and no NBJ appears.

Even though J is independent of μ, P is determined by δ_1 and μ, so P is related to the strength of heat source. In typical operation of a UFAD system, NBJ from a diffuser is mainly driven by momentum, not buoyancy, because the buoyancy flux from a diffuser is relatively small compared to the heat source in a room. Therefore, $J \gg P$ is assumed to be a good approximation for simplifying (3.72).

Since $\Gamma = \frac{Q_i}{Q_o}$, (3.72) becomes with the approximation of $J \gg P$,

$$\Gamma \cong \sqrt{\pi}\beta\eta\zeta + 1. \tag{3.44}$$

With the simplified analytic solution of NBJ, (3.20)-(3.20) can be defined simply as

$$\frac{d\zeta}{d\tau} = -\sqrt{\mu}\zeta^{5/3} + (1 + E(\sqrt{\pi}\beta\eta\zeta + 1))\frac{1}{\sqrt{\mu}}, \tag{3.45}$$

$$\frac{d\delta_1}{d\tau} = -\frac{(1 + E(\sqrt{\pi}\beta\eta\zeta + 1))}{\sqrt{\mu}\zeta}\delta_1 + \frac{E(\sqrt{\pi}\beta\eta\zeta + 1)}{\sqrt{\mu}\zeta}\delta_2, \tag{3.46}$$

$$\frac{d\delta_2}{d\tau} = \frac{\sqrt{\mu}}{(1-\zeta)}\{\zeta^{5/3}(\delta_1 - \delta_2) + 1\} \tag{3.47}$$

and the steady-state solutions (3.27) and (3.28) become

$$\mu\zeta_{ss}^{5/3} - E\sqrt{\pi}\beta\eta\zeta_{ss} - (E+1) = 0 \tag{3.48}$$

$$\delta_1^{ss} = \mu\frac{E(\sqrt{\pi}\beta\eta\zeta_{ss} + 1)}{1 + E(\sqrt{\pi}\beta\eta\zeta_{ss} + 1)} \tag{3.49}$$

where ζ_{ss} is the steady state height and δ_1^{ss} is the lower-layer buoyancy at steady state.

ζ_{ss} of (3.48) can be solved numerically when β, η E and μ are constant at steady-state. Since $0 \leq \zeta_{ss} \leq 1$, any solution of ζ_{ss} not satisfying this inequality is treated as unrealistic. According to the solutions of (3.48) and (3.49), larger μ corresponds to lower ζ_{ss}, which represents the situation where the strong thermal source pushes

the interface down to the floor and larger η lifts the interface ζ_{ss} up caused by larger momentum flux from the diffuser. The limiting value $\mu = 1$ for the two-layer model of mechanical DV in chapter 2 does not guarantee the validity of the two-layer model in UFAD because the penetrative entrainment, Q_e, is added to total ventilation rate, Q_{tot}, which needs to be carried by the plume. The limiting μ of UFAD varies with β, η and E in (3.48) and (3.49) is given as

$$\mu^{limit} = \delta_1^{limit} \tag{3.50}$$

$$= 1 + E(\sqrt{\pi}\beta\eta + 1). \tag{3.51}$$

When $\mu \leq \mu^{limit}$, the system will be in the well-mixed regime, and the two-layer model developed here no longer applies.

3.2.2.4 Richardson number of negatively buoyant jet

In our study, *Ri* is the dominant parameter to represent the strength of the perturbation of the interface and to estimate the mixing between upper and lower density layers. The source of the perturbation is the penetrated discharged jet from the floor diffuser and the local Richardson number, *Ri*, can be estimated from the width of the jet, $\bar{B}$, the velocity of the jet, $\bar{W}$ (both parameters are obtained by top-hat representation of the jet) and the upper and lower layer density or buoyancy, $\acute{g}_1$ and $\acute{g}_2$. By definition, *Ri* is given by

$$Ri = \frac{(\acute{g}_2 - \acute{g}_1) \cdot \bar{b}(z)}{\bar{w}(z)^2}. \tag{3.52}$$

With three important non-dimensional parameters ζ, $\delta_{1\ or\ 2}$ and μ, each term of

right hand side of (3.52) is redescribed as

$$\acute{g_2} - \acute{g_1} = (\delta_2 - \delta_1)\frac{B^{2/3}}{CH^{5/3}}. \tag{3.53}$$

$$\bar{w}(\zeta) = Q_i(\zeta)/(\pi \bar{b}(\zeta)^2) \tag{3.54}$$

$$= \frac{\Gamma C B^{1/3} H^{5/3}}{\pi \mu H^2 (\beta\zeta + \frac{1}{\sqrt{\pi}\eta})^2} \tag{3.55}$$

$$\bar{b}(z) = H(\beta\zeta + \frac{1}{\sqrt{\pi}\eta}). \tag{3.56}$$

Substituting (3.53),(3.55) and (3.56) into (3.52), we can get

$$Ri = (\delta_2 - \delta_1)(\beta\zeta + \frac{1}{\sqrt{\pi}\eta})^5 (\frac{\mu\pi}{\Gamma})^2 \frac{1}{C^3}. \tag{3.57}$$

With the simplified Γ relation of (3.44), *Ri* can be given as

$$Ri = (\delta_2 - \delta_1)\pi(\frac{\beta\zeta}{C} + \frac{1}{C\sqrt{\pi}\eta})^3 (\frac{\mu}{\eta})^2. \tag{3.58}$$

3.2.3 Time-dependent buoyancy and ventilation flow rate

The heat load on a building is not constant during its operational period, so the building under dynamic transition of its heat load is important to be understood. In the model previously derived, the buoyancy is fixed in time. For simulating dynamic change of the heat load in time, the reference buoyancy B_{rf} is needed to fix the time scales. Additionally, by adjusting the room set point temperature by increasing or decreasing the ventilation rate, the reference ventilation rate Q_{rf} is also fixed by

$$T_f^{rf} = \frac{S}{C B_{rf}^{1/3} H^{2/3}}, \quad T_n^{rf} = \frac{SH}{Q_{rf}} \tag{3.59}$$

where B_{rf} is the reference buoyancy and Q_{rf} is the reference ventilation flow rate.

Given T_f^{rf} and T_n^{rf}, the reference operating condition, μ_{rf} is given as

$$\mu_{rf} = T_n^{rf}/T_f^{rf} = \frac{CB_{rf}^{1/3}H^{5/3}}{Q_{rf}}, \tag{3.60}$$

$$t = \tau\sqrt{T_n^{rf}T_f^{rf}}. \tag{3.61}$$

α and λ are normalized by the change of buoyancy and ventilation rate in time, according to

$$\alpha = \frac{B_{op}}{B_{rf}} \tag{3.62}$$

$$\lambda = \frac{Q_{op}}{Q_{rf}} \tag{3.63}$$

where B_{op} is the operational buoyancy and Q_{op} is the operational ventilation rate. α is the fraction of the operational buoyancy given the reference buoyancy and λ is the fraction of the operational ventilation rate upon the reference ventilation rate. Using simplified Γ, substitute (3.59)-(3.61) into (3.20)-(3.22) to get

$$\frac{d\zeta}{d\tau} = -\alpha^{1/3}\sqrt{\mu_{rf}}\zeta^{5/3} + (1+E(\sqrt{\pi}\beta\eta\zeta+1))\frac{\lambda}{\sqrt{\mu_{rf}}}, \tag{3.64}$$

$$\frac{d\delta_1}{d\tau} = -\lambda\frac{(1+E(\sqrt{\pi}\beta\eta\zeta+1))}{\sqrt{\mu_{rf}}\zeta}\delta_1 + \lambda\frac{E(\sqrt{\pi}\beta\eta\zeta+1)}{\sqrt{\mu_{rf}}\zeta}\delta_2, \tag{3.65}$$

$$\frac{d\delta_2}{d\tau} = \alpha^{1/3}\frac{\sqrt{\mu_{rf}}}{(1-\zeta)}\{\zeta^{5/3}(\delta_1-\delta_2)+\alpha^{2/3}\}. \tag{3.66}$$

Once μ_{rf} is fixed in time, α and λ are two important parameters to determine the transient responses of ζ, δ_1 and δ_2. λ affects the response of ζ and δ_1 in (3.64) and (3.65) and α is explicitly related to ζ and δ_2 in (3.64) and (3.66).

Substituting μ with μ_{rf}, (3.85) became

$$Ri = (\delta_2-\delta_1)\pi(\frac{\beta\zeta}{C}+\frac{1}{C\sqrt{\pi}\eta})^3(\frac{\mu_{rf}}{\eta\lambda})^2. \tag{3.67}$$

Because *Ri* is a parameter only related to the diffuser, λ only affects *Ri*. By changing α, *Ri* is indirectly changed due to the change of $\delta_2-\delta_1$. The equations given above are

used to predict transient responses at the start of or the end of demand response activities in next section.

3.2.4 Models for multiple plumes and Multi diffusers

In a real application of a UFAD system, multi plumes and jets are located in a localized area, so it is important to investigate any system response change due to an increase or decrease of the number of the plumes and jets. At first, by revisiting the plume equation (3.10) with total buoyancy flux B_p and the number of the equal strength plumes m, we get

$$Q_p^{tot} = mC(B_p/m)^{1/3}H^{5/3}\zeta^{5/3} \tag{3.68}$$

$$= m^{2/3}CB_p^{1/3}H^{5/3}\zeta^{5/3}. \tag{3.69}$$

By increasing or decreasing the number of diffusers, the penetrative entrainment flow rate Q_e may change. Q_e for multi jets configuration is redefined as

$$Q_e = E\Gamma_{md}Q_{tot} \tag{3.70}$$

where

$$\Gamma_{md} = \frac{Q_i}{Q_{tot}} = \sqrt{\pi}[(\eta/n)^3(\beta\zeta + \frac{1}{\sqrt{\pi}\eta})^3 - \frac{3\sqrt{\pi}}{4C^2n}\delta_1\mu^2(\beta\zeta + \frac{1}{\sqrt{\pi}\eta})^3(\beta\zeta^2 + 2\frac{1}{\sqrt{\pi}\eta}\zeta)]^{1/3} \tag{3.71}$$

$$= \sqrt{\pi}[J(\zeta,\eta,\beta,n) - P(\zeta,\eta,\beta,\delta_1,\mu,n)]^{1/3}. \tag{3.72}$$

n is the number of equal diffusers, Q_{tot} is total ventilation flow rate on a room, and the ventilation flow rate of each diffuser is $Q_o = Q_{tot}/n$.

By modifying the mass and buoyancy balance equations (3.8)-(3.10) with (3.69)

and (3.70), non dimensional equations of the balance equations are obtained:

$$\frac{d\zeta}{d\tau} = -m^{2/3}\sqrt{\mu}\zeta^{5/3} + (1+nE\Gamma_{md})\frac{1}{\sqrt{\mu}}, \tag{3.73}$$

$$\frac{d\delta_1}{d\tau} = -\frac{(1+nE\Gamma_{md})}{\sqrt{\mu}\zeta}\delta_1 + \frac{nE\Gamma_{md}}{\sqrt{\mu}\zeta}\delta_2, \tag{3.74}$$

$$\frac{d\delta_2}{d\tau} = \frac{\sqrt{\mu}}{(1-\zeta)}\{m^{2/3}\zeta^{5/3}(\delta_1-\delta_2)+1\}. \tag{3.75}$$

According to (3.73)-(3.73), m and n affect the system of equations explicitly.

With the simplified relation $\Gamma_{md} = \frac{1}{n}(\sqrt{\pi}\beta\eta\zeta+1)$ ($J \gg P$) in (3.44), (3.73)-(3.73) turns into

$$\frac{d\zeta}{d\tau} = -m^{2/3}\sqrt{\mu}\zeta^{5/3} + (1+E(\sqrt{\pi}\beta\eta\zeta+1))\frac{1}{\sqrt{\mu}}, \tag{3.76}$$

$$\frac{d\delta_1}{d\tau} = -\frac{(1+E(\sqrt{\pi}\beta\eta\zeta+1))}{\sqrt{\mu}\zeta}\delta_1 + \frac{E(\sqrt{\pi}\beta\eta\zeta+1)}{\sqrt{\mu}\zeta}\delta_2, \tag{3.77}$$

$$\frac{d\delta_2}{d\tau} = \frac{\sqrt{\mu}}{(1-\zeta)}\{m^{2/3}\zeta^{5/3}(\delta_1-\delta_2)+1\}. \tag{3.78}$$

Splitting the ventilation flow rate do not affect the system with simplified Γ, however, splitting the buoyancy flux affects the system and we get a different answer. In this situation, n only affects E, so accurate prediction of E is important to estimate the dependency on n in UFAD system. Steady state solutions are

$$\mu = \frac{1+nE\Gamma}{m^{2/3}\zeta_{ss}^{5/3}}, \tag{3.79}$$

$$\frac{\delta_1^{ss}}{\delta_2^{ss}} = \frac{nE\Gamma}{1+nE\Gamma}, \tag{3.80}$$

$$\delta_2^{ss} - \delta_1^{ss} = \frac{1}{m^{2/3}\zeta_{ss}^{5/3}}, \tag{3.81}$$

Using the simplified Γ assumption, we get

$$m^{2/3}\mu\zeta_{ss}^{5/3} - E\sqrt{\pi}\beta\eta\zeta_{ss} - (E+1) = 0 \tag{3.82}$$

$$\delta_1^{ss} = \mu\frac{E(\sqrt{\pi}\beta\eta\zeta_{ss}+1)}{1+E(\sqrt{\pi}\beta\eta\zeta_{ss}+1)} \tag{3.83}$$

$$\delta_2^{ss} = \mu. \tag{3.84}$$

If we consider equal strength of multi diffusers, (3.58) is modified to

$$Ri = n^2(\delta_2-\delta_1)\pi(\frac{\beta\zeta}{C}+\frac{1}{C\sqrt{\pi}\eta})^3(\frac{\mu}{\eta})^2 \tag{3.85}$$

where n is the number of diffusers.

From (3.85), Ri is proportional to $\delta_2-\delta_1$, μ^2 and n^2. With a fixed number of diffusers, a physical interpretation of the relation is that when the larger buoyancy source exist in a room and is cooled by UFAD (when μ is large), the penetrative entrainment is characterized by larger Ri. In this case, Liu [37] suggested a proportional relation of $E \sim Ri^{-1}$ when $Ri \geq 8$ and other studies forms similar relation for larger Ri. The number of diffuser N is also an important parameter to determine the range of Ri. Based on (3.85) and $E \sim Ri^{-1}$, we can get

$$E \sim (\frac{1}{\mu n})^2. \tag{3.86}$$

Based on (3.86), E approaches zero when μ or n is large, which means that the penetrative entrainment along the density interface decreases when μ or n increases.

3.3 Experiments

3.3.1 Method

Salt-water experiments were performed, simulating the thermal plumes and diffuser fountains which are the two important physical phenomena in a UFAD system. Similar to the DV experimental set up in chapter 2, the plume was mounted at the center of the top of the tank and the diffusers positioned symmetrically around the plume.

To avoid any interaction between the plume and the diffusers, the distance between the plume and the diffusers was longer than the combined maximum width of the plume and the diffuser jet.

Two circular diffusers with 1.27 cm diameter were installed at the same height as the plume source and were positioned symmetrically apart from the source, by 15 cm. The end of each diffuser was covered with fine mesh with aperture size approximately 0.15 cm $\times$ 0.15 cm to promote turbulence of the diffuser flow.

The salt source simulating a heat source in a room was colored with a red dye which acts as a surrogate for salinity and so, by calibration, provided width-averaged density from measurements of light intensity (Figure 3.2). The detailed description of the dye attenuation technique was described in Chapter 2.3. Processing the image provided the two-dimensional spatial density distribution of the whole tank averaged from front to back. The vertical density profile was obtained by taking a horizontal average at each vertical height, avoiding the disturbed density field by the plume and diffuser jets.

A digital camera recorded experiments in a digital video format with resolution 1440×1050 pixels and the digital format guaranteed no loss of information of the recorded images during repeated postprocess. The resolution of vertical height from bottom to top of the tank is approximately 500 pixels for $H = 25$cm and approximately 900 pixels for $H = 39$cm for capturing whole density field of the tank.

3.3.1.1 Density interface

The theoretical two-layer representation assumes the stratification consists of lower and upper layer densities, δ_1 and δ_2, respectively, and a density interface at height ζ. However, experimental results of a UFAD system typically show a relatively smooth density transition between lower and upper layer compared to the ideal two-layer distribution and some stratification in each layer. The penetrative entrainment due to the impinging diffuser jets across the density interface causes mixing which forms this transitional region. The theory defines the position of the density interface in (3.10) as a vertical position to satisfy mass flux balance among Q_p, Q_i and Q_e. Our experimental technique does not provide us with explicit measurement of the balance at the interface

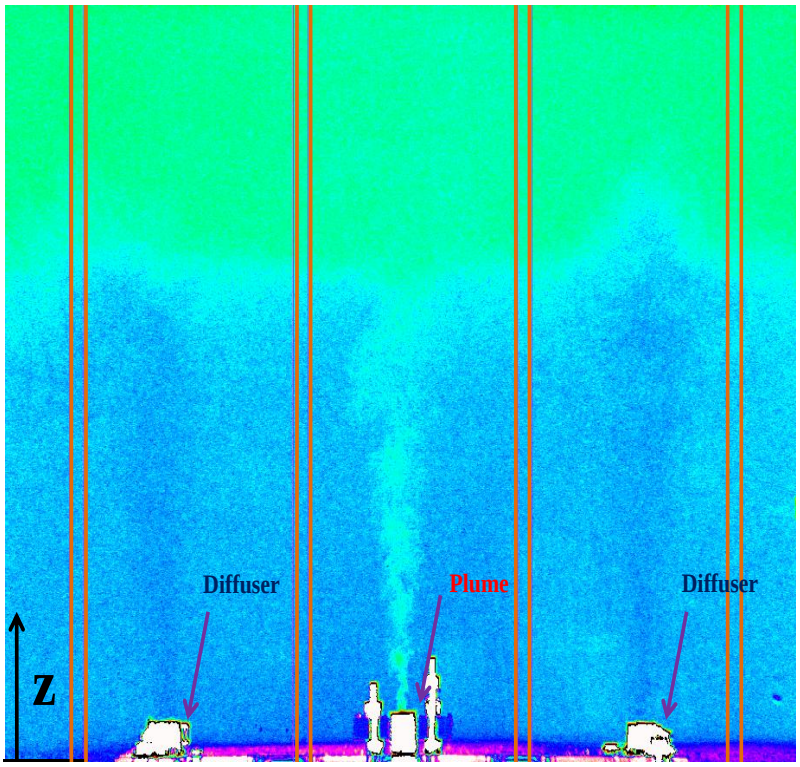

Figure 3.2: Corrected image of experiments : The 8 vertical solid lines are used for collecting data in time.

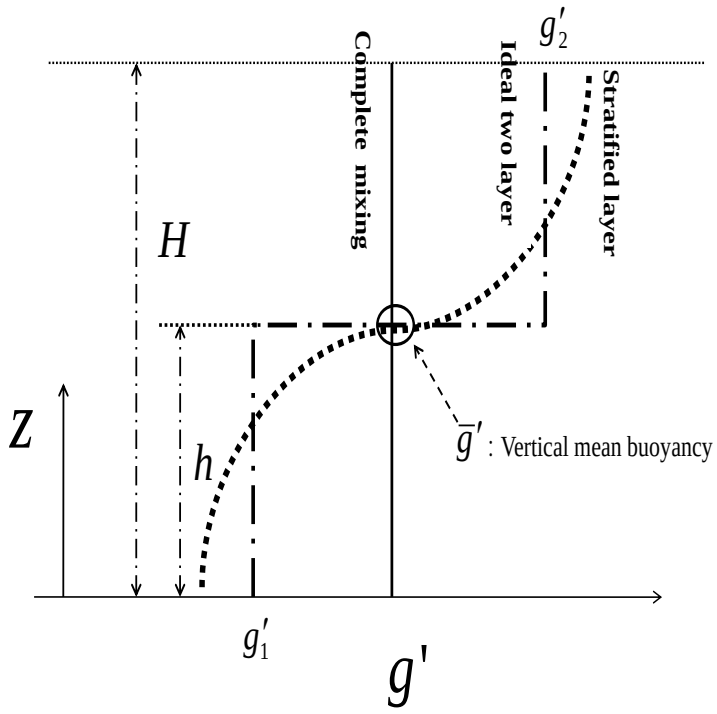

Figure 3.3: Schematics of various vertical density as reduced gravity profile of 1. complete mixing (Solid line), 2. ideal two layer stratification (dot dash line) 3. stratified layer(dot line)

(by measuring Q_p, Q_i and Q_e), so it is not possible to get the exact point of the density interface. Consequently, we need to determine the equivalent position ζ from the measured vertical density distributions.

The thickness ε of the transitional layer is important for determining the height ζ. If ε is small, it is relatively straight forward to determine ζ. However, once ε is relatively large, we can only define upper and lower bounds of the interface within which ζ may exist. To find ζ and the bounds of the layer, "Optimizing Scheme" (OS) and "Linear Fit Scheme" (LFS) are proposed on next paragraphs.

Any representation of the density interface height should satisfy the mass balance equation given as

$$\bar{\rho}H = \bar{\rho_1}h + \bar{\rho_2}(H-h), \tag{3.87}$$

where

$$\bar{\rho} = \frac{1}{H}\int_0^H \rho(z)dz, \tag{3.88}$$

$$\bar{\rho_1} = \frac{1}{h}\int_0^h \rho(z)dz, \tag{3.89}$$

$$\bar{\rho_2} = \frac{1}{H-h}\int_h^H \rho(z)dz, \tag{3.90}$$

where $\rho(z)$ is the vertical density distribution from experimental measurement and z is the vertical position from the plume source (see Figure 3.2). We nondimensionalize the above equations as before (see Chapter 2). Then, we convert (3.87)-(3.90) into

$$\bar{\delta} = \delta_1\zeta + \delta_2(1-\zeta) \tag{3.91}$$

where

$$\bar{\delta} = \int_0^1 \delta(\hat{\zeta})d\hat{\zeta}, \tag{3.92}$$

$$\delta_1 = \frac{1}{\zeta}\int_0^\zeta \delta(\hat{\zeta})d\hat{\zeta}, \tag{3.93}$$

$$\delta_2 = \frac{1}{1-\zeta}\int_\zeta^1 \delta(\hat{\zeta})d\hat{\zeta}, \tag{3.94}$$

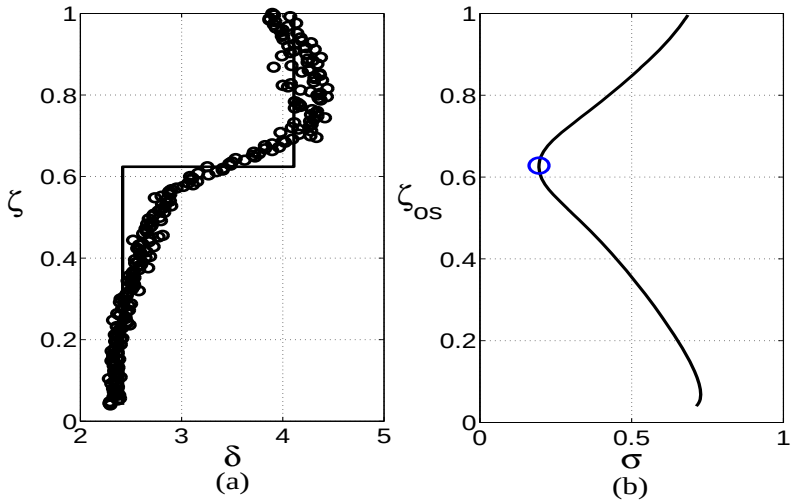

Figure 3.4: Example of two-layer representation using optimizing scheme (OS) : (a) experimental measurement is instantaneous non-dimensional vertical density profile at $t = 3000s$ at case HMG (homogeneous initial environment) case C-1 and the two-layer representation is estimated by OS; (b) vertical σ distribution

where δ in the non-dimensional density of experimental measurements and only a function of $\hat{\zeta}$ where $\hat{\zeta} = z/H$. The two methods to measure ζ are presented below.

3.3.1.1.1 Optimizing scheme .

"Optimizing Scheme (OS)" is a method to find the interface height ζ. Once we know ζ, δ_1 and δ_2 are estimated by (3.93) and (3.94). There are various combinations of δ_1 and δ_2 along ζ, but most of combinations do not fit well with the experimental measurements. To find ζ which has the best fit with the measurement, we define a cost function σ as evaluating how wells the two-layer representations fits the measurements. The cost function σ is defined as

$$\sigma(\zeta) = \int_{\hat{\zeta}=\zeta}^{\hat{\zeta}=1} |\delta(\hat{\zeta}) - \delta_2| d\hat{\zeta} + \int_{\hat{\zeta}=0}^{\hat{\zeta}=\zeta} |\delta(\hat{\zeta}) - \delta_1| d\hat{\zeta}. \tag{3.95}$$

We find ζ to minimize σ and the ζ obtained by OS method is ζ_{opt}. An example of the two-layer representation with the OS method is given at Figure3.4 which gives a minimum at $\zeta_{opt} = 0.62$. From the corresponding experimental profile in Figure3.4(a),

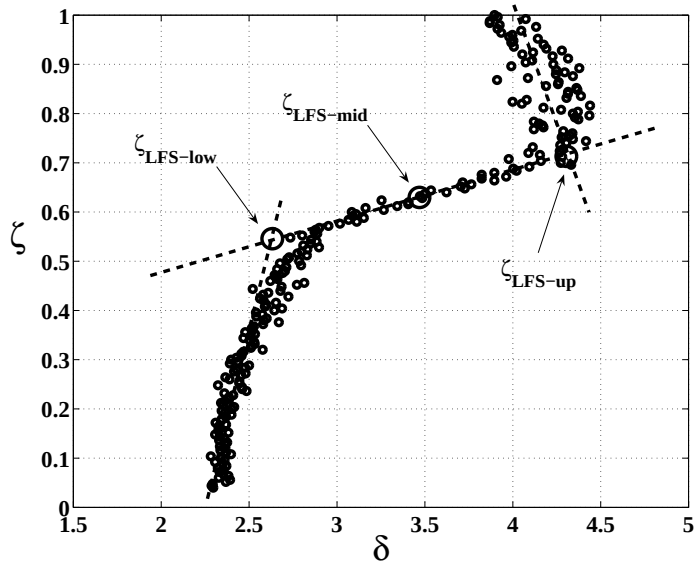

Figure 3.5: Example of two-layer representation using Linear-Fitting Scheme (LFS) : Experimental measurement is instantaneous non-dimensional vertical density profile at $t = 3000s$ at HMG (homogeneous initial environment) case B and the two-layer representation is estimated by LFS. ζ_{LB}, ζ_{MD} and ζ_{UB} are the intersection points of each curve. ε is the thickness of the transitional layer by $\varepsilon = \zeta_{UB} - \zeta_{LB}$

we see that ζ_{opt} is positioned within transitional layer between lower and upper layer. δ_1 and δ_2 corresponding to ζ_{opt} are calculated by (3.93) and (3.94) by substituting ζ_{opt} into ζ.

However, this method cannot provide us the thickness of the transitional layer, so next, we propose a scheme based on linear-fit of lower, transition and upper layer to capture the thickness.

3.3.1.1.2 Linear fit scheme .

To identify the thickness of the transitional layer, we use a "Linear Fit Scheme" (LFS) which fits curves to the lower layer, transitional layer and upper layer, and we define the intersection of the curves to mark the intersections from the lower layer to the interface etc. We denote the intersection of the lower layer and transitional layer as ζ_{LB} and that of the curves of transitional layer and upper layer as ζ_{UB}. δ_{LB} and

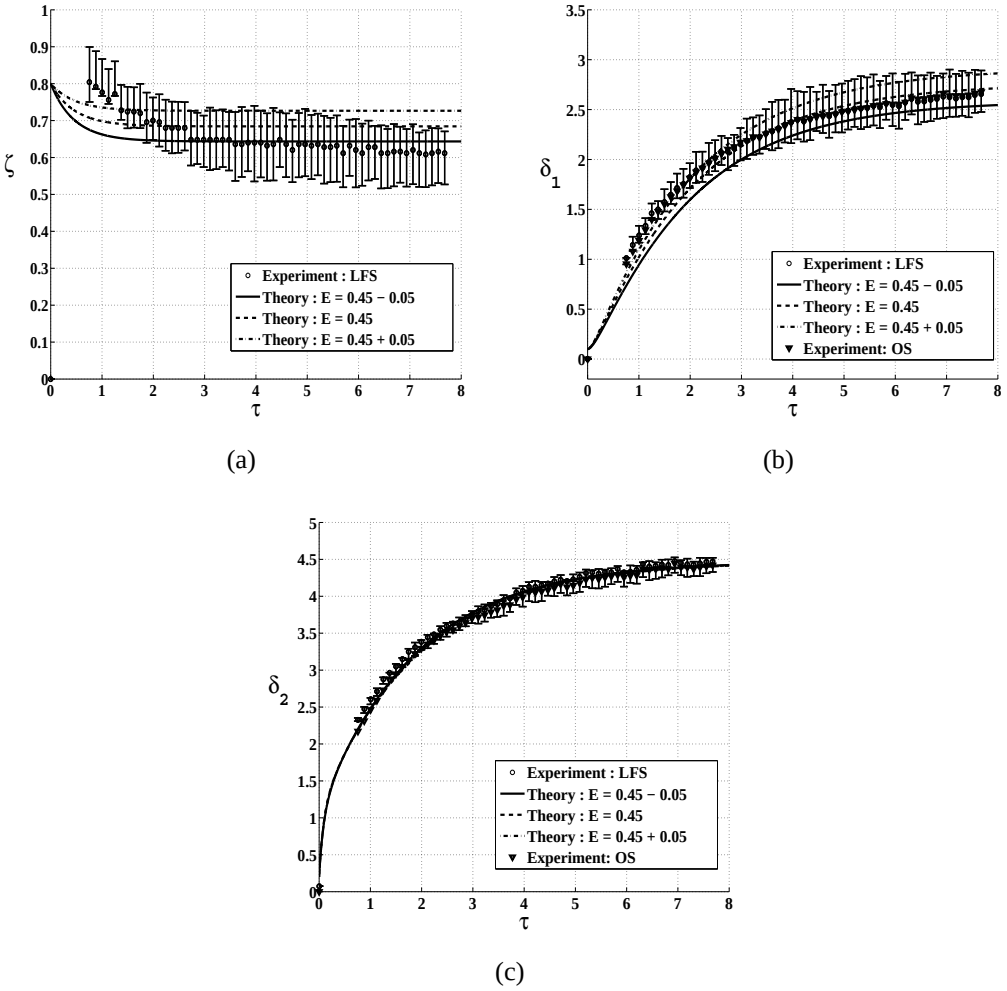

Figure 3.6: Comparison between experimental data and theoretical prediction of HMG case B: three theoretical predictions are provided; $E = 0.45 \pm 0.05$ (a) LFS interface height ($\zeta_{LFS-mid}$) and lower errorbar is $\zeta_{LFS-low}$ and upper errorbar is ζ_{LFS-up} (b) transient lower layer density; lower and upper bound of the density are calculated when $\zeta_{LFS-low}$ and ζ_{LFS-up} (c) transient upper layer density; lower and upper bound of the density are calculated when $\zeta_{LFS-low}$ and ζ_{LFS-up}

δ_{UB} are densities at ζ_{LB} and ζ_{UB}, respectively. The middle point ζ_{MD} between ζ_{LB} and ζ_{UB} is obtained by $\zeta_{MB} = \frac{\zeta_{LB}+\zeta_{UB}}{2}$ and corresponding density at δ_{MB} is defined as $\delta_{MB} = \frac{\delta_{LB}+\delta_{UB}}{2}$. These two parameters ζ_{MB} and δ_{MB} represent the density interface of LFS method. The thickness of the transitional layer ε is defined as $\varepsilon = \zeta_{UB} - \zeta_{LB}$.

In order to determine ζ_{LB} and ζ_{UB}, linear best-fit straight lines were fitted to the experimental data points satisfying $\delta(\hat{\zeta}) < \delta_1$ and $\delta(\hat{\zeta}) > \delta_2$, where δ_1 and δ_2 are defined by (3.93) and (3.94) with $\zeta = \zeta_{opt}$, respectively. In the interface, a straight line was fitted through datapoints such that $\zeta_{opt} - 0.05 < \delta < \zeta_{opt} + 0.05$. An example is shown in Figure3.5, and it provides a reasonable description of the measured profile. Using the linear curves of each layer, ζ_{LB}, ζ_{MD} and ζ_{UB} are obtained by finding the intersections among the curves and experimental measurements fit well in the curves. Therefore, transitional layer between lower and upper layer is successfully described as ζ_{LB} and ζ_{UB} through the LFS method.

Comparing the measurement to the the theory which do not allow to have transitional layer and in which the density interface is described as the position of step-change between lower and upper layer, ζ_{opt} of OS method and ζ_{MD} of LFS method do not guarantee to represent the exact position of theoretical density interface which is assumed to be within the transitional layer, $\zeta_{LB} \leq \zeta \leq \zeta_{UB}$. Because ζ varies within the bounds, corresponding δ_1 and δ_2 also varies such as

$$\delta_1^{LB} \leq \delta_1 \leq \delta_1^{UB} \tag{3.96}$$

$$\delta_2^{LB} \leq \delta_2 \leq \delta_2^{UB} \tag{3.97}$$

where δ_1^{LB} and δ_2^{LB} are calculated by (3.93) and (3.94) with $\zeta = \zeta_{LB}$ and δ_1^{UB} and δ_2^{UB} are calculated by (3.93) and (3.94) with $\zeta = \zeta_{UB}$. Figure3.6(a)-3.6(c) show how much δ_1 and δ_2 are affected when ζ moves up or down within the transitional layer. δ_2 is less influenced than δ_1 by the variation of ζ.

The penetrative entrainment rate E is an important parameter to determine the transient behaviors of ζ and δ_1. Previous studies ([29] and [37]) suggested $err(E) \sim \pm 0.05$. Therefore, we plot three curves corresponding to $E = 0.40$, 0.45 and 0.50 in Figures 3.6(a)- 3.6(c). The three curves fall within the uncertainty of the measurements after the upper layer becomes well-mixed ($\tau > 2$. Based on these comparisons, the

transitional layer measured by LFS method is a reasonable way to compare experiments and theory.

3.3.1.2 Reproducibility of experiments

It is important to confirm whether the experiments have any systematic errors preventing experimental reproducibility of transient responses for experiments with the same initial condition and operating conditions (B_p and Q). To check the reproducibility, two experimental cases, HMG (homogeneous initial environment) case C and HMG case D in Table 3.1 are chosen. Each case was performed three times with identical conditions. To get the same initial conditions, the tank was filled with fresh water and fixed flow rates for the plume and the diffuser were set for each run. To quantify the reproducibility, the Standard Error of the Mean (SEM) is chosen for error estimation, where SEM is defined by

$$SEM = \frac{STD_{sample}}{N_{sample}} \tag{3.98}$$

where STD_{sample} is the standard deviation of instantaneous samples corresponding to the same time of each run and $N_{sample} = 3$ is the number of the identical runs.

Figures 3.7(a)-3.7(c) show SEM of each object, ζ_i, δ_1 and δ_2 obtained by the OS method. Both cases show good matches among the identical runs proven, as shown by small values of SEM. The HMG case D shows better reproducibility than HMG case C, which is possibly explained by lower interface height of HMG case D. Due to the reduced Q_e of HMG case D, corresponding to lower ζ_i, the thickness of the transitional layer is expected to be narrower than the HMG case C, so the OS method will have more consistency. However, HMG case C still shows comparable consistency among the runs.

3.3.2 Experiment matrix

Experiments were performed to reveal transient responses of a UFAD system under various operating conditions and also used for validating two-layer theoretical model to simulate realistic temporal responses of a UFAD system. Initial conditions of experiments are important to determine how much the system changes in transitional period.

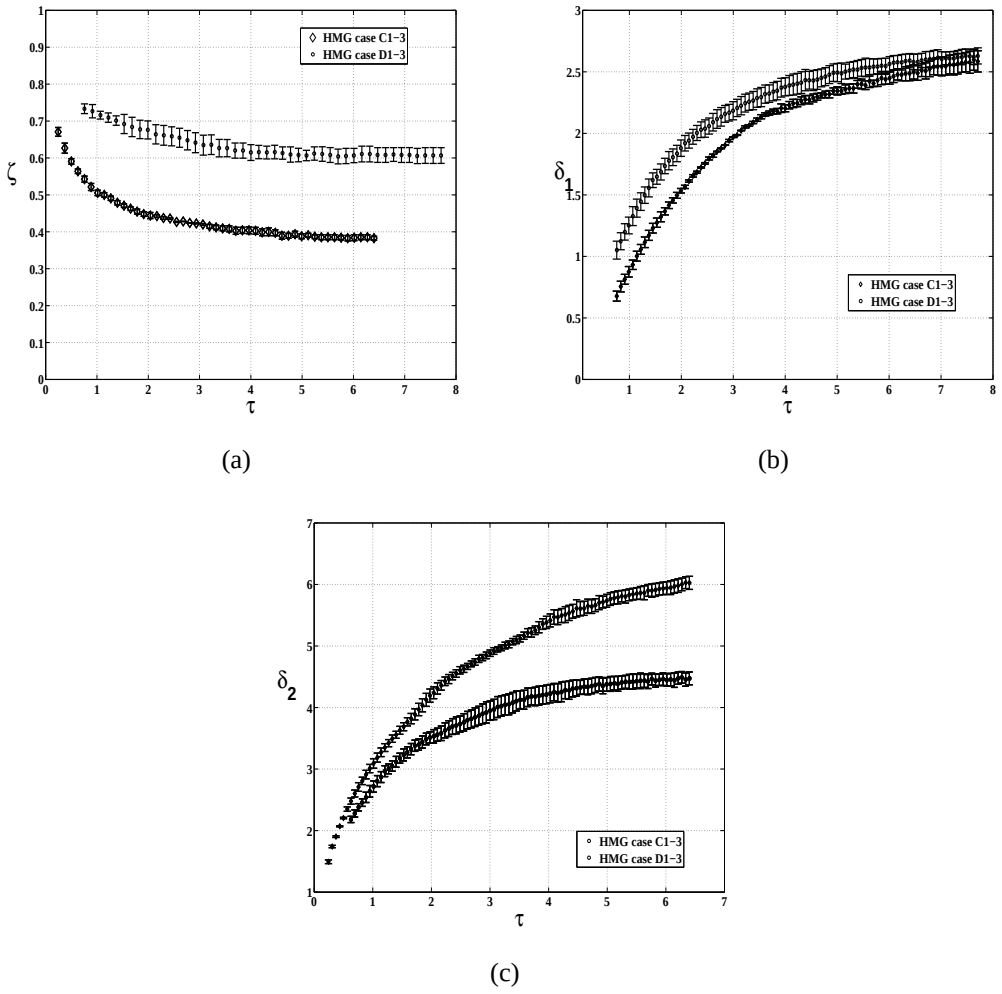

Figure 3.7: Experiments for confirming reproductivity of HMG case C1-C3 and HMG case D1-D3: (a) ζ_i, (b) δ_1 and (c) δ_2; The errorbars of each plot represent instantaneous *SEM* of each quantity in time

Table 3.1: Experimental parameters of homogeneous environment initial conditions (Initial transient): The cases A-D are experimental situations when the density of the environment and diffuser are the same; the density of the diffuser is 0.9986 g/cm^3.

	Initial condition (g/cm^3)	Operational buoyancy flux (cm^4s^{-3})	Operational Total ventilation flow rate (cm^3/s)	Operational μ	Geometric parameter η	Height (cm)
HMG-A	0.9986	39.5	28.31	8.80	32.60	39
HMG-B	0.9986	39.5	35.84	6.97	32.60	39
HMG-C-1	0.9986	50.79	28.31	6.03	20.90	25
HMG-C-2	0.9986	50.79	28.31	6.03	20.90	25
HMG-C-3	0.9986	50.79	28.31	6.03	20.90	25
HMG-D-1	0.9986	50.79	20.79	4.45	20.90	25
HMG-D-2	0.9986	50.79	20.79	4.45	20.90	25
HMG-D-3	0.9986	50.79	20.79	4.45	20.90	25

Every experimental cases should be understood by a combination of initial condition and operating conditions.

The combination of initial condition and operating conditions are given in Tables 3.1 and 3.2. Table 3.1 presents various experimental cases starting from a homogeneous environment which represents a pre-mixed or well-mixed room before normal HVAC operation. Before the HVAC operation, typically, in a morning, the room has been cooled during the night time without any internal heat source so no thermal stratification exists. When the HVAC turns on, because conditioned air of diffuser flow has temperature close to initial room temperature, in other words, no buoyancy driven flow exists (experimentally, initial density of a tank is same as that of diffuser flow), initial discharging flow from the diffuser reaches the ceiling of the room. However, the room is thermally stratified after thermal plumes of internal heat loads form the upper heat air zone. The diffuser flow becomes negatively buoyant along its vertical propagation, so the flow falls back to the bottom in the upper zone. Most the experimental cases in Table 3.1 simulate this situation and reveal how a UFAD system works to cool a room down in the morning when transient responses of the system is important for providing occupant's thermal comfort.

Table 3.2 shows a different category of the combination of initial conditions and operating conditions. A stratified environment as initial condition is examined for investigating the situation in which a UFAD system changes its operating condition as DR activity to reduce peak load demand. Demand Responses (DR) are actions to reduce instantaneous electricity consumption (W) for relieving the peak electricity load in a building. The actions are mainly categorized as; 1. Reduce internal heat load or 2. Decrease ventilation flow rate by increasing room set temperature. Even though both DR actions reduce the total cooling load in a room or building, the physical interpretations of the actions are different; 1. Reducing the internal heat load corresponds to decreasing the strength of thermal plume 2. Decrease ventilation flow rate is regarded as decreasing the strength of cold air fountains from floor diffusers. A typical DR strategy, "Step Up or Down" which reduce or decrease the internal heat load and ventilation rate, respectively, is used for evaluating effectiveness of both DR strategies and estimating thermal comfort of occupants in several experimental cases. Theoretical prediction are provided for experimental data.

In our study, the initial conditions of the stratified environment are regarded as the steady state of normal operation or DR operation which are at the beginning of DR operation and at the end of DR operation, respectively. μ of each operation corresponds to vertical stratification at steady state (represented by ζ, δ_1 and δ_2), so the initial stratified environment is obtained by running a UFAD system with as μ_{NO} (normal operation) or μ_{DR} (DR operation) until the steady states when the density profile reaches 99% of their steady state values in experiments is reached. By changing operating conditions by increasing or decreasing the strength of internal heat load (situations of Buoyancy Step Up (BSU) or Step Down (BSD)) and the flow rate of diffuser flow (situations of Ventilation rate Step Up (VSU) or Step Down (VSD)), a UFAD system experience dramatic changes of its thermal environments described by steep gradient of changes of ζ, δ_1 and δ_2 in time. An immediate change of buoyancy flux of the plume or ventilation flow rate of the diffuser is applied to simulate stepping change of operating parameters to reduce peak demand). Transient responses of those changes are investigated through various experimental conditions to study how much the occupied zone thermally is affected by DR activities.

Table 3.2: Experimental parameters for stratified density initial conditions : initial stratifications are obtained by running experiments with initial buoyancy flux and total ventilation flow rate for three hours.

	Initial condition : Buoyancy flux (cm^4s^{-3})	Initial conditions : Total ventilation flow rate (cm^3/s)	Operational Buoyancy flux (cm^4s^{-3})	Operational total ventilation flow rate (cm^3/s)	η	Height (cm)
BSD-A	26.62	28.31	52.6	20.76	20.90	39
BSD-B	13.42	28.31	39.0	28.31	20.90	25
BSD-C	39.0	28.01	26.85	28.31	20.90	39
BSU-A	26.85	28.31	13.42	28.31	20.90	39
BSU-B	39.01	20.5	26.85	28.31	20.90	39
VSD-A	39.00	35.02	39.00	13.42	20.90	39
VSD-B	39.00	35.02	39.00	20.5	20.90	39
VSD-C	39.00	20.79	39.00	28	20.90	39
VSU-A	39.00	13.42	39.00	35.02	20.90	39
VSU-B	39.00	20.5	39.00	35.02	20.90	39
VSU-C	39.00	24.5	39.00	35.02	20.90	39

3.4 Experimental Results

3.4.1 Homogeneous environment

We examined the transient responses when the initial density environment is homogeneous. Experiments starting from a homogeneous environment experienced transient processes before forming the two-layer stratification. Turning on the plume and the diffusers simultaneously at the beginning of the experiments, the flow of the plume and the diffusers met at the ceiling (the bottom of the tank in salt-water analogy) and formed a buoyant upper layer near the ceiling. The detail description of the initial transitional period to form the initial buoyant layer is given below.

3.4.1.1 Initial formation of two layer stratification

The formation of the upper layer was not an instantaneous process, as observed from vertical density profiles measured during initial transient responses. Figures 3.8(a)-3.8(d) show the initial transient responses of the density profiles for the cases, HMG-A to HMG-D. The overall density averaged over the whole depth increased in time. However, a well-mixed upper layer developed on a different time scale. These temporal differences in forming the upper layer can be explained by the strength of the plume and the diffuser flows. To investigate the relation between the temporal differences and the strength of the plume and the diffuser flows, we measured the time of initial appearance of the upper layer τ_{up}, which is defined as the time when two-layer stratification becomes to be clearly identified in a vertical density profile. Because the upper layer is initially stratified, we estimated upper layer stratification from the buoyancy frequency, $N = \sqrt{\frac{\partial g'}{\partial z}}$ within the upper layer. The time τ_{up} was measured to be the time when N reached to be a threshold as 90% of steady-state value of N when the upper layer is assumed to be well-mixed. We observed well-mixed upper layer in all cases, possibly because that the layer was relatively narrow during initial transition and the plume flow was strong enough to keep the layer well-mixed.

In Figures 3.8(a) and 3.8(b), HMG-B took longer compared to HMG-A which had larger μ compared to HMG-B. Additionally, in Figures 3.8(c) and 3.8(d), There is a correlation between τ_{up} and μ such that increasing μ implies decreasing τ_{up}. A possible

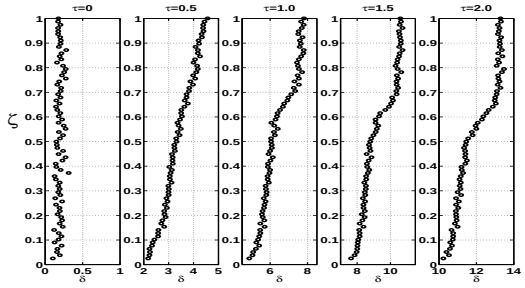

(a)

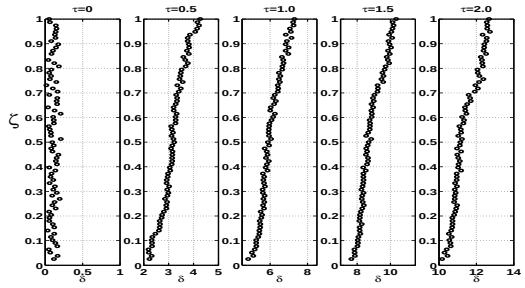

(b)

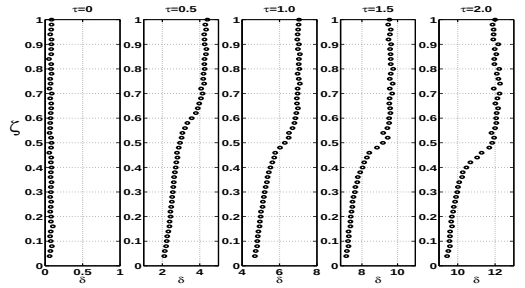

(c)

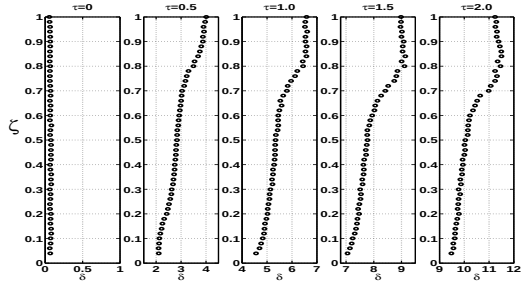

(d)

Figure 3.8: Initial transient responses of vertical density profile of homogeneous initial condition at $\tau = 0$, $\tau = 0.5$, $\tau = 1.0$, $\tau = 1.5$ and $\tau = 2.0$: the operating condition is (a) HMG-A : $\mu = 8.53$ and $\eta = 32.60$, (b) HMG-B : $\mu = 6.94$ and $\eta = 32.60$, (c) HMG-C: $\mu = 6.03$ and $\eta = 20.90$ and (d) HMG-D: $\mu = 20.90$ and $\eta = 4.45$

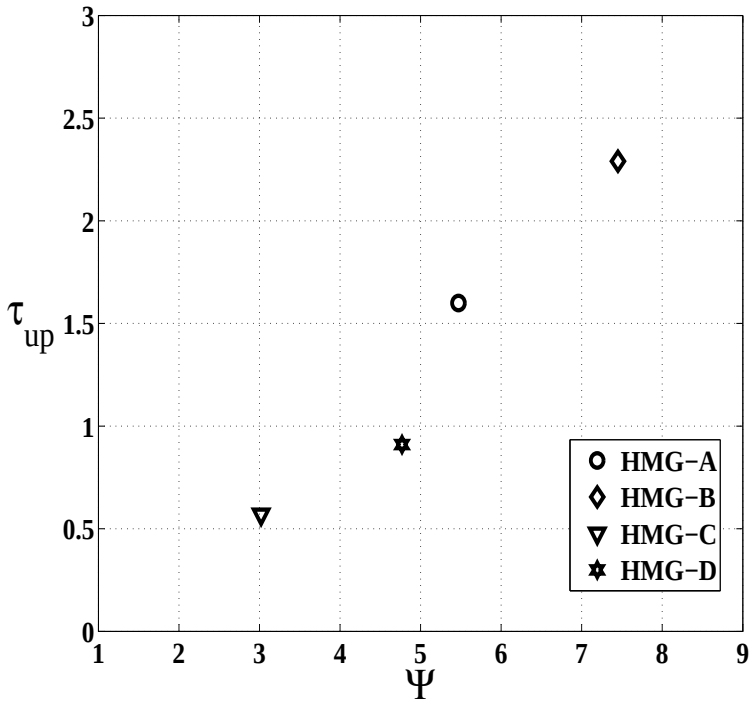

Figure 3.9: The relation between the time delay to form a well-mixed upper layer τ_{up} and the dimensionless competition between the mixing and the stratification, Ψ, for HMG-A to HMG-D

scenario of layer formation is that the buoyant flow of the plume travels over the ceiling and displaces initial diffuser flow from the ceiling. Because the filling box time scale T_f is inversely proportional to μ, the layer will form in relatively a short time when μ is large.

Furthermore, the cases of lower η (HMG-C and HMG-D) show earlier formation of the upper layer compared to those of higher η (HMG-A and HMG-B). η, a dimensionless representation of momentum flux competition between stratification (represented by μ) and mixing (represented by η) may determine the time when the well-mixed upper layer forms. Lin & Linden [30] suggested the competition between them as dimensionless parameter Ψ (in their study, the symbol was Γ) such that

$$\Psi = \frac{Q^{3/2}}{A_d^{5/4} B_p^{1/2}} \tag{3.99}$$

for a single plume and single diffuser. By using the definition of μ and η with multiple equal-strength diffusers, (3.99) becomes

$$\Psi = \sqrt{\frac{C^3 \eta^5}{n^3 \mu^3}} \tag{3.100}$$

where $n = 2$ in our case as the number of diffusers. When Ψ is large, mixing is dominant,but when Ψ is small, the stratification dominates to form a two-layer stratification. In Figure 3.9, τ_{up} increases monotonically with Ψ, which supports the idea that when the mixing is strong (larger Ψ), the formation of two-layer stratification is delayed (smaller τ_{up}). However, the number of experimental cases was not sufficient to reveal an explicit relation between τ_{up} and Ψ.

3.4.1.2 E and Ri relation

Mixing across a density interface is one of important physical processes to explain the buoyancy flux balance between lower and upper layer and the penetrative entrainment rate E as a function of local Ri. To confirm the relation between E and Ri, experimental data which were interpreted by ζ, δ_1 and δ_2 through the LFS method are used to estimate E influencing temporal responses of the system. The temporal rate

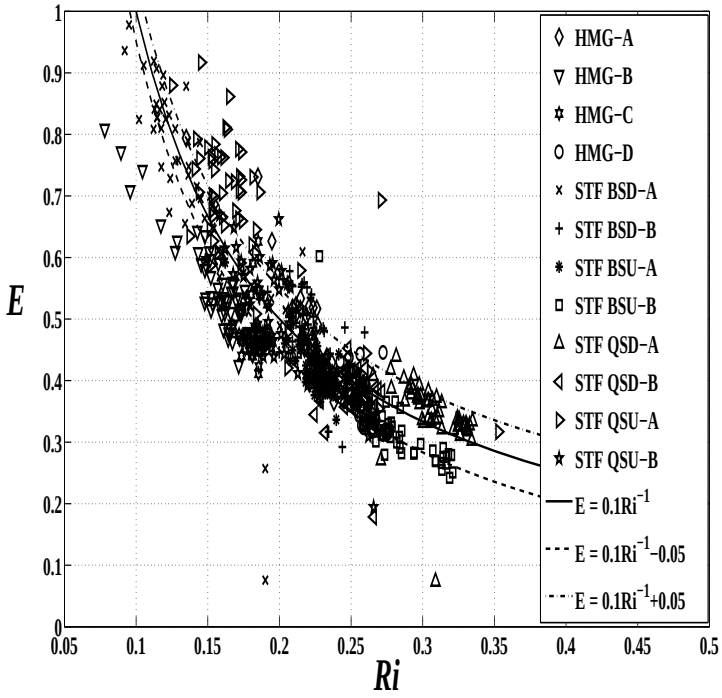

Figure 3.10: E .vs. *Ri* relation among our experimental cases: Solid curve corresponds to $E = 0.1Ri^{-1}$ and dashed and dot-dashed line represent the error bound $err(E) \sim \pm 0.05$

of change of δ_1, $d\delta_1/d\tau$ are chosen to estimate E because transient response of δ_1 is strongly influenced by E, which is an important parameter to determine the rate of mixing in lower layer. The influence of E over δ_1 was proposed in (3.21) and we reformulate (3.21) to get instantaneous E

$$E = \frac{\sqrt{\mu}\zeta}{(\delta_2 - \delta_1)\Gamma}\left(\frac{d\delta_1}{d\tau} + \frac{\delta_1}{\sqrt{\mu}\zeta}\right). \tag{3.101}$$

The first of derivative, $d\delta_1/d\tau$ was measured by a fourth-order finite difference scheme with $d\tau < 0.05$.

Hence, we could not explicitly measure penetrative flow rate of a diffuser flow across the interface without velocity measurement of diffuser flow, so we used the theoretical negatively buoyant jet model in (3.55) to estimate *Ri*.

Figure 3.10 shows the relation between E and *Ri*. Most of the experiments in our study corresponded to relatively low *Ri*, so the powers of -1 or $-3/2$ can not be distinguishable within the range. For those reasons, we chose -1 power law as standard in our study instead of $-3/2$. Both experimental data of homogeneous and stratified initial conditions sit within $E = 0.1 * Ri^{-1} \pm 0.05$. Because the range of *Ri* of the measurements was narrow, the given relation between E and *Ri* is only considered as a possible one. However, the UFAD operating condition also has relatively low *Ri*, where neither buoyancy difference between the layer nor diffusion is relevant to physical process of the mixing. Therefore, the relation $E = 0.1Ri^{-1}$ is assumed to represent the physical process of mixing in small-scale experiment and in UFAD system in our study.

3.4.1.3 Comparison between theory and experiments

The experimental data were processed using two different density interface process methods, OS and LFS in the previous section and Figure 3.11 shows the density interface measurement using OS and LFS method as functions of time. The density interface heights estimated by the two methods are similar to each other except for $\tau < 1$ before two-layer stratification formed. The match between OS and LFS method means that the middle point of the transitional layer after initial transition period($\tau > 1$) is also the point of the best fit two-layer stratification out of given experimental density profile.

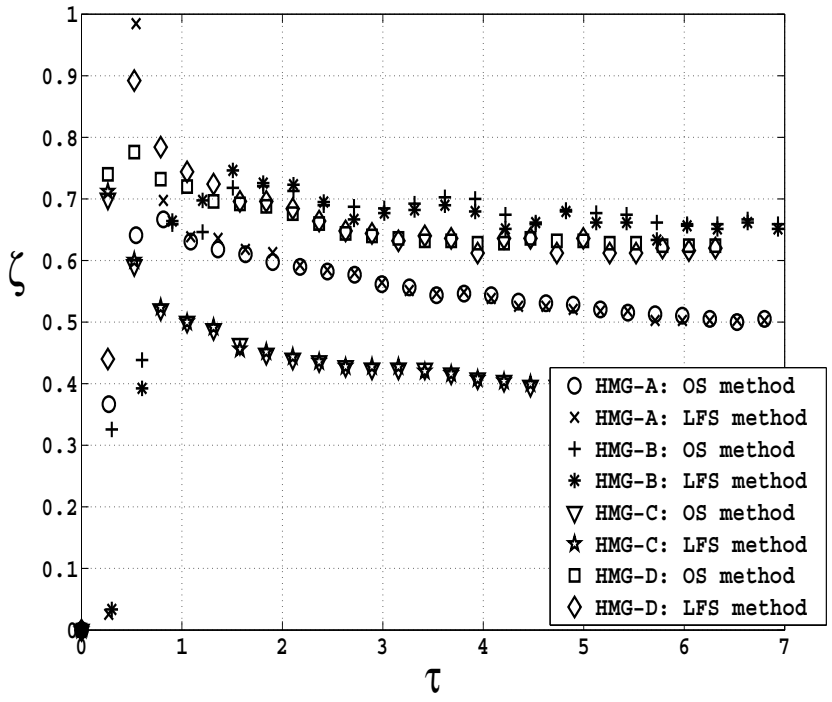

Figure 3.11: Density interface height measurement by OS and LFS method

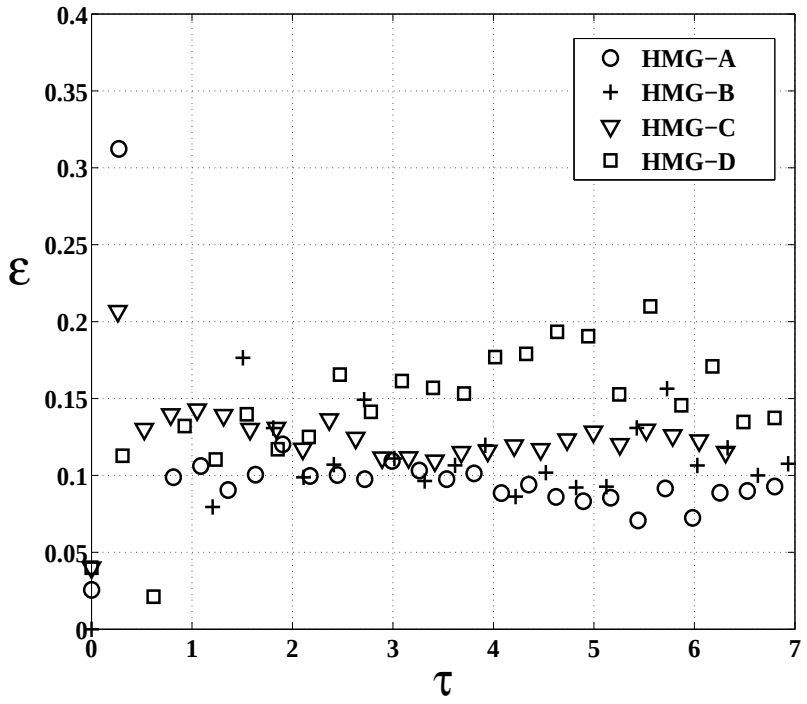

Figure 3.12: Transitional layer thickness ε measurement by LFS method

Temporal histories of interfacial thickness ε among HMG-A to HMG-D are provided in Figure 3.12. $\varepsilon < 0.2$ in almost all vertical density profiles is a relatively low value compared to the thickness for the lower and upper layers, so the results support that vertical density profile in the experiments maintained a sharp interface during their transitional period and a two-layer representation with sharp interface is acceptable for comparison purposes between experiments and theory.

Because all experimental cases of homogeneous environment initial condition except HMG-E starts with a non-buoyant environment in which the initial density was the same as diffuser density, once we turn on the plume and diffuser, the density of lower and upper layer gradually increased in time. From Figures 3.13(a) & 3.13(b), once two-layer stratification formed, the gradual increases of the densities of the layers are shown. The density difference between lower and upper layer of HMG-B remained the same once the two-layer stratification formed, but that of HMG-C gradually increased in time. Based on steady state theories in (3.23)-(3.25), the difference increases when E decreases and in experiment, HMG-C corresponded to lower E compared to HMG-A ($E \sim 0.3$ at HMG-C and $E \sim 0.6$ at HMG-A). Comparing transient responses of HMG-C and HMG-A, it is reasonable to say that the difference of lower and upper layer densities of a system with smaller E increases slowly compared to a system with larger E.

Figures 3.14(a)-3.15(b) show comparisons between experimental data and theoretical predictions of transitional responses for examples of homogeneous initial condition. Processing experimental data, the vertical positions of lower and upper bounds of the transitional layer are assumed to be limits of error of ζ measurement because ζ is a vertical position to satisfy mass and buoyancy flux balance in theoretical model and is hard to define as a certain point by observing the density profile when two layer stratification does not exist and the density gradually changes, or is gradually stratified in transition layer. The position of the lower and upper bounds are seen as error bar in Figures 3.14(a) and 3.15(a), and the δ_1 and δ_2 measurements corresponding the lower and upper bounds are also seen as error bar in Figure 3.14(b) & 3.15(b). The transition layer thicknesses between HMG-A and HMG-C are similar ($\varepsilon \sim 0.1$) and corresponding errors of δ_1 and δ_2 due to stratified transition layer of HMG-A are less affected than that of HMG-C because density changes on the transitional layer of HMG-A is smaller than

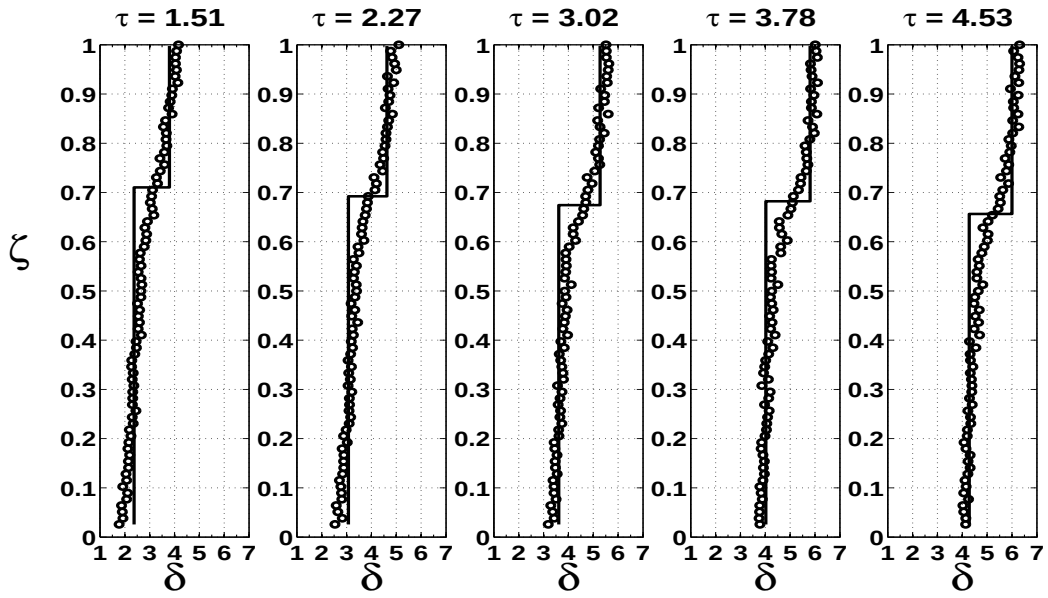

(a)

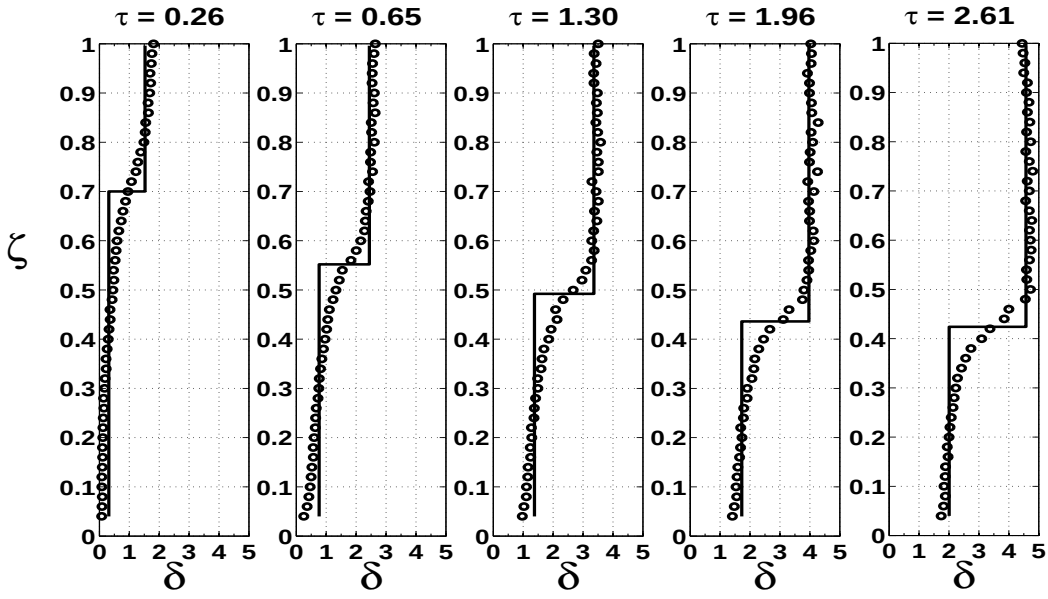

(b)

Figure 3.13: Examples of vertical density profile in time : (a) initial transition of HMG-B (b) initial transition of HMG-C; circles represent experimental measurements and solid line represent equivalent two-layer densities processed by the LFS method

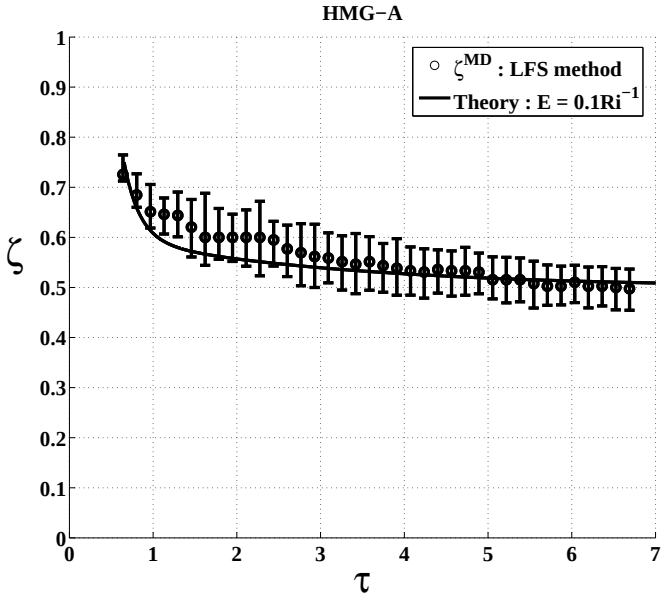

(a)

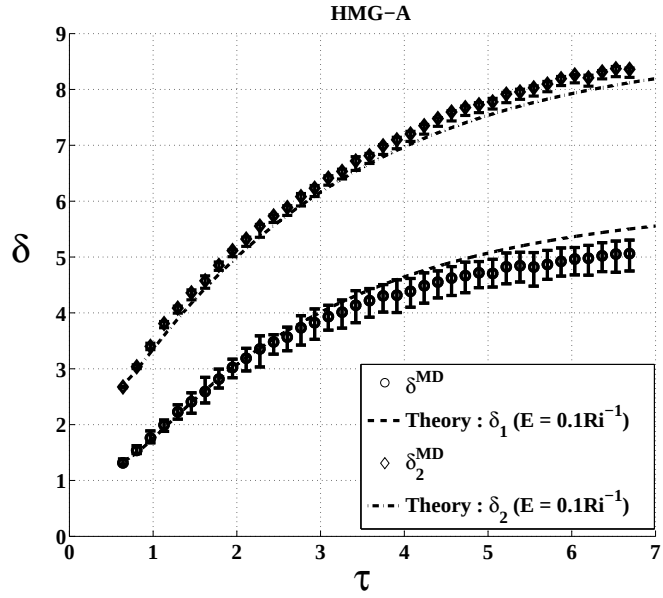

(b)

Figure 3.14: Transient responses of initial transient of HMG-A : (a) Temporal responses of density interface (b) Temporal responses of lower and upper layer density

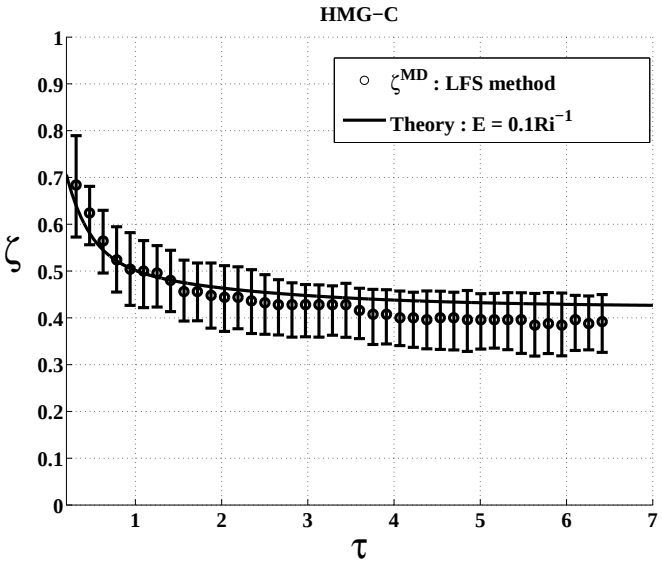

(a)

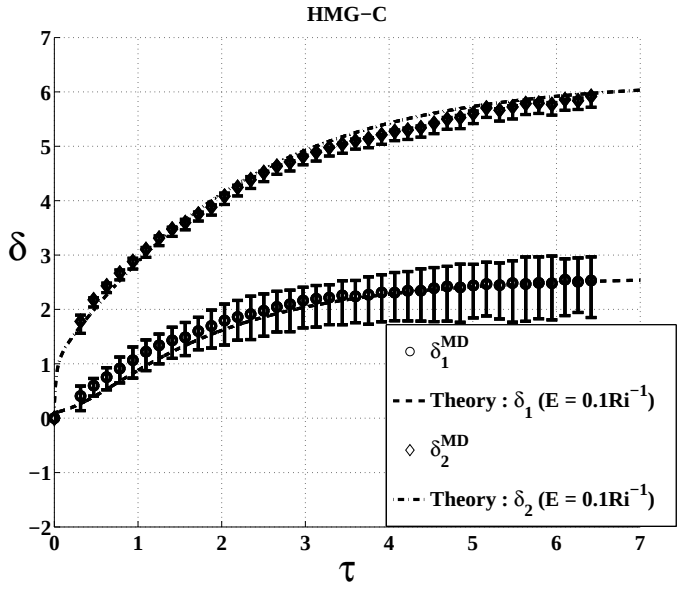

(b)

Figure 3.15: Transient responses of initial transient of HMG-C : (a) Temporal responses of density interface (b) Temporal responses of lower and upper layer density

HMG-C. The vertical position of mid point of the transition layer is assigned to be ζ^{MD} and its corresponding lower and upper layer density are δ_1^{MD} and δ_2^{MD}, respectively and hereinafter, ζ^{MD}, δ_1^{MD} and δ_2^{MD} are representative values of the interface height, the density of lower layer and the density of upper layer in experiment, respectively.

In Figures 3.14(a) and 3.15(a), ζ^{MD} moved to converge its steady state in a relatively shorter time compared to movements of δ_1^{MD} and δ_2^{MD}. Quicker responses of ζ^{MD} compared δ_1^{MD} and δ_2^{MD} were observed in other HMG cases. The responses of δ_1^{MD} and δ_2^{MD} in time were synchronized as a result of the strong correlation between lower and upper layer density through penetrative entrainment in theoretical models of (3.21) and (3.22). Buoyancy difference between lower and upper layers steeply increased and ζ^{MD} changes significantly during the transition period.

Theoretical predictions of HMG-A and HMG-C by solving the equations, (3.45)-(3.47) agreed well with experimental data when $E = 0.1Ri^{-1}$. The theory to predict ζ of HMG-C matched well with ζ^{MD} during overall measurement time. However, theoretical prediction of HMG-A was delayed to start at $\tau \sim 0.65$ because a two layer stratification did not exist during the early initial transition period and the ζ prediction of HMG-A sat below than the experiment during initial transition when $\tau < 2$ and the prediction and ζ^{MD} of the experiment merge together after $\tau > 3$ to show that the theory matched well the experiment as the system reached to steady state. In both cases, the midpoint values δ_1^{MD} and δ_2^{MD} coincided with theoretical prediction well and all prediction curves were within the limits of the transitional layer's lower and upper bound. The theory plausibly described the influences among ζ, δ_1 and δ_2 by good matches between the experiments and the theoretical prediction with various η and μ in homogeneous initial condition.

3.4.2 Stratified initial condition

We examined the transient response when the initial vertical density profile has a two-layer stratification with a sharp density density interface. The initial density profiles were obtained by running experiments by turning on the buoyancy source and the diffuser flow for three hours for letting the system reach steady state. By readjusting the buoyancy flux and ventilation flow rate, the density profiles were rearranged to reach to steady-state. The readjustments were applied as a "Stepping" method, in which the

buoyancy flux and ventilation flow rate instantaneously increased or decreased. There exist two different operating conditions are defined by μ_o and μ_s respectively. Unlike the cases of the homogeneous initial conditions which had only one operating condition described in previous section, the stratified initial conditions used a reference operating condition, μ_{rf} for establishing non dimensional parameters, τ, δ_1 and δ_2, which were introduced in §3.2.2.1. For instance, once we set $\mu_o = \mu_{rf}$, μ_s is described as

$$\mu_s = \frac{\alpha^{1/3}}{\lambda}\mu_{rf}, \tag{3.102}$$

where α is the ratio of the operating buoyancy flux to the reference buoyancy flux, and λ is the ratio of the operating ventilation flow rate to the reference ventilation flow rate as defined in (3.62) and (3.63), respectively. The corresponding δ_2 at the time to reach steady state, τ_{ss}, is expected to be

$$\delta_2|_{\tau_{ss}} = \frac{\alpha}{\lambda}\mu_{rf} \tag{3.103}$$

based on the theoretical steady state solutions, (3.64)-(3.66). Similarly, if $\mu_s = \mu_{rf}$, α becomes the ratio of the initial buoyancy flux to the reference buoyancy flux and λ becomes the ratio of the initial ventilation flow rate to the reference ventilation flow rate. μ_o and δ_2 at τ_o, at the initial steady state are given as

$$\mu_o = \frac{\alpha^{1/3}}{\lambda}\mu_{rf}, \tag{3.104}$$

$$\delta_2|_{\tau_o} = \frac{\alpha}{\lambda}\mu_{rf}. \tag{3.105}$$

Table 3.3 summarizes the reference buoyancy and ventilation flow rate, the initial operating conditions to get the stratified initial conditions and the operating conditions in terms of μ_o, μ_s, α and λ. The difference between μ_o and μ_s, $|\mu_o - \mu_s|$, indicates the level of the systematic changes between the initial operating conditions and the operating condition and the cases of buoyancy flux step change, BSD or BSU had relatively small $|\mu_o - \mu_s|$ compared to the cases of ventilation flow rate step change, VSU or VSD because μ_o or μ_s are proportion to $\alpha^{1/3}$ and λ.

We measured the transient responses to reach the secondary steady state after

Table 3.3: Parametrization of the initial condition and the operating condition of the stratified initial condition experiments : α is the ratio of the operating buoyancy flux to the reference buoyancy flux, and λ is the ratio of the operating ventilation flow rate to the reference ventilation flow rate as defined in (3.62) and (3.63) ; μ_o, α_o, and λ_o represents the operating conditions to get the stratified initial condition and μ_s, α_s, and λ_s represents the operating conditions

	B_{rf}	Q_{rf}	μ_o	μ_s	$\lvert\mu_o-\mu_s\rvert$	α_o	α_s	λ_o	λ_s
BSU-A	39.00	28.31	5.67	8.79	3.12	0.33	1	1	1
BSU-B	50.98	20.05	5.15	6.47	1.32	0.5	1	1	1
BSD-A	26.62	28.31	7.74	6.07	1.67	1	0.5	1	1
BSD-B	39.00	28.31	8.79	7.83	0.96	1	0.73	1	1
VSU-A	39.00	35.01	16.92	7.11	9.81	1	1	0.42	1
VSU-B	39.00	35.01	12.47	7.11	5.36	1	1	0.57	1
VSD-A	39.00	35.01	7.11	16.16	9.05	1	1	1	0.44
VSD-B	39.00	35.01	7.11	12.47	5.36	1	1	1	0.57

the readjustment was applied and the responses of ζ, δ_1 and δ_2 were measured. We also investigated whether theoretical predictions agreed with the experiments.

3.4.2.1 Buoyancy step up or down

Beginning with the stratified initial condition, we examined that buoyancy flux on the plume increased in a stepping manner (Buoyancy flux Step Up (BSU)). We assigned that $\mu_s = \mu_{rf}$ and the differences of μ between μ_o and μ_s were 2.53 ($\alpha : 0.33 \rightarrow 1$) for BSU-A and 1.32 ($\alpha : 0.50 \rightarrow 1$) for BSU-B (Table 3.3). η in both cases set 32.60 and 20.90 for BSU-A and BSU-B respectively and fixed during all operation period (Table 3.2). Increasing strength of the plume was expected to lower the density interface and increase densities of upper and lower layer. From Figure 3.16(a), the densities of the lower and upper layer increased in time and two layer stratification at the beginning of the BSU-A experiment was weak, but, the level of stratification which can be represented by $\delta_2 - \delta_1$ got stronger in time. Observing the vertical profiles of lower and upper layer, the lower and upper layer appeared to be well-mixed because there happened no or very weak stratification on both layers ($d\delta/d\zeta \sim 0$) during the initial transitional period. Similarly, BSU-B (Figure 3.16(b)) also showed that the lower and upper layer densities increased and $\delta_2 - \delta_1$ got larger in time.

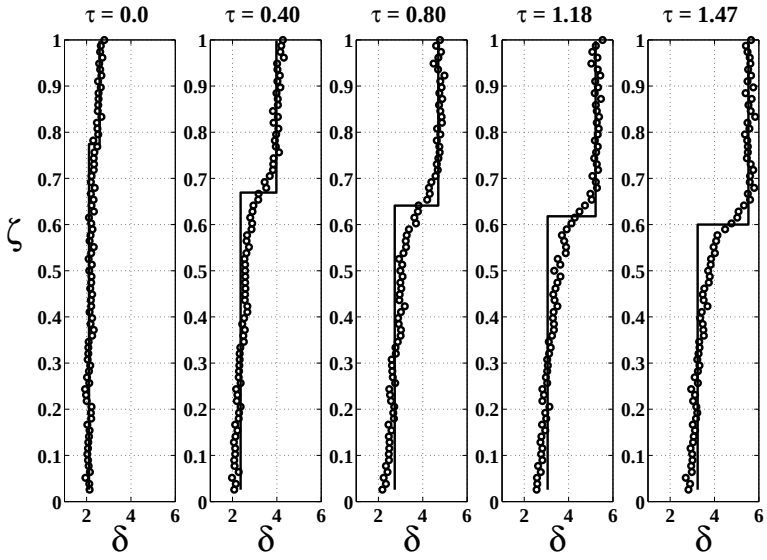

(a)

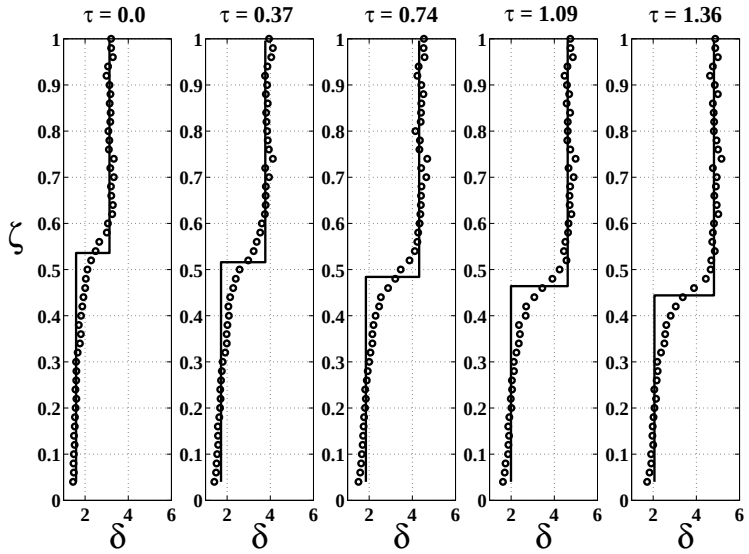

(b)

Figure 3.16: Time evolution of vertical density profiles of buoyancy step Up (BSU) cases (circle represents experimental measurement and solid line is two-layer stratification corresponding to the given vertical density profile by LFS method) : (a) BSU-A : $\alpha : 0.33 \rightarrow 1$, $\mu_{rf} = \mu_s = 8.79$ and $\eta = 32.60$ (b) BSU-B : $\alpha : 0.50 \rightarrow 1$, $\mu_{rf} = \mu_s = 6.47$ and $\eta = 20.90$

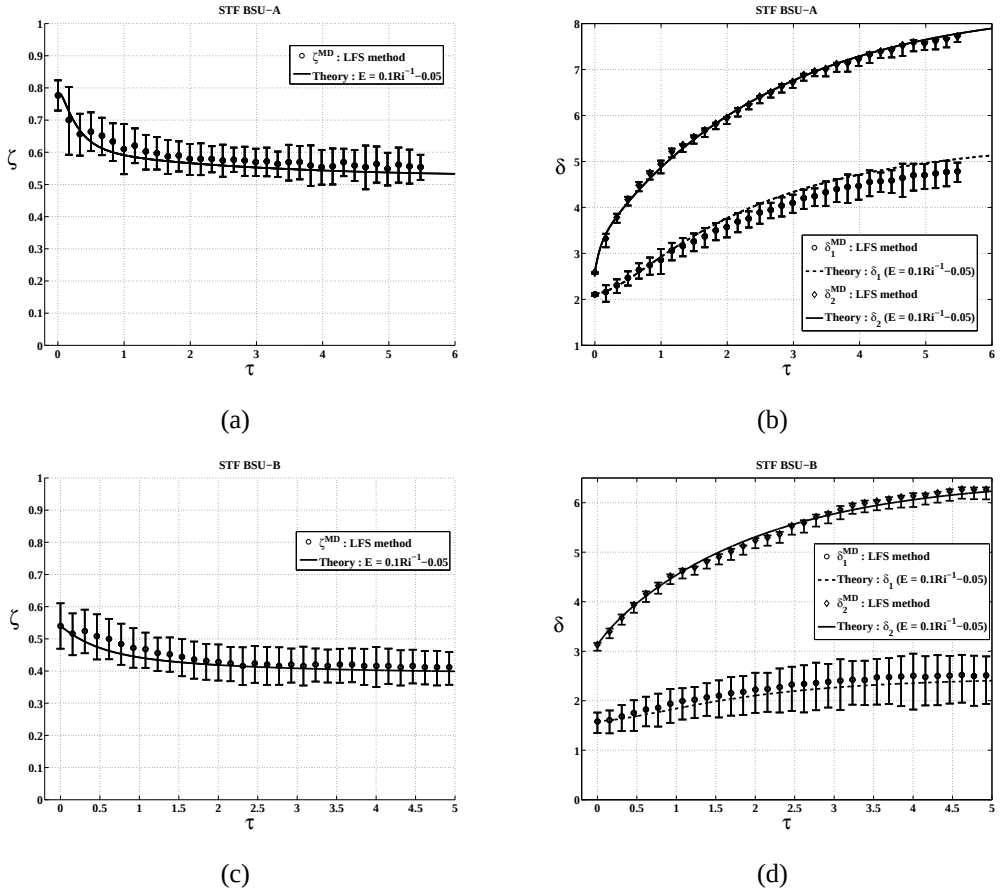

Figure 3.17: Experimental results and comparison to theoretical prediction of Buoyancy flux Step Up (BSU) cases; 1. BSU-A : (a) temporal movement of ζ (b) Temporal movement of δ_1 and δ_2. 2. BSU-B : (c) temporal movement of ζ (d) Temporal movement of δ_1 and δ_2. (Circles represents ζ^{MD} and solid line represent theoretical prediction for (a) and (c), and circles and diamonds represent δ_1^{MD} and δ_2^{MD} and solid line and dashed line represent theoretical prediction of δ_1 and δ_2 respectively for (b) and (d))

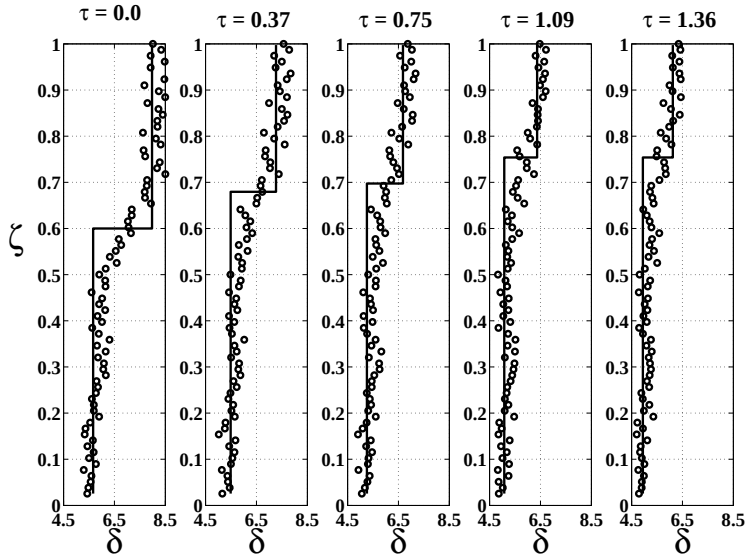

(a)

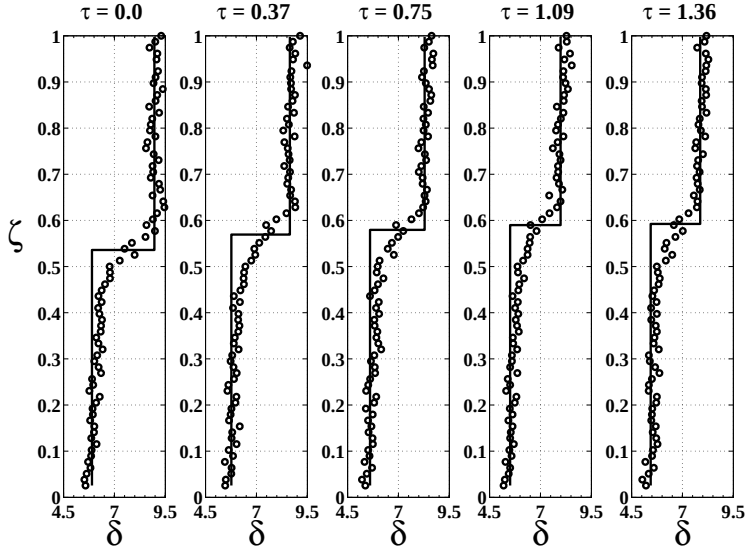

(b)

Figure 3.18: Time evolution of vertical density profiles of buoyancy step Up (BSD) cases (circle represents experimental measurement and solid line is two-layer stratification corresponding to the given vertical density profile by LFS method): (a) STF BSD-A : $\alpha : 1 \rightarrow 0.5$, $\mu_{rf} = \mu_o = 7.74$ and $\eta = 32.60$ (b) STF BSD-B : $\alpha : 1 \rightarrow 0.73$, $\mu_{rf} = \mu_o = 8.79$ and $\eta = 32.60$

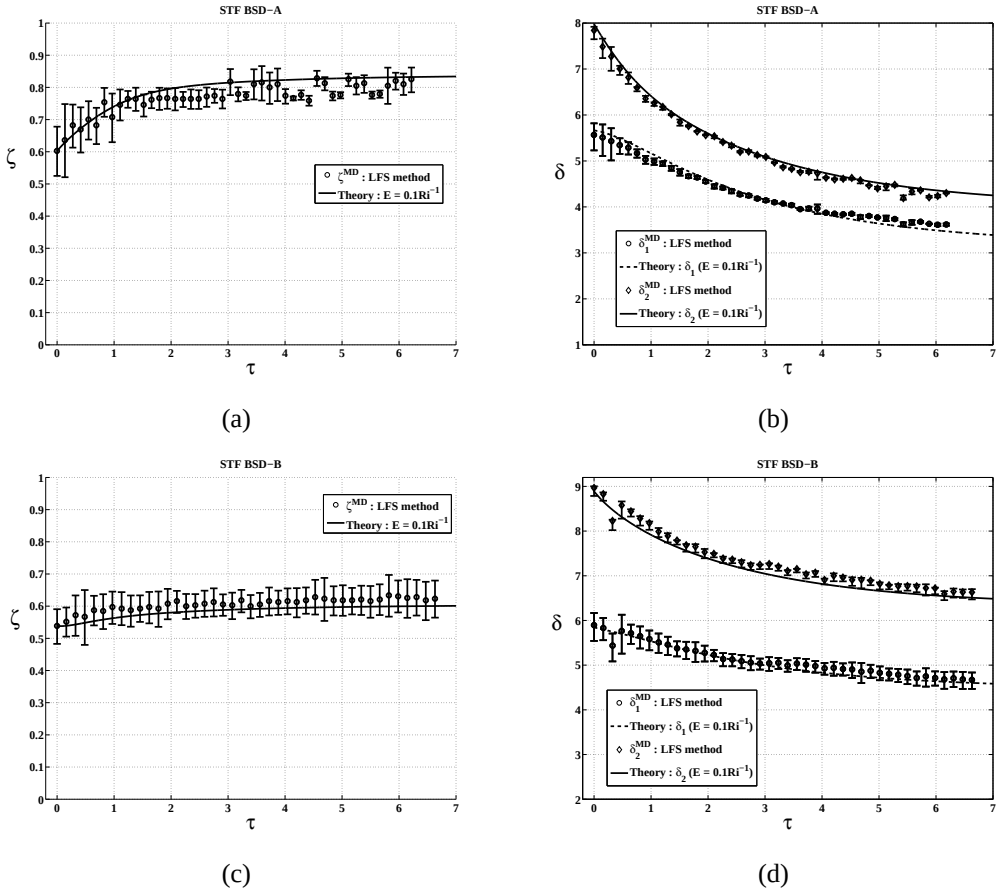

Figure 3.19: Experimental results and comparison to theoretical prediction of Buoyancy flux Step Down (BSD) cases ; 1. BSD-A : (a) temporal movement of ζ (b) Temporal movement of δ_1 and δ_2. 2. BSD-B : (c) temporal movement of ζ (d) Temporal movement of δ_1 and δ_2. (Circles represents ζ^{MD} and solid line represent theoretical prediction for (a) and (c), and circles and diamonds represent δ_1^{MD} and δ_2^{MD} and solid line and dashed line represent theoretical prediction of δ_1 and δ_2 respectively for (b) and (d))

Considering the opposite cases as the buoyancy flux on the plume decreased (Buoyancy flux of plumes Step Down (BSD)), ζ was expected to increase and δ_1 and δ_2 to decrease. For these cases, μ_{rf} is assigned as μ_o and the differences of μ between μ_o and μ_s were 1.67 ($\alpha : 1 \rightarrow 0.5$) for BSD-A and 0.96 ($\alpha : 1 \rightarrow 0.725$) for BSD-B and η of both cases were 32.60 (Table 3.3). In Figures 3.18(a) and 3.18(b), the lower and upper layers remained well-mixed during the transition and the buoyancy difference between the lower and upper layer increased in time. During the initial transition of BSD, the upper and lower layer buoyancy decreased simultaneously and the interfacial height reached the steady state in relatively short time.

Figures 3.19(a) and 3.19(c) showed the comparison for ζ between the theory and the experiments of BSD-A and BSD-B respectively. ζ also converged to steady state in relatively short time and the theoretical curves predicted the monotonic increase of ζ which was shown in the experiment. Temporal responses of δ_1 and δ_2 were shown in Figure 3.19(b) for BSD-A and Figure 3.19(d) for BSU-B. On both cases, monotonic decreases of δ_1 and δ_2 were observed and the level of stratification, $\delta_2 - \delta_1$, rapidly decreased in both cases during earlier transitional period then stages the same after the period. The reason is that while the rate of change of δ_2 was larger than that of δ_1 when $\tau < 2$, the rate of change difference between δ_1 and δ_2 became smaller when $\tau > 2$. The theoretical predictions of δ_1 and δ_2 also agreed with δ_1 and δ_2 at all times for all BSU cases.

The theoretical predictions of ζ, δ_1 and δ_2 matched well with the experimental data for both BSD cases. By changing buoyancy flux from initial operating condition forming an initial two layer stratification, while ζ reached steady state in a relatively short time when $\tau < 2$, δ_1 and δ_2 monotonically increased or decreased in time in all the cases. The level of stratification, $\delta_2 - \delta_1$ converged in relatively short time on all BSD and BSU cases. The density interface and the densities of the lower and upper layers quickly moved in relatively short time.

3.4.2.2 Ventilation flow rate step up or down

Transient responses of the system by adjusting ventilation flow rate are examined in this section. At first, we investigated the cases when we stepped the ventilation flow

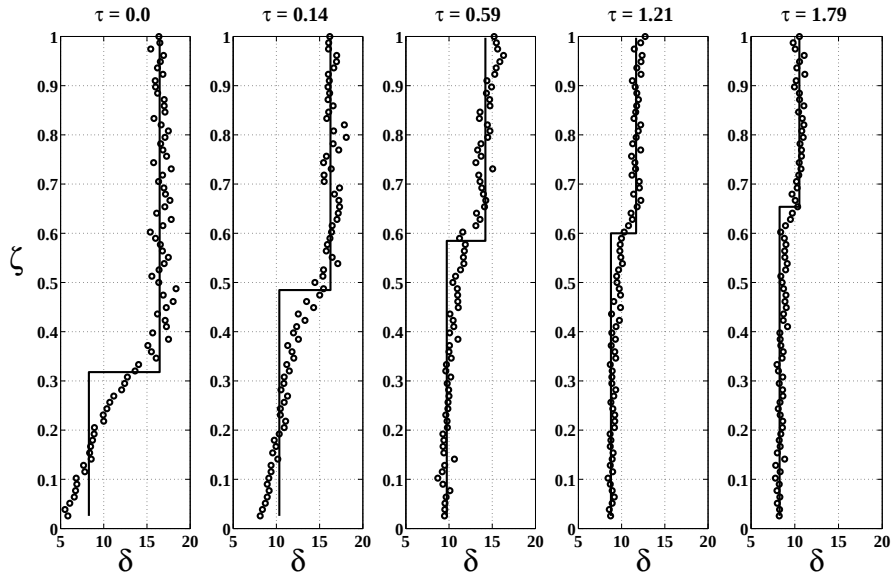

(a)

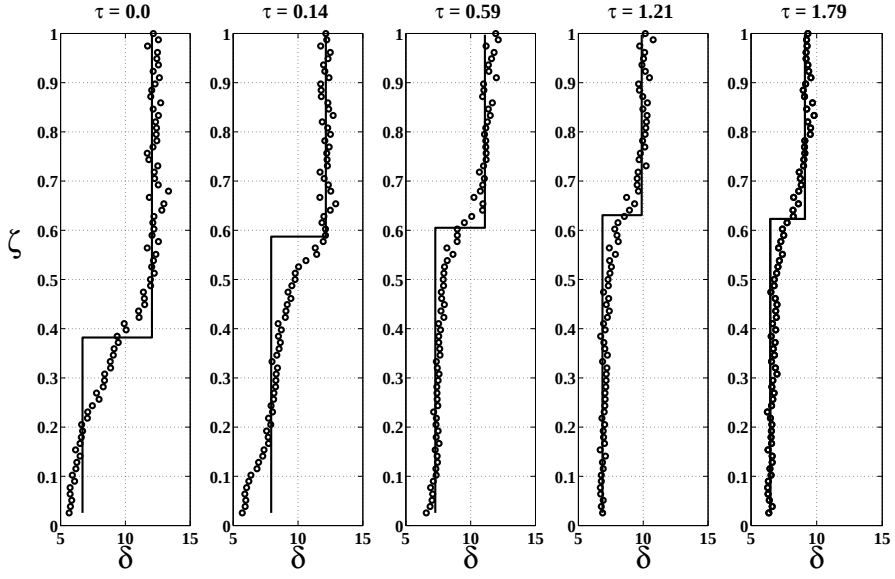

(b)

Figure 3.20: Time evolution of vertical density profiles of Ventilation flow rate Step Up (VSU) cases : (a) VSU-A : $\alpha : 0.33 \rightarrow 1$, $\mu_{rf} = \mu_s = 8.2$ and $\eta = 32.60$ (b) VSU-B : $\alpha : 0.50 \rightarrow 1$, $\mu_{rf} = \mu_s = 6.49$ and $\eta = 20.90$

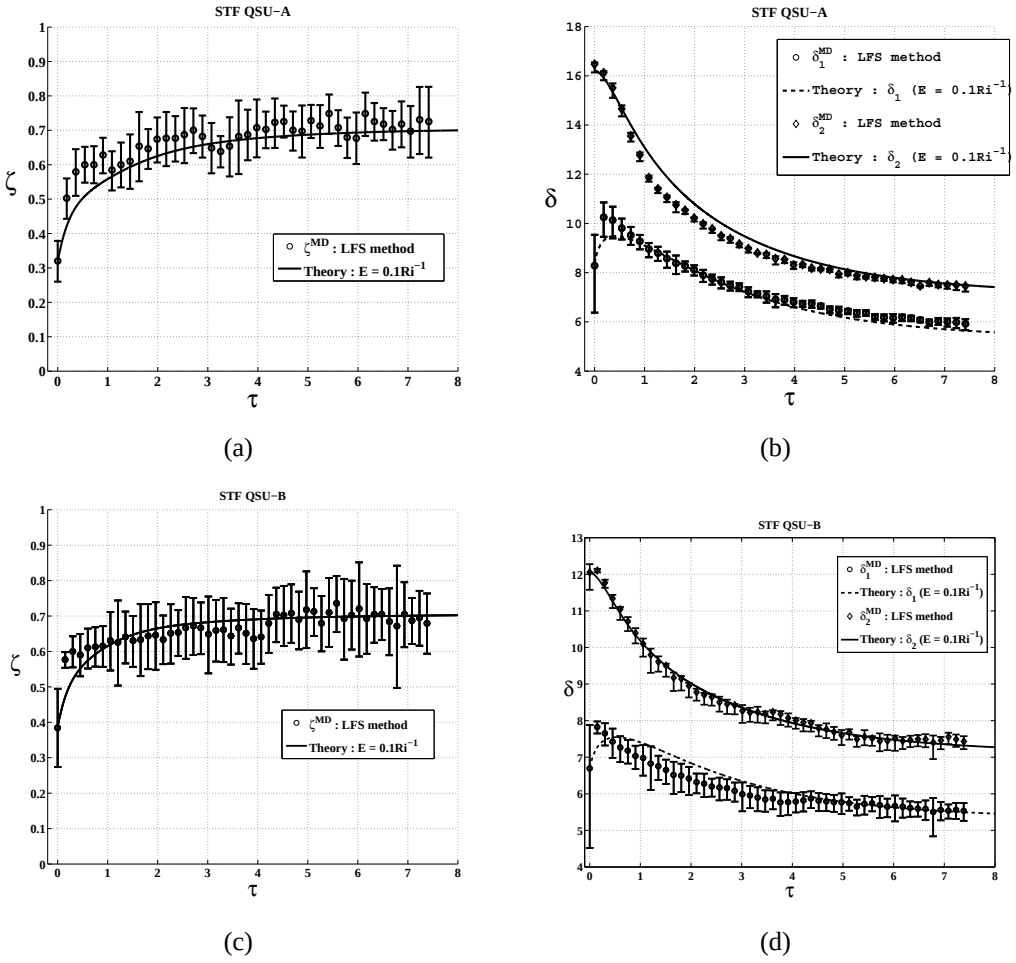

Figure 3.21: Experimental results and comparison to theoretical prediction of Ventilation flow rate Step Up (VSU) cases ; 1. VSU-A : (a) temporal movement of ζ (b) Temporal movement of δ_1 and δ_2. 2. VSU-B : (c) temporal movement of ζ (d) Temporal movement of δ_1 and δ_2. (Circles represents ζ^{MD} and solid line represent theoretical prediction for (a) and (c), and circles and diamonds represent δ_1^{MD} and δ_2^{MD} and solid line and dashed line represent theoretical prediction of δ_1 and δ_2 respectively for (b) and (d))

rate up (Ventilation flow rate Step Up: VSU). The result of VSU is expected to be that ζ moves up, and δ_1 and δ_2 decreased similarly to BSD cases. We assign that $\mu_{rf} = \mu_s$ which gives $\mu_{rf} = 6.91$, the same for VSU-A and VSU-B, and η of both cases were 32.60. The difference of μ_o and μ_s for VSU-A were 9.54 ($\lambda : 0.42 \rightarrow 1$) and the difference for VSU-B is 5.19 ($\lambda : 0.7 \rightarrow 1$) in Table 3.3. Both cases were chosen to represent typical cases of VSU which consider various situations of stepping μ down from μ_o to μ_s and μ_o to μ_s were chosen to be various differences between μ_o and μ_s.

Figures 3.20(a) and 3.20(b) showed transitional responses of the vertical density profile. $|\mu_o - \mu_s|$ of VSU-A in Figure 3.20(a) is larger than that of VSU-B in Figure 3.20(b), so the responses of VSU-A is expected to be more dynamical than that of VSU-B. In both cases, ζ converged to steady state positions in a relatively short time, similarly to the cases of buoyancy flux step change in §3.4.2.1. However, δ_2 of VSU-A decreased more quickly than that of VSU-B for the given time periods ($\tau < 1.79$). The response of δ_1 did not agree with the decreasing trend of δ_2. δ_1 temporarily increased by approximately 30 percentage or 15 percentage of initial δ_1 for VSU-A and VSD-B respectively. From the vertical density profiles of Figures 3.20(a) and 3.20(b), the density of the upper part of the lower layer increased during earlier transitional period, so the lower layer was intermediately stratified. However, the stratification disappeared soon and the lower layer became well-mixed again. During the transitional period, the density difference between the lower and upper layer, $|\delta_2 - \delta_1|$ steeply decreased in time.

The comparison between the experiment and the theory of VSU-A are plotted at Figures 3.21(a) and 3.21(b). The movement of ζ of the experiments matched well to the theory except the initial transitional period, $\tau < 2$ in Figure 3.21(a). When $\tau < 1$, the theoretical curve of ζ sits below the experimental measurement. The experimental measurement of δ_2 converged quickly to the steady state and the theoretical curve showed the similar convergence to the experiment and corresponded to the experimental measurement during most of the time in Figure 3.21(b). For δ_1, there exists a discrepancy between the experiments and the theory when $\tau < 1$ (the theory curve underpredicted the maximum of δ_1 and showed time delay to have the maximum). However, after $\tau = 1$, the theory and the experiments matched well.

Similar to VSU-A, the comparisons of VSU-B showed good matches of ζ, δ_1

and δ_2 in time from Figures 3.21(c) and 3.21(d). However, the maximum increase of δ_1 compared to its initial values of VSU-B was lower than VSU-A (δ_1 of the minimum of VSD-A was 10.5 compared to the initial condition $\delta_1 = 8.2$ and that of VSD-B was 7.8 compared to the initial condition $\delta_1 = 6.8$), but the timing to have the maximum of VSU-B was the same as that of VSU-A. The theory curve still underpredicted the maximum and showed the time delay to have the maximum. However, the theory curve was acceptable to describe the transient responses of δ_1 during most of time.

Secondly, the experiments of Ventilation flow rate Step Down (VSU) were performed to reveal characteristics of transient responses when the ventilation flow rate was reduced. The result of VSD is expected to be that ζ moves down and δ_1 and δ_2 increases similarly to the BSU cases in §3.4.2.1. We assign that $\mu_{rf} = \mu_o$ which let $\mu_{rf} = 6.91$ the same for VSD-A and VSD-B and η of both cases were 32.60. The difference of μ_o and μ_s for VSD-A were 8.79 ($\lambda : 1 \rightarrow 0.44$) and the difference for VSU-B is 5.21 ($\lambda : 1 \rightarrow 0.57$) in Table 3.3. Both cases were chosen to represent typical cases of VSD.

In Figures 3.22(a) and 3.22(b), transitional responses of vertical density profile from the experiments are plotted. Because $|\mu_o - \mu_s|$ of VSD-A in Figure 3.22(a) is larger than that of VSD-B in Figure 3.22(b), larger change of ζ and δ_1 and δ_2 were expected for VSD-A. Similarly to other cases, ζ converged to steady state positions in relatively short time and δ_2 of VSD-A and VSD-B had a similar rate of increase in time for given time periods ($\tau < 1.79$) unlike the VSU cases. The response of δ_1 did not shows the increasing trend of δ_2. δ_1 temporarily decreased by approximately 20 percentage of the initial condition δ_1 for VSD-A, and slightly decreased then increased of VSD-B while δ_2 increased. From the vertical density profiles of Figures 3.20(a) and 3.20(b), the lower and upper layers remained well-mixed ($d\delta/d\zeta \sim 0$) during the transitional period.

The comparison plots of VSD-A was given at Figures 3.23(a) and 3.23(b). There were good matches between the experiments and the theory for the ζ movement during most of time, even when ζ steeply decreased when $\tau < 2$. The experimental measurement of δ_2 gradually converged to steady state and the theory curve showed similar convergence to the experiment with a good coincidence all the time in Figure 3.21(b). For the initial transition period, $\tau < 2$, there existed mismatches of δ_1 between the experiments and the theory. The theory curve overpredicted the minimum of δ_1, however,

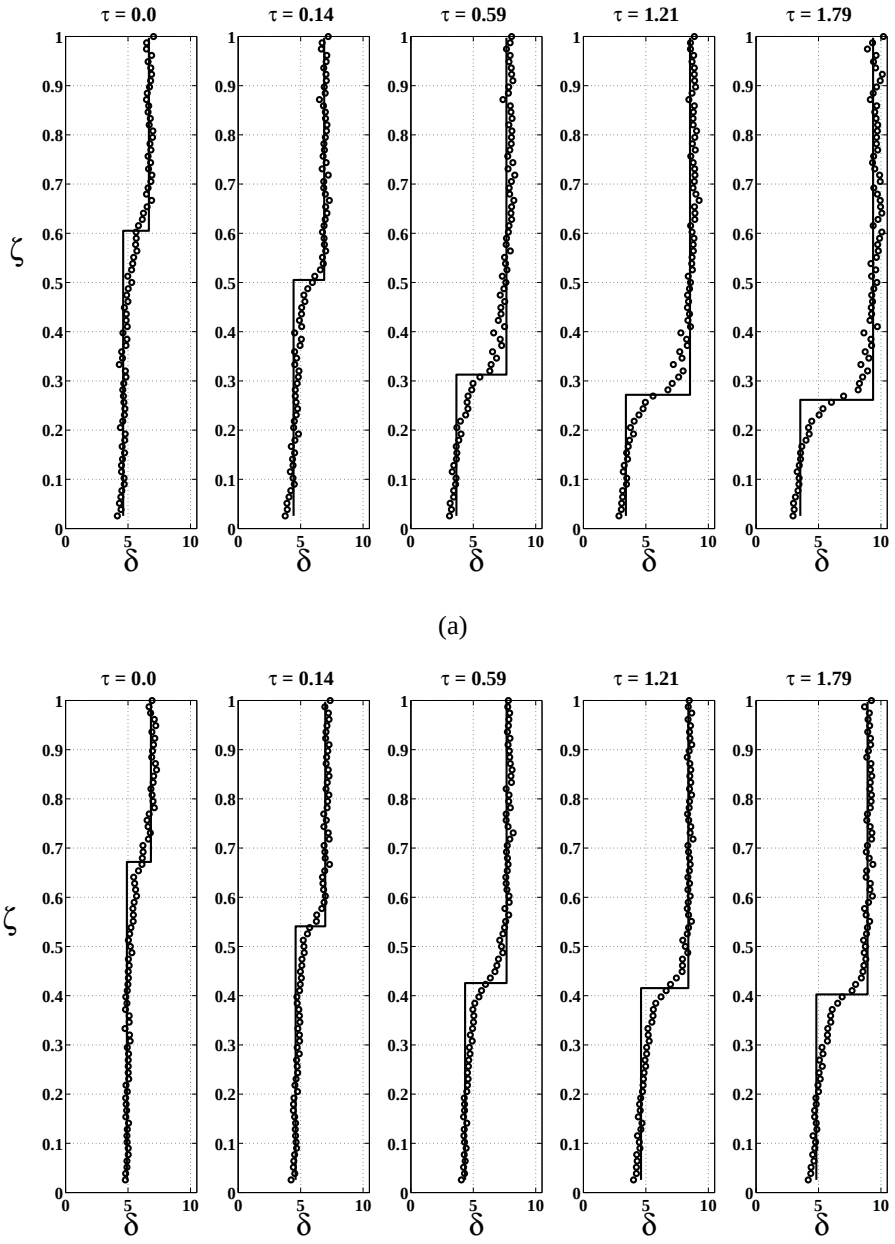

Figure 3.22: Time evolution of vertical density profiles of Ventilation flow rate Step Down (VSD) cases : (a) VSD-A : $\alpha : 1 \rightarrow 0.5$, $\mu_{rf} = \mu_o = 7.97$ and $\eta = 32.60$ (b) VSD-B : $\alpha : 1 \rightarrow 0.725$, $\mu_{rf} = \mu_o = 8.72$ and $\eta = 32.60$

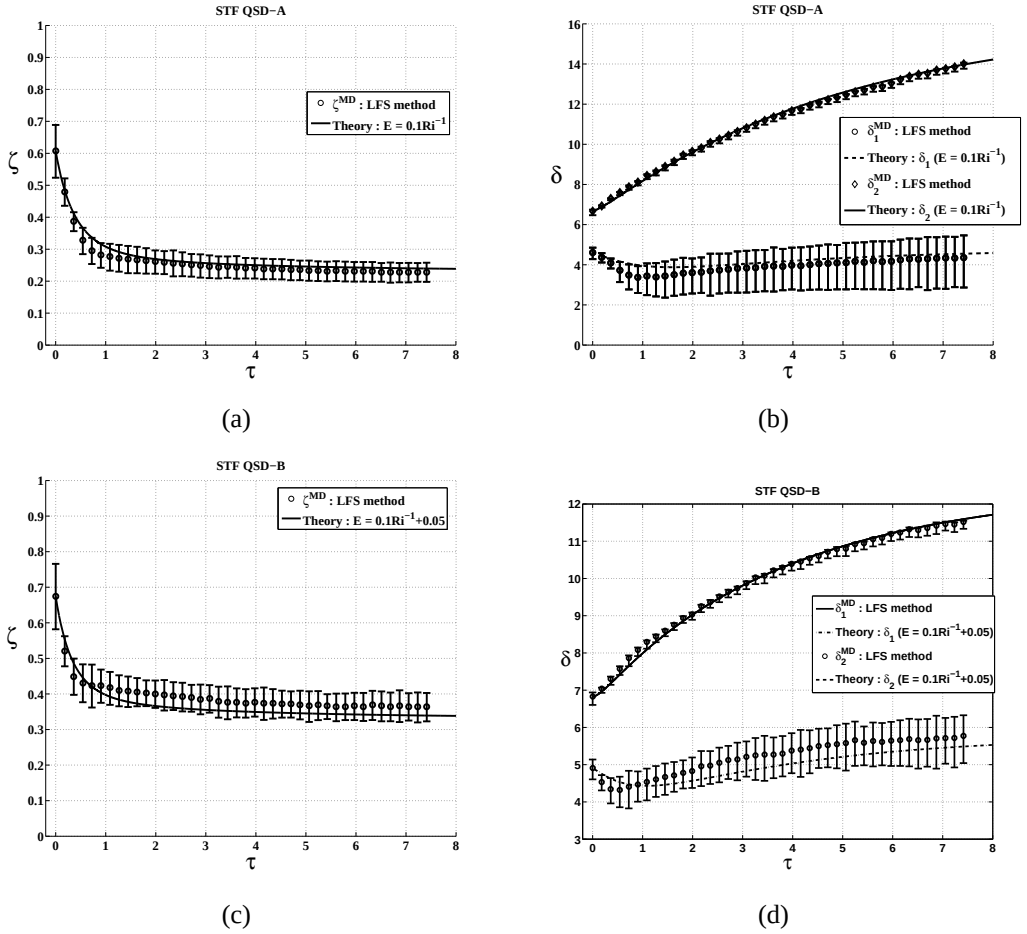

Figure 3.23: Experimental results and comparison to theoretical prediction of Ventilation flow rate Step Down (VSD) cases ; 1. VSD-A : (a) temporal movement of ζ (b) Temporal movement of δ_1 and δ_2. 2. VSD-B : (c) temporal movement of ζ (d) Temporal movement of δ_1 and δ_2. (Circles represents ζ^{MD} and solid line represent theoretical prediction for (a) and (c), and circles and diamonds represent δ_1^{MD} and δ_2^{MD} and solid line and dashed line represent theoretical prediction of δ_1 and δ_2 respectively for (b) and (d))

after $\tau = 2$, the theory and the experiments matched well.

Similar to VSU-A, the comparisons of VSU-B showed good matches of ζ, δ_1 and δ_2 in time seeing Figures 3.23(c) and 3.23(d). However, the minimum of decrease of δ_1 compared to its initial values of VSD-B was lower than VSD-A (δ_1 of the minimum of VSD-A was 3.5 and that of VSD-B was 4.2 and initial $\delta_1 = 4.9$ and 4.6 for VSD-A and VSD-B respectively) and the timing to have the maximum of VSD-B in the theory curve was delayed compared to the experiments. The theory curve overpredicted the minimum and showed the time delay to have the minimum. However, the theory curve illustrated similar transient responses of δ_1 in the experiment during most of time.

The experiments and corresponding theoretical predictions of the VSU and VSD cases matched well in most of time except for predicting the temporal responses of δ_1 during the initial transitional period. δ_1 overshoot for the VSU cases and undershoot on the VSD cases, and the level of overshoot or undershoot of δ_1 corresponded to $|\mu_o - \mu_s|$ and when $|\mu_o - \mu_s|$ was large, that of δ_1 increased. The theoretical curves slightly underestimated the overshoot or undershoot on all VSU and VSD cases. However, the curves appropriately described the temporal responses of δ_1 during most of time. The experimental measurements of δ_2 coincided with the theory curves well on all VSU and VSD cases.

3.5 Discussion

3.5.1 Steady State solutions

To confirm that the transient two-layer model proposed in § 3.2 had the correct limit at steady state, the steady state equations, (3.82) and (3.83), were solved by an iterative numerical method. When we assumed that there existed only jet-like negatively buoyant jet for the diffuser flow, the simplified Γ was used to solve (3.82) and (3.83). The Richardson number *Ri* was estimated by (3.58) and E was calculated by the E and *Ri* relation, $E \sim 0.1Ri^{-1}$ as described in § 3.4.1.2.

Plots of the steady state solutions are given in Figures 3.24(a)-3.24(d). For validating the limit of the systems, a mechanical DV system and an ideal well-mixed system are used. The mechanical DV system represents the situation in which $E = 0$, in

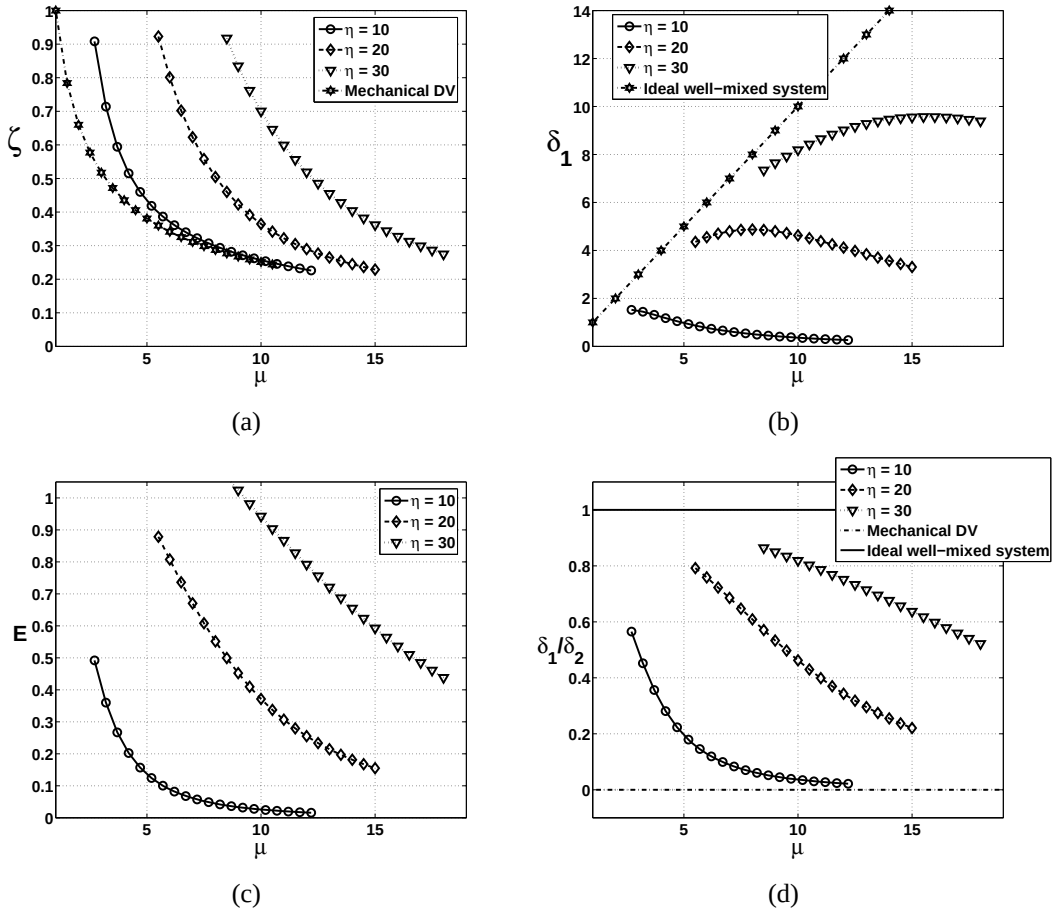

Figure 3.24: Plots of the steady state solutions of (3.82) and (3.83) with (3.58) and $E = 0.1Ri^{-1}$ for a single plume and a single diffuser: (a) ζ .vs. μ, (b) δ_1 .vs. μ, (a) E .vs. μ, (a) δ_1/δ_2 .vs. μ

other words, the system do not allow mixing across the density interface. The ideal well-mixed system has complete mixing (E = 1) and the vertical thermal stratification disappears.

Figures 3.24(a) - 3.24(d) show the relations between operating condition μ and various system parameters such as ζ, δ_1, E and δ_1/δ_2 representing the level of the thermal stratification. Each graph shows the relations for various η ($\eta = H/\sqrt{A_d}$) which characterizes the momentum flux discharge through the diffuser.

From Figure 3.24(a), when μ gets larger, ζ decreases at steady state . When η decreases, the curve between μ and ζ becomes similar to that of the mechanical DV

system. In Figure 3.24(d), the curve between μ and δ_1/δ_2 with small η also converges more rapidly to $\delta_1/\delta_2 = 0$, which corresponds to the ideal DV system, compared to the curves with larger η. Based on these results, the UFAD system behaves as the ideal mechanical DV system when μ increases and η decreases because reduced diffuser momentum flux caused by large area of diffuser (small η) and strong plume source buoyancy flux (larger μ) decreases the level of mixing across the interface.

However, from Figures 3.24(b) and 3.24(d), when η increases, the curve between μ and δ_1 approaches to that of ideal well-mixed system which has no thermal stratification and $\delta_1 = \delta_2$. Physically, increased momentum flux through a small diffuser area (large η) lifts the interface up to the ceiling and entire volume of the room is mixed by the diffuser flow.

The relation between E and μ for various η is shown in Figure 3.24(c). Combining (3.58) with $E \sim 0.1Ri^{-1}$, proportional relations, $E \sim \mu^{-2}$ and $E \sim \eta^5$ are suggested, which explains why E decreases when μ increases and small η make the curve more rapidly converge to zero compared to larger η when μ increases.

Based on the results, the UFAD system behaves as the ideal DV system when relatively strong buoyancy source exists, which corresponds to large μ. When low momentum flux discharged from the diffuser (small η), UFAD rapidly converges to the DV system with relatively small μ. However, when higher momentum discharges from the diffuser (large η), UFAD converges slowly to the DV system even with larger μ.

3.5.2 Transient responses of *Ri* and *E*

Penetrative entrainment is an important physical process to explain density stratification or thermal stratification. The entrainment process can be analyzed in terms of a local *Ri* which is defined as a function of the density difference $\delta_2 - \delta_1$ and the dimensionless penetrative flow rate Γ. Γ is proportional to the momentum flux across the density interface and is a function of ζ in simplified form. When *Ri* is large, the density gradient across the interface also becomes large, so the vertical motions of the mixing are hampered. Consequently, the mixing between lower and upper layer is inhibited and the diffuser flow brings less fluid from the upper layer to the lower layer. However, when *Ri* is small, higher momentum flux across the density interface enhances the mix-

ing and the diffuser flow brings more fluid from the upper layer to the lower layer. In our study, the hampered mixing when *Ri* is large is described as small value of E (typically, $E < 0.3$) and the enhanced mixing when *Ri* is small corresponds to large value of E ($E > 0.5$). For estimating temporal histories of E from experimental measurements, (3.101) is used. Physically, the increase in the lower zone temperature above the supply temperature is solely a result of the penetrative entrainment (when the heat plume is only a heat source in a room and all exterior walls are ideally insulated).

Before reaching steady state, *Ri* presumably varies in time. Especially, during the initial transitional period (typically $\tau < 2$ based on the experimental results in §3.4.1, § 3.4.2.1 and § 3.4.2.2), there are dynamical temporal responses of *Ri* because ζ, δ_1 and δ_2 vary significantly within the period. E also varies in time corresponding to the temporal responses of *Ri*. However, the temporal dependence between *Ri* and E can be addressed by comparing the theoretical predictions to the experimental measurements.

Theoretical curves of *Ri* and E are obtained by solving (3.45)-(3.47) combined with $E = 0.1Ri^{-1}$ (which was suggested by empirical relation between E and *Ri* at § 3.4.1.2) and any error caused by wrong estimation of ζ, δ_1 and δ_2 on the lower and upper bounds of the transitional layer were used to estimate lower and upper error bar respectively on Figures 3.25, 3.26, 3.27 and 3.28.

First, we show two examples of the comparisons of the temporal dependance between *Ri* and E for homogeneous initial conditions in Figures 3.25(a) and 3.25(b). In Figure3.25(a), experimental measurements of *Ri* and E fitted well with the theoretical relations, which explained the good agreement of the theoretical prediction and the experiments in the corresponding experimental cases (which are seen in Figures 3.14(a) and 3.14(b)). Even though temporal histories of E of the HMG cases showed mismatches between the theory and the experiments during the initial transition period $\tau < 1$ when large temporal change of E exists in short time. ζ reaches steady state when $\tau \sim 4$ and δ_1 and δ_2 reaches steady state when $\tau \sim 7$.

Secondly, we examine the cases of stratified initial conditions of buoyancy flux step-change of the plume source. Adjusting the buoyancy flux of the plume source caused $\delta_2 - \delta_1$ changes in time, so *Ri* of the diffuser flows also are changed. Stepping down the buoyancy flux, *Ri* decreases and E increases. In Figure 3.26(a), good agree-

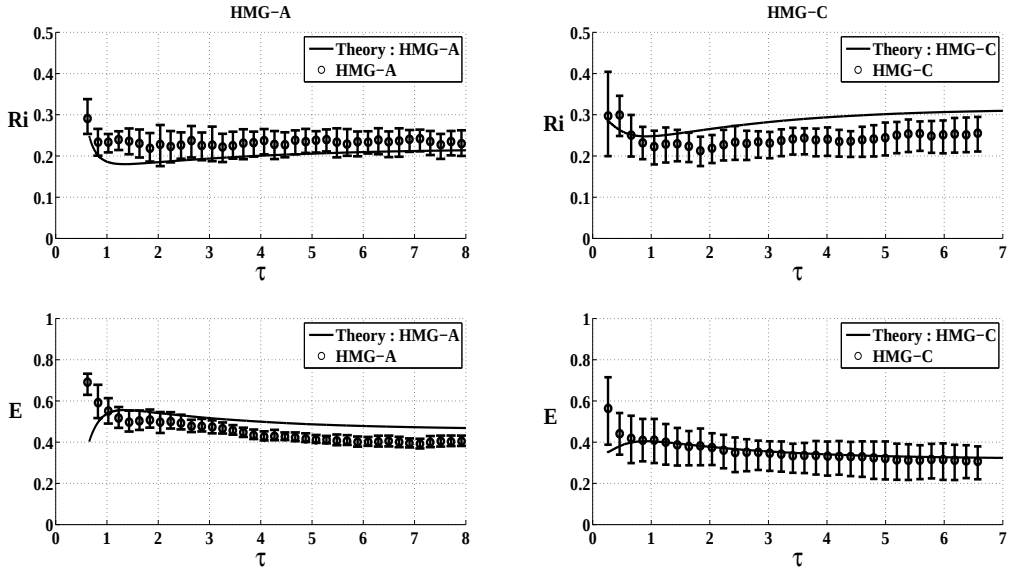

Figure 3.25: Temporal histories of *Ri* and *E* of the homogeneous initial condition cases: (a)HMG-A and (b)HMG-C

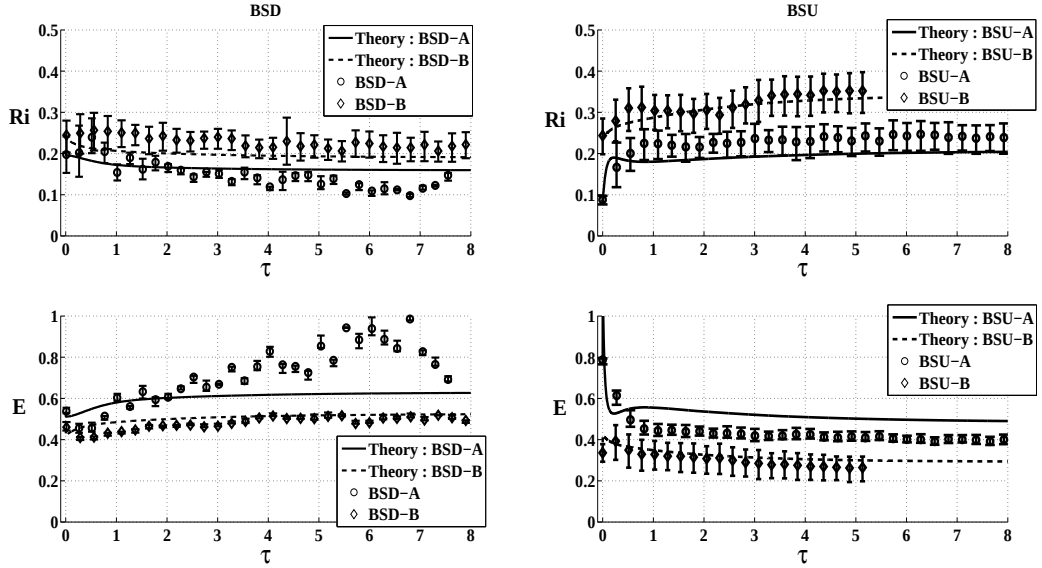

Figure 3.26: Temporal histories of *Ri* and *E* of the BSD and BSU cases: (a) BSD and (b) BSU

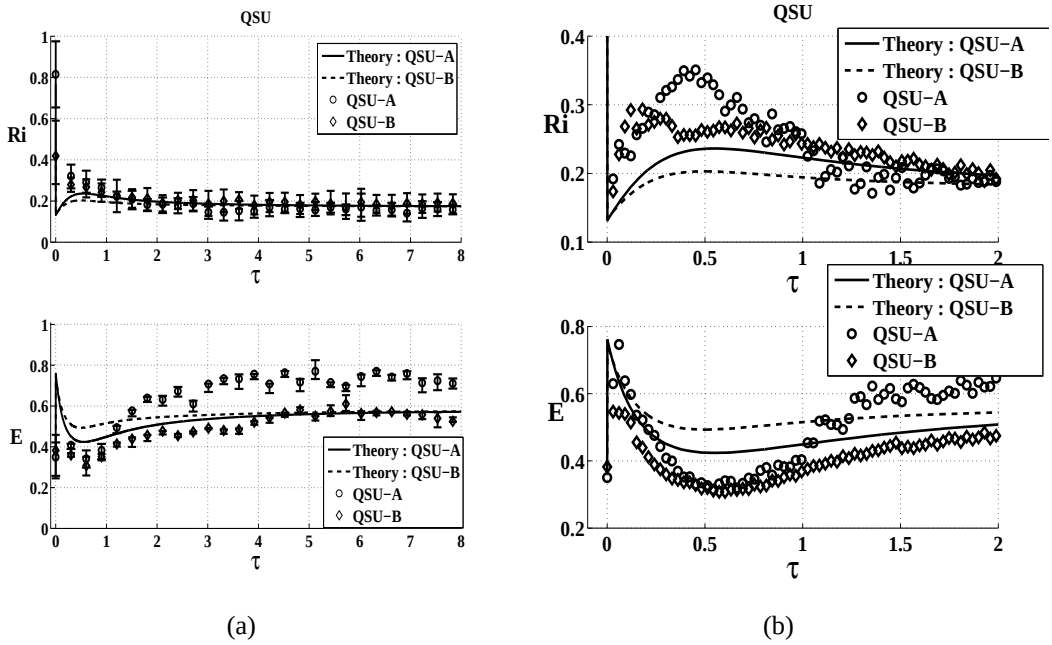

Figure 3.27: Temporal histories of *Ri* and E of the VSU cases: (a) and (b)

ments of *Ri* between the theory and the experiments were shown in BSD-A and BSD-B. The experimental measurements of E of BSD-A increased before $\tau = 6$ then decreased to approach to the steady state. However, E of BSD-B keeps track of the theoretical curve most of the time. One possible explanation of the mismatch of E of BSD-A is that the closeness between δ_2 and δ_1 of BSD-A in Figure 3.17(b) caused overestimation of E. Stepping up the buoyancy flux, *Ri* increases and E decreases. From Figure 3.26(b), we see that the experimental measurements of *Ri* agree with the theory. When α was highly step-changed at the beginning of the experiments of BSU, *Ri* increased more steeply in the initial period and corresponding E decreased rapidly in the period. The experimental measurement of *Ri* and E of BSU-A monotonically increased and decreased respectively unlike the theory curves which showed overshoot of *Ri* or undershoot of E in the initial period. Because E converges quickly in a short time for BSU-A, similar to the HMG cases, $E = 0.1Ri^{-1}$ does not appear to be appropriate to predict instantaneous E when the system moves quickly in the BSD or BSU cases.

Thirdly, the cases of controlling ventilation flow rate of the diffusers are investigated. When the ventilation flow rate changes, *Ri* also changes instantaneously

in (3.67). For a step-change of λ, there was a corresponding step change in *Ri* was also step-changed at the beginning of the cases of VSD or VSU in Figures 3.27(a) and 3.28(a), and the theoretical curves of *Ri* and E corresponded to the experiments most of the time except the initial period.

Physical interpretations of initial temporal response of *Ri* and E of the VSU cases are given by the following scenarios; 1. due to the step-up increase of momentum flux of the diffuser flow, the disturbance of the density interface instantaneously increased, and *Ri* decreased and E increased from these initial values 2. As ζ increased, the momentum flux across the density interface decreased, which caused an increase of *Ri*. 3. Once ζ converged to steady state in a relatively short time ($\tau \sim 0.5$), $\delta_2 - \delta_1$ still decreased in time, so *Ri* again decreased and E increased in time.

From the temporal history of *Ri* in Figure 3.27(b) (zoom-in plot of Figure 3.27(a)), even though the theory with $E = 0.1Ri^{-1}$ still showed similar temporal history to the experiments in time, the theory could not predict exact amount of overshoot *Ri* or undershoot E during the initial period. The mismatch of *Ri* between the theory and the experiments can be explained by the wrong estimation of ζ and corresponding δ_1 and δ_2. During the period, the diffuser jet overshoot above the density interface strongly influenced or disturbed the density interface to make the transitional layer wider seen in Figures 3.20(a) and 3.20(b), so an exact vertical position of the density interface was hard to find and it was likely the LFS method did not measure appropriate lower and upper bounds of the transitional layer.

The given physical interpretation of underestimated *Ri* and overestimated E of the VSU cases in theory possibly explains the reason of the initial mismatch of δ_1 between the experiments and the theory in Figure 3.21(b) for VSU-A and Figure 3.21(d) for VSU-B.

Stepping down the ventilation flow rate, *Ri* increased at the beginning of measurement then approached steady state as seen in Figure 3.28. Even though *Ri* of the experimental measurement and the theory of the VSD cases match well most time including the initial period, E of the experimental measurement was significantly less than E of the theory during the initial period. E during the period is even below zero, which violates the definition of E in § 3.2.1. When the diffuser jet cannot reach the density

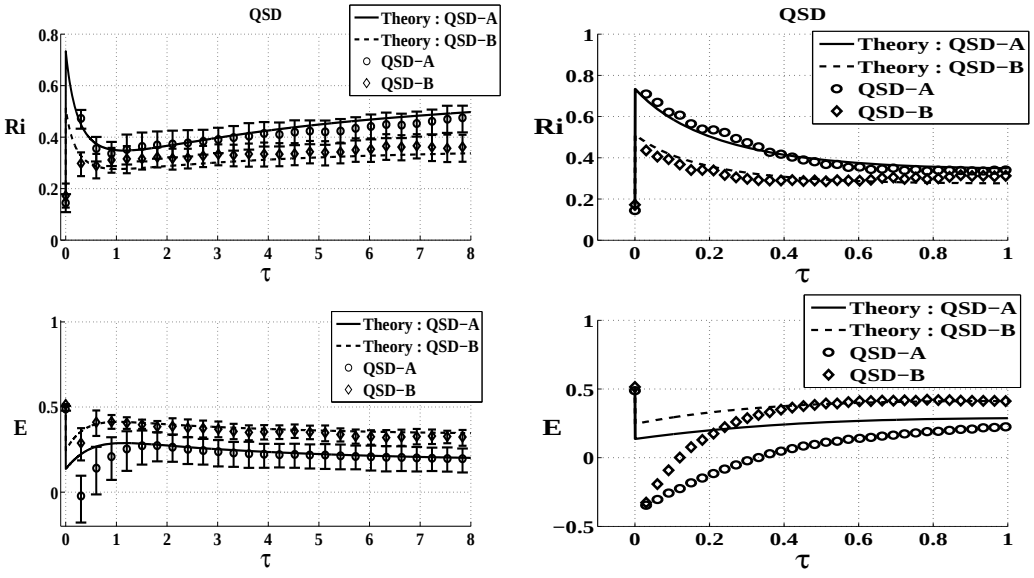

Figure 3.28: Temporal histories of *Ri* and E of the VSD cases: (a) $0 < \tau < 8$ and (b) $0 < \tau < 1$

interface height and ζ is not assumed to be the shooting height of the diffuser flow (or the shoot height is lower than ζ), we suppose to have negative E due to wrong estimation of Γ (which is non-dimensional Q_i of the diffuser jet). In other words, actual Γ of the diffuser jet across the density interface was less than $\Gamma(\zeta)$ during the initial period. To change the estimate of Γ, two different vertical heights are needed to satisfy the mass and buoyancy flux balance. However, the situation in which two different vertical heights exist in a room violates the two-layer model which has only one vertical height for the balances. The rapid responses of ζ of the VSD cases is supposed to shorten the violation period, so the violation of the two layer model of the VSD cases (or the negative E of the VSD cases) only existed within $\tau < 0.3$ for VSD-A and $\tau < 0.1$ for VSD-B in Figure 3.28(b). Hence, the effect of the violation is negligible in the prediction of the temporal responses of a UFAD system through the two-layer model. Revisiting Figures 3.23(a)-3.23(d), the mismatch of E between the theory and the experiments caused the theory to overestimate δ_1 slightly for the initial period, so the match of E did not make any significant influence of temporal responses of a UFAD system in time.

In conclusion for temporal dependencies of the relation between *Ri* and *E*, except the initial transitional period when ζ responded quickly compared to δ_1 or δ_2, the relation of $E = 0.1Ri^{-1}$ corresponds to the experimental measurements most of the time. Relating the mismatch of *E* or *Ri* to the comparison results between the experiments and the theory in § 3.4.1, § 3.4.2.1 and § 3.4.2.2, the initial mismatch mainly influenced the initial transition of δ_1 and the discrepancy of δ_1 between the theory and the experiments were assumed to be negligible. Because δ_1 represents the occupied zone temperature in a real UFAD-operated room, the theoretical predictions of δ_1 in time are expected to be available for analyzing occupant's thermal comfort which is discussed in § 3.5.3 and § 3.5.4.

3.5.3 Engineering perspectives of the experiments of homogeneous and stratified initial conditions

3.5.3.1 Homogeneous condition

Realistic situations of the homogeneous initial condition cases correspond as a room which was pre-cooled during night time. The room starts to be cooled when any activities of occupants or equipments starts and those activities emit heat. At the beginning of cooling, the initial temperature of the room is close to or lower than that of conditioned air temperature of the diffusers. Thermal plumes caused by any heat source rises and forms upper hot air zone from the ceiling, in other words, lower buoyancy enclosure is filled with thermal plume and negatively buoyant fountains. The similar situation in [24] was called as "Initial Transient"(IT) for validating the transient model of the displacement ventilation system only driven by interior heat plume. The experiments with homogeneous initial conditions in our study simulated the same situation of IT in salt-water analogy.

According to the experiments described in § 3.4.1, a UFAD system with single or multi thermal plume and cooling diffusers during the initial period is expected to respond as follows: 1. Each heat source generates its thermal plume which propagates upward due to its positive buoyancy and spreads along the ceiling of the room. Simultaneously, an initial neutral buoyant jet discharges from the diffuser to reach the ceiling. 2. Once

the buoyancy flux of the plume is dominant over the momentum flux from the diffuser jet near the ceiling, upper hot air zone near ceiling is formed and a sharp density or temperature interface exists between the lower occupied zone and the upper hot air zone. 3. Penetration of the diffuser jet disturbs the interface to bring the hot air from the upper layer to the lower layer, which was explained by a penetrative entrainment process.

After the initial period, the experiments show how a UFAD system fills the lower occupied zone balancing the heat source and the cooling air. The hot air zone thickens to reach steady-state interface height in a relatively short time compared to the temperatures of the lower and upper layers. Even though the temperatures of the lower and upper layers increase in time, the physical processes related to the temperature increases of the lower and upper layers are different. The upper layer is directly heated by thermal plume, but the lower layer heated by the penetrative entrainment of the interface.

The two-layer model in § 3.2 successfully predicted temporal responses of thermal stratification in a room. The quicker response of ζ compared to that of δ_1 and δ_2 was observed in the experiments and the theoretical predictions. To predict ζ is important to provide desirable thermal comfort to occupants and the model predictions are expected to be useful to analyze or improve the comfort.

3.5.3.1.1 Time delay of upper hot air zone formation .

The process forming the upper layer of UFAD is similar to that of the mechanical DV system described at § 2.5.1 or the natural ventilation system described in [24]. However, none of those systems have any competition between the plume flow and diffuser flow near ceiling to form the upper layer. Hence, the DV or natural ventilation system had negligible time delays to form the upper layer, but the competition of the UFAD causes a temporal delay in forming the upper layer. From the time delays among the various operating conditions in § 3.4.1.1, the non-dimensional parameter Ψ explains how the competition affects the time delay. The time delay τ_{up} increases when Ψ increases, which means that when the momentum of the diffuser flow is stronger than the buoyancy of the plume, it takes more time to form the upper hot air zone and when the buoyancy is stronger than the momentum, and vice versa.

In real operation of UFAD, existence of an upper hot air zone in UFAD is a key

feature to increase return air temperature and improve uniformity of return temperature among the ceiling vents. When τ_{up} shortens, the ventilation efficiency is regarded as being improved. To take advantage of shortening the time delay, according to the relation between Ψ and τ_{up}, the initial operation of UFAD should keep Ψ low by increasing μ (for instance, decreasing total ventilation rate Q) or decreasing η (for example, increasing A_d for variable area diffuser). Without the explicit relation between τ_{up} and Ψ, further discussion can not be completed. Ψ is a key parameter for improving ventilation efficiency of UFAD during initial transitional period.

3.5.3.2 Stratified condition

The cooling operation of UFAD maintains two-layer stratification within a room and any activities of changing of the strength of the heat source or the diffuser flow change the level of the room stratification, in other words, the activities change occupied zone temperature, T_{OZ}. Changing T_{OZ} happens when reducing electricity consumption of HVAC cooling operation during peak time periods, which is commonly called Demand Response (DR). Applying DR in a room, we attempt to decrease the cooling load by increasing T_{OZ}, and reducing the heat source strength or the diffuser flow rate are popular choices for increasing T_{OZ}. After DR finishes, the increased T_{OZ} returns to normal T_{OZ} by increasing the diffuser flow. During the starting and ending periods of DR, the level of the room stratification changes within a initial transitional period.

For realizing initial transitional changes of the room stratification, it is important to understand the physical processes when the thermal plume or the diffuser flow changes. In our study, the changes are applied as a “Stepping method”, which is an immediate change of the plume strength or the diffuser flow. At first, considering a immediate change of the strength of the plume, the DV system in Chapter 2 showed that the upper layer was temporarily stratified because more buoyant plume fluid can reach the ceiling. Because mixing on the upper layer in the DV system was only driven by the strength of the plume flow, the strong plume flow delivered more buoyant plume fluid to the ceiling to make the upper layer stably stratified. However, from the initial vertical density profiles of Figures 3.16(a) and 3.16(b), the upper layer of the UFAD system remained well-mixed in the same situation because additional kinetic energy

due to penetrated diffuser flow in the upper layer of UFAD enhanced mixing in the upper layer compared to the DV system. Due to the enhanced mixing in the upper layer of UFAD, the two-layer stratification during initial transition was preserved even if the system changed dramatically. By comparing the theoretical prediction and experiments, the enhanced mixing explained a good match between the theory and the experiments in Figures 3.17(a)-3.17(d), because the theory assumed that a two-layer stratification exists during the transitional period.

Secondly, immediate changes of increasing or decreasing the diffuser flow are considered as a popular way of DR in a Variable Air Volume (VAV) UFAD system. To reduce cooling demand during peak load period by increasing T_{OZ}, the ventilation rate decreases during the start of DR period (the cases of VSD) and to return the normal operation, the ventilation rate increases to decrease T_{OZ} after the end of the DR period (the cases of VSU). Similarly to the buoyancy flux change, the interface and lower and upper layer buoyancies change in relatively short time. By comparing theoretical prediction to experimental results, the penetrative entrainment coefficient E of all cases fits with $E = 0.1Ri^{-1}$. Lower and upper layer buoyancies of most cases agree well with theoretical prediction and the interface height also agrees with the predictions. From Figures 3.21(b) and 3.21(d), overshoots of the lower layer buoyancy δ_1 are seen in experiments and the predictions. The overshoot can follow a scenario of physical process in which the density interface moves upward quickly, and the increased Q_i by higher interface height and additional ventilation flow rate bring excessive Q_e with higher buoyancy from the upper layer down to the lower layer to warm the lower layer. The model predicts the excessive Q_e during the initial transition.

Undershoots of δ_1 are also shown in Figures 3.23(b) and 3.23(d) during the initial period. The physical process to explain the undershoots can be that the lowered ζ and decreased ventilation flow rate decreases Q_i during the initial period. Hence Q_e also decreases and lower layer buoyancy also decreases. The predictions still agree well with the experiments and the undershoots occur within $\tau \leq 1$ and δ_1 increases in time. The undershoots of VSD which simulated the start of the DR period are regarded as a plausible characteristic of thermal comfort of DR in UFAD. When the ventilation rate decreases and the overall room temperature increases, the undershoot of δ_1 for

the initial period keeps the occupied zone cool if the density interface sits above the occupied zone. However, if the density interface sits below the occupied zone during the transition, the advantage of the undershoot should be carefully considered because occupants may experience steep thermal stratification near their upper bodies based on ASHRAE standard 91. Hence. we should consider the interface height and the lower layer buoyancy as two important parameters for occupant's thermal comfort.

3.5.4 Phase diagram of interface and lower and upper layer buoyancy

When an ideal OH system relies on well-mixed assumption, there is no thermal stratification in a room. However, thermal stratification in a UFAD system makes the well-mixed assumption improper to represent the occupied zone temperature, T_{OZ}. The two-layer model provides us the way of representing T_{OZ} as δ_{OZ} such as

$$\delta_{OZ} = \frac{1}{\zeta_{OC}} \int_0^{\zeta_{OC}} \delta(\hat{\zeta}) d\hat{\zeta} \tag{3.106}$$

where ζ_{OZ} is dimensionless height of the occupied zone, if $\hat{\zeta} < \zeta$, $\delta(\hat{\zeta}) = \delta_1$ and if $\hat{\zeta} > \zeta$, $\delta(\hat{\zeta}) = \delta_2$ when $\zeta < \zeta_{OZ}$. When $\zeta > \zeta_{OZ}$, $\delta(\hat{\zeta}) = \delta_1$, so (3.106) is converted into

$$\delta_{OZ} = \int_0^{\zeta_{OZ}} \delta_1 d\hat{\zeta} = \delta_1. \tag{3.107}$$

With the Boussinesq assumption, T_{RM} is obtained given by

$$T_{OZ} = (\frac{\delta_{OZ}}{g} \frac{B_{rf}^{2/3}}{CH^{5/3}} + 1) T_{rf} \tag{3.108}$$

where T_{rf} is the reference temperature, g is acceleration of gravity and B_{rf} is the reference buoyancy flux. Because thermal comfort of any occupant directly affected by ζ, δ_1 and δ_2 in UFAD system is important during DR period, to determine temporal responses of T_{OZ}, ζ, δ_1 and δ_2 are important when the system dynamically moves during the start period and the end period of DR.

Dynamical temporal responses of ζ, δ_1 and δ_2 exists during DR period when

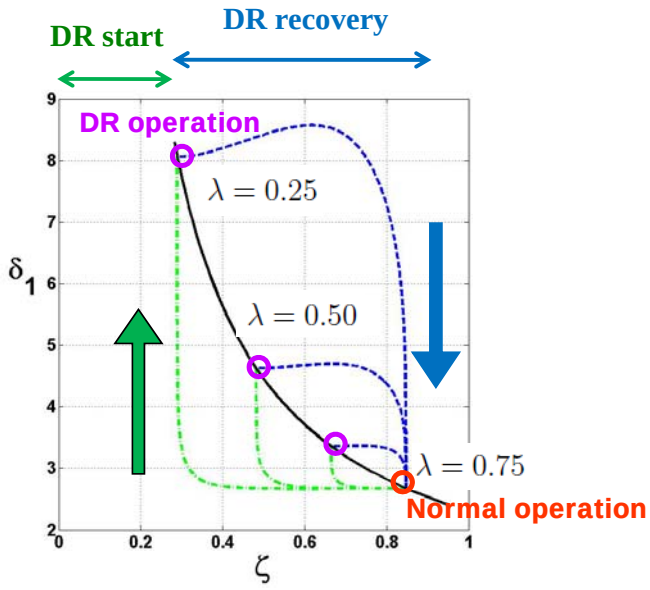

(a)

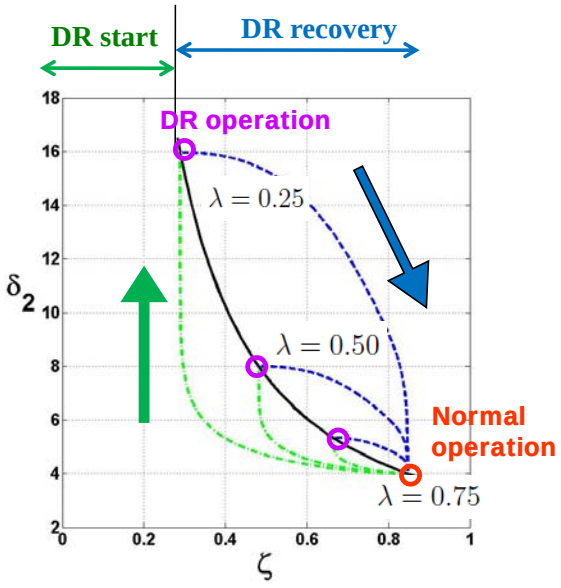

(b)

Figure 3.29: Phase diagram during the start and end period of DR with $\mu_{rf} = 4.0$: (a) ζ .vs. δ_1 and (b) ζ .vs. δ_2

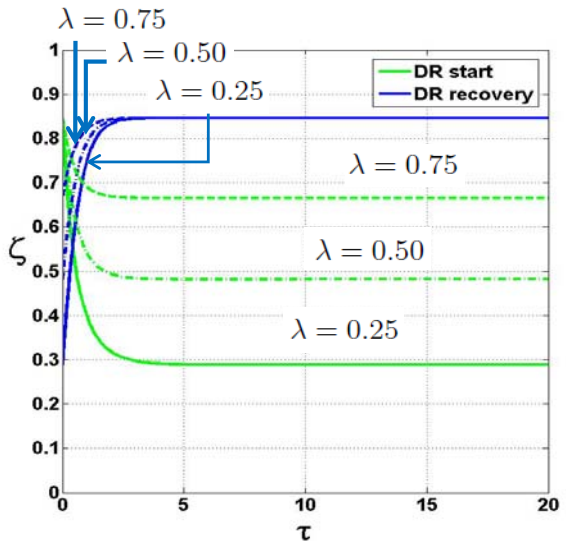

(a)

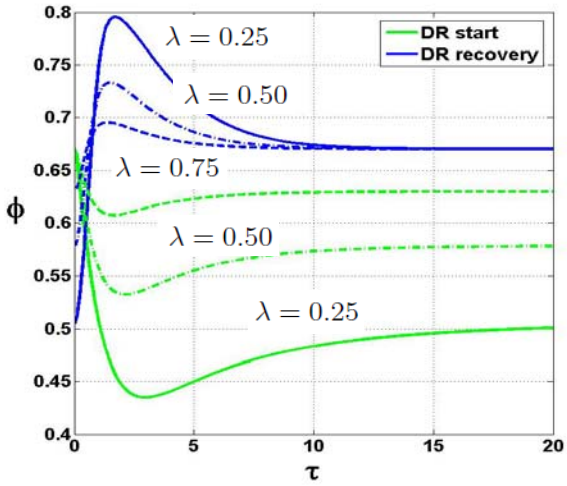

(b)

Figure 3.30: Temporal responses on the start and end period of DR with $\mu_{rf} = 4.0$: (a) τ .vs. ζ and (b) τ .vs. ϕ

occupied zone temperature under normal operation, T_{OZ}^{NO} is readjusted to occupied zone temperature under DR operation, T_{OZ}^{DR} on the starting period or T_{OZ}^{DR} returns to T_{OZ}^{NO} during recovering period. To adjust T_{OZ}, the VSD method for applying DR or the VSU method for recovering to the normal operation were used.

Assuming the normal operating condition to maintain T_{OZ}^{NO} as the reference operating condition, μ_{rf}, the DR operating condition to readjust T_{OZ} to T_{OZ}^{DR} is described by the cases of $\lambda \leq 1$ (λ is the ventilation flow rate during DR normalized by the flow rate of the normal operation in 3.63). When ζ sits above ζ_{OC} during the normal operation and DR operation, T_{OZ}^{NO} and T_{OZ}^{DR} corresponds to δ_1^{NO} and and δ_1^{DR}, respectively.

An example of the phase diagrams of ζ .vs. δ_1 and ζ .vs. δ_2 are obtained by numerically solving (3.64)-(3.66) with the given λ in Figures 3.29(a) and 3.29(b). Figure 3.29(a) shows the relation between ζ and δ_1 with various λ during the start and end of DR. The mid solid line is the steady state solutions and the normal operation and steady state DR operation should sit on the line. The temporal responses of ζ and δ_1 deviate from the steady state line during the transitional period of the start and the end period of DR. Looking at the trajectories of ζ .vs. δ_1 at the start period of DR, ζ moves at first, then δ_1 moves. During the DR recovery period, if λ stepped up as λ from 0.25 to 1, overshoot of δ_1 occurred, but when the difference of λ decreases, the overshoot of δ_1 also decreases. Concerning δ_2 in Figure 3.29(b), δ_2 gradually increased during ζ moved and there was no overshoot or undershoot of δ_2 during the DR start period and DR end period with various λ.

Comparing Figures 3.30(a) and 3.30(b), the responses of δ_1 vs. ζ and δ_2 vs. ζ shows how ζ, δ_1 and δ_2 influences occupant thermal comfort in time. A ζ moves, the lower-layer temperature represented as δ_1 stays cool at the start period of DR and the temperature stays hot at the end of DR period when ζ always sits above ζ_{OZ} during the DR operation. The time delayed responses of UFAD is clearly different from conventional OH system, so the UFAD system can utilize the advantage to have the time delay of temperature increase during the start period of DR. However, the slow responses of the end period of DR suggest that the pre-adjustment of operating condition is needed to maximize the thermal comfort.

When ζ sits below ζ_{OZ} during the DR operation in a room, the advantage or

disadvantage of the time delay during initial transition is no longer valid. From Figure 3.30(b), if $\zeta < \zeta_{OZ}$, the level of thermal stratification $\phi = \delta_1/\delta_2$ within the occupied zone was steeply changed during the initial transition period ($\tau < 3$ in Figures 3.30(a) and 3.30(b)), so any occupants in the room may experience discomfort caused by the thermal stratification. Once ϕ becomes small and changes rapidly in short time period, the existence of the thermal stratification may be harmful for the occupants. To avoid the discomfort, the system maintains ζ above the occupied zone or slows ζ movement down by slowly adjusting the ventilation flow rate in time. Even though time dependent strategies of the adjustment of the ventilation flow rate are beyond our interest, the transient two layer model is expected to be useful to improve thermal comfort for the occupants during the initial period.

3.6 Conclusion

Assuming two-layer stratification exists in a room, transient two-layer models were proposed for single or multiple plumes and diffusers. The model was nondimensionalized with two time scales, the filling box time scale T_f and the replenishment time scale T_n. The operating condition $\mu = \frac{Q_p \text{ at H}}{Q}$ and the geometrical configuration of the diffuser $\eta = \frac{H}{\sqrt{A_d}}$ were determined to be the two parameters that describe the evolution of the transient vertical temperature distribution. The stratification was described in terms of three nondimensional variables, the interface height and the lower and upper layer buoyancies, ζ, δ_1 and δ_2, respectively. The system of equations for ζ, δ_1 and δ_2 were derived for a single plume and a single diffuser in (3.20) - (3.22) and for multi plumes and multi diffusers in (3.73) - (3.75)

An analytic solution for a negatively buoyant jet was derived to calculate how much the diffuser jet entrained its surrounding fluid and to estimate Q_i which was defined as penetrative flow rate of the diffuser at the density interface. Γ was defined as non-dimensional Q_i normalized by total ventilation flow rate, Q_{tot}. In most of UFAD operations, the negative buoyancy flux played a weaker role than momentum flux, so Γ was simply defined as a function of ζ and η in (3.44).

The penetrative entrainment across the density interface is an important phys-

ical process of mixing between the lower and upper layers. The entrainment process was parameterized by the local Richardson number *Ri* and the penetrative entrainment rate coefficient E. *Ri* was analytically estimated by $\delta_2 - \delta_1$, η, μ and ζ in (3.58) and according to the E .vs. *Ri* relation in Figure 3.10, $E = 0.1Ri^{-1}$ was used to estimate E.

Small-scale salt-water analogy experiments were performed to validate the transient model. With digital technology (high resolution video camera and a digital linkage between the camera and a workstation) to capture and process the experiment, more accuracy and higher resolution of vertical density measurements compared to analog video system enabled us to take transient density measurements over whole experiment tank. To simulate various UFAD operating conditions, the sets of the experiments were categorized by their initial conditions such as "Homogeneous initial condition" and "Stratified initial condition".

Processing the experimental data, we converted horizontal-averaged vertical density distribution into the two-layer stratification through two quantitative methods, "Optimized Scheme (OS)" and "Linear Fit Scheme (LFS)" in terms of ζ, δ_1 and δ_2. Additionally, the LFS method provided information on the lower and upper bounds of the transition layer between the lower and upper layers, and was used to reveal any processing errors measuring δ_1 and δ_2 associated with the estimation of ζ.

In the experiments of homogeneous initial condition §3.4, once the upper layer was formed, the layer thickened to the steady state and the lower and upper layer buoyancy increased in time. Ψ, a non-dimensional parameter describing the competition between the buoyancy driven flow and the momentum driven flow in a space and the diffuser flow possibly explained why it took different times to form the initial upper layer. The experiments of the HMG cases showed good agreement with the theoretical predictions for varying μ and η.

The stratified initial conditions represented the thermal environment when a UFAD system ventilated a room for cooling. By stepping up or down the strength of buoyancy flux of the plume source (the BSD or BSU cases) or ventilation flow rate of the diffuser flow (the VSD or VSU cases), the initial buoyancies of the lower and upper layers increased or decreased in time. The BSD or BSU cases showed monotonic decrease or increase of the lower and upper layer buoyancies, δ_1 and δ_2 respectively,

during the entire transitional period. However, undershoot or overshoot of the temporal responses of the lower layer buoyancy δ_1 for the VSD or VSU cases, respectively, were observed during the early transitional period. For all the cases of the homogeneous and stratified initial condition, the time response of the interface height ζ was quicker than the temporal buoyancy responses of the lower and upper layers.

The temporal histories of Ri and E provided an explanation of why the initial transition of δ_1 of the VSD or VSU cases had undershoot or overshoot responses which did not follow overall temporal responses of δ_1 such as increasing trends of the VSD and decreasing trends of the VSU. For the initial transitional period of the VSD, the experimental estimation of E suddenly dropped down to $E \leq 0$ when the ventilation flow rate stepped down, and then recovered to approach to the theoretical prediction of E. The theoretical prediction of E also predicted similar trends of the experiments. However, during the initial transitional period, the prediction underestimated the reduction of E at the beginning of the period, because the theory was unable to simulate the situation in which the diffuser jet remained below the the density interface. The initial periods of the VSD cases were relatively short compared with the entire temporal responses of δ_1 and δ_2, so the theoretical predictions of δ_1 agreed well with the experiments in most of time.

Considering the initial transitional period of the VSU cases, both the theoretical predictions and the experiments showed sudden step-up then decaying temporal trends of E. However, the minimum of E during the period in the experiments was below that of the theory, which can be explained by inappropriate experimental estimation of ζ and δ_1 caused by the wider transition layer. However, similar to the VSD cases, the initial mismatch of E did not affect the agreement with the theoretical prediction and the experiments during majority of the transient response.

Extending the model to predict the interior temperature profile and occupant's thermal comfort under various UFAD operating conditions, careful consideration is needed to adjust occupied zone temperature by changing ventilation flow rate, because there may be unexpected temperature responses such as overshoot or undershoot of the lower-layer temperature when the flow rate abruptly increases or decreases, respectively.

In conclusion, the two-layer model examined by various experimental condi-

tions enabled us to depict the various temporal responses of vertical density distribution in terms of ζ, δ_1, and δ_2. Because the model predicts transient room temperature change corresponding to various operating conditions in real UFAD system, the model's predictions are also useful to design a control strategy to adjust a room temperature or operating schedules to optimize occupant thermal comfort while maximizing energy efficiency.

Chapter 4

Comparison study of building energy performance for overhead system and Underfloor Air Distribution system

4.1 Introduction

Climate change is leading to a global trend of increasing building energy consumption for cooling during summer. Electric cooling systems are popular in both residential and commercial buildings, but to satisfy recent increases in cooling demands additional power plants or an increase in the efficiency of the existing electricity grid are required. However, those are capital intensive projects and therefore, in order to minimize the cost and manage future electricity demands efficiently, predicting future cooling demands is important. Building energy simulations for existing or newly constructed buildings are considered to be only way to predict the future demand accurately.

Since 1960, several building simulation program have been developed, such as DOE-2 developed by Lawrence Berkeley National Laboratory, BLAST developed by the U.S. Army Construction Engineering Research Laboratories and the University of Illinois, CLIM 2000 developed by the Buildings Branch of the French utility company, *Electricité de France* and etc. Even though building energy simulations have been performed for various type of buildings, i.e. residential or commercial buildings, accurate

measurement of building energy consumption is not easily obtained without precise estimation of heat balance between the interior and exterior environments of a building. Because the heat balance is strongly influenced by the climate in which a building exists, it is necessary to have realistic weather data including outdoor temperature, humidity and etc. to achieve accurate heat balance estimation. The Department of Energy (DOE) developed a format of weather data which includes 1042 locations in the USA, 71 locations in Canada, and more than 1000 locations in 100 other countries throughout the world to establish a standard of a format of weather data for various building energy simulations to improve accuracy of building energy simulation.

To reduce energy demand in existing or newly-constructed buildings, an UFAD system is a strong candidate for replacing a conventional overhead (OH) ventilation system. Significant energy saving can be achieved by replacing existing OH by UFAD due to improve ventilation efficiency [7]. Even though UFAD has been used since 1970, a room air model to simulate the UFAD ventilation efficiency was only recently implemented for building energy simulations ([38]). With the UFAD room air model, we can accurately estimate reduced energy consumption due to UFAD compared to OH. Additionally, we can also predict the DR effectiveness of UFAD through the simulation, too.

In this chapter, we compare the performance of OH and UFAD systems with respect to annual building energy consumption. For this purpose, we uses EnergyPlus, which is a full-scale system simulation package developed by the US DOE.

In § 4.2, we describe basic model input parameters, such as building geometry, internal heat load, etc.. For the building geometry, we consider a multi-stories prototype building. Each floor is partitioned into perimeter zones and interior zones for a realistic estimation of thermal loads. Additionally, the UFAD building has a supply-air plenum, which is a crucial component for distributing conditioned air. The building is equipped with a water-based cooling plant consisting of an electric chiller and a cooling tower, as well as a heating plant consisting of a natural gas boiler, as standard HVAC equipment. The UCSD-UFAD room air model [38] was used for simulating the thermal stratification, which is another key characteristic of the UFAD system.

In § 4.3, we describe the matrix of simulations to investigate energy consump-

tion. The energy consumption cases varied building location (San Francisco (SF), Los Angeles (LA) and Sacramento (SC)), window-to-wall ratio and internal heat load. The metrics to evaluate energy usage are described in § 4.3.2.

In § 4.4, annual energy consumptions of OH and UFAD are presented for various locations and various operating scenarios. Thermal decay, or thermal deficiency due to heat exchange between supply air and return air, and the effectiveness of the economizer (a type of outside air mixer which bring cool outside air to reduce chiller cooling load) are two important characteristics to explain the difference of energy consumption between OH and UFAD. A detailed discussion of the thermal decay and the economizer will be provided in § 4.5

4.2 Modeling

While UFAD system is regarded as a potential ventilation systems to replace traditional OH systems, it is necessary to make a proper comparison of whole building energy consumption for the two systems. The comparisons can not be easily achieved without making two identical buildings which are equipped OH and UFAD separately. Therefore, virtual prototype buildings developed by UCSD and CBE at U.C. Berkeley ([34]) are proposed for this comparison using EnergyPlus which is a full scale system simulation package developed by Department of Energy (DOE), USA.

4.2.1 EnergyPlus building energy simulation model

The U.S. Department of Energy developed and supported the development of DOE-2 and BLAST, two building simulation programs that have become industry standards for building energy simulations. Combining the advantages of both of the programs, EnergyPlus was released for integrating DOE-2 and BLAST and adapting advanced energy efficient HVAC schemes, such as a UFAD system. The simulation engine and individual modules in EnergyPlus are open to developers who want to add newly developed systems or features and incorporate them to simulate any building. For these reasons, EnergyPlus is considered to be a strong candidate to become the benchmark building energy simulation program.

4.2.1.1 Thermal stratification of UFAD

In contrast to an OH system, thermal stratification produced by a UFAD system is a key feature to improve cooling efficiency by increasing the return temperature, and must be included in the model. To simulate the stratification, we used the UCSD two-layer stratification model proposed in [37] and validated by full scale experiments in [17]. The model defines two vertical temperature zones within a room; the first zone is the occupied zone next to the floor, containing the room occupants and heat sources such as workstations, copiers, etc. and the second is the upper hot-air zone, next to the ceiling, containing heated air from the occupied zone and any heat from ceiling lighting.

4.2.1.2 Heat transfer of underfloor plenum

The underfloor plenum (UFP), which is the space below the raised floor used for distributing conditioned air to floor diffusers, is one of the unique HVAC components in a UFAD system. Due to adopting the UFP for air distribution, instead of the supply ducts used in an OH system, the static pressure of UFAD for delivering the conditioned air to rooms is significantly lower than that of an OH system as a result of reducing head loss in the ducts.

The heat transfer through the UFP impacts the cooling capacity of the occupied zone because of the adjacency of the UFP to the occupied zone. EnergyPlus can handle these two important characteristics of the UFP, namely, the lower static pressure and the heat transfer to the UFP, thereby providing a realistic simulation of a UFAD system.

4.2.1.3 Integrated simulation capability of heat transfer of interior and exterior of a building and HVAC plant energy consumption

Cooling or heating load calculations need to include both wall heat transfer and HVAC performance. EnergyPlus is able to simulate both of these for any given condition. Furthermore, if annual weather data are available at the building location, the model can simulate transient heat conduction of room air or building thermal materials, relevant, for example, for utilizing night cooling or reducing electricity demand during a peak load period by pre-cooling [52].

4.2.2 Model characteristics

The simulation model must contain building geometry, HVAC equipment, schedules of internal heat loads, such as lighting, equipment, occupancy, etc.. and HVAC operation. Combined with annual weather data, cooling or heating demand corresponding to room set point temperature and weather condition, as well as energy consumption to satisfy the cooling and heating demand are calculated for OH and ,UFAD systems.

4.2.2.1 Building geometry

The building has three stories (ground floor (GF), middle floor (MF), top floor (TF)) providing a representation of a office building equipped with a water-based cooling plant consisting of an electric chiller and a cooling tower. Each floor is partitioned into perimeter zones and interior zones for realistic estimation of thermal loads (Figure 4.1). The model can simulate both OH and UFAD systems by changing the configuration of zones and HVAC components. To model a UFAD system instead of an OH system, some major changes in the configuration of the building envelope and HVAC system are needed because of the existence of the UFP. The presence of the UFP, while maintaining the same overall height and volume, requires the UFAD building to have a shallow return plenum. The UFP is positioned adjacent to and below each occupied zone. The detailed building geometry is given in Table 4.1.

The model can also vary the window-to-wall ratio (WWR) to simulate different ratios of conductive heat transfer to exterior building envelope and radiative heat transfer of interior heating or cooling loads through interior solar gains. The values considered here were 20 %, 40 % (baseline) and 60 %, which are a percentage of window area over total are of all vertical exterior envelopes. The windows are arranged in a horizontal strip along the exterior wall of each perimeter zone, so their vertical extent is determined by the WWR. Because the WWR has a strong correlation with the thermal loads of the perimeter zones, the WWR is a key feature of the building geometrical configuration. The windows are chosen to have low-emissivity, and their properties are calculated by the “Window 5” program to satisfy California Title 24 [13]. Due to the low emissivity of the windows, sensitivity to the presence or absence of window blinds is negligible (Appendix A of [34]).

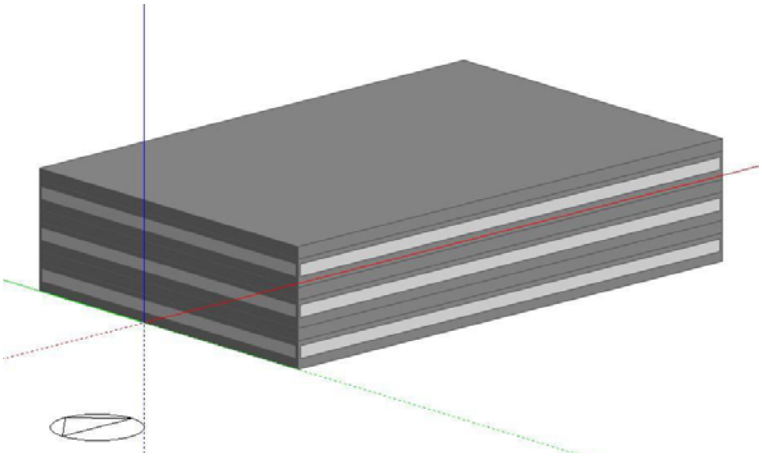

(a)

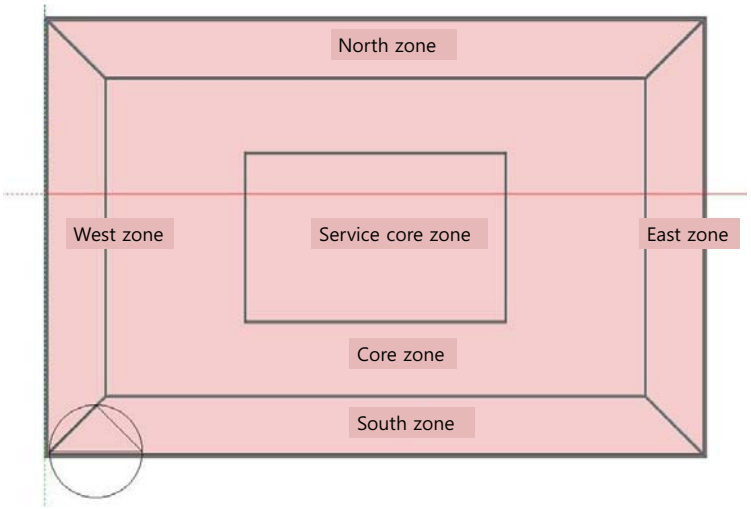

(b)

Figure 4.1: (a) Overview of prototype building. (b) Floor plan of the building (each story has the same floor plan) : The space is partitioned into 4 perimeter zones, 1 core zone, and 1 (unoccupied) service core zone.

Table 4.1: Building geometry of OH and UFAD configuration

	OH	**UFAD**
Total floor area (m^2)	5574	5574
Number of floors	3	3
Thermal zones	4 perimeter zones (39.6%) 1 interior zone (44.9%) 1 service core zone (15.5%)	4 perimeter zones (39.6%) 1 interior zone (44.9%) 1 service core zone (15.5%)
Perimeter zone depth (m)	4.57	4.57
Floor to floor height (m)	3.96	3.96
Supply plenum height (m)	N/A	0.405
Return plenum height (m)	1.22	0.81

4.2.2.2 Internal Loads and Schedules

Occupants and electrical equipment are treated as internal heat loads, which are adjustable by schedules of occupancy and usages of lighting and equipment. The occupancy is estimated by the number of people within a occupied zone and for simplicity, it is assumed that each person emits 75 W of thermal load. The lighting and equipment usages are described as a fraction of their maximum values. Both usages generate thermal loads within a room where they are present, and can affect cooling or heating demand according to the season. For example, increase of either usage may reduce heating demand or increase cooling demand, and vice versa. The internal load scenarios are given in Table 4.2

The schedules of the internal loads, given in Figure 4.2 remain the same for the entire year. The fractions of occupancy, lighting and electrical equipments are the fractions are the ratios between the actual values of the occupancy or the usages and the peak values of them (given in Table 4.2). The occupancy are scheduled from 08:00 am to 18:00 weekdays and 08:00 to 12:00 on weekends. During the occupancy period (from 08:00 to 18:00) on weekdays, the lighting and equipment usage set to 90 % and 100 %, respectively. The usages maintain at the minimum values of 30 % and 17 %, respectively, during non-occupancy period on weekdays and all day on weekend.

Table 4.2: Internal Load scenarios. Each scenarios described the peak values of occupancy and the lighting and electrical equipment usages

	Interior load # 1	Interior load #2	Interior load #3
People (m^2 / person)	22.3	11.2	8.4
Lighting (W / m^2)	10.8	11.8	12.9
Equipment (W / m^2)	8.6	22.6	35.5

4.2.2.3 HVAC operation

Energy sources for heating and cooling conditioned air are natural gas and electricity, respectively (see Table 4.3). Energy consumption of both sources is expressed in units of W/m^2. Because purchasing costs for the gas and electricity per W/m^2 are different, their energy consumptions are treated differently.

Both systems primarily circulate conditioned air by an air handling unit (AHU) fan and return air (RA) fan as seen in Figure 4.3. The supply air temperatures of the AHU (AHU SAT) are different between OH and UFAD systems. In a UFAD system, the conditioned air is discharged from a floor diffuser, which is much closer to the room occupants compared to the ceiling diffuser of an OH system, so the UFAD diffuser temperature is required to be higher than that of OH to avoid occupant thermal discomfort. In our study, AHU SAT for an OH system is 13.9 ^oC and that of UFAD is 17.2 ^oC.

For cooling, cooling coils in which heat exchange between hot return air and chilled water provides cooling energy to the air circuit. The water chiller uses electricity to keep the water cool. For heating, a hot water boiler provided heating energy to heating coils of AHU and reheaters. The central plant includes a central chiller with variable speed pumps and cooling tower.

As noted earlier, the AHU fan static pressure of the UFAD system is significantly lower than for an OH system; in our study by about 67 %. With this lower static pressure, we expect the UFAD system to have lower energy consumption when both systems deliver the same volume of conditioned air. However, while OH uses variable air volume (VAV) boxes without a fan (Figure 4.3(a)), UFAD has air terminal unit (ATU), which has a variable speed fan, to compensate for depressurization due to leakage from the UFP when cooling or heating demand occurs in a zone (Figure 4.3(b)). Therefore, even

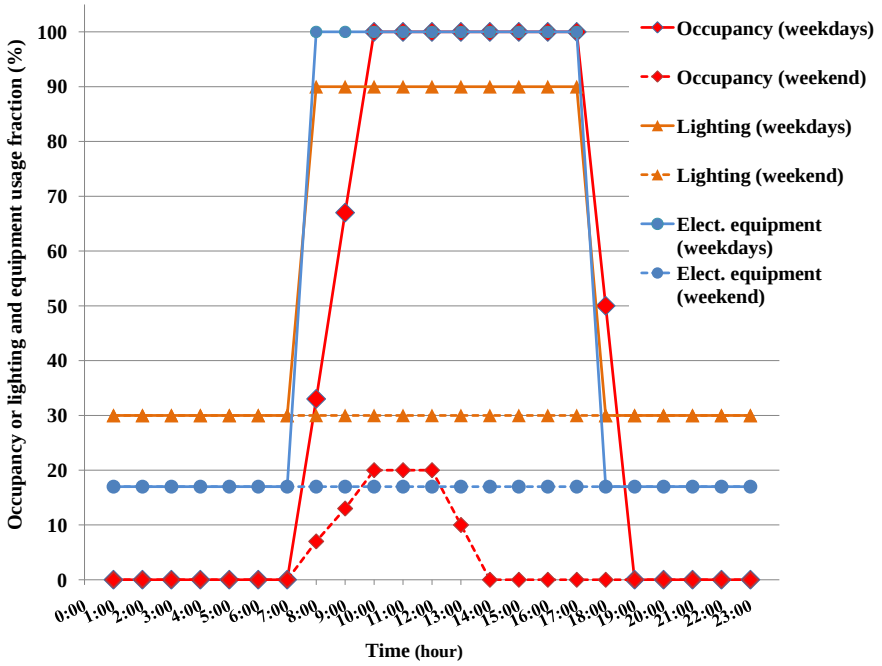

Figure 4.2: Schedules of occupancy and the lighting and electrical equipment usages: the fractions are the ratios between the actual values of the occupancy or the usages and the peak values of them (the peak values are given in Table 4.2)

though UFAD has significant advantage to save AHU fan energy due to the lower static pressure, the ATU fan energy consumption of UFAD can trade off the advantage of the AHU fan energy savings.

To provide required fresh air to occupants, an outside air (OA) mixer is installed in an air circuit between the return air and the AHU. To improve energy efficiency using "free cooling", in other words, obtaining additional cooling by mixing colder outside air with hotter return air in the circuit, the OA controller uses an "Economizer" scheme. According to the scheme, the OA mixer discharges the return air to the outside and introduces cold outside air into the air circuit when the outside air temperature, T_{OUT}, is colder than the return temperature T_{RT}. Detailed discussion of the cooling effectiveness of the Economizer is given in § 4.5.2.

HVAC operations for both the OH and UFAD systems follow the occupancy schedule defined in Table 4.2, which means that when occupants are in the building, the HVAC system turns on to achieve room set point temperature (T_{RST}) by heating or

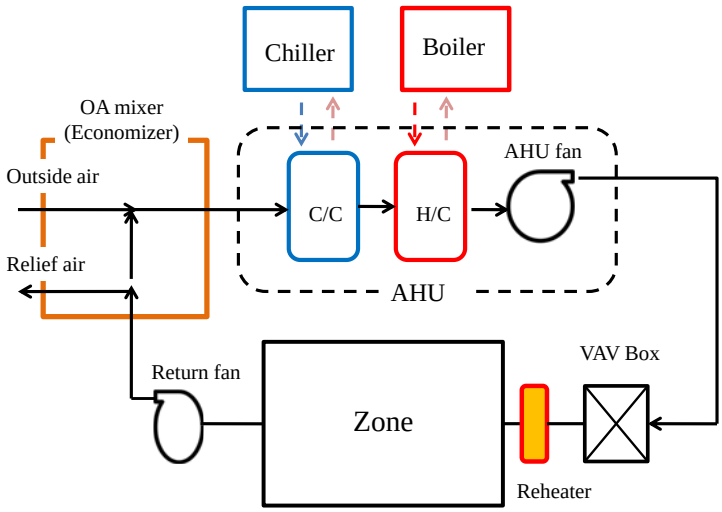

(a)

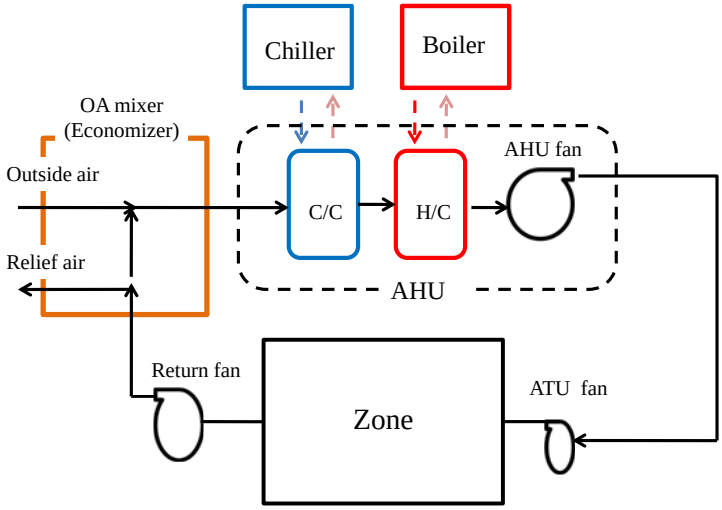

(b)

Figure 4.3: Schematics of HVAC (heating, ventilation and air conditioning) air circuit.: C/C is cooling coils and H/C is heating coils. Chiller and boiler deliver cooling and heating energy through water circuits, respectively. (a) HVAC systems for OH with VAV box and reheater for all zones (b) HVAC systems for UFAD with air terminal unit (ATU) for all perimeter zones

Table 4.3: HVAC operating conditions.

		OH	UFAD
System Type	Heating	Gas Boiler	
	Cooling	Screw chiller	
	Air Terminal Unit	VAV box with reheat (interior and perimeter)	VAV Box with no reheat (interior) VS FCU with rehear (perimeter)
HVAC sizing	Chiller	Autosized (Min Part load ratio and min unloading ratio 0.1 and 0.15)	
	Boiler	Autosized	
	VAV box	Zone cooling design SAT = AHU SAT + 1.0 ^{o}C	Zone cooling design SAT = AHU SAT + 1.3 ^{o}C (interior) = AHU SAT + 1.0 ^{o}C (serv. core) = AHU SAT + 3.9 ^{o}C (perimeter)
Operation	Cooling	Screw chiller with a reference COP of 5	
	Heating	Hot water boiler with an efficiency of 0.80	
	AHU SAT	13.89 ^{o}C	17.22 ^{o}C
	Chilled water supply temp	7.22 ^{o}C	
	Heated water supply temp	80 ^{o}C	
	OA controller	Economizer (min OA 2.83 m^3/hour/m^2(area))	
	Ventilation	25.5 m^3/hour / person	
	Infiltration	0.30 Air Change Rate per Hour	
	AHU supply fan static pressure	1.125 kPa (4.5 iwc)	0.75 kPa (3.0 iwc)
	AHU supply fan static part load shutoff	0.25 kPa (1.0 iwc)	0.125 kPa (0.5 iwc)
	AHU fan efficiency	75 %	75 %
	ATU fan efficiency	N/A	15 %

cooling. The HVAC systems operate from 05:00 to 19:00 on weekdays and from 05:00 to 13:00 on weekends and holidays. The heating or cooling demands are determined by maintaining the room temperature at T_{RST} in a room.

4.3 Simulation runs for sensitivity studies

In this section, we describe sensitivity studies of annual energy simulation on various locations, building geometries and interior heat load. We conducted the annual energy simulations from January 1st to December 31st with the weather data released by DOE.

4.3.1 Annual energy consumption

Annual building energy consumption can be strongly influenced by both the interior conditions, for example, the number of occupants or activities, and the exterior environment, such as the weather. We have chosen to explore the influence of the following parameters of building energy consumption: (1) Location, (2) Window-to -wall ratio, and (3) Internal heat load.

1. Location

We have chosen San Francisco, Sacramento, and Los Angeles to represent northern Californian coastal cities, inland cities and southern Californian coastal cities, respectively. San Francisco has a relatively mild summer and winter, so we expect the smallest energy use. Sacramento represents an inland California climate, which has a hot and dry summer and relatively cold winter. Los Angeles located within the Los Angeles basin and surrounded by mountains, has a relatively hot summer and mild winter.

2. Window-to-wall ratio

Heat input by radiation through windows strongly influences the interior heating or cooling load. The level of the heat input is largely governed by the type of window and the size of window along the building envelope. In our simulation, low-emissivity windows have been chosen satisfying the "Title 24" standard recommended by the California energy commission. For parameterizing the size of window, we define the window-to-wall ratio, or WWR, as the ratio of the height of the window to the total height of the floor. In our prototype building, the windows extend in a strip around the entire perimeter of each floor, with the window height determined by the WWR. We have investigated three values for WWR, namely, 20 %, 40 % (baseline) and 60 %. We expect more heat input when a building has larger size of window, i.e. larger WWR.

3. Internal heat load

Both the building occupancy and any sources of electricity consumption (lighting and electrical equipment such as computer, copiers, etc.) should be considered as heat sources in the interior environment. These interior heat sources are estimated in units of $\mathrm{W/m^2}$. We consider three different levels of usage, as given in Table 4.2, following the fixed schedule given in Table 4.2. Internal Load #1 is considered as baseline for comparison between OH and UFAD.

The matrix of simulation runs for annual energy consumption is given in Table 4.4. For each location, five simulations are performed: the three WWR values with Internal Load #1 (baseline); and the two internal load scenarios, internal load #2 and internal load #3, with WWR $= 40$ %. Each series of 15 simulations is repeated for OH and UFAD systems.

Table 4.4: Sensitivity study simulation for annual energy consumption.

			Run comparisons	
Parameter	**Values**	**Purpose**	**UFAD Model**	**OH Model**
City	SF	Sensitivity to weather	X	X
	SC		X	X
	LA		X	X
WWR	20% (baseline)	Sensitivity to perimeter vs. interior loads	X	X
	40%		X	X
	60%		X	X
Internal load level	#1 (baseline)	Sensitivity to internal load level	X	X
	#2		X	X
	#3		X	X
AHU SAT set point	13.9 ^{o}C	Impact of AHU SAT		X
	17.2 ^{o}C		X	
AHU Design static pressure	0.75 kPa (3 iwc)	Degree of ducting in SA plenum	X	
	1.125 kPa (4.5 iwc)			X

4.3.2 Metric for annual energy performance

To operate HVAC on our proto-type building over an entire year, both electricity and natural gas are used for cooling and heating, respectively. This means that we need to consider electricity consumption and gas consumption separately because actual costs to purchase electricity and the gas are different. The gas is only used for heating air, but the electricity is used for cooling, and for operating pumps and fans.

Our principal metric to compare the energy consumption across the scenarios described in § 4.3 is the "Energy Utilization Index (EUI)", or EUI, measured in $\mathrm{kWh}/\mathrm{m}^2$, for annual or monthly energy consumption. In our study, EUI is the energy consumption related to HVAC equipment and averaged over the total building floor area.

4.4 Results

4.4.1 Two layer stratification in a UFAD system

The buildings adopting the OH and UFAD systems were simulated under the same weather conditions and operating conditions. However, the cooling demand of

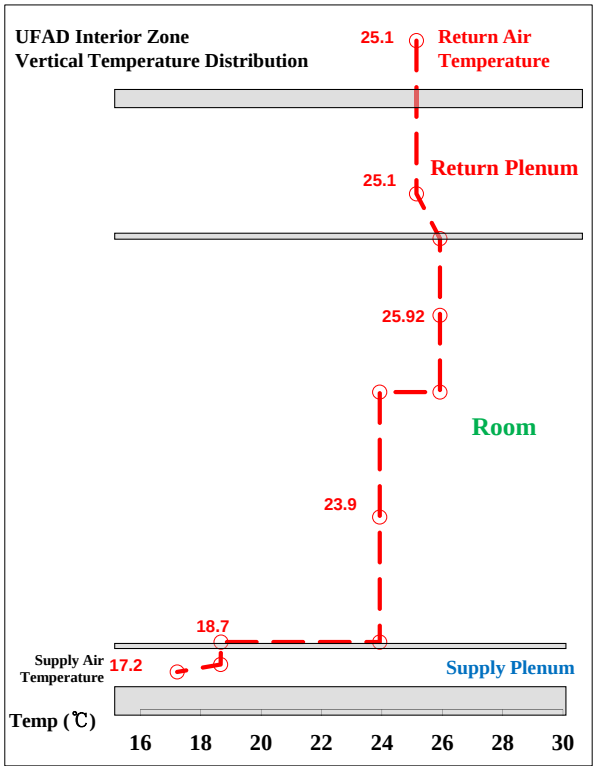

Figure 4.4: Vertical temperature profile of UFAD system in the core zone at the middle floor at 14:00 on a summer day in San Francisco : Room set point temperature = 23.9 ^{o}C and supply air temperature is 17.2 ^{o}C.

the UFAD system must be estimated differently from that of the OH system. While only one room temperature needs to be taken into consideration for OH, UFAD needs to consider stratification in the room temperature in order to calculate realistic cooling or heating demands in a space. An EnergyPlus UFAD room air model (briefly described in § 1.3.1) was used to determine two temperature zones, an occupied zone and an upper hot air zone, as a simplified model of the stratification. Then the room set point manager in EnergyPlus determined how much conditioned air was needed to maintain 24 ^{o}C in the occupied zone. An example of the EnergyPlus estimation of the thermal stratification was shown in Figure 4.4. The occupied zone maintained 23.8 ^{o}C (75 ^{o}F) and the temperature difference between the lower and upper layer was 1.1 ^{o}C (2 ^{o}F). Further discussion on comparing the cooling demands of the OH and UFAD systems will be provided in § 4.5.1.

4.4.2 Annual energy consumption of OH and UFAD

Using weather data provided by DOE, we performed calculations of cooling or heating loads in the proto-type building and corresponding energy consumptions of HVAC equipment. To compare the energy consumption between the OH and the UFAD systems, we measured monthly and annual EUI of both systems. Sensitivity studies were presented under three different categories; (1) location, (2) window-to-wall ratio (WWR) and (3) the internal load configuration. As the baseline configuration for the sensitivities studies, WWR = 40 % and internal load level #1 are chosen.

4.4.2.1 Effect of building locations

We considered the three locations, SF, LA and SC, to represent typical Californian climates, namely Coastal, Los Angeles Basin, and Inland, respectively. The weather data for all locations included solar radiation, dry bulb temperature, humidity ratio wind speed, etc. to provide all outdoor environmental data that directly influences the cooling and heating load for all seasons. The simulation also enables us to analyze the relation between the environmental data and actual cooling and heating demands of the proto-type building.

4.4.2.1.1 Degree days .

The concept of Degree Day (DD) has been widely used to estimate the cooling and heating demand and to analyze weather sensitivity of each location in the absence of real measurements. We performed a comparison study between DD and the simulation results to estimate the relation between the weather and the heating or cooling demand of the proto-type buildings.

A DD is primarily determined by the difference between the daily average temperature and a base temperature, which assumes that the HVAC equipments operated during 24 hours. Monthly or annual DD were estimated by summing DD of each day during a given month or entire year, respectively. However, because the HVAC equipments operated from 6:00 to 18:00 on a weekday and from 6:00 to 12:00 on weekends in our study, the common definition of DD for 24 hours HVAC operation is inadequate. Therefore, we redefined monthly DD, categorized as Cooling Degree Day (CDD) and

Heating Degree Day (HDD), as

$$\mathrm{CDD} = \sum_{\mathrm{i=1}}^{\mathrm{N_{day}}} \sum_{\mathrm{j=1}}^{24} \nu_{\mathrm{i,j}}^{\mathrm{CDD}} (\mathrm{T_{i,j}} - \mathrm{T_b}) \tag{4.1}$$

and

$$\mathrm{HDD} = \sum_{\mathrm{i=1}}^{\mathrm{N_{day}}} \sum_{\mathrm{j=1}}^{24} \nu_{\mathrm{i,j}}^{\mathrm{HDD}} (\mathrm{T_b} - \mathrm{T_{i,j}}) \tag{4.2}$$

respectively, where $T_{i,j}$ is hourly averaged outdoor temperature at certain time (i represents a day and j is a hour), T_b is the base temperature which is 18.3 ^{o}C (65 ^{o}F) for CDD and HDD. (The base temperature in our study follows the climatography of the United States No. 20). N_{day} is the number of the days in a particular month (i represents a day and j is a hour) and ν^{CDD} is $1/24$ when $T_{i,j} > T_b$ during HVAC operating period (6:00 - 18:00) and zero when $T_{i,j} < T_b$ or during HVAC non-operating period (0:00 - 6:00 and 18:00 - 24:00) and ν^{HDD} is $1/24$ when $T_{i,j} < T_b$ during the HVAC operating period and zero when $T_{i,j} > T_b$ or HVAC was the non-operating period. The annual CDD or HDD were calculated by summing all monthly CDD or HDD over the year. The CDD and HDD, which assumed to be simplified estimations of the cooling and heating demand, respectively, are parameters that quantify a weather data at each location.

The annual CDD and HDD were plotted in Figure 4.5 for the three different locations. The heating demand of SF is dominant over the cooling demand, while cooling demand in LA is dominant over heating demand. However, in SC, the cooling and heating demand were approximately balanced.

The chiller EUI and the gas EUI are also plotted against CDD and HDD respectively to show the relation between Degree Day and the EUI of the protype building. CDD and HDD at LA and SC agreed well with the chiller and gas EUI. However, those at SF did not coincide with the EUIs well. The mild climate in SF caused the discrepancy between the DD and the EUI because the given internal load is relatively higher than heat transfer through the building envelope due to the mild climate. Because the DD is only influenced by the building envelope heat transfer, when a building is affected by a relatively strong internal heat load, the CDD and HDD are not expected to agree with the actual cooling or heating demand. Additionally, the relatively strong internal

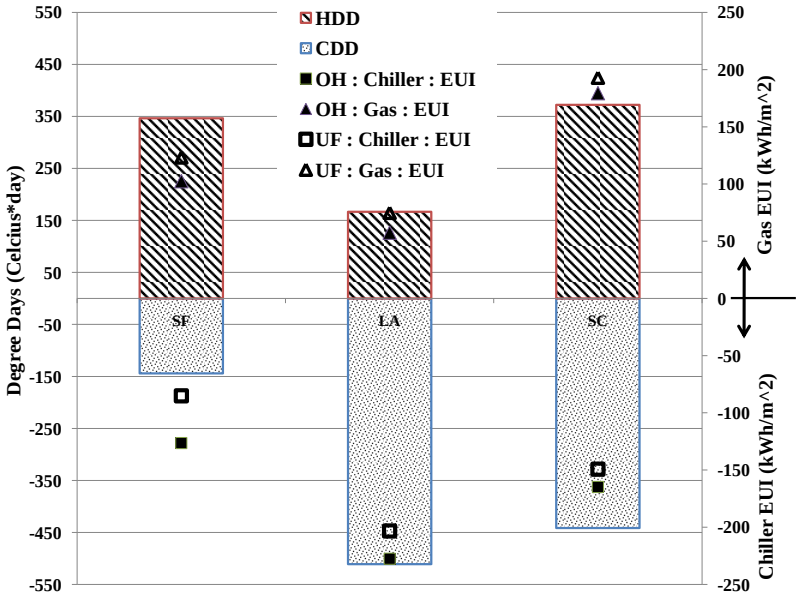

Figure 4.5: A graph of annual CDD and HDD among the locations: corresponding yearly chiller EUI and gas EUI on OH and UFAD are co-plotted. ; CDD and chiller EUI were plotted as negative values for comparison purpose; The base temperature was 18.33 ^{o}C

load can reduce heating demand during the winter and increase cooling demand during the summer, which explains the higher chiller EUI consumption and the lower gas EUI at SF.

To reveal the seasonal trend of cooling and heating demand, we also estimated monthly CDD and HDD for the entire year. By normalizing the monthly CDD and HDD over the annual CDD and HDD, we define PMCDD (percentage of the monthly CDD to the annual CDD) and PMHDD (percentage of the monthly HDD to the annual HDD) as normalized monthly CDD and HDD given as,

$$\text{PMCDD} = \text{CDD}_{\text{month}}/\text{CDD}_{\text{year}} \times 100\ (\%) \tag{4.3}$$

$$\text{PMHDD} = \text{HDD}_{\text{month}}/\text{HDD}_{\text{year}} \times 100\ (\%) \tag{4.4}$$

where $\text{CDD}_{\text{month}}$ and $\text{HDD}_{\text{month}}$ are monthly CDD and HDD, respectively, CDD_{year} and HDD_{year} are the annual CDD and HDD, respectively.

PMCDD and PMHDD are useful for explaining how much cooling demand is required for a building under the given weather data among the locations. The comparison graphs of PMCDD and PMHDD are plotted in Figures 4.6(a) and 4.6(b), respectively. In Figure 4.6(a), the highest PMCDD occurred in September at SF while the PMCDD peaked in July in LA and SC during the summer. LA had relatively high PMCDD compared to the other locations during the winter. The PMCDD for SC showed a symmetrical trend from March to November, but the PMCDD of SF and LA were not symmetrical during this period, and were relatively low during spring (March to May) compared to that at SC.

To summarize the trend of the PMCDD, SF requires relatively low cooling demand until September, LA needs higher cooling demand during winter and spring, and SC had a symmetrical distribution of cooling demand from March to November with peak cooling demand in July. Additionally, SF and SC had negligible cooling demand during winter. In Figure 4.6(b), all locations showed maximum heating demand on December and January. During summer (June to September), LA and SC showed negligible heating demand but SF had some heating demand even in the summer except September.

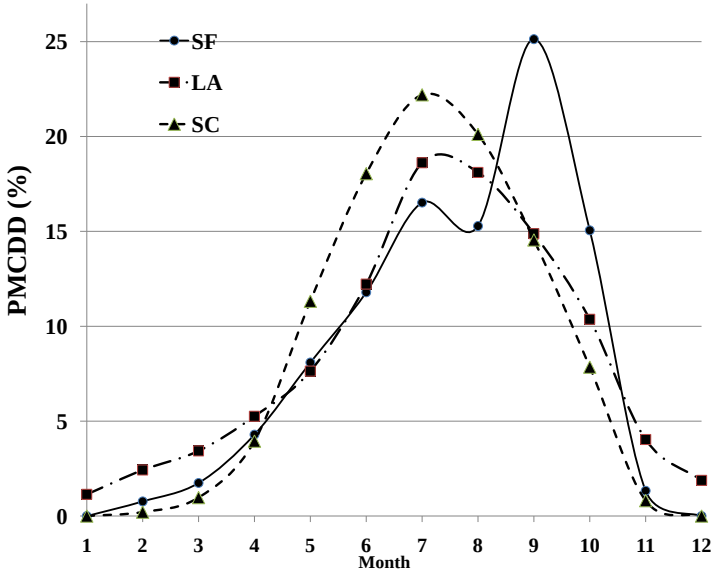

(a)

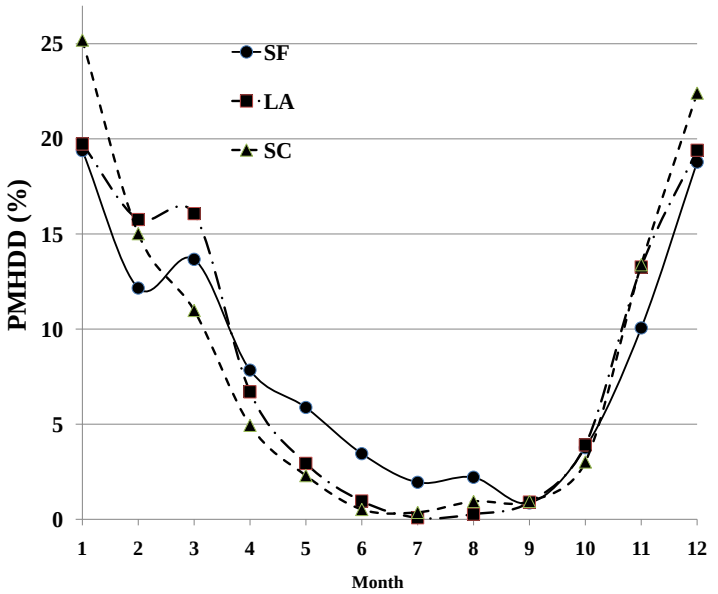

(b)

Figure 4.6: PMCDD and PMHDD at all locations; SF, LA and SC

Table 4.5: Purchasing costs of electricity and natural gas per kWh. The electricity cost per kWh is obtained from U.S. Energy Information Administration. The gas cost per kWh is calculated from residential and commercial gas prices per unit volume, U.S. dollar/m^3 (residential : 0.337 U.S. dollar/m^3 and commercial : 0.278 U.S. dollar/m^3). Heat content of natural gas (LNG) in U.S. is 11.67 kWh/m^3.

Cost (U.S. dollar / kWh)	Residential	Commercial
Electricity	0.11	0.1
Natural gas (LNG)	0.029	0.024

4.4.2.1.2 Annual energy consumption .

To show the variation of cooling or heating energy consumption with different Californian climates, the annual electricity EUI and gas EUI are plotted in Figure 4.7 for each location. From the annual electricity EUI (Figure 4.7(a)) and gas EUI (Figure 4.7(b)) averaged between OH and UFAD, it can be seen that SF has the smallest annual electricity EUI and LA the smallest gas EUI, while LA has the largest annual electricity EUI and SC the largest gas EUI. In detail, the electricity EUI in LA and SC is approximately 70 % and 30 % higher than that in SF, respectively, and the gas EUI in SF and SC is approximately 70 % and 180 % higher than that in LA, respectively. The EUI results agree well with previous CDD and HDD estimation in previous paragraph.

In all climates, the gas EUI is always smaller than the electricity EUI. The gas EUI in LA, SF and SC is approximately 20 %, 60 % and 70 % of the electricity EUI, respectively. From the results, electricity is a dominant energy usage in all climates, although in SF and SC, relatively high gas consumption is required.

Comparing OH and UFAD, UFAD has smaller total annual electricity EUI for all climates. The electricity EUI of UFAD is approximately 20 % lower than that of OH in SF and approximately 5 % lower than that of OH in other climates (LA and SC). The large electrical energy savings in SF can be explained by its relatively mild summer compared to SC and LA: UFAD has more opportunities to utilize the “free cooling” of the economizer under the mild summer conditions compared in SF. Further discussion about the “free cooling” of the economizer will be given in § 4.5.2.

In contrast, the UFAD annual gas EUI is always larger than that of OH across all climate zones. UFAD has approximately 20 % higher gas EUI than OH in SF, approxi-

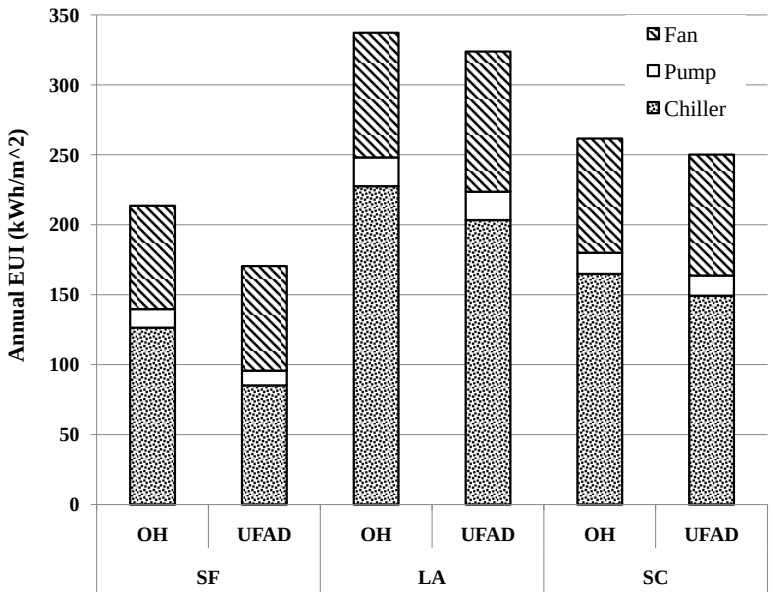

(a)

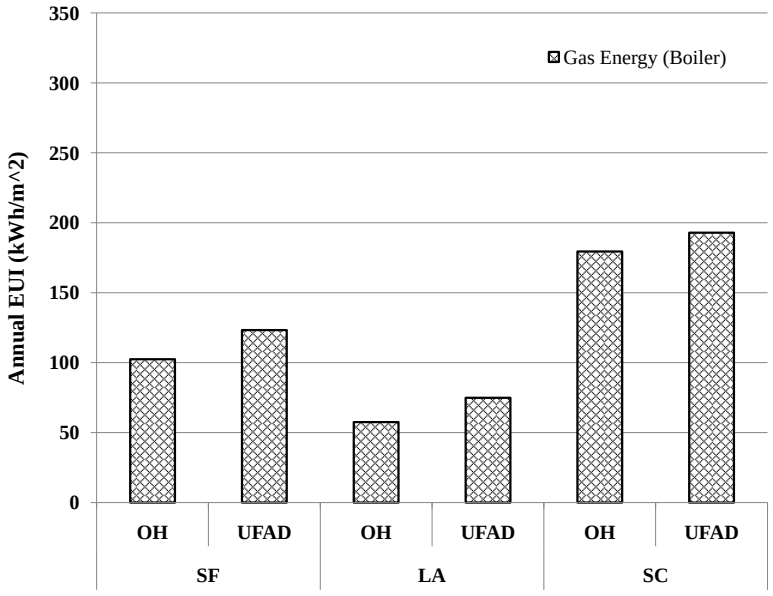

(b)

Figure 4.7: Annual energy consumptions among the locations (a) annual electricity EUI (including chiller, pump and fan) and (b) annual gas EUI consumption for cooling and heating, respectively, at each location.

Table 4.6: Annual HVAC operating costs per unit area (Dollar/m^2) for the prototype building simulations in different climate zones for OH and UFAD. Costs are given for both residential and commercial usage, based on prices given in Table 4.5.

		Residential (Dollar/m^2)			Commercial (Dollar/m^2)		
		Electricity	Gas	Total	Electricity	Gas	Total
SF	OH	23.81	2.96	26.77	21.54	2.44	23.98
	UFAD	19.00	3.56	22.56	17.19	2.93	20.12
LA	OH	37.60	1.66	39.26	34.03	1.36	35.39
	UFAD	36.10	2.16	38.26	32.67	1.78	34.45
SC	OH	29.18	5.19	34.36	26.40	4.27	30.67
	UFAD	27.89	5.58	33.47	25.24	4.59	29.83

mately 30 % higher in LA and approximately 7 % higher in SC. Careful consideration is therefore required to determine whether or not UFAD consumes less energy than OH. For example, if we sum the electricity EUI and the gas EUI for each climate to give a total EUI, this total EUI for UFAD in SF is still lower than that of OH by 10 %, but, the UFAD total EUI in LA and SC is comparable to that of OH because the advantage of the electricity EUI is traded off by the disadvantage of the gas EUI. However, the cost of purchasing the electricity EUI and gas EUI is expected to be different in actual building operation. Based on average retail prices of electricity and natural gas (LNG) in 2009 in the U.S. (obtained from the U.S. Energy Information Administration), the actual cost to purchase electricity EUI is approximately 4 times higher than the cost to purchase gas EUI (see Table 4.5). Based on these cost per electricity EUI and gas EUI, we have estimated actual HVAC operating costs of OH and UFAD in the different climates, and these are given in Table 4.6. This shows that UFAD always has a lower HVAC operating cost compared to OH at all locations and with the biggest difference occurring between OH and UFAD in SF. Based on these results, we can conclude that UFAD is likely to out-perform OH according to HVAC operating cost based on recent energy markets for electricity and natural gas in the U.S.

A further point to note concerns the effect of “thermal decay”, i.e. thermal losses due to heat exchange between supply air and return air. While thermal decay was included for the UFAD simulations, the thermal decay for OH was not simulated as it is outside the scope of the current EnergyPlus version (v2.1.1). Because the OH sim-

ulations in our study are idealizations due to the omission of thermal decay, the EUI consumptions of for OH should be considered underestimates compared to the actual EUI of OH. Therefore, the advantage of the HVAC operating cost of UFAD compared to OH will be larger when we consider thermal decay in the OH simulations. Further discussion of the effects of thermal decay will be provided in § 4.5.1.

The chiller, which keeps the water cool in the water circuit between the chiller and the air handling unit (AHU; within the AHU, the heat exchange between the water and return air occurs in the cooling coil), makes the dominant contribution to the electricity EUI. The pump, which drives the water circuit between the chiller and the AHU, has the smallest annual electricity EUI, while the fan EUI, which is the sum of electricity usages of all fans delivering conditioned air within the building, is the second largest. UFAD has a smaller chiller EUI than OH, while the fan EUI of UFAD is 5-10 % higher than OH. However, because the chiller is dominant in all climates, annual electricity EUI of UFAD is always lower than that of OH.

4.4.2.1.3 Monthly energy consumption .

To investigate seasonal trends of electricity and gas consumption at each location, we now consider monthly electricity EUI and gas EUI. The details of the energy consumptions for each climate are as follows.

A. San Francisco

Among various microclimates in San Francisco, we chose the Californian coastal area which is a most popular residential or commercial area. Because the mild climate is common to most California coastal cities, this simulations represents building energy consumption appropriate to many coastal cities. According to the climatography of the United States No. 20, the annual average temperature in San Francisco during 1971-2000 was 13.89 ^{o}C and the average temperature difference between summer and winter was only 6.93 ^{o}C (summer average temperature 17.18 ^{o}C and winter average temperature 10.24 ^{o}C). Compared with other Californian inland cities, the coastal cities have cool summers and warm winters with relatively small temperature variation over the year. Under such a mild climate, relatively less energy is expected to be required to

maintain a desirable indoor temperature over all seasons.

Figure 4.8 shows the seasonal trends of building energy consumption according to the monthly electricity EUI (Figure 4.8(a)) and monthly gas EUI (Figure 4.8(b)). In each graph, the left-hand bar in a given month corresponds to the EUI consumption of OH and the right-hand bar to that of UFAD. From Figure 4.8(a), the monthly total electricity EUI shows a minimum in January (the beginning of the year) and grows steadily until July. From July to September, the EUI remains within a similar range except that September shows a slightly higher EUI. Starting from October, the EUI gradually decreases as it gets colder.

Focusing now on the breakdown of the electricity EUI, the UFAD chiller EUI was approximately 20 % less than OH while the UFAD fan EUI was 16 % higher than OH due to the UFAD's higher AHU SAT (AHU SAT of the OH = 13.89 ^{o}C and AHU SAT of the UFAD = 17.22 ^{o}C) during the summer (June to September). Because the chiller was dominant during the summer, UFAD still had a 10 % advantage over OH for total electricity EUI. During the winter (November to February), UFAD showed significantly lower chiller EUI than OH with a similar range of fan EUI. The lower chiller EUI of UFAD around the year can be explained by the extensive use of the economizer due to the mild climate of SF. This will be discussed further in § 4.5.2. Considering the gas EUI (Figure 4.8(b)), both systems had a peak gas EUI in December and January and showed a gradual decrease in the EUI towards summer. The gas EUI of the UFAD was 20 % higher than that of the OH for the sum of monthly EUI over the year.

Based on these electricity usage results, the chiller was the dominant HVAC component over summer and the fans were dominant over the winter. The pump had the smallest EUI for all seasons. Comparing the electricity EUI of OH to UFAD, the UFAD system consumed approximately 50 % less EUI than the OH system for the chiller, while it had a comparable fan EUI to OH. The fan showed less seasonal sensitivity compared to the chiller because the fan was used for air delivery to interior spaces for cooling or heating as well as ventilation providing a fresh air to occupants. Therefore, the electricity EUI of the chiller rapidly grows compared to that of the fan as the season approached the summer.

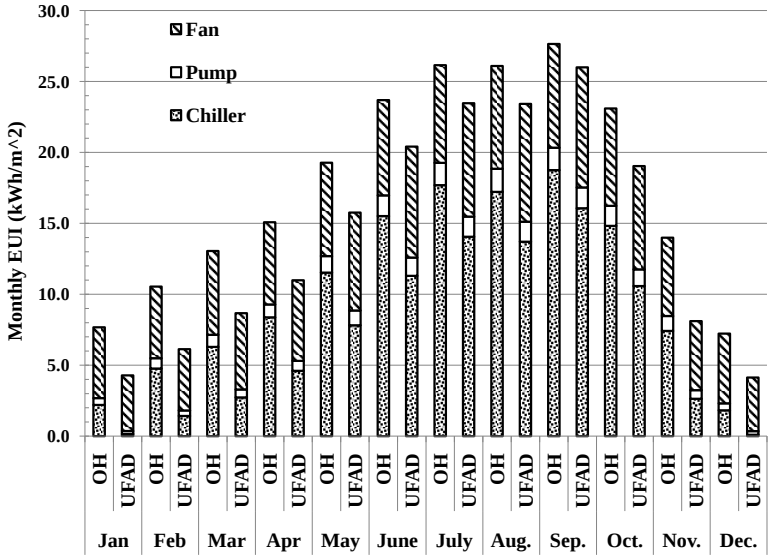

(a)

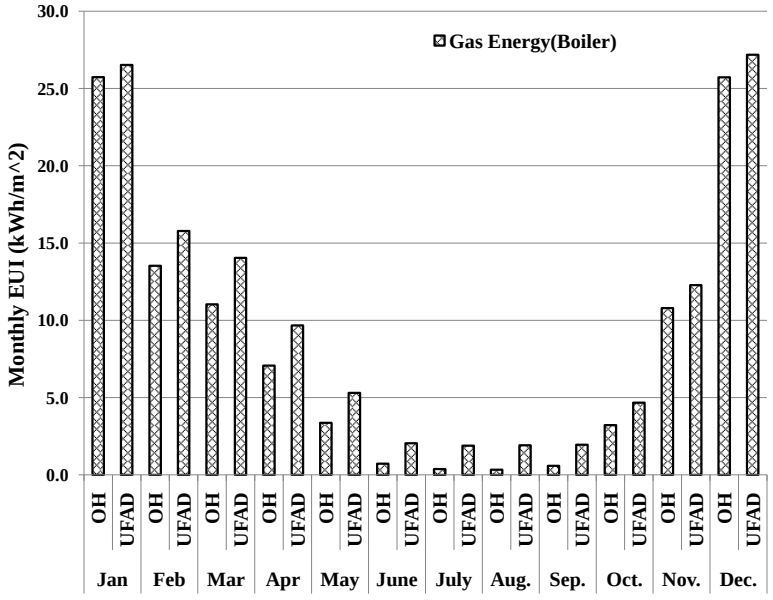

(b)

Figure 4.8: Comparisons of monthly energy consumption by OH and UFAD for (1) electricity and (b) gas in baseline building located in San Francisco.

B. Sacramento

Sacramento (SC) is chosen as an example of a Californian inland city, where it is relatively hot in summer and colder in winter among the locations considered. The annual average temperature in Sacramento during 1971-2000 was 16.17 ^{o}C and the average temperature difference between summer and winter was 13.44 ^{o}C (summer average temperature 22.97 ^{o}C and winter average temperature 9.53 ^{o}C). From the climate characteristics of SC, relatively higher electricity and gas consumption should be required for cooling and heating, respectively.

Looking at the electricity EUI breakdown by each HVAC component, the chiller and the pump of the UFAD system uses approximately 10 % and 5 % lower EUI than the OH system, respectively, while the fan of the UFAD system consumes approximately 6 % more than the OH system.

The trends of monthly electricity EUI and gas EUI in SC are given in Figures 4.9(a) and 4.9(b). Based on seasonal comparison between OH and UFAD systems, total electricity EUI of OH is higher than that of the UFAD during most seasons except summer, due to lower chiller energy consumption. The total electricity EUI of UFAD during summer is approximately 5 % higher than that of OH because the UFAD system consumed approximately 25 % and 5 % higher fan and pump EUI, respectively, compared with the OH system during this period, while also losing its advantage of a smaller chiller EUI, which becomes comparable to that of OH.

C. Los Angeles

Located in the Los Angeles basin, Los Angeles has a relatively hot climate throughout the year compared to the other Californian cities. The annual average temperature in Los Angeles during 1971-2000 was approximately 19.00 ^{o}C and the average temperature difference between summer and winter was only approximately 7.53 ^{o}C (summer average temperature 23.04 ^{o}C and winter average temperature 15.51 ^{o}C). Due to the relatively warm climate year-round, a building in LA is expected to have relatively higher cooling demand compared to that in other Californian cities.

The monthly electricity and gas EUI comparisons between the OH and UFAD

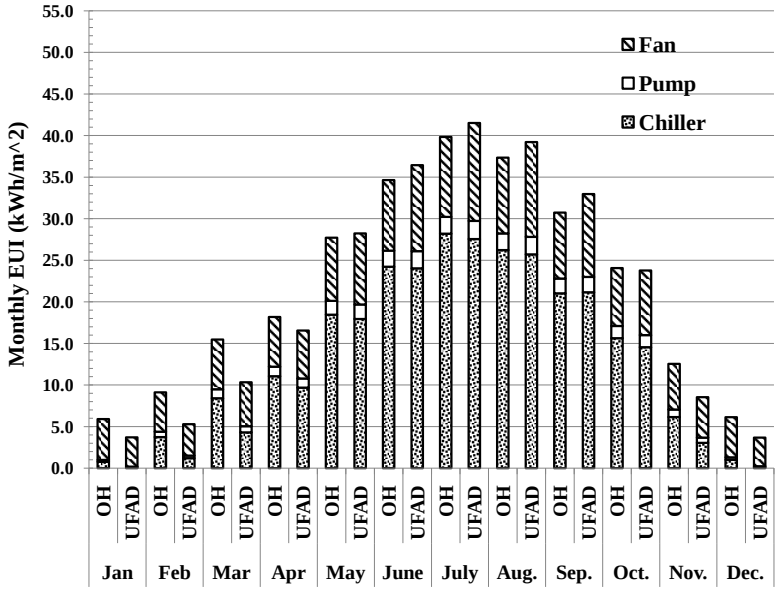

(a)

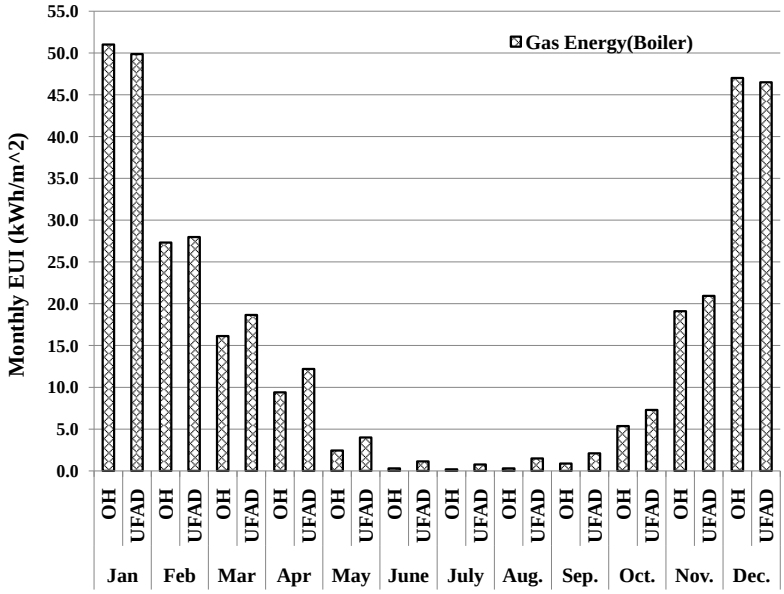

(b)

Figure 4.9: Comparison of monthly energy consumption by OH and UFAD for (a)electricity and (b)gas baseline building located in Sacramento.

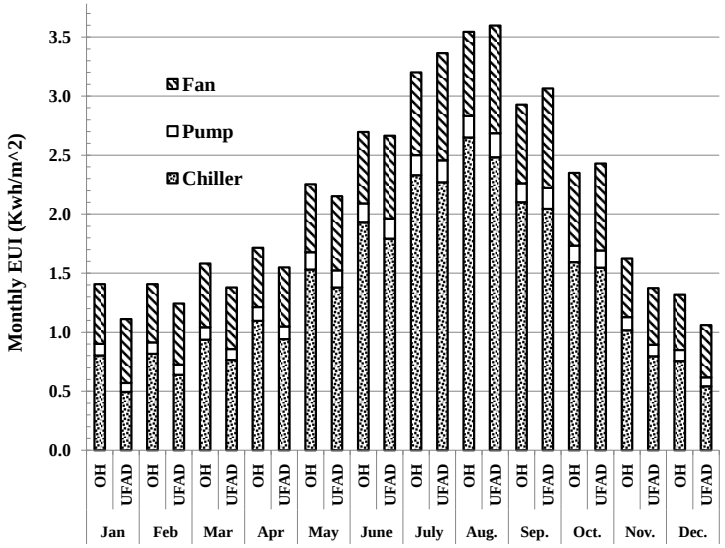

(a)

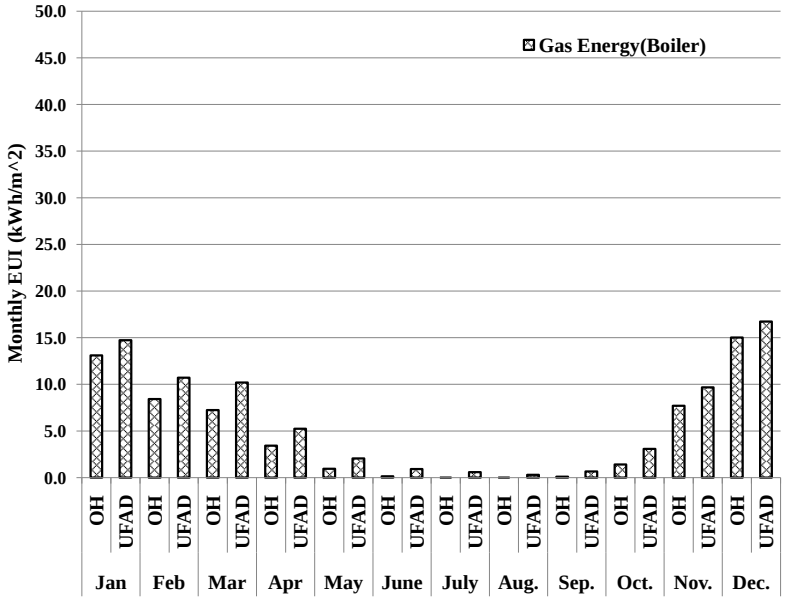

(b)

Figure 4.10: Comparison of monthly energy consumption by OH and UFAD for (a) electricity and (b) gas in baseline building located in Los Angeles.

systems in LA are given in Figure 4.10. Looking at the seasonal EUI consumption, the total electricity EUI during the summer is approximately 50 % of the annual total EUI for both OH and UFAD, while the gas EUI during the winter is approximately 70 % of the annual total gas EUI.

During the summer, while fan EUI of UFAD was approximately 25 % than that of OH, UFAD had equivalent EUI to OH because chiller, a dominant HVAC component for cooling, had approximately a 5 % advantage over OH for trading off the EUI deficit for the fan energy consumption. Additionally, during the winter, UFAD had 14.6 % additionally gas EUI compared to OH, which was 5 % smaller than the SF results.

Based on the summer and winter results, UFAD loses its advantage for reducing the electricity EUI during the summer but gains some advantage for the gas EUI during the winter compared to the SF results. The summer results imply that the chiller energy saving due to the higher AHU SAT of the UFAD weakened, while the additional fan energy consumption due to the higher AHU SAT of UFAD strengthened due to the relatively hot climate in LA. Additionally, a relatively mild winter climate in LA offset the higher heating demand of UFAD compared to SF.

4.4.2.2 Window-to-wall ratio

The window-to-wall ratio (WWR) affects both the convective heat transfer of the building envelope and the radiative heat transfer through the window simultaneously, so any changes to both heat transfers from varying the WWR directly influences cooling or heating demands. In this section, for comparison purposes, we present the annual EUI consumption for different WWR values normalized by the annual EUI consumption of the baseline configuration (WWR = 40 % and internal load #1). We also focus on SF and LA.

Figure 4.11(a) showed the sensitivity of WWR in SF. Compared to the baseline configuration, the total electricity EUI consumption decreased by approximately 20 % when WWR= 20 % and increased by approximately 20 % when WWR= 60 % for the OH and the UFAD in SF. Similarly, in Figure 4.11(b), the electricity EUI consumption for LA decreased by approximately 12 % when WWR= 20 % and increased by approximately 12 % when WWR= 60 % for both systems. The results showed that SF is more

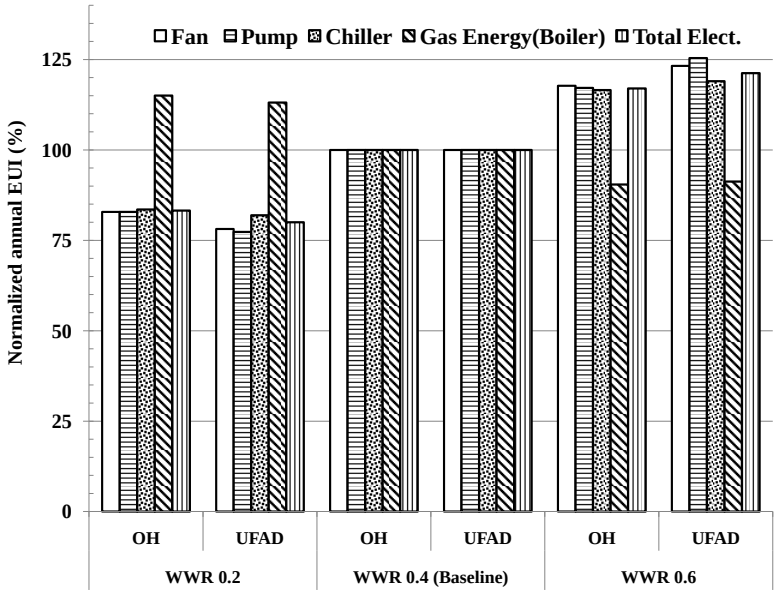

(a)

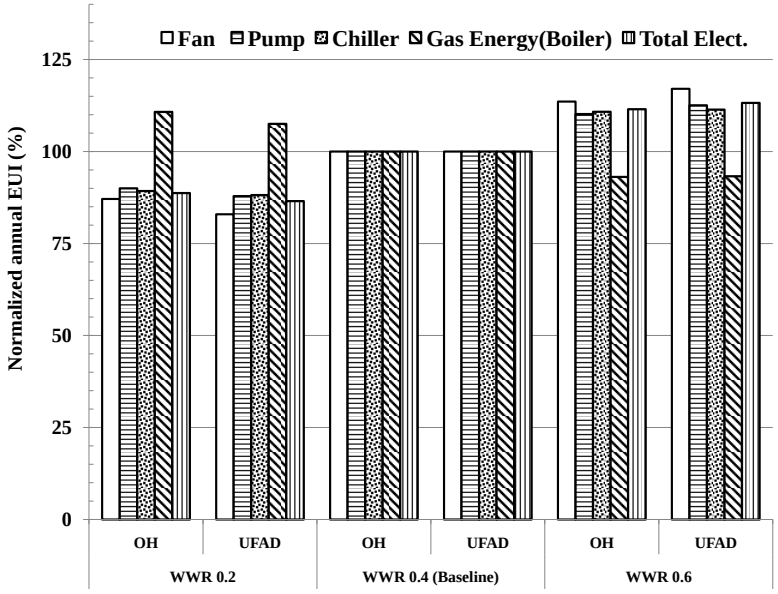

(b)

Figure 4.11: Normalized annual EUI consumption for different WWR values in (a) SF and (b) LA. The baseline configuration is WWR 0.4 and internal load #1.

sensitive to the WWR changes compared to LA.

Comparing the sensitivity of total electricity consumption between both systems, UFAD showed more sensitive than OH for decreasing WWR (WWR= 20 %) and increasing WWR (WWR= 60 %), however, the difference of the normalized annual EUI between both systems for various WWR changes was relatively small (less than 5 %). There was negligible difference of sensitivity of WWR between both systems.

Because larger WWR reduced heating demand by increasing radiative heat transfer through a larger window area, the gas EUI increased when WWR decreased and decreased when WWR increased, as confirmed in Figure 4.11. Based on the gas EUI sensitivity of various WWR values in SF and LA, a building in SF also was again more sensitive than one in LA, as for the total electricity EUI.

4.4.2.3 Internal heat load

The level of internal heat load strongly influenced the cooling and heating demand in a similar way to the WWR. We examined how the given HVAC systems responded when the internal load increased. Based on the internal load scenarios in Table 4.2, if we assume that a person emits 75 W, the heat load per unit area (W/m^2) of the occupancy increased by 100 % for the #2 level and 165 % for the #3 level compared to the baseline configuration, the #1 level. The sum of the heat loads per unit area of the occupancy, the lighting and the equipment increased by 181 % for the #2 level and 252 % for the #3 level compared to the baseline configuration. Comparing Figure 4.11 to Figure 4.12, the internal load configuration affected the annual EUI consumption more than WWR.

In SF (Figure 4.12(a)), the total electricity EUI increased by approximately 160 % for the #2 level and by 230 % for the #3 level compared to the baseline (Internal load #1), and the EUI in LA (Figure 4.12(b)) increased by 150 % for the #2 level and by 190 % for the #3 level. Similar to the WWR results, SF is more sensitive to the internal load change compared to LA for total electricity consumption between both systems. Additionally, UFAD had similar sensitivity of OH when Internal load level increased.

The gas EUI of both systems decreased by approximately 40 % for #2 level and 60 % for #3 levels, which confirmed that increasing the internal load resulted in reduced

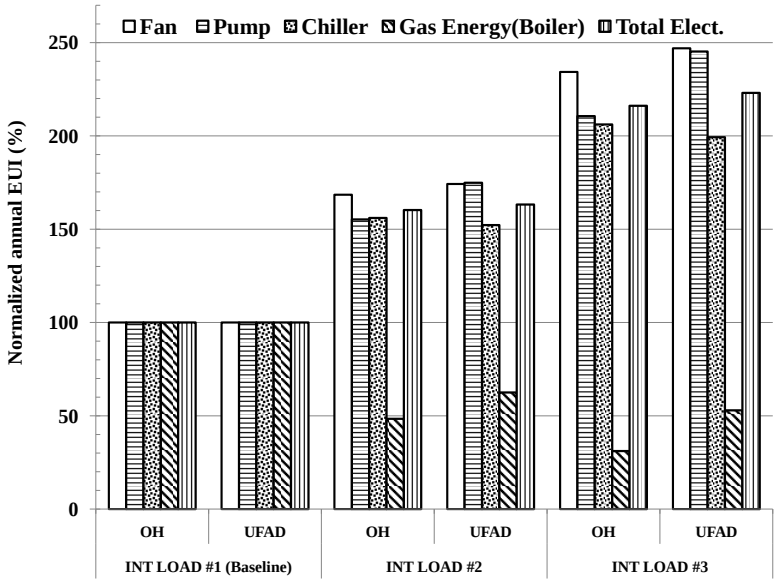

(a)

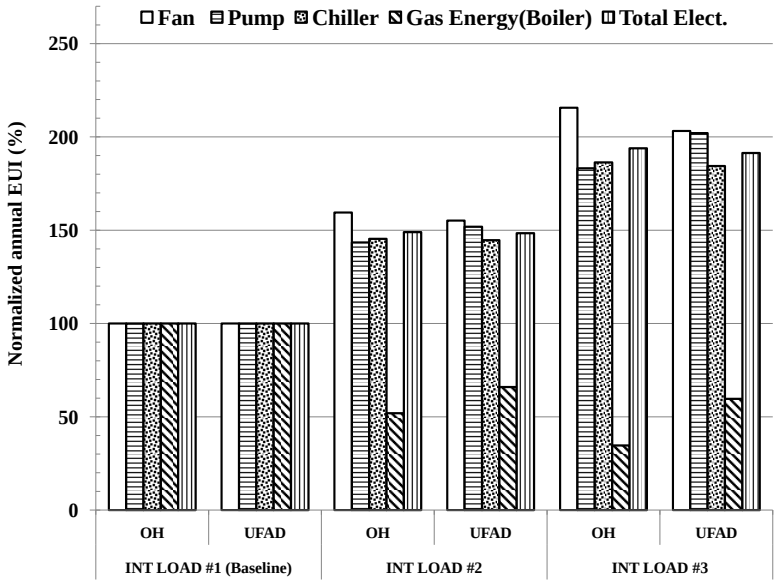

(b)

Figure 4.12: Normalized annual EUI consumption for different internal load levels in (a) SF and (b) LA. The baseline configuration is WWR 0.4 and internal load #1

gas consumption over a year. A building in SF had similar sensitivity for gas EUI than one in LA. The gas EUI of OH is more sensitive than that of UFAD on both locations.

Based on the results of the WWR and internal load configurations, we summarize that the difference of sensitivity of electricity consumptions between OH and UFAD is negligible for WWR and the internal loads. However, there is noticeable difference between SF and LA in terms of the sensitivity of total electricity consumptions. For both configurations, SF is more sensitive than LA for both systems for electricity consumption. The gas consumptions of both systems were similar sensitivities for the WWR changes, but, the gas consumption of OH is more strongly influenced by the internal loads changes compared to UFAD.

4.5 Discussion

4.5.1 Thermal loss due to heat exchange between supply air and return air

The way in which supply air (SA) to a room is introduced to a room is the primary difference between the OH and UFAD systems. While OH delivers air to the room through ducts, UFAD uses a separate plenum, the “Underfloor Plenum” or “supply plenum” (SP), positioned below the raised floor, to deliver the air to the room. The return plenum (RP), through which the return air (RA) from the room is extracted is common between both OH and UFAD systems and causes undesirable heat exchange between the supply air (cold in the HVAC cooling operation) and the return air (hot in the cooling operation). Due to this heat exchange, the temperature of the SA increases while the temperature of RA decreases. This energy loss caused by the heat exchange between the SA and the RA is called “thermal decay”. To compensate this thermal decay, additional energy is required in the form of cooling energy for the chiller and fan power in a VAV system.

Let us look in more detail at thermal decay. In an OH system, the supply duct is located within the return plenum which is the hottest place within a building. and therefore, heat exchange between the ducts and the return air is inevitable. Furthermore,

leakage of the supply air due to pressurized air delivery in the duct or poor air tightness of the supply duct connection causes additional thermal loss. In a recent report on the thermal decay of an OH system in a large commercial building ([62]), this thermal decay was significant, close to 10-30 % of total cooling energy. Thermal decay also occurs for the UFAD system. For example, the heat exchange between the supply plenum of an upper floor and the return plenum of the adjacent lower floor in a multi-story building adopting the UFAD system was reported by Webster ([8]). There is also heat exchange into the supply plenum due to heat transfer from the room above.

In the EnergyPlus simulations, the thermal decay of the UFAD system was estimated by simulating heat exchange between SP and RP and including them as explicit building features. However, thermal decay for the OH system was not included because it is not possible to simulate the heat transfer between SA and RA in the RP in the current EnergyPlus version (v2.1.1). Therefore, the HVAC energy simulation results for OH must be considered as ideal results without thermal decay. Consequently, the actual HVAC energy consumption of OH is higher than the simulation results by approximately 10-30 % due to additional chiller and fan energy consumption.

To estimate the magnitude of the thermal loss for UFAD in our proto-type building, it is important to have an ideal cooling load estimation by running an ideal UFAD building simulation with no thermal decay. We ignored any heat transfer involving the SA within the supply plenum without removing it from the building geometry. We chose the baseline building geometry configuration (WWR $=$ 40 % and internal load #1) and the same HVAC configuration for both OH and UFAD. As a climate, Los Angeles is chosen because of its hottest summer when the largest thermal decay occurs. We ran the ideal UFAD simulation with two AHU SAT, 13.89 ^{o}C (the same AHU SAT of the OH system) and 17.22 ^{o}C (the same AHU SAT of the UFAD system) to investigate the sensitivity to AHU SAT.

On each floor, the 5 partitioned zones (north, east, south, west, central Core) were mechanically cooled and the zones were vertically split by SP, room, and RP for the UFAD system or room and RP for the OH system. The sum of the cooling loads of the 5 zones represented total cooling load of each floor level. We separately sum the cooling loads for SP, room and RP and stacked the loads to show the total cooling

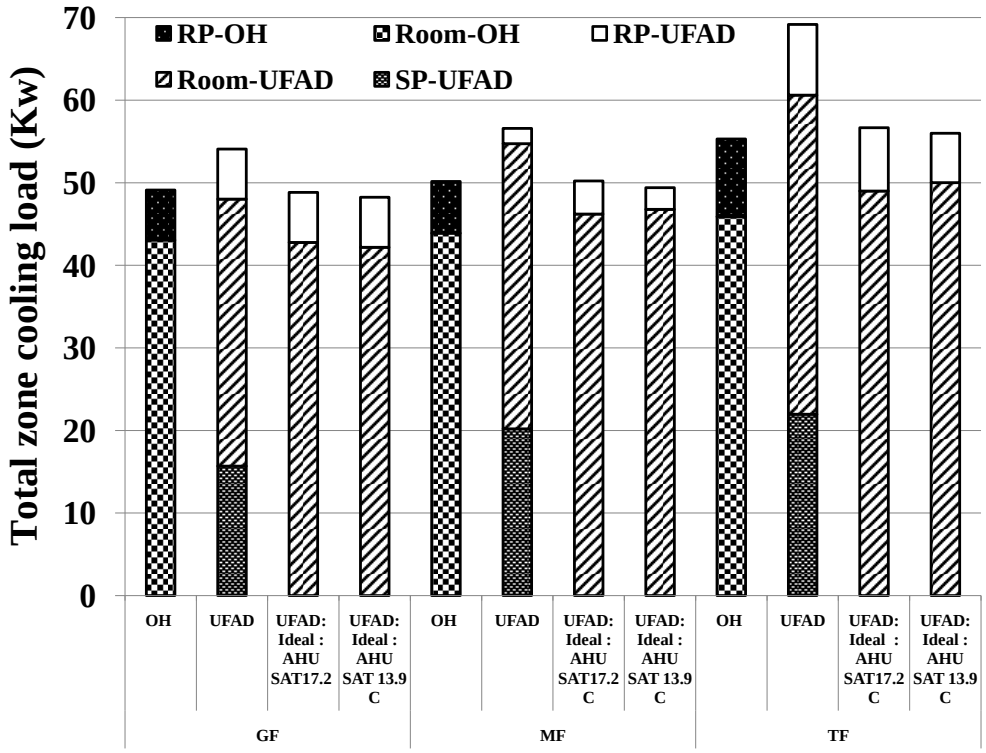

Figure 4.13: Total zone cooling load of each floor averaged over summer weekday afternoon(12:00 - 18:00) in Los Angeles : "OH" is the simulation data without the thermal decay, "UFAD" is the simulation data including the thermal decay, "UFAD: Ideal: AHU SAT 17.2 ^{o}C" is the ideal UFAD simulation (no thermal decay) with AHU SAT 17.2 ^{o}C and "UFAD: Ideal: AHU SAT 13.9 ^{o}C" is the ideal UFAD simulation (no thermal decay) with AHU SAT 13.9 ^{o}C.

loads of the each level (Figure 4.13). Because high cooling load may occur on a summer weekday afternoon when daily peak electricity demand was required (Figure 5.2), the cooling loads were averaged over the weekday afternoon (12:00 - 18:00) during summer (June- Sep.) on each floor level (GF : Ground Floor, MF : Middle Floor, TF : Top Floor).

In the UFAD system, the room loses or gains cooling load by heat exchange between SP and the room or between RP and the room, so it is difficult to compare cooling efficiencies of both systems in regard of the room cooling load. For example, in Figure 4.13, the room cooling load of the UFAD at the each floor was approximately 20 % lower than that of the OH, however, due to the heat exchange between SP and the room and between the room and RP, total cooling load of the UFAD at the each floor

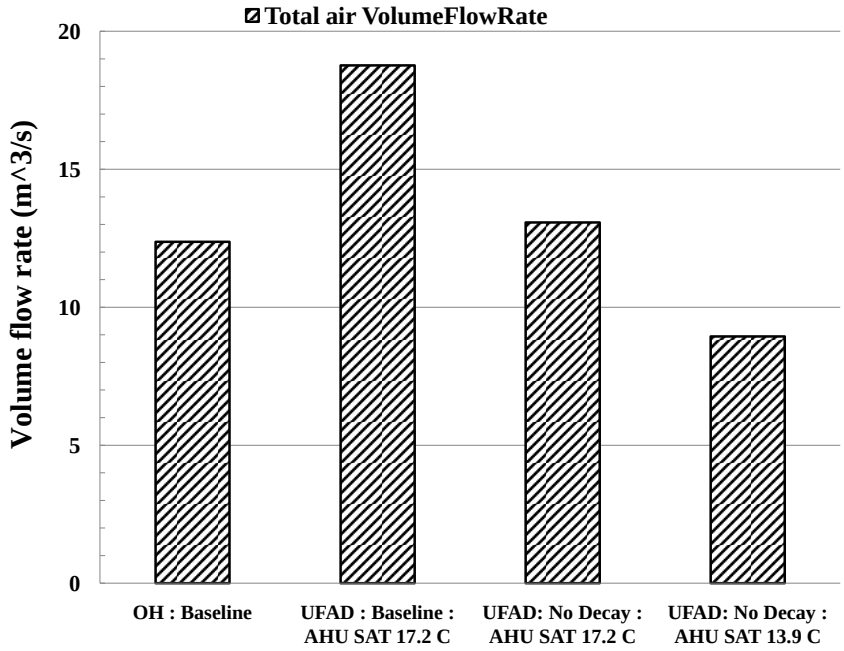

Figure 4.14: Comparison of total volume flow rate averaged over summer weekday afternoon(12:00 - 18:00) in Los Angeles : "OH" is the simulation data without the thermal decay, "UFAD : Baseline AHU SAT 17.2 ^{o}C" is the simulation data including the thermal decay, "UFAD: Ideal: AHU SAT 17.2 ^{o}C" is the ideal UFAD simulation (no thermal decay) with AHU SAT 17.2 ^{o}C and "UFAD: Ideal: AHU SAT 13.9 ^{o}C" is the ideal UFAD simulation (no thermal decay) with AHU SAT 13.9 ^{o}C.

was higher than the OH system. The total cooling loads of the UFAD at GF, MF and TF were 10, 13 and 25 % higher than that of the OH, respectively. Because of the thermal decay of the UFAD system, GF only lose its cooling load through the top of RP while TF only gained its cooling load through the bottom of SP. This is why the load of the GF is a lowest and that of the TF is the highest.

We also summed the zone cooling load over all three floors in Figure 4.13, to give the total building cooling load for the different HVAC systems. The overall load of the normal UFAD was 15 % higher than that of the OH, while the ideal UFAD system with AHU SAT 17.22 ^{o}C had approximately 15 % less overall cooling load over the building compared to the normal UFAD system, i.e. the same cooling load as OH (which did not allow for thermal decay). Based on the results, the 15 % additional overall cooling load of the normal UFAD system is explained by the thermal decay and this additional load appears as additional chiller energy consumption. Comparing the ideal system with AHU SAT 13.89 ^{o}C to AHU SAT 17.22 ^{o}C, we observe that the overall cooling load is not relevant to AHU SAT, which support that AHU SAT do not influence the thermal decay.

In Figure 4.14, we plotted total ventilation flow rate for each case. The normal UFAD system used approximately 50 % more conditioned air compared to the OH. However the ideal system with the same AHU SAT of the OH (AHU SAT 13.89 ^{o}C) used approximately 20 % less conditioned air than the OH because of the thermal stratification implied a higher return air temperature. When we increased AHU SAT to 17.22 ^{o}C of the ideal UFAD system, the 50 % higher volume flow rate of the conditioned air than the OH reduced to 20 %. By removing the effect of the thermal loss in UFAD simulation, 30 % of the volume flow rate of the air was reduced, which corresponds to reduction of fan energy consumption.

To confirm how thermal loss affects cooling energy consumption, we examined hourly EUI consumptions including fan, pump and chiller over the summer weekday. The baseline UFAD system showed the highest hourly EUI and the ideal UFAD with AHU SAT 13.89 ^{o}C showed the lowest EUI in Figure 4.15. The normal UFAD, the ideal UFAD with AHU SAT 17.22 ^{o}C and the ideal UFAD with AHU SAT 13.89 ^{o}C were 4 % higher, 10 % lower and 14 % lower combined EUI (chiller + pump + fan), respectively,

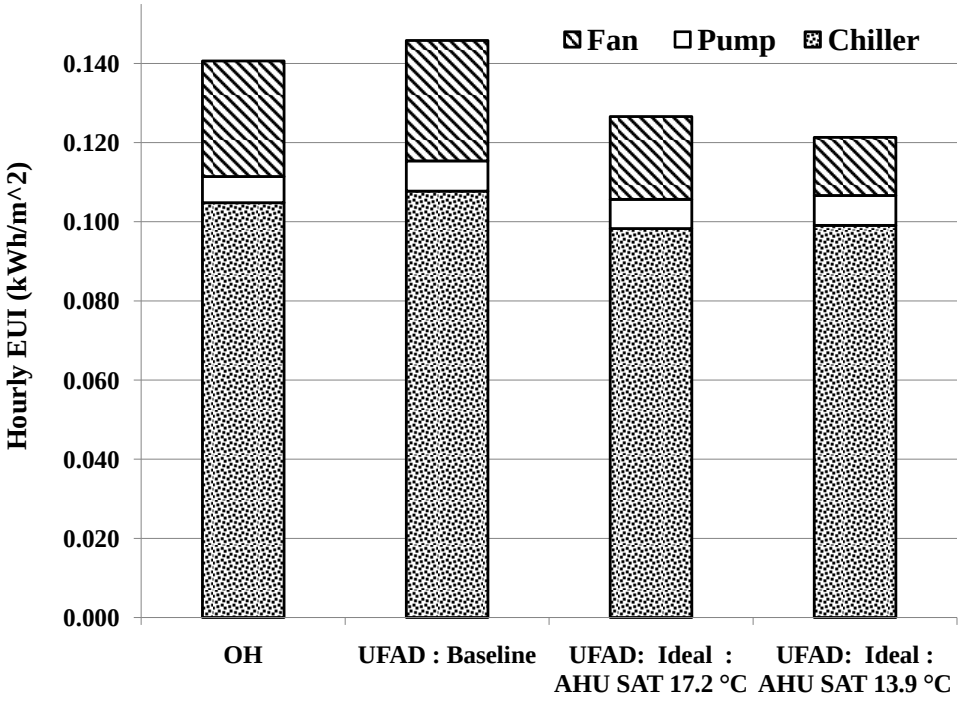

Figure 4.15: Hourly EUI consumption averaged over summer weekday afternoon(12pm-6pm) in Los Angeles : "OH" is the simulation data without the thermal decay, "UFAD : Baseline" is the simulation data including the thermal decay, "UFAD: Ideal: AHU SAT 17.2 ^{o}C" is the ideal UFAD simulation (no thermal decay) with AHU SAT 17.2 ^{o}C and "UFAD: Ideal: AHU SAT 13.9 ^{o}C" is the ideal UFAD simulation (no thermal decay) with AHU SAT 13.9 ^{o}C

than OH. By removing thermal decay, the ideal UFAD system showed approximately 12 % less combined EUI than OH. Additionally, the normal UFAD is approximately 15 % lower than the ideal UFAD cases. Because the results of the ideal UFAD were estimated when the building was expected to have the highest cooling load (the thermal decay also was maximum when the cooling load was maximum), the ideal UFAD simulation indicate how much additional cooling demand occurs due to the thermal decay.

4.5.2 Economizer

An economizer is an OA (outside air) mixer that reduces chiller energy consumption by replacing hot return air by relatively cold outside air when the outside air temperature T_{out} is lower than return air temperature T_{RT}. For a HVAC system without the economizer (such as a HVAC system which has a completely closed-loop air circuit), the chiller is required to cool the return air down to the AHU SAT. By replacing relatively cold outside air for the hot return air, additional cooling is achieved without the chiller. When $T_{out} > T_{RT}$, the economizer is only used to provide the fresh air to occupants at the minimum ventilation rate to maintain desirable Indoor Air Quality (IAQ) (see the minimum outside air requirement in Table 4.3).

This reduced chiller cooling rate due to the economizer is called “free cooling”. However, the “free cooling” of the economizer is limited by weather conditions which is technically interpreted as T_{out} in a HVAC operation. For simplicity, we only consider sensible cooling on cooling coil of the AHU instead of the latent cooling.

Californian coastal cities have relatively mild summers. In San Francisco, a building equipped with the economizer is expected to have extra energy saving by the “free cooling”, but in inland cities (i.e. Sacramento) or Los Angeles (located in Los Angeles Basin), the energy saving by the “free cooling” are limited because $T_{out} > T_{RT}$ during most summer days.

Even though the effectiveness of the economizer is strongly influenced by the weather condition, we still have opportunities to enhance the “free cooling” by controlling HVAC operation. The economizer will save more energy by increasing T_{RT} or AHU SAT which are two important features of the UFAD system compared to the OH system. The increased T_{RT} is achieved by thermal stratification and increased AHU SAT

is caused by the relatively higher floor diffuser temperature. Due to the two features, a UFAD system increases the hours of economizer operation compared to the OH system for additional cooling energy consumption in [6].

4.5.2.1 Daily economizer operation

The whole building prototype simulation enables us to compare the economizer effectiveness of OH to that of UFAD under equivalent weather conditions and building envelopes. In Figures 4.16(a) and 4.16(b), we plot samples of daily economizer operation for San Francisco and Los Angeles weather, respectively. For San Francisco summer weather, the daily maximum temperature on most weekdays was less than 24 ^{o}C (which was categorized as a "cool day"), so T_{out} sit below T_{RT} during the HVAC operation hour (06:00 - 18:00) as seen in Figure 4.16(a). The economizer was fully open to provide free cooling during the hour. T_{RT} of UFAD is higher than that of OH, so additional free cooling of the UFAD reduced the chiller cooling rate. Therefore, for San Francisco climate, UFAD is expected to have an advantage of additional free cooling.

However, for the Los Angeles summer climate, daily maximum $T_{out} > 29$ ^{o}C on most summer weekdays (which was categorized as a "hot day"). So $T_{out} > T_{RT}$ during most HVAC operation hours (Figure 4.16(b)). After 10:00, $T_{out} > T_{RT}$, so free cooling of the economizer disappeared, which reduced the advantage of chiller energy saving of the UFAD.

4.5.2.2 The effectiveness of the economizer

The economizer only operated when $T_{out} < T_{RT}$, so weather conditions of each climate zone affected the economizer operating hours. Additionally, the operating hours of the economizer of both systems were different due to the difference of the T_{RT}. The monthly HVAC operating hours over summer were approximately 240 hours. From we see that Figure 4.17, there were about twice as many hours of economizer operation in SF compared with LA and the hours of UFAD economizer operation were slightly higher than that of OH in every climate zone because of the higher T_{RT} of the UFAD. In SF, the economizer operated for most of the summer weekday hours.

When the economizer was open, hot return air was replaced by cool outside air,

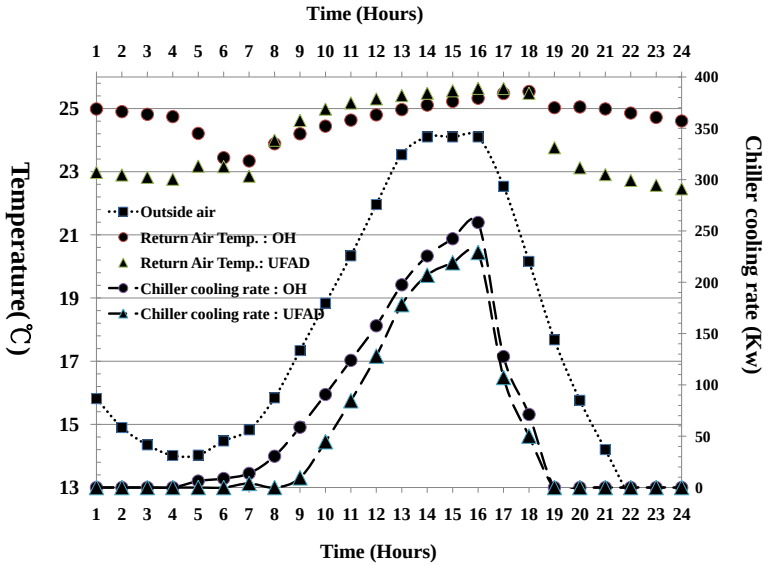

(a)

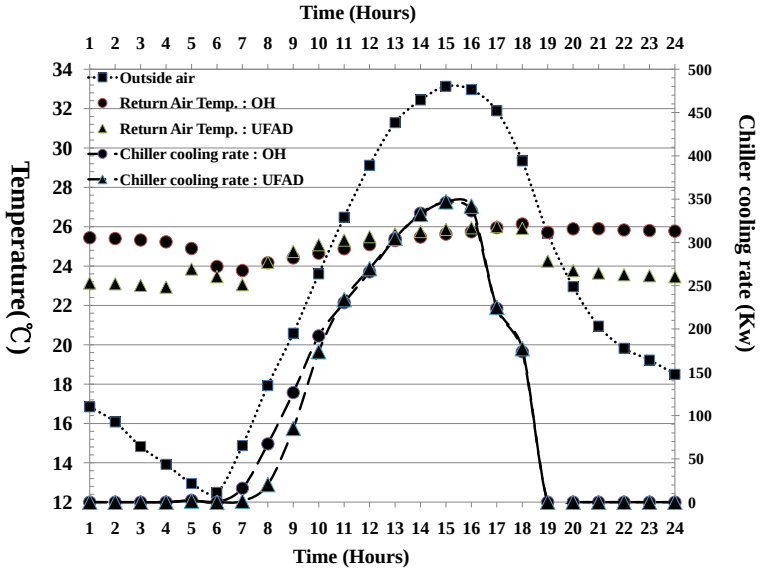

(b)

Figure 4.16: Hourly outside air temperature, return air temperature and the chiller cooling rate of the OH and the UFAD at a summer weekday in (a) San Francisco and (b) Los Angeles

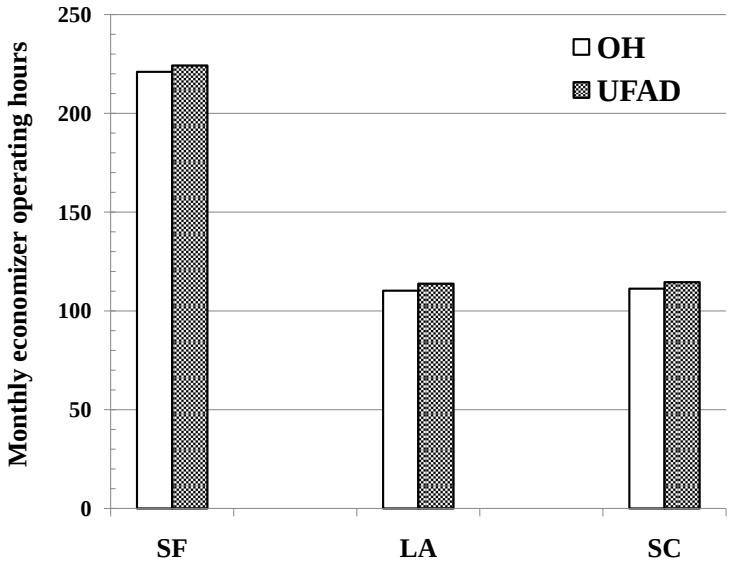

Figure 4.17: Monthly economizer operating hours during summer weekday of the OH and the UFAD

but when the economizer was closed, hot outside air mixed with relatively cold return air to introduce additional heat into the main air circuit and Q_{OA} was fixed as the minimum ventilation flow rate to provide fresh air to occupants ($Q_{OA} = 4.12$ m^3/s for internal load # 1 scenario). To estimate how much outside air was brought into the economizer, we plotted the air volume flow rate of the main air circuit and outside air when the economizer opened or closed in Figures 4.18(a) and 4.18(b), respectively. In SF (Figure 4.18(a)), when the economizer was open, the air volume flow rates of the outside air and the main air circuit, Q_{OA} and Q_{main} respectively, circuit were close to each other.

The ratio of air volume flow rate between the minimum outside air and the main air circuit, Q_{OA}/Q_{main} when the economizer closed were approximately 35 % for OH and 22 % for UFAD, which imply that the OH system brought more heat into the air circuit compared to the UFAD. In LA (Figure 4.18(b)), the ratio was approximately 30 % for OH and 20 % for the UFAD, so the additional heat within the air circuit due to the economizer similarly influenced the cooling load of the AHU cooling coil.

To investigate the additional heat through the economizer when the economizer closed, we considered the heat budget relations for the inputs and outputs. When the

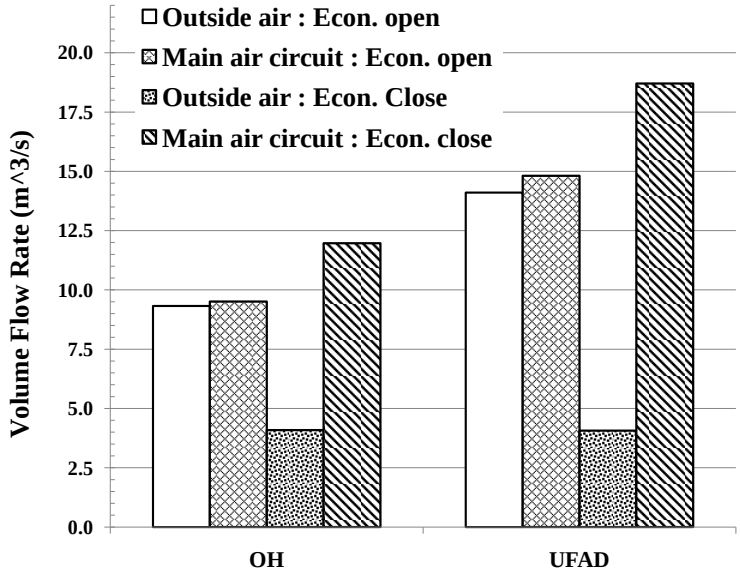

(a)

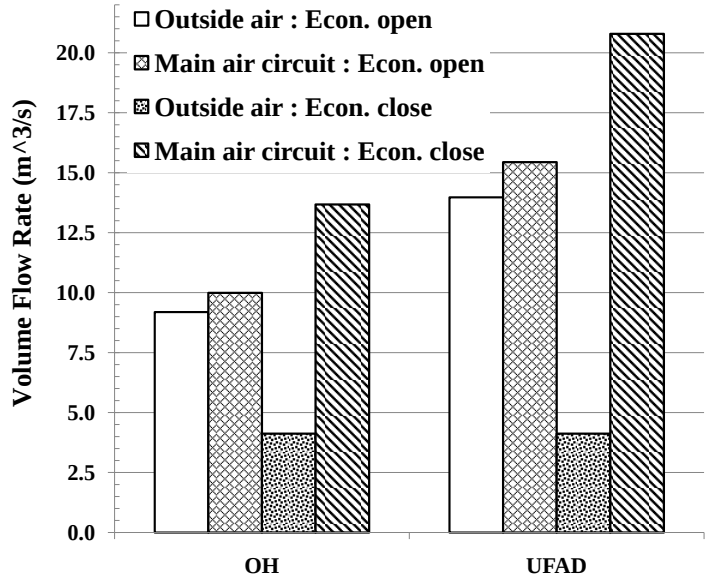

(b)

Figure 4.18: Volume flow rate of the outside air through the economizer and the main air circuit when the economizer opened or closed in (a) San Francisco and (b) Los Angeles

economizer was fully open, the hot return air was completely replaced by the cold outside air. Q_{OA} became Q_{main} and T_{mixed} is the same as $T_{outside}$. However, when the economizer was closed, Q_{OA} fixed at the minimum ventilation flow rate and from mass balance and heat balance over the economizer, a relation to determine the output temperature of the main air circuit on the economizer, T_{mixed} is given as

$$\frac{Q_{OA}}{Q_{main}} = \frac{T_{RT} - T_{mixed}}{T_{RT} - T_{outside}}. \tag{4.5}$$

We assign $\varphi = \frac{Q_{OA}}{Q_{main}}$ and rearrange (4.5), so that T_{mixed} is estimated by

$$T_{mixed} = \varphi(T_{outside} - T_{RT}) + T_{RT}. \tag{4.6}$$

When φ was higher, T_{mixed} increased and vice versa. Because T_{mixed} is the input temperature of the AHU cooling coil, higher T_{mixed} corresponds to higher chiller cooling load. Therefore, the higher φ (equivalent to the ratio Q_{OA}/Q_{main}) of the OH than the UFAD as seen in Figures 4.18(a) and 4.18(b) increased T_{mixed} to raise chiller energy consumption when the economizer closed.

Based the heat budget relation along the the HVAC air circuit,

$$\dot{H}_{BD} = \dot{H}_{OA} + \dot{H}_{CC}, \tag{4.7}$$

where

$$\dot{H}_{BD} = \rho C_p Q_{main}(T_{RT} - \text{AHU SAT}), \tag{4.8}$$

$$\dot{H}_{OA} = \rho C_p Q_{main}(T_{RT} - T_{outside}), \tag{4.9}$$

$$\dot{H}_{CC} = \rho C_p Q_{main}(T_{mixed} - \text{AHU SAT}), \tag{4.10}$$

$$\tag{4.11}$$

and $\dot{H}_{BD}$ is cooling load of the proto-type building, $\dot{H}_{OA}$ is cooling load of the economizer, or the OA mixer, and $\dot{H}_{CC}$ is cooling load of the AHU cooling coil. The overall cooling load of the building $\dot{H}_{BD}$ was removed by the economizer and the cooling coil on the main air circuit. All the cooling loads are assumed to be sensible cooling loads.

$\dot{H}_{BD}$ and $\dot{H}_{CC}$ were always positive for the HVAC cooling operation but $\dot{H}_{OA}$ can become positive or negative depending on the economizer operating condition. With the economizer opened, $\dot{H}_{OA}$ became positive to reduce $\dot{H}_{CC}$ as "free cooling", but, $\dot{H}_{OA}$ became negative when the economizer closed and brought outside hot air into the main air circuit. When $\dot{H}_{OA}$ decreased, the chiller consumed more electricity.

To estimate how much cooling load the economizer and the AHU cooling coil have with respect to the cooling load of the building, we normalized $\dot{H}_{OA}$ and $\dot{H}_{CC}$ with $\dot{H}_{BD}$, $\dot{H}_{OA}/\dot{H}_{BD}$ and $\dot{H}_{CC}/\dot{H}_{BD}$ respectively, and plotted them separately when the economizer opened and when the economizer closed over the summer weekday for all climates zones. Figure 4.19(a) shows that the highest $\dot{H}_{OA}/\dot{H}_{BD}$ and lowest $\dot{H}_{CC}/\dot{H}_{BD}$ occurs at SF, which means that relatively higher chiller energy saving existed in SF compared to the other two climates. UFAD even showed that the economizer removed up to 60 % of $\dot{H}_{BD}$ compared to 45 % of OH. As seen in Figure 4.17, the economizer opened for most of the HVAC operating period. These results explain why SF had a relatively lower chiller EUI consumption and UFAD in SF had considerably lower EUI compared to OH. Even in LA where the highest $\dot{H}_{CC}/\dot{H}_{BD}$ occurred and in SC, UFAD showed approximately 10 % lower $\dot{H}_{CC}/\dot{H}_{BD}$ than OH because the economizer of UFAD was more effective then that of OH due to the higher T_{RT} and AHU SAT.

With the economizer closed, $\dot{H}_{CC}/\dot{H}_{BD}$ in every climate showed more than 100 % (Figure 4.19(b)) implying that the chiller was required to handle the cooing load over the building as well as the additional heat generation to maintain the minimum outside air volume flow rate even when $T_{RT} < T_{outside}$. $\dot{H}_{CC}/\dot{H}_{BD}$ in SF was the lowest among the locations because of SF's mild summer climate, and those in LA and SC were 10 % higher. Among all the climates, Figure 4.19(b) showed a slight advantage of $\dot{H}_{CC}/\dot{H}_{BD}$ for UFAD compared to OH, however, the advantage of the UFAD was less than 2 %.

In conclusion, a study of the economizer under California climates was performed to show its effectiveness on the OH and UFAD systems. Due to longer economizer operating hours, the increased "free cooling" in SF produced higher chiller energy savings over summer compared to the other climates. The economizer in SF removed 45 % for OH and 60 % for UFAD of the building cooling load, which suggests that the economizer is the most important HVAC component to handle the building cooling load.

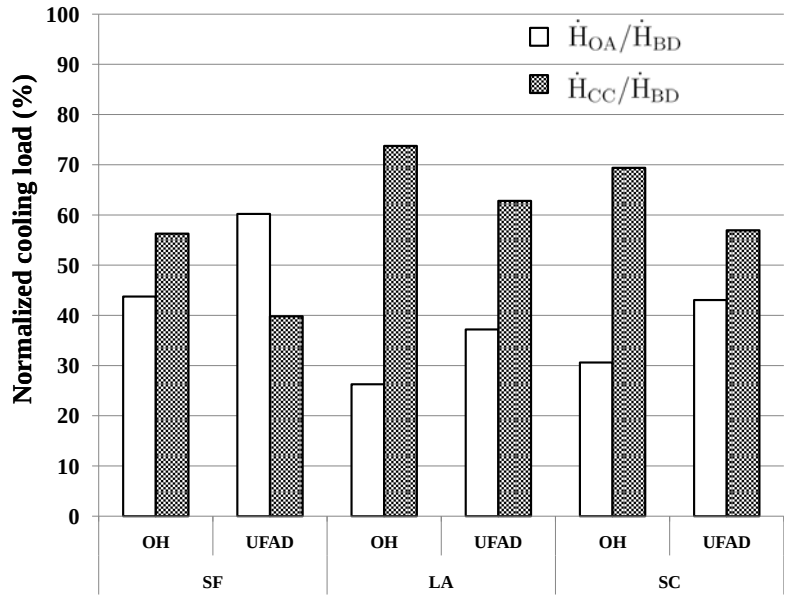

(a)

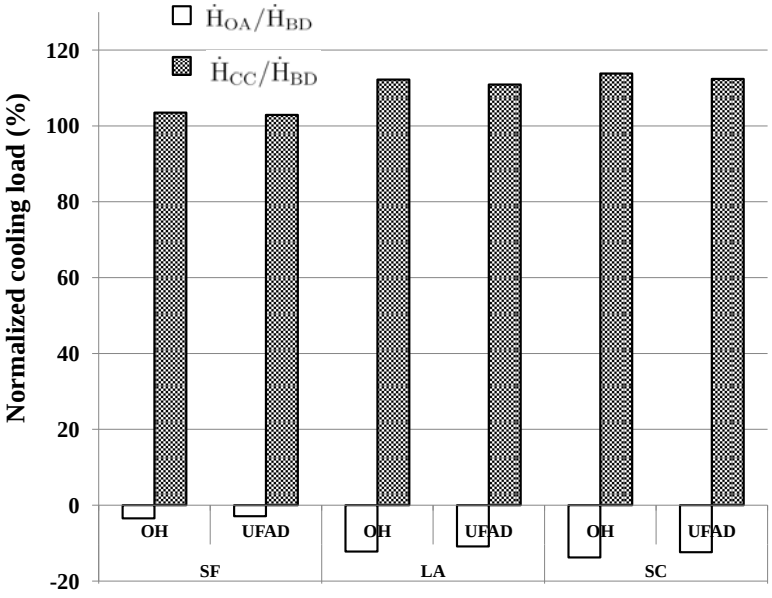

(b)

Figure 4.19: Normalized cooling load of the economizer $\dot{H}_{OA}/\dot{H}_{BD}$ and the chiller $\dot{H}_{CC}/\dot{H}_{BD}$ (a) when the economizer opened and (b) the economizer closed.

The UFAD system had more “free cooling” than OH (due to higher AHU SAT) and to have additional economizer operating hours (due to higher T_{RT}). Additionally, relatively higher air volume flow rate on the main air circuit of the UFAD reduced undesirable heat from the economizer when it closed.

4.6 Conclusion

Building energy simulations were performed to investigate differences in energy consumption between OH and UFAD. EnergyPlus, which is a widely-used building energy simulation program, was used to simulate a multi-stories proto-type building in various climates, such San Francisco, Los Angeles and Sacramento. The impact of energy consumption due to various building geometry and internal heat load was also studied.

Cooling or heating demand of each climate zone was estimated by CDD and HDD which quantify annual climate data as single value. Based on CDD and HDD, SF had higher heating demand than cooling demand, while in LA cooling demand was dominant compared to heating demand. SC showed balanced cooling and heating demand.

From the annual energy simulations, the smallest annual electricity EUI and gas EUI happened in SF and LA, respectively, while LA and SC had the largest annual electricity EUI and gas EUI, respectively. In all climates, the electricity EUI was larger than the gas EUI and the chiller EUI was dominant among all electrical HVAC equipments, which confirms that a building in the Californian climate consumes more cooling energy than heating energy.

In Californian climates, annual electricity consumption of UFAD is always lower than that of OH by 20 % in SF and 5 % for other climates. Due to longer economizer operating hours, the increased “free cooling” in SF produced higher chiller energy savings over summer compared to the other climates. The economizer was shown to be the most important HVAC component to reduce cooling energy. UFAD had more “free cooling” than OH due to higher AHU SAT and additional economizer operating hours due to higher T_{RT} of UFAD increased the advantage of cooling energy saving.

Even though the fan EUI of UFAD is approximately 5-10 % higher than OH, UFAD has less chiller EUI than OH, so the annual electricity EUI of UFAD is always lower than that of OH for all climates, primarily due to chiller energy savings. However, UFAD had the disadvantage of higher gas consumption for all climates compared to OH. Nevertheless, because the actual cost to purchase electricity EUI is approximately 4 times higher than the cost to purchase gas EUI in the recent energy market, UFAD still has the advantage on overall HVAC operating cost (electricity + gas) compared to OH.

We also performed the sensitivity studies of the WWR and internal load configurations on both systems on SF and LA. In both configurations, SF is more sensitive than LA for the total electricity consumptions of both systems. However, in most cases, the differences of the sensitivities of the total electricity consumptions between OH and UFAD for both configurations were negligible on both climates.

Thermal decay of UFAD, which is primarily due to heat exchange between supply air and return air in the underfloor plenum, caused an increase in the electricity EUI of the normal UFAD, i.e. including thermal decay, by approximately 15 % compared to the ideal UFAD system for cooling. Without thermal decay, the ideal UFAD system had approximately 10 % lower electricity EUI than OH. Because thermal decay of OH was reported to be approximately 10-30 % of total cooling energy, the savings in electricity EUI for UFAD compared with OH will increase.

Chapter 4, in part, includes reprints of the material as it appears in “Final report: Simulation of energy performance of Underfloor Air Distribution (UFAD) system”, *Building energy research grant (BERG) program.*, (Grant number: 54917A/06-05B), Linden, P., Webster, T., Bauman, F., Yu, J.K., Lee, K.H., Schiavon S., and Daly, A. 2009. The dissertation author was the primary investigator and author of the paper.

Chapter 5

Comparison study of demand response effectiveness for overhead system and Underfloor Air Distribution system

5.1 Introduction

"Blackout", a short or long-term electric power outage to an area, has become an important issue in the control and management of building electricity demand after the massive blackout of the Northeastern U.S. in 2003. Hot weather in northeastern area in U.S. was shown to be the cause of the abnormally high electrical demand. Another series of "Blackout" related to hot weather happened globally, for example, the power outage to London, UK in July 2006 caused by 2006 European heat wave, and the outage to Victoria and Melbourne, Australia in January 2008 caused by a record heat wave [2]. Because residential and commercial buildings solely relied on electric cooling system, abnormal high electrical demand for cooling occurs. Therefore, to avoid "Blackout" events caused by the abnormal electricity demand for cooling, upgrading existing electricity grid or increasing power generation capacity was advised. However, both remedies cannot be easily provided without considerable time and costs. It is difficult to predict how much cooling electricity demand corresponding to the abnormal hot weather is required without knowing accurate electricity demand responses in a

building. The remedies also requires extensive studies of the cooling electricity demand responses for a building.

An alternative remedy to avoid “Blackout”, one management strategy, demand response (DR), is widely suggested for building HVAC operations on the area affected to the hot weather. Peak electricity demand reduction (the peak demand happens typically during afternoon (12:00-16:00)) is the primary concern of DR strategies because instantaneous high peak demand (kW) caused by the hot weather can damage the electricity grid. In the DR, building owners agree to reduce energy consumption during periods of peak demand, e.g. for ventilation on a hot day, in return for incentives such as a lower tariff. For example, UCSD has such an agreement with PG&E. DR can be achieved by increasing room set point temperature, limiting lighting or equipment usage, etc. While these are effective ways to reduce the peak demand, determining an appropriate demand response is not a simple question. Such activities influence the heat balance over the entire building, and the HVAC electricity demand will respond dynamically. Furthermore, because DR activities affect occupant comfort or limit occupant activities, the DR effectiveness needs to take these factors into account. Consequently, building energy simulations are required to estimate the heat balance and occupant thermal comfort in order to predict the details of the demand response.

Even though UFAD was shown to be energy efficient system compare to OH in previous chapter, the effectiveness of electricity demand reduction due to the DR activities of UFAD has not been studied before. Therefore, in this chapter, we carefully study responses of electricity demand for cooling of the OH and UFAD systems in various climates among Californian cities. We compare performance of the effectiveness of applying DR strategies for reducing the electric demand for cooling. For this purpose, we uses the prototype building proposed in the previous chapter and perform various DR simulations with Energyplus.

In § 5.2, we describes a metric to evaluate the effectiveness of the DR activities for reducing peak electricity demand and simulation matrix to investigate the DR effectiveness. The simulations were performed only during summer because the DR strategies considered electricity demand for cooling. As DR activities, we chose several parameters such as duration of DR, room set point temperature, lighting and equipment

electricity usage.

In § 5.3, comparison studies of hourly electricity demand between the OH and UFAD systems showed electricity demand responses of the various DR activities. Sensitivity studies of DR effectiveness of the OH and UFAD systems were also conducted for various locations. The comparison studies were also performed to reveal which system had better DR effectiveness. Detailed discussion in § 5.4 show why the difference of DR performances between the two systems occurred.

5.2 DR effectiveness

Demand response (DR) consists of a set of strategies or activities to reduce peak electricity demand (PED). Activities such as dimming or shutting off interior lighting, reducing equipment loads or increasing room set point temperature are examples of methods to respond to a DR request. These DR activities, operated manually or by semi- or fully-automated controls, are simple but effective means for reducing electricity demand [25]. However, careful design of DR activities and their scheduling is important because they can affect the comfort of building occupants. In our study, simple but realistic, semi-automated DR activities are used, in which various building operation are followed by pre-programmed operating schedules.

This study measures dynamic responses to DR activities using the metric of peak electricity demand reduction (PEDR) over the DR period. PEDR is calculated to reveal the effectiveness of electricity demand reduction of a particular DR activity. For simplicity DR activities were implemented using a “Step Method”, in which each DR activity was instantaneously triggered at the beginning of the DR period and returned back to normal operation at the end of the DR period.

To perform sensitivity studies of the DR activities and to compare the DR effectiveness between OH and UFAD, the prototype buildings of both systems which were described in § 4.2 are chosen. Among the various configurations of the building, the baseline configuration (WWR $=$ 40% and internal load #1) is selected for both systems.

As we defined EUI for a metric to measure annual energy consumption in the

previous chapter, a metric is also required to measure the effectiveness of DR strategies. The details of the metric for the DR effectiveness will be described below.

5.2.1 Metric for DR effectiveness

Reducing peak electricity demand (PED) of the HVAC system is the primary objective for any DR activities. PED of the prototype building is different between the OH and UFAD systems, so we normalized the PED for comparison purposes to estimate the effectiveness of DR activities. The normalized Peak Electricity Demand Reduction (PEDR) was defined as

$$\mathrm{PEDR} = \frac{\mathrm{ED}^{\mathrm{DR}}_{\mathrm{HVAC}}(\mathrm{t}^{\mathrm{DR}}_{\mathrm{peak}})}{\mathrm{ED}^{\mathrm{NO}}_{\mathrm{HVAC}}(\mathrm{t}_{\mathrm{peak}})} \tag{5.1}$$

where t_{peak} is time when $\mathrm{ED}^{\mathrm{NO}}_{\mathrm{HVAC}}$ is maximum, where $\mathrm{ED}^{\mathrm{NO}}_{\mathrm{HVAC}}(\mathrm{t})$ is the hourly-averaged electricity demand of HVAC energy consumption of normal operation (NO). The time $\mathrm{t}^{\mathrm{DR}}_{\mathrm{peak}}$is the time when $\mathrm{ED}^{\mathrm{DR}}_{\mathrm{HVAC}}$ is maximum during DR and $\mathrm{ED}^{\mathrm{DR}}_{\mathrm{HVAC}}$ is the hourly-averaged ED of HVAC energy consumption during DR.

Each location has different weather conditions during the summer season, so daily results are characterized in terms of ‘cool’ ‘warm’ or ‘hot’ weather as defined in Table 5.1. Each location has different numbers of days within each weather category in Figure 5.1. Counting the days, we only considered working days which operated the HVAC system from 05:00 to 19:00 because the DR activities were supposed to be effective when the HVAC system run 12:00 to 18:00. In Figure 5.1, SF has about 70 % of ‘warm’ summer working days, while LA and SC have about 70 % characterized as ‘hot’. These differences between the locations may influence PEDR results when we average the daily PEDR over the summer season.

5.2.2 Simulation runs for DR effectiveness

Sensitivity studies of PEDR for a defined set of DR activities were performed at the same three California climate zones used in the energy performance studies; i.e., San Francisco (SF), Los Angeles (LA) and Sacramento (SC) to investigate DR performance sensitivity to outdoor temperature, solar radiation, and so on. The base line configu-

Table 5.1: Weather Categorization: Cool, Warm & Hot : $T_{ambient}^{day\ max}$ is daily maximum ambient temperature.

Weather categories	Range of $T_{ambient}^{day\ max}$
Cool	$T_{ambient}^{day\ max} < 23.9\ ^oC\ (75\ ^oF)$
Warm	$24\ ^oC\ (75\ ^oF) \leq T_{ambient}^{day\ max} \leq 29.4\ ^oC\ (85\ ^oF)$
Hot	$T_{ambient}^{day\ max} > 29.4\ ^oC\ (85.4\ ^oF)$

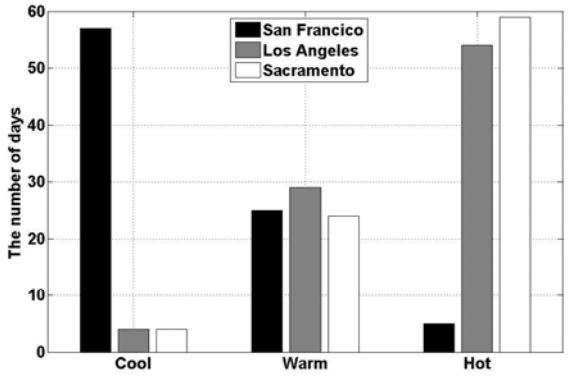

Figure 5.1: Histograms of the numbers of days for “Cool”, “Warm” and “Hot” days under the weather categorization given in Table 5.1., total number of working days during summer is 87 days.

Table 5.2: Demand response activity table; 1. DT^{DR}_{RST} : Difference of room set-temperature between baseline and DR (^oC). 2. LMT^{DR}_{light} : percentage of lighting usage limit (%) 3. LMT^{DR}_{equip} : percentage of equipment usage limit (%)

DT^{DR}_{RST} (^oC)	Room Setpoint Temperature Adjustment (RSTA) during DR	LMT^{DR}_{light} (LLT)	Lighting usage (%)	LMT^{DR}_{equip} (ELT)	Equipment usage (%)
0	24 ^{o}C (baseline)	0	100	0	100
1	25 ^{o}C	10	90	10	90
2	26 ^{o}C	20	80	20	80
3	27 ^{o}C	30	70	30	70
4	28 ^{o}C	40	60	40	60
				50	50

ration of WWR = 40% and internal Load #1 was chosen for fair comparison between OH and UFAD. This study only considers DR activities for cooling during the summer season, June 01 – September 30, since typical California weather is hot in summer and mild in winter. Additionally, DR activities are only conducted on working days, not on weekends or holidays.

Three DR time periods were used. The DR periods have the same end time, T^{End}_{DR}, but different start times, T^{Start}_{DR}, because the start time is considered to have a stronger relation to PEDR and occupant comfort. The baseline DR period lasts 6 hours from 12:00 to 18:00; shorter DR periods of 4 and 5 hours, starting later at 13:00 and 14:00, were also evaluated.

Three DR activities were simulated; room set-point temperature adjustment (RSTA), interior lighting usage limit (LLT) and interior electrical equipment usage limit (ELT). Detailed schedules for DR activities are shown in Table 5.2. The RSTA directly affects HVAC electricity demand (ED_{HVAC}) and occupant thermal comfort and DT^{DR}_{RST} corresponded to the increase in room set-point temperature (RST) from the RST in the normal operation taken here to be 24 ^{o}C.

The lighting usage limit, LMT^{DR}_{light} and the equipment usage limit, LMT^{DR}_{equip}, mainly reduce the building electricity demand (ED_{bldg}) which includes all electricity

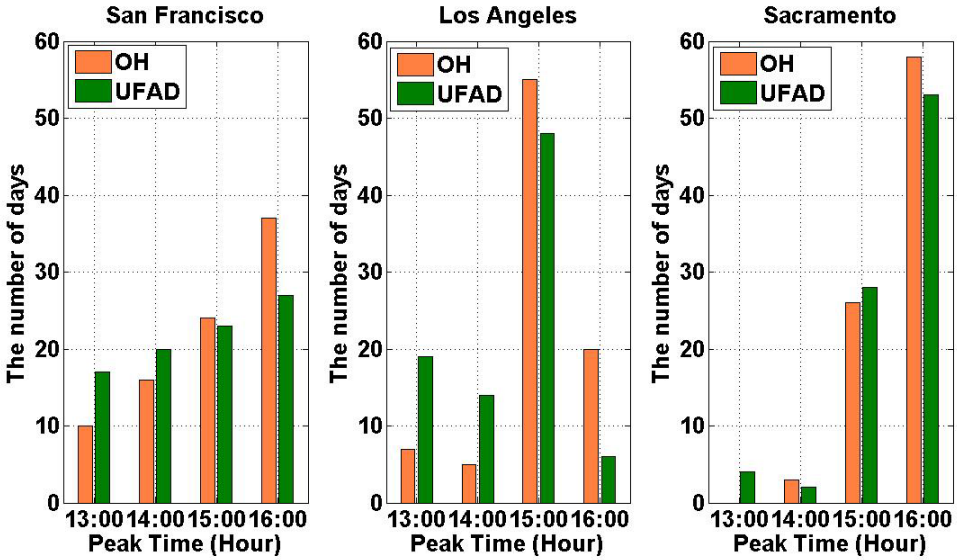

Figure 5.2: The number of the days of various time when the peak HVAC electricity demand existed among the three different locations, SF, LA and SC (weather data follows TMY (Typical Meteorological Year) weather data. The total number of days in the summer season is 87.

usage except HVAC. However, both reductions also involve ED_{HVAC} because lighting and equipment also emit heat and contribute to the internal cooling load (Table 4.2). Each DR action was simulated separately to determine the individual contributions.

5.3 Results

5.3.1 Hourly DR effectiveness

According to comparison between annual energy consumption of OH and UFAD in Chapter 4, both systems showed different electricity consumption over the summer. The HVAC system including electrical chiller, fan and pump consumed electricity with peak demands typically from 12:00 to 18:00. For example, in Figure 5.2, the HVAC had the peak demand between 13:00 to 16:00 over all summer days and more than 50 % of the days had the peak demand from 15:00 to 16:00 for all three locations.

Examples of hourly HVAC electricity demands for different DR activities on OH and UFAD systems are given in Figure 5.3 on a typical summer day. The DR activities

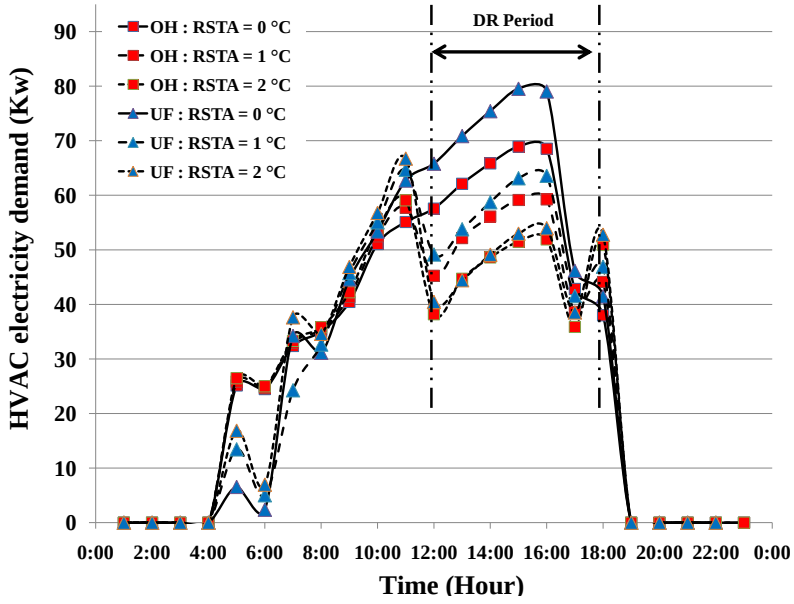

(a)

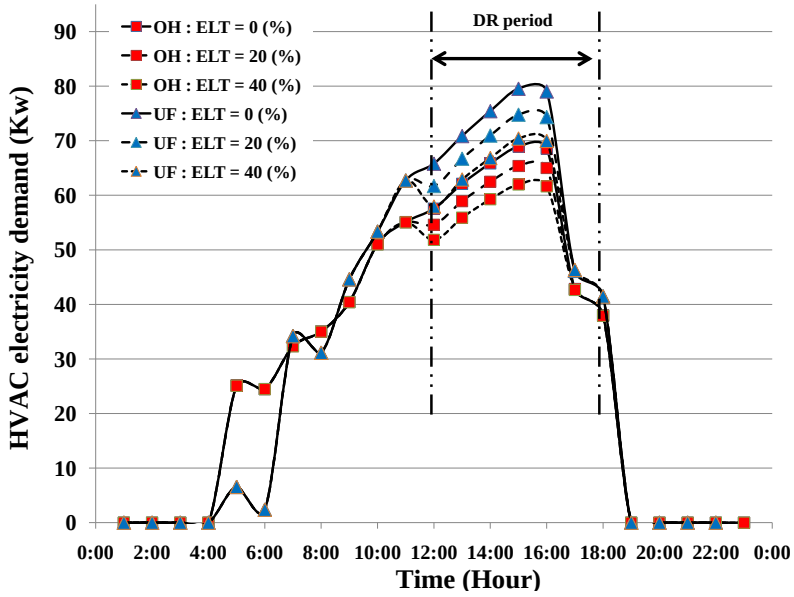

(b)

Figure 5.3: Hourly electricity demand on a typical summer day in LA during which $T_{ambient}^{max}$ is 30.5C^{o} for OH and UFAD systems operating DR activities (a) RSTA (b) ELT.

for both OH and UFAD system effectively reduced the HVAC demands during the given period, from 12:00 to 18:00. Comparing the electricity demand of OH to that of UFAD in Figure 5.3(a) and Figure 5.3(b), the RSTA activity was a more effective DR activity than ELT for the given ranges of the RSTA and ELT, $0^{o}\text{C} \leq \text{RSTA } (\text{DT}_{\text{RST}}^{\text{DR}}) \leq 2^{o}\text{C}$ and $0 \leq \text{ELT } (\text{LMT}_{\text{Equip}}^{\text{DR}}) \leq 40\%$, respectively. By adjusting the room set point temperature during the DR period (RSTA), the electricity demand reduction of UFAD had higher peak demand reduction compared to the that of OH; i.e. even though OH had 15 % higher electricity demand than UFAD under normal operation, the reduced peak demand of OH with RSTA when $\text{DT}_{\text{RST}}^{\text{DR}} = 2\ ^{o}\text{C}$ became close to that of UFAD in Figure 5.3(a).

Based on the results, UFAD had an advantage to reduce the peak demand compared to the OH when both systems had the same room set point temperature during the DR period. Applying other DR activity, such as ELT or LLT, the peak demand reduction of ELT or LLT was less effective than RSTA. For example, in Figure 5.3(b), while the peak demand reduced by approximately 25 % for OH and 33 % for UFAD when RSTA was 2^{o}C, the demand reduction when ELT $= 40$ % was approximately 10 % for OH and 11.5 % for UFAD. Even though the demand reduction of the ELT is smaller than that of the RSTA, UFAD still had an advantage for the demand reduction compared to OH. Further discussions to compare the DR of the OH and UFAD systems of various DR activities and under various locations are given in terms of PEDR in §5.3.2.

For the RSTA results, there are additional HVAC demands during the off-peak period (before and after the DR period), because additional heat transfer caused by increased room setpoint temperature warms the structural building mass during DR periods and affects next days' electricity consumption. Because the building simulation did not have night cooling, any additional heat during the previous day through building thermal mass is transferred to the next day. From Figure 5.3(a), we see that the electricity demand during the off-peak period increased when the RSTA increased, which can be explained by heated building mass due to increased room set point temperature during the DR period. However, interior equipment usage limit (ELT) or interior light usage limit (LLT) only reduced interior cooling demand, and did not affect the building thermal mass capacity. Hence, there are no thermal impacts on the off-peak periods due to the ELT or LLT. As shown in Figure 5.3(b), no additional HVAC demands on the

off-DR period were observed.

5.3.2 Sensitivity studies of DR effectiveness

It is convenient to characterize DR effectiveness by taking the average of the daily PEDR over weekdays during summer to give a single value for each location, DR activity and HVAC type, and groups of curves are presented for the three different DR activities. PEDR curves associated with room set point temperature adjustment (RSTA) showed steeply decreasing trends for both OH and UFAD systems and all three climates in Figure 5.4(a), which indicated that RSTA was effective in reducing the HVAC electric demand for all climate zones and HVAC modes. When the change in room set point temperature (DT^{DR}_{RST}) was 4 ^{o}C (corresponding to a room set point temperature (RST) of 28 ^{o}C), the PEDR decreased to less than 70 % for OH and 60 % for UFAD. In hot climates (LA and SC), PEDR of UFAD decreased more than that of OH, indicating that the RST increase provides higher reduction demand reduction in UFAD.

The differences of PEDR between OH and UFAD, ΔPEDR, demonstrate how much additional peak electricity demand reduction was achieved by the UFAD system, i.e. a positive value corresponds to a greater reduction for UFAD than OH. Figure 5.4(b) shows that for hot climates ΔPEDR steeply increased until $DT^{DR}_{RST} = 2$ ^{o}C then increased more slowly for $DT^{DR}_{RST} \geq 2$ ^{o}C. However, ΔPEDR in SF, representing a mild climate, was maximized when $DT^{DR}_{RST} = 1$ ^{o}C and then decreased. Considering variations in the start time of the DR period, T^{start}_{DR}, the PEDR decreased and ΔPEDR increased for the given DT^{DR}_{RST} for the all climate zones when the DR activities start time was delayed from 12:00 to 13:00 and 14:00. Because PED occurs often around 15:00 or 16:00 during in the summer days (Figure 5.2), once T^{start}_{DR} delayed from 12:00 to 14:00, the time gap between the peak time to have PED and T^{start}_{DR} decreased. According to the results, the PEDR can be reduced for both OH and UFAD systems, and the UFAD can have additional PEDR reduction compared to the OH system by shortening the time gap between T^{start}_{DR} and the peak time.

PEDR responses corresponding to LMT^{DR}_{Light} are given in Figures 5.5(a) and 5.5(b). By maximizing LMT^{DR}_{Light} by 40 %, PEDR decreases to approximately 84 % in SF, 86 % in SC and 88 % in LA. Unlike the PEDR curve of the RSTA, a linear

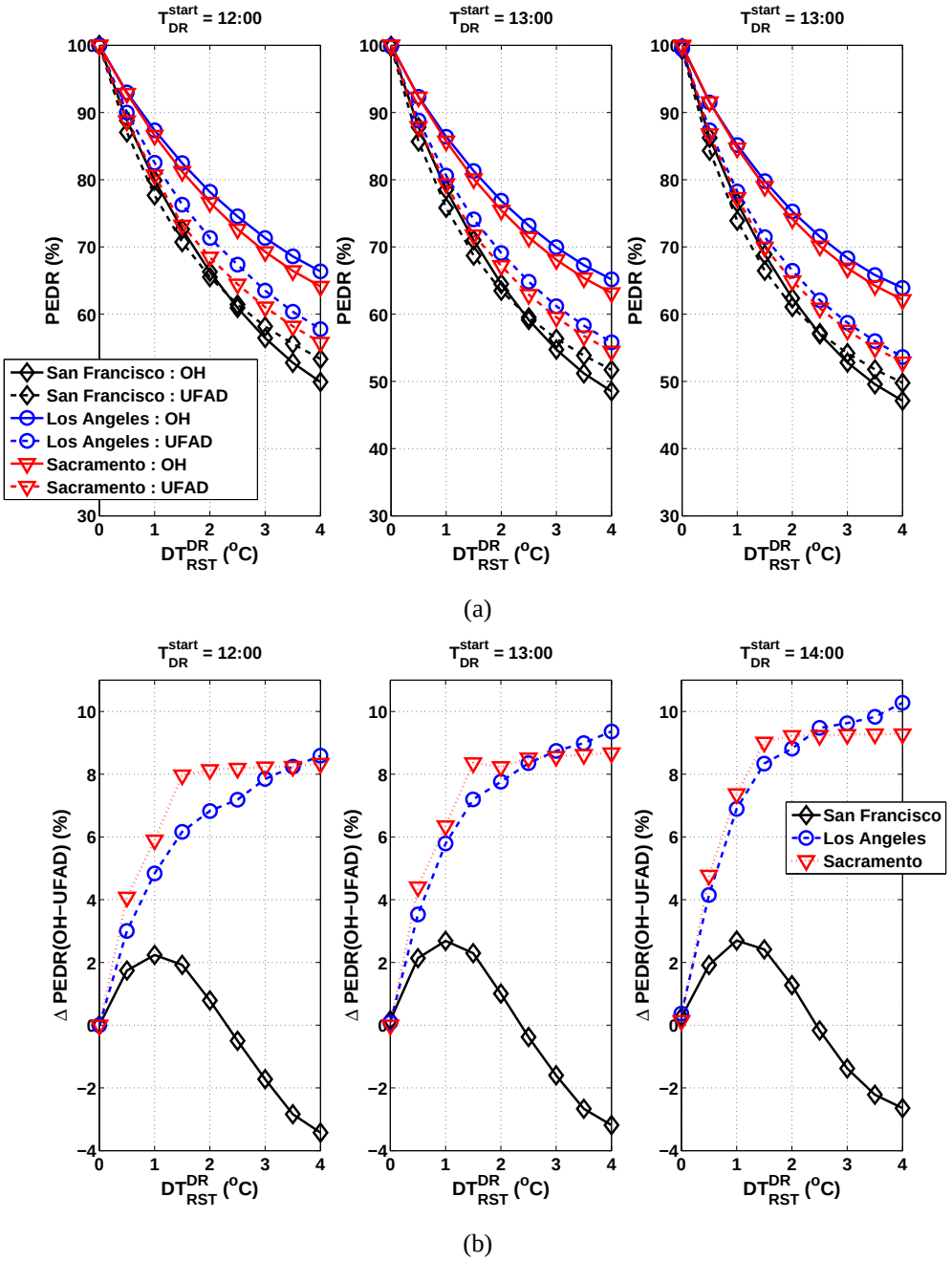

Figure 5.4: PEDR (Peak Electricity Demand Reduction) responses of the RSTA DR activities for three building locations and different start times for the DR period. (a) PEDR curves for OH and UFAD (b) The difference of PEDR between the OH and UFAD systems, ΔPEDR .

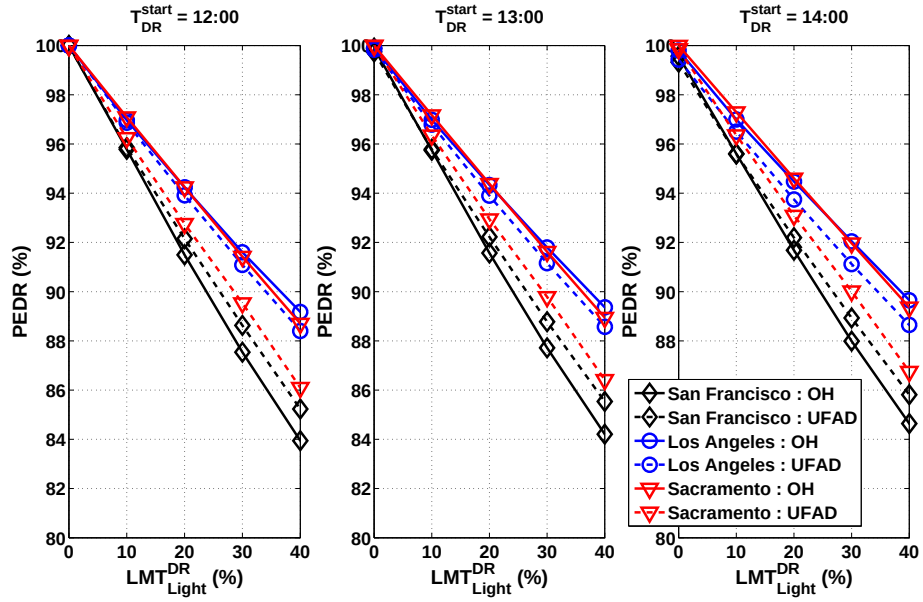

(a)

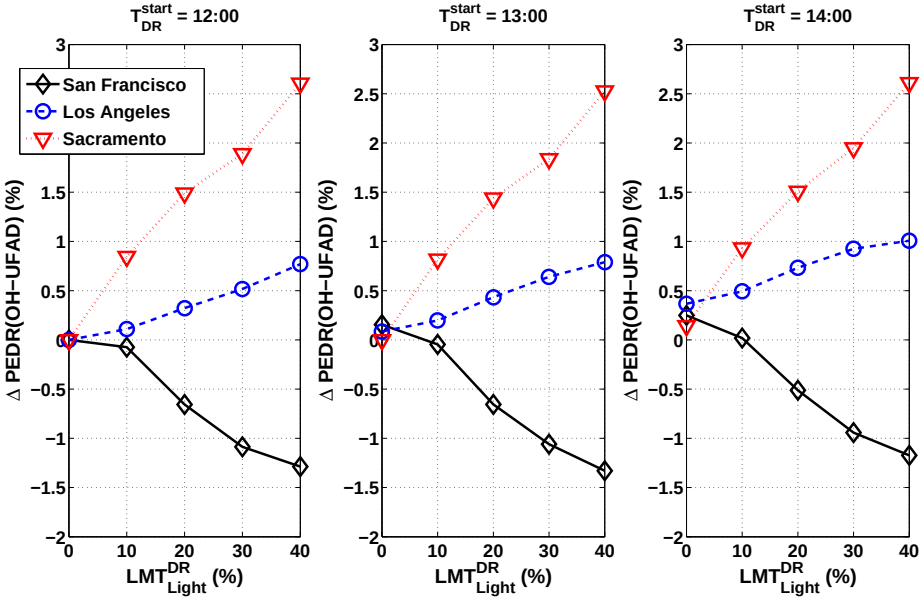

(b)

Figure 5.5: PEDR responses of the lighting usage limit DR activities (LLT) for three building locations and different start times for the DR period. (a) PEDR curves for OH and UFAD (b) The difference of PEDR between the OH and UFAD systems (ΔPEDR)

relation between LMT^{DR}_{Light} and PEDR was observed in all the climate zones.

The DR effectiveness of limiting lighting was much less than RSTA: the spread in PEDR at lighting reduction of 40 % was approximately equivalent to the effect of RSTA when $DT^{DR}_{RST} \sim 1\ ^{o}C$. In Figure 5.5(b), even though the UFAD system still appeared to be more effective that the OH system in hot climates, the maximum ΔPEDR values for SC and LA were less than 3 %, c.f. 8-10 % for RSTA, so the advantage of the UFAD system was much smaller. Delaying T^{start}_{DR} also had negligible influence on the DR effectiveness.

Concerning the DR effectiveness of limiting interior equipment usage (ELT), since the interior heat load of the equipment was lower than that of the lighting in the baseline configuration (for interior load #1 in Table 4.2, the heat generation of the equipment per unit area is 20 % smaller than that of lighting), the DR effectiveness of the equipment was expected to be lower than that of the lighting. From Figure 5.6(a), we observe that PEDR when $LMT^{DR}_{equip} = 40$ %, decreased down to approximately 86 % in SF, 89 % in SC and 90 % in LA, which is the 2 % worse in all climate zones compared to the LLT.

The trends of the PEDR and ΔPEDR curves in Figures 5.6(a) and 5.6(b) were similar to the curves for LLT DR activities. Because the DR activities of ELT and LLT only influence the interior heat loads unlike the RSTA, any possible DR activities only related to the interior heat load are expected to give similar responses of PEDR and ΔPEDR shown in Figures 5.5(a) and 5.5(b) or Figures 5.6(a) and 5.6(b)

5.3.2.1 Weather categorization

Each climate zone had different weather trends over the summer (seeing in Figure 5.1. Most summer weekdays in SF are categorized as ‘cool’ while the majority of LA and SC summer days are classified as ‘hot’. The summer weather trends strongly influenced the DR effectiveness of the given DR activities. To find more a explicit relation between the weather conditions and PEDR, the PEDR averaged over the “cool”, “warm” and “hot” days as defined in Table 5.1, for all the climate zones (rather than averaged over all summer weekdeays as in the previous section).

In Figures 5.7(a) and 5.7(b), the PEDR and ΔPEDR curves of both OH and

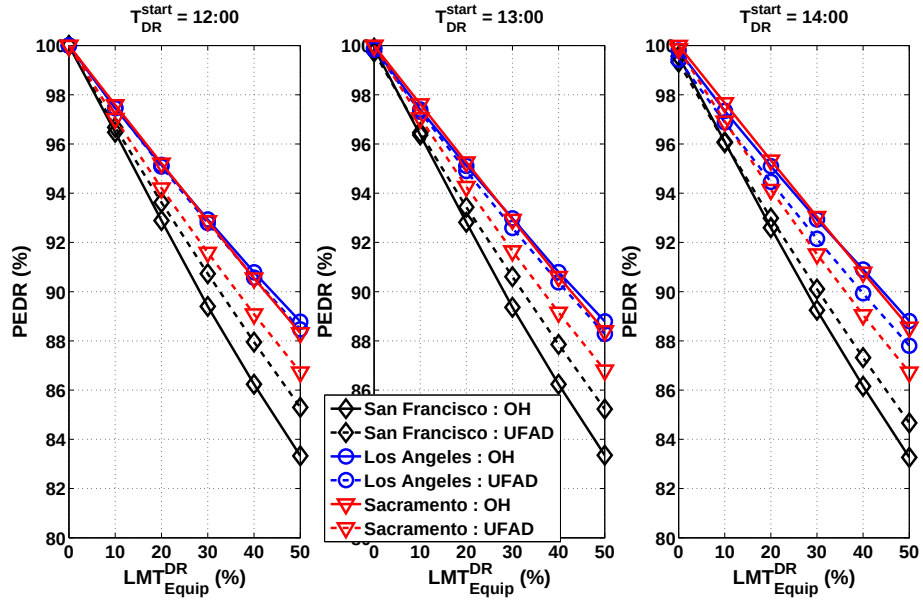

(a)

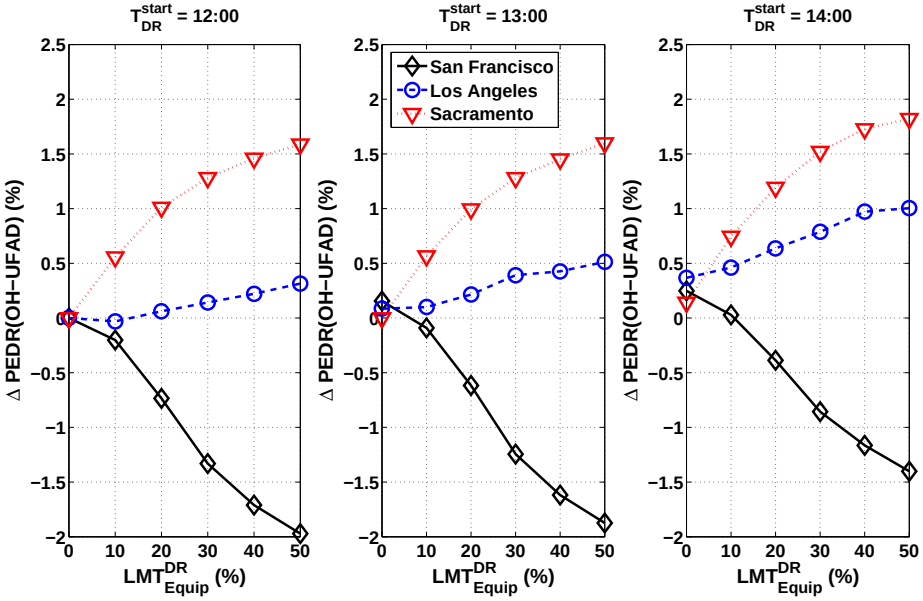

(b)

Figure 5.6: PEDR responses of the lighting usage limit DR activities (ELT) for three building locations and different start times for the DR period. (a) PEDR curves for OH and UFAD (b) The difference of PEDR between the OH and UFAD systems (ΔPEDR)

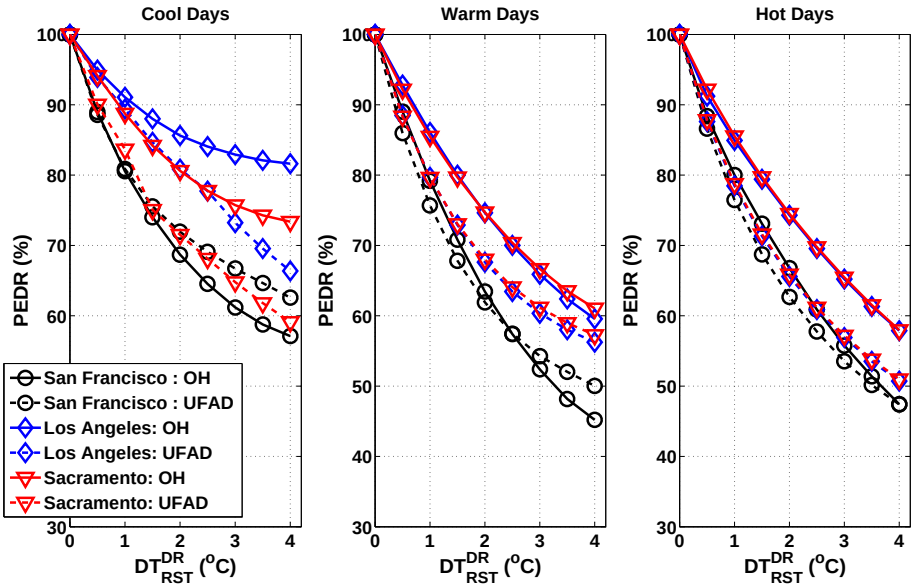

(a)

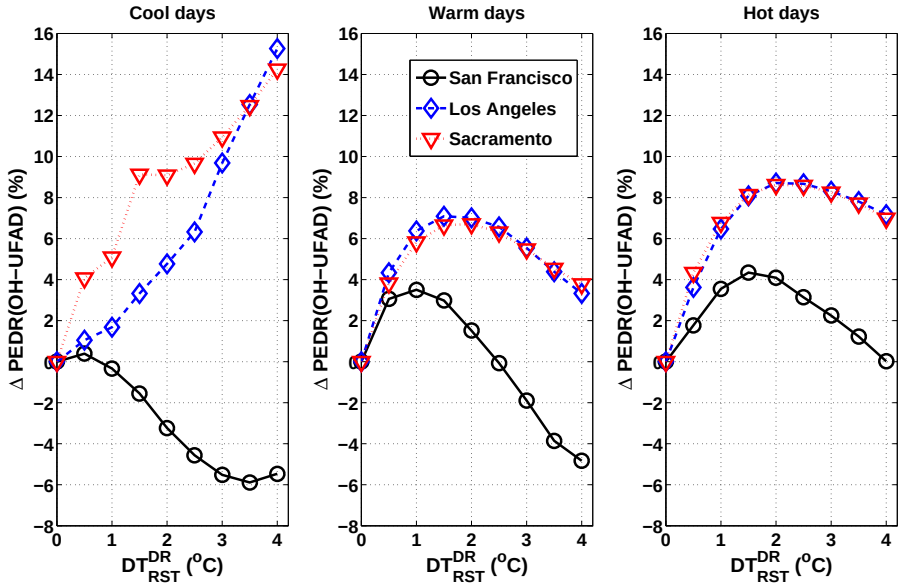

(b)

Figure 5.7: PEDR of the RSTA DR activities according to the summer weather categorization: (a) PEDR curves (b) The difference of PEDR between the OH and UFAD systems

UFAD systems at LA and SC matched well on ‘warm’ and ‘hot’ days. These curves provide general behavior in warm, dry climates. PEDR results for ‘cool’ days were inconsistent between LA and SC and have no relation to the ‘warm’ or ‘hot’ day results, possibly since less than 5 % of summer weekdays are classified as ‘cool’, so that the statistical sample is small. At LA and SC, the PEDR of UFAD on ‘hot’ days is about 3 % below that of ‘warm’ days when DT_{RST}^{DR} = 2 ^{o}C and 5 % when DT_{RST}^{DR} = 4 ^{o}C. Thus UFAD is particularly effective at reducing peak demand in hot climates. Figure 5.7(b) shows that ΔPEDR was maximum on ‘hot’ days when DT_{RST}^{DR} is 2 ^{o}C (RST 26 ^{o}C) at LA and SC and 1.5 ^{o}C (RST 25.5 ^{o}C) at SF

Weather-categorized results (Figures 5.8(a) and 5.8(b)) for the lighting and equipment DR activities were similar to the whole-summer weekday results shown in Figures 5.5(a) - 5.6(b), and showed less sensitivity to the weather categories. These similarities imply that the DR activities that reduced the convective heat transfer of internal loads were not influenced by weather conditions.

5.4 Discussion and conclusion

5.4.1 DR effectiveness by room set temperature adjustment

Based on the results of the DR effectiveness of the OH and UFAD systems in the various climates, the UFAD system always showed lower PEDR for the same DR activities. Among the DR activities, RSTA was proven to be the most effective DR activity compared to limiting light or equipment usage in § 5.3.2, so we focus on the HVAC responses corresponding to the RSTA to reveal why the UFAD have more energy saving than the OH on the DR activity.

At first, we examined reduction of overall building cooling load $\dot{H}_{BD}$ of OH and UFAD by increasing room set point temperature T_{RST}. In Figure 5.9 (left), the cooling loads against DT_{RST}^{DR} on various weather categorization are plotted. In normal operation ($DT_{RST}^{DR} = 0$ ^{o}C), $\dot{H}_{BD}$ for warm days and hot days on both systems were approximately 30 % and 60 % higher than $\dot{H}_{BD}$ of cool days, respectively. When DT_{RST}^{DR} increased (up to $DT_{RST}^{DR} = 4$ ^{o}C), $\dot{H}_{BD}$ monotonically decreased down to approximately 64 % for a cool day, 67 % for a warm day and 70 % for a hot day compared to the value in the

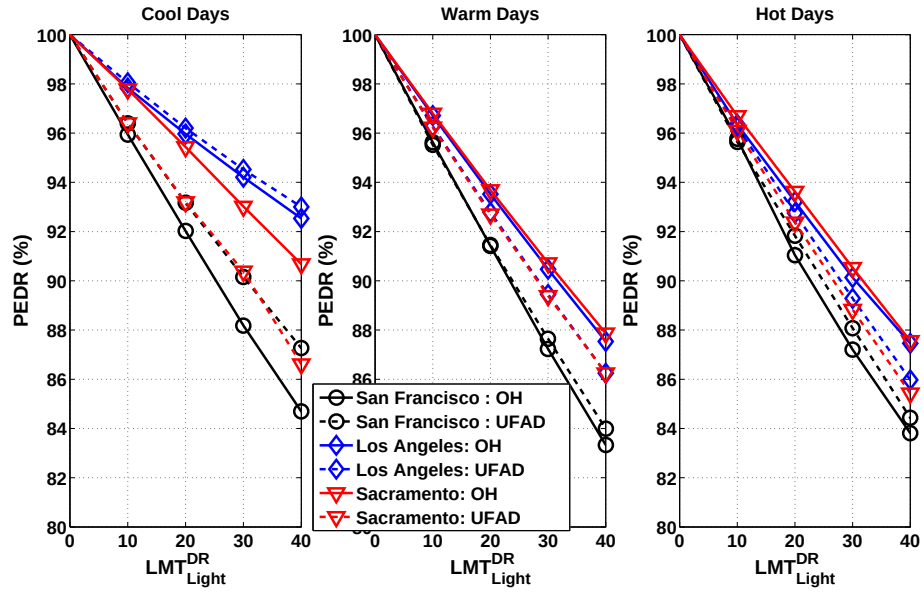

(a)

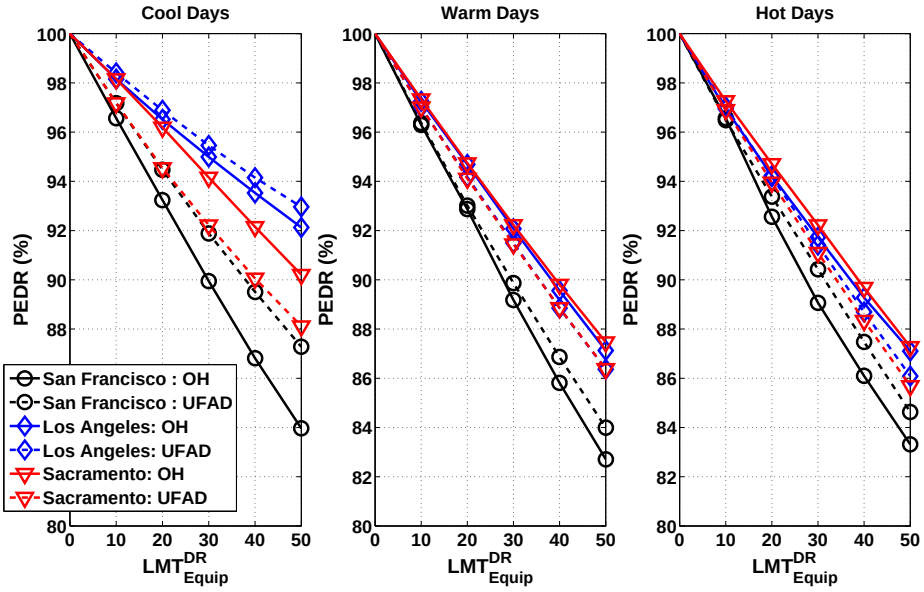

(b)

Figure 5.8: PEDR of the ELT and LLT DR activities according to the summer weather categorization : (a) ELT and (b) LLT

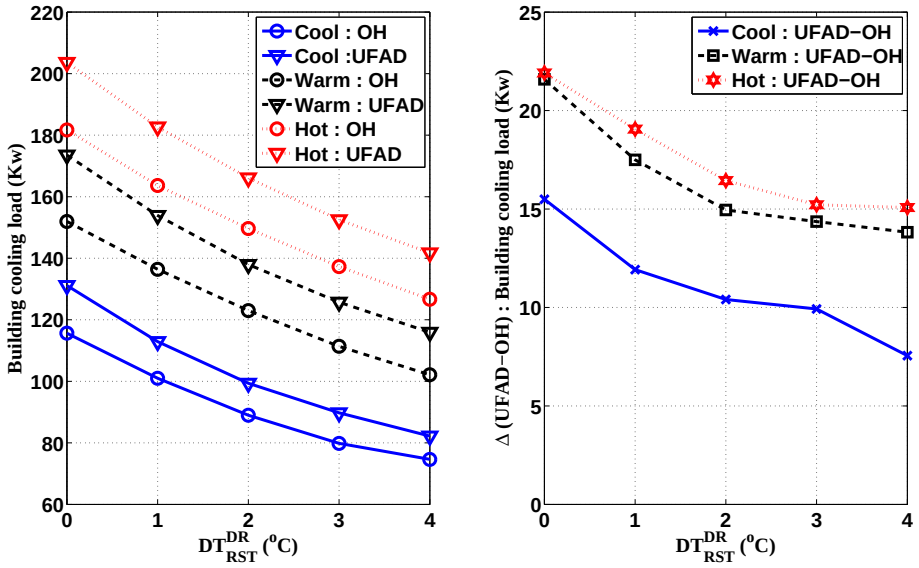

Figure 5.9: Building cooling load change due to the RSTA DR activity following the weather categorization. : the building cooling load (left) and the difference of the building cooling load between the OH and the UFAD (right).

normal operation.

$\dot{H}_{BD}$ of UFAD is always higher than that of OH in the weather categorizations, which is explained by thermal decay of UFAD described in § 4.5.1. The difference of $\dot{H}_{BD}$ between both systems decreased when DT^{DR}_{RST} increases in Figure 5.9 (right), which support that UFAD have higher building cooling load reduction than OH corresponding to DT^{DR}_{RST}.

Secondly, to explain the better DR effectiveness of UFAD, we examined the total air volume flow rate reduction due to the RSTA. Because we employed a VAV (variable air volume) system to control RST for both systems, any attempt to increase or decrease RST influenced total air volume flow rate of the HVAC air circuit. Therefore, the RSTA DR activity reduced total air volume flow rate compared to the flow rate of the normal operation. To estimate how much the air volume flow rate reduced by the RSTA, we measured total air flow rate reduction ratio (TARR), the air flow rate corresponding to DT^{DR}_{RST} normalized by the flow rate under the normal operation, (Figure 5.10). In all location, TARR is lower than 50 % for the both system when $DT^{DR}_{RST} = 4\ ^{o}C$. The TARR

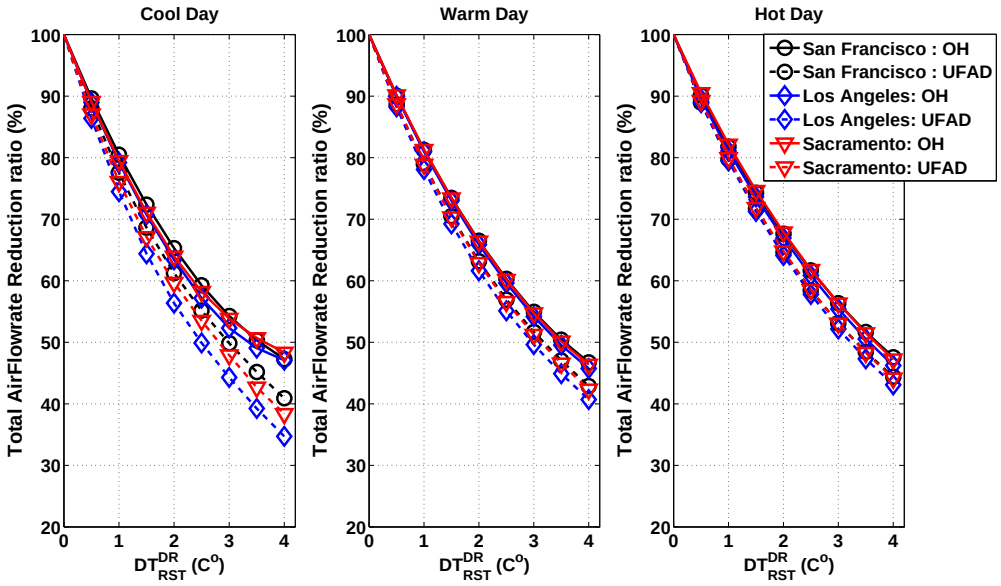

Figure 5.10: Total air flow rate reduction due to the RSTA DR activity following the weather categorization averaged over the DR period on the summer weekday

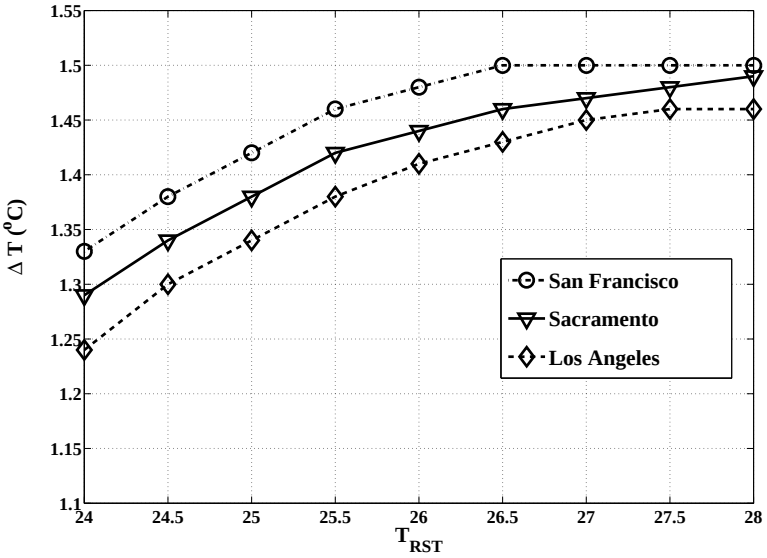

Figure 5.11: A comparison graph of the temperature difference between the lower occupied zone and the upper hot air zone, ΔT against room set point temperature T_{RST} among the three different climates on summer weekdays; the data points were measured by averaging hourly ΔT over DR period

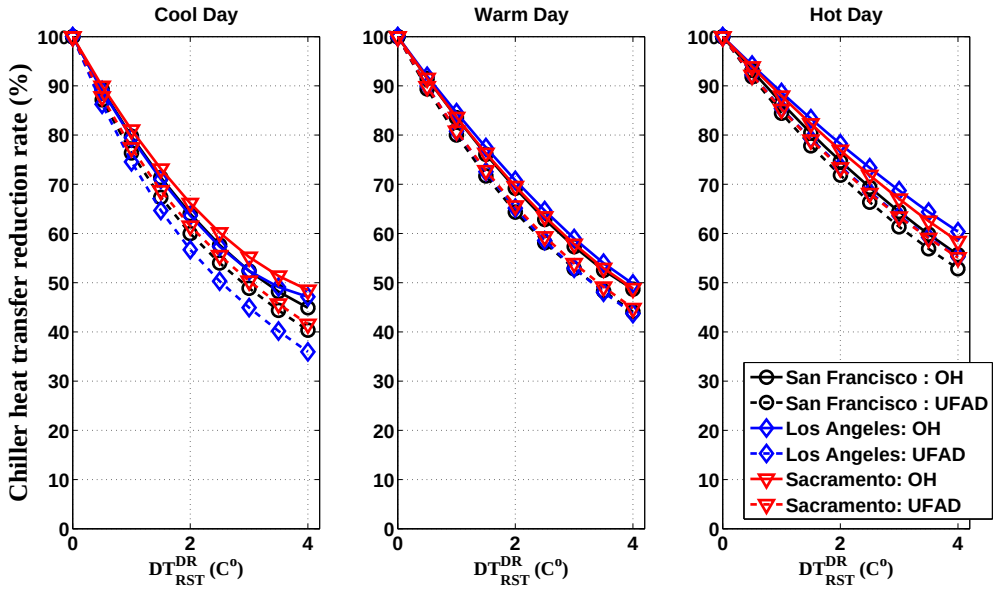

Figure 5.12: The chiller heat transfer rate reduction ratio due to the RSTA DR activity averaged over the DR period on the summer weekday following the summer categorization

of UFAD on the cool day was approximately 40 % of the value of the normal operation. Additionally, UFAD had a reduced air flow rate compared to OH for all locations and weather conditions.

The UFAD's advantage of reducing the air flow rate can be explained by the thermal stratification which was an unique characteristic for the UFAD to have higher return temperature T_{RT} than the OH under the same operating condition. Stronger thermal stratification existed in a room, T_{RT} get higher to reduce air volume flow rate for satisfying heat budget in a room. From Figure 5.11, as T_{RST} (room set point temperature) increased, or DT^{DR}_{RST} increased, the temperature difference between the occupied zone and the upper hot air zone also increased in all climates, which caused T_{RT} relative to the occupied zone temperature to be higher than the normal operation. Therefore, the additional air flow rate reduction due to increased thermal stratification happened when DT^{DR}_{RST} increased. Because the air flow rate was directly related to the fan energy consumption, UFAD was more effective in reducing the fan energy compared to OH for the RSTA DR activity.

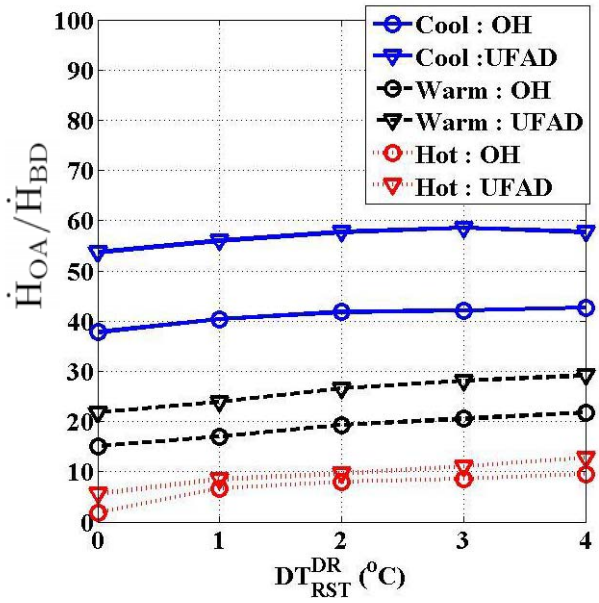

Figure 5.13: Normalized cooling load of the economizer $\dot{H}_{OA}/\dot{H}_{BD}$ change due to the RSTA DR activity averaged over the DR period on the summer weekday following the summer categorization

Thirdly, we investigated how much the chiller energy can be saved by the RSTA. The chiller heat transfer rate reduction due to the RSTA was plotted for different weather categorizations in Figure 5.12. Independent of the climate zones, the reduction for UFAD was greater than that of OH, which is similar to the results of the $\dot{H}_{BD}$ reduction in Figure 5.9. The reason of UFAD's higher effectiveness to reduce the chiller heat transfer rate is explained by additional "free cooling" of the economizer of UFAD. The economizer which open when $T_{outside} < T_{RT}$ should have more "free cooling" when T_{RT} increases. While $T_{RT} = T_{RST}$ in OH, T_{RT} in UFAD is higher than T_{RST} due to thermal stratification when the same RSTA applied both systems. Furthermore, when DT_{RST}^{DR} increased, as seen in Figure 5.11, T_{RT} of UFAD got higher than T_{RT} of OH because $T_{RT} = T_{Room}$ in OH. The economizer open when $T_{outside} < T_{RT}$ (as described in § 4.5.2), so higher T_{RT} should increase a chance to have more "free cooling". From Figure 5.13, the normalized cooling load of the economizer $\dot{H}_{OA}/\dot{H}_{BD}$ of UFAD is higher than that of OH; as $\dot{H}_{OA}/\dot{H}_{BD}$ increased, the chiller heat transfer rate decreased. In other words, higher $\dot{H}_{OA}/\dot{H}_{BD}$ corresponds to more "free cooling" for reducing chiller heat transfer

rate. Therefore, the increased thermal stratification as DT_{RST}^{DR} increased let UFAD have more chiller heat transfer rate reduction compared to OH.

5.5 Conclusion

We examined the effectiveness of DR strategies to investigate difference of electricity demand of OH and UFAD. Applying the DR strategies such as RSTA, ELT or LLT, a building reduce, its electricity demand of HVAC to relieve its peak electricity demand to avoid overloading the electricity grid. To examine DR effectiveness on DR strategies, baseline-building configurations of OH and UFAD with an internal load configuration (internal load #1) are chosen and the performance of the DR strategies is inspected among three different climate zones. RSTA shows better DR effectiveness compared to LLT or ELT. RSTA on UFAD is more effective than OH on LA and SC in which higher electricity demands are needed during summer.

By RSTA as a DR activity, UFAD have higher building cooling load reduction than OH when DT_{RST}^{DR} increases. UFAD also have higher total air flow rate reduction compared to OH due to relatively higher T_{RT} of UFAD caused by the thermal stratification. The higher total air flow rate reduction of UFAD corresponds to fan energy saving. Additionally, by increasing T_{RT}, UFAD also reduced the chiller heat transfer rate for additional chiller energy savings compared to OH because the economizer of UFAD had more “free cooling” than that of OH. Combining those results, the higher DR effectiveness of UFAD was explained by the fan and chiller energy reduction compared to OH.

UFAD reveals the greatest DR effectiveness on ”Hot” days ($T_{ambient}^{daymax}$ is higher than 29.4 ^{o}C), when intensive DR activities are needed. In practice, better DR effectiveness of UFAD provides occupants with more thermal comfort or achieve deeper electricity demand reduction than OH. Based on those results, UFAD is considered as an enhanced HVAC system offering more benefits to occupants or building operation during DR activities than a traditional OH ventilation system.

Chapter 5, in part, includes reprints of the material as it appears in “Final report: Simulation of energy performance of Underfloor Air Distribution (UFAD) sys-

tem", *Building energy research grant (BERG) program.*, (Grant number: 54917A/06-05B), Linden, P., Webster, T., Bauman, F., Yu, J.K., Lee, K.H., Schiavon S., and Daly, A. 2009. The dissertation author was the primary investigator and author of the paper.

Bibliography

[1] Alberson, M.L., Dai, Y.B., Jensen, R.A. & Rouse, H. 1950 Diffusion of submerged jets. *Trans. ASCE.*, **115**, 639–697.

[2] Anonymous List of power outages Wikipedia

[3] Ansong, J.K., Kyba, P. & Sutherland, B.R. 2008 Fountains impinging on a density interface. *J. Fluid Mech..*, **595**, 115–139.

[4] Baines, W. D. & Turner, J.S. 1969 Turbulent buoyant convection in a source in a confinned region *J. Fluid Mech.*, **37**, 51–80.

[5] Baines, W.D. 1975 Entrainment by a plume or jet at a density interface. *J. Fluid Mech.*, **68**, 309–320.

[6] Bauman, F. & Webster T. 2001 Outlook for Underfloor Air Distribution *ASHRAE Journal.*, **Vol. 43, No. 6, June**, 18–27.

[7] Bauman, F. 2003. *Underfloor Air Distribution (UFAD) Design Guide.* Atlanta: ASHRAE, American Society of Heating, Refrigerating, and Air-Conditioning Engineers.,

[8] Bauman, F., Jin, H., and Webster, T. 2006. Heat Transfer Pathways in Underfloor Air Distribution (UFAD) Systems. *ASHRAE Transactions.*, **Vol. 112, Part 2.**, 567–580

[9] Bolster D. & Linden P.F. 2007 Contaminants in ventilated filling boxes *J. of Fluid Mech..*, **591**, 97–116.

[10] Bloomfield L.J. & Kerr R.C. 1998 Turbulent fountains in a stratified fluid. *J. Fluid Mech..*, **358**, 336–356.

[11] Bloomfield L.J. & Kerr R.C. 2000 A theoretical model of a turbulent fountain. *J. Fluid Mech..*, **424**, 197–216.

[12] Cardoso, S. S. S. & Woods, A. W. 1993 Mixing by a turbulent plume in a confined stratified region *J. Fluid Mech..*, **250**, 277–305.

[13] California Energy Commission, 2007, Title 24 of the California Code of Regulations (California Building Standards Code). *California Energy Commission*

[14] Chenvidyakarn T. & Woods, A.W. 2008 On underfloor air-conditioning of a room containing a distributed heat source and a localised heat source *Energy and Building.*, **40**, 1220–1227.

[15] Crawley, D.B., Pederson, C.O., Lawrie, L.K., & Winkelmann F.C. 2000 EnergyPlus: Energy Simulation Program *ASHRAE Journal.*, **42**, 49-56.

[16] Various authors Engineerging reference *Energyplus documentation.*

[17] Daly, A. 2006. Underfloor vs. Overhead: A Comparative Analysis of Air Distribution Systems using the EnergyPlus Simulation Software. *Master's Thesis, Department of Architecture, University of California, Berkeley.*

[18] Djuric, N., Novakovic, V., Holst, J., & Mitrovic Z. 2007 Optimization of energy consumption in buildings with hydronic heating systems considering thermal comfort by use of computer-based tools *Energy and Building.*, **39**, 471–477.

[19] Dominique, M. & Guitton P. 1997 *The Performance of Displacement Ventilation Systems . Experimental and Theoretical Studies Proc. of Building Simulation 1997.* **Vol. 26**

[20] Fisher H.B. John List E., Koh, R.C.Y. Imberger J. & Brooks N.H. Mixng in inlnad and coastal waters *Academic Press 1979*

[21] Hunt, G. R. & Kaye, N. G Virtual origin correction for lazy turbulent plumes. *J. Fluid Mech.*, **435**, 369–377.

[22] Jin, H., F. Bauman, and T. Webster. 2006. Testing and Modeling of Underfloor Air Supply Plenums. *ASHRAE Transactions.*,, **Vol. 112 Part 2.**, 581–591

[23] Kato A. & Phillips, M. On the penetration of a turbulent layer into a stratified liquid. *J. Fluid Mech.*, **37**, 643–655.

[24] Kaye, N.B. & Hunt, G.R. 2004 Time-dependent flows in an emptying filling box *J. Fluid Mech.*, **520**, 135–156.

[25] Kiliccote, Piette & Hansen 2006 Advanced Controls and Communications for Demand Response and Energy Efficiency in Commercial Buildings *Second Carnegie Mellon Conference in Electric Power Systems: Monitoring, Sensing, Software and Its Valuation for the Changing Electric Power Industry, January 12, 2006, Pittsburgh, PA.*

[26] Kumagai, M. 1984 Turbulent buoyant convection from a source in a confined two-layered region. *J. Fluid Mech.*, **147**, 105–131.

[27] Lee, J. & Chu, V. 2003 Turbulent Jets and Plumes : A Lagrangian Approach *Kluwer Academic Publishers, Boston (2003).*

[28] Lee, K.H. & Strand R.K. 2008 The cooling and heating potential of an earth tube system in buildings *Energy and Building.*, **40** , 486–494 .

[29] Lin, Y.J.P. 2003 Plumes and jets in Semi-Confined Spaces. *Ph.D. thesis.*,University of California, San Diego.

[30] Lin, Y.J.P. & Linden P.F. 2005 A model for an underfloor air distribution system. *Energy and Building.*,**37**, 399–409 .

[31] Lin, Y.J.P. & Linden P.F. 2005 The entrainment due to a turbulent fountain at a density interface. *J. Fluid Mech.*, **542**, 25 –52 .

[32] Linden P.F. 1973 The interaction of a vortex ring with a sharp density interface: a model for turbulent entrainment *J. Fluid Mech..*, **60**, 467–480.

[33] Linden PF, Laneserff GF & Smeed DA Emptying filling boxes - The fluid-mechanics of natural ventilation *J. Fluid Mech.*, **212**, 309 –335 .

[34] Linden, P., Webster, T., Bauman, F., Yu, J.K., Lee, K.H., Schiavon S., and Daly, A. Final report: Simulation of energy performance of Underfloor Air Distribution (UFAD) system *Building energy research grant (BERG) program.*, **Grant number: 54917A/06-05B**

[35] List, E. J. 1982 Turbulent jets and plumes. *Ann. Rew. Fluid Mech..*, **14**, 189–212.

[36] Liu Li & Mak C.M. 2007 The assessment of the performance of a windcatcher system using computational fluid dynamics. *Building and Environment.*, **42**, 1135–1141 .

[37] Liu, Q. 2006 Flow dynamics of Underfloor Air Distribution System *Ph.D. thesis.*,University of California, San Diego.

[38] Liu, Q. and Linden, P. 2008. The EnergyPlus UFAD Module. *Proceedings of SimBuild 2008, Berkeley, CA, July 30-August 1.*

[39] McDougall, T. J. 1981 Negatively buoyant veritcal jets. *Tellus* ., **33**, 313–320.

[40] Mcdonell G. 2003 Underfloor & Displacement; why ther're not the same. *ASHRAE Journal* ., **July**, 18–22

[41] McLauchlan, D.J. 2008 BACnet for Green Library *ASHRAE Journal* ., **Vol. 50, No. 11**, B37–41

[42] Miyazaki, T., Akisawa, A., & Kashiwagi 2005 Energy savings of office buildings by the use of semi-transparent solar cells for windows. *Renewable Energy* ., **30**, 281–304

[43] Morton, B.R. 1959 Forced plumes *J. Fluid Mech.*, **5**, 151–163.

[44] Morton, B.R., Taylor, G.I. & Turner, J.S. 1956 Turbulent gravitational convection from maintained and instantanious sources *Proc. Royal Soc. A.*, **234**, 1–23.

[45] Morton, B.R. & Middleton, J. 1973 Scale diagrams for forced plumes *J. Fluid Mech.*, **58**, 165–176.

[46] Munt E. 1996 *The Performance of Displacement Ventilation Systems . Experimental and Theoretical Studies Building Services Engineering KTH, Stockholm.*, Ph. D. Thesis, Bulletin N38.

[47] Naguib, R. The author responds *ASHRAE Journal* ., **Vol 51, No. 7**, 12.

[48] Olesen B.W. 2002 Radiant Floor Heating In Theory and Practice. *ASHRAE Journal.*, **July**, 19–24 .

[49] Orans, R. et al. 2006 Phase 1 Results: Incentives and Rate Design for Energy Efficiency and Demand Response *California Energy Commission, PIER DRRC.*, **LBNL.60133. April 2006**

[50] Papanicolaou, P.N., Papakonstantis, I.G. & Christodoulou, G.C. 2008 On the entrainment coefficient in negatively buoyant jets *J. Fluid Mech.*, **614**, 447–470.

[51] Rees, S.J. & Haves, H. *A nodal model for displacement ventilation and chilled ceiling systems in office spaces Building and Environment.*, **Vol. 26**, 753-762.

[52] Roth, K., Dieckmann, J. & Brodrick J. Using Off-Peak Precooling *ASHRAE Journal* **Vol.51(3)**, 80–83

[53] Sandberg M. and Blomqvist C. 1989 *Displacement ventilation systems in office rooms ASHRAE Trans..*, **95 (2)**, 1041–1049.

[54] Sodec, F., & Craig, R. 1990 The underfloor air supply system.the European experience *ASHRAE Trans* ., **Vol. 96, Part 2**

[55] Svensson, A.G.L 1989 Nordic experiences of displacement ventilation systems *ASHRAE Trans* ., **Vol. 95, Part 2**

[56] Turner, J. S. 1966 Jets and plumes with negative or reversing buoyancy. *J. Fluid Mech.*, **26**, 779–792.

[57] Turner, J. S. 1968 The influence of molecular diffusivity on turbulent entrainment across a density interface. *J. Fluid Mech.*, **33**, 639–656.

[58] Wilde P., Rafiq Y. & Beck M. 2008 Uncertainties in predicting the impact of climate change on thermal performance of domestic buildings in the UK. *Building Serv. Eng. Res. Technol..*, **29(1)**, 7-26.

[59] Wright, F.L. The Early Work of Frank Lloyd Wright: The "Ausgefuhrte Bauten" of 1982 *Dover publications, Inc.*.

[60] Wyon, D.P. & Sandberg, M. 1980 Thermal manikin prediction of discomfort due to displacement ventilation *ASHRAE Trans..*, **96(1)**, 67 – 75.

[61] Weidner S., Doerger J., and Walsh M. 2009 Cooling with less air *ASHRAE Journal* ., **Vol. 51 No. 12**, 34–40

[62] Xu, T.T., Carrie, F.R., Dickerhoff, D.J., Fisk, W.J., McWilliams, J., Wang, D. & Modera M.P. Performance of thermal distribution systems in large commercial buildings *Energy and Buildings.*, **34**, 215–226.

[63] Yeo M.S., Yang, I.H. & Kim K.W. 2003 Historical changes and recent energy saving potential of residential heating in Korea *Energy and Buildings.*, **35**, 715-727.